

**GEOLOGICA ULTRAIECTINA**

**MEDELINGEN VAN DE  
FACULTEIT GEOWETENSCHAPPEN  
UNIVERSITEIT UTRECHT**

**No. 231**

**Heterogeneity, Uncertainty and Process Identification  
in Early Diagenesis:**

**New Model Developments with Applications to Biological Mixing**

**Christof Meile**

GEOLOGICA ULTRAIECTINA

MEDELINGEN VAN DE  
FACULTEIT GEOWETENSCHAPPEN  
UNIVERSITEIT UTRECHT

No. 231

Heterogeneity, Uncertainty and Process Identification  
in Early Diagenesis:

New Model Developments with Applications to Biological Mixing

Christof Meile

**Heterogeneity, Uncertainty and Process Identification  
in Early Diagenesis:**

**New Model Developments with Applications to Biological Mixing**

**Heterogeniteit, onzekerheid en proces-identificatie in  
vroeg diagenese:**

**Nieuwe modelontwikkelingen met toepassingen op het gebied van biologische  
menging**

(met een samenvatting in het Nederlands)

Dissertation presented for the degree of doctor at Utrecht University  
under the authority of the rector Prof. W.H. Gispen  
to be defended in public on September 22, 2003 at 12.45 o'clock,  
in accordance with the decision made by the Board for the Conferral of Doctoral Degrees

by

Christof Dieter Meile

~~born in Münsterlingen, Switzerland, on August 20, 1970~~

---

Supervisor:  
Prof. P. Van Cappellen  
Department of Geochemistry  
Faculty of Earth Sciences  
Utrecht University

The doctoral dissertation was produced with the financial support of the Institute for Paleoenvironments and Paleoclimate Utrecht (IPPU) and the Netherlands Organisation of Scientific Research (NWO-Pionier)

ISBN 90-5744-089-X

Piaget: What makes the wind?

Julia: The trees.

Piaget: How do you know?

Julia: I saw them waving their arms.

Piaget: How does that make the wind?

Julia (waiving her hands): Like this. Only they are bigger. And there are lots of trees.

Piaget: What makes the wind on the ocean?

Julia: It blows there from the land. No. It's the waves...

*Dialogue attributed to Jean Piaget (1896-1980)*

## TABLE OF CONTENTS

<b>ACKNOWLEDGMENTS</b>	<b>9</b>
<b>SUMMARY/SAMENVATING</b>	<b>11</b>
<b>CHAPTER 1</b>	<b>13</b>
Introduction	
<b>CHAPTER 2</b>	<b>25</b>
Meile, C., and Van Cappellen, P. (2003). Global estimates of enhanced solute transport in marine sediments. <i>Limnology and Oceanography</i> 48(2): 777-786.	
<b>CHAPTER 3</b>	<b>43</b>
Meile, C., Koretsky, C.M., Van Cappellen, P. (2001). Quantifying bioirrigation in aquatic sediments: An inverse modeling approach. <i>Limnology and Oceanography</i> 46(1): 164-177.	
<b>CHAPTER 4</b>	<b>63</b>
Koretsky, C.M., Meile, C., Van Cappellen, P. (2002). Quantifying bioirrigation using ecological parameters: A stochastic approach. <i>Geochemical Transactions</i> 3(3): 17-30.	
<b>CHAPTERS</b>	<b>87</b>
Meile, C., Tuncay, K., and Van Cappellen, P. (2003). Explicit representation of spatial heterogeneity in reactive transport models: Application to bioirrigated sediments. <i>Journal of Geochemical Exploration</i> 78-79: 231-234.	
<b>CHAPTER 6</b>	<b>93</b>
Meile, C., and Van Cappellen, P. (in preparation). Particle age distribution and O <sub>2</sub> exposure time: Timescales in bioturbated sediments.	
<b>CHAPTER 7</b>	<b>111</b>
Meile, C. and Regnier, P. (in preparation). Towards a flexible modeling framework for objective analysis of dynamic aquatic systems.	
<b>CURRICULUM VITAE</b>	<b>135</b>

## **ACKNOWLEDGMENTS**

I would like to thank Philippe Van Cappellen for his advice, support, the freedom of exploration, friendship and the possibility for my extensive stays abroad. The members of my reading committee, B. Boudreau, C. Heip, R. Jahnke, J. Middelburg, M. Schluter, P. Regnier and B. van der Zwaan, are thanked for carefully reading the thesis and valuable feedback.

Not to a small part, my life in Utrecht was fun due to the excellent company I had with Christelle, Parisa, and occasionally Jeff, in the office, and the Geochemistry department as a whole. I truly enjoyed the interactions with our more experimentally working group members. For getting the thesis printed, thanks go to C6line and Pien. I also would like to thank Anniet and Caroline for the Dutch translation of the summary and Kagan, Parisa, Pien'e, David and Ralf for the nice collaborations and common projects still to come.

I also would like to thank Carla Koretsky for the continued collaboration and Bernhard Wehrli, who introduced me to science and made my initial journey across the Atlantic, which later lead to my move to the Netherlands, possible.

Financial support from the Institute for Paleoenvironments and Paleoclimate Utrecht (IPPU) and the Netherlands Organisation of Scientific Research (NWO-Pionier), and the hospitality I experienced both at the School of Marine Sciences at the University of Georgia, USA. and at the Hanse Institute for Advanced Study in Delmenhorst, Germany, are gratefully acknowledged.

Finally, I want to thank my parents for the strong and unconditional love and support. I hope to be able to follow their example. And I want to thank Mandy for not getting too tired of the long transatlantic commutes over the years. Support for mental balance from Casey Bubba, Ben "the animal" and Tobs is also acknowledged.

Christof Meile

## ***SUMMARY***

Within the last decades, there have been spectacular developments in experimental and analytical techniques that allow geochemists and biologists to acquire ever more detailed data sets on aquatic sediments. These data sets often combine high-resolution chemical distributions with rate determinations, and information on resident biological communities and their activities. This wealth of data, in turn, creates a need for new diagnostic models that account for the complex interactions documented by field and experimental studies. Models of early diagenesis must therefore integrate knowledge from a wide variety of scientific fields, from transport theory and chemistry, to molecular biology and benthic ecology. Only by incorporating meaningful representations of the dominant processes, are these models able to scale reactive transport interactions from the local to the regional and, ultimately, global scale.

This thesis focuses on the quantitative description of (1) biologically-induced transport processes, and (2) the coupling of reaction and transport processes. It presents three innovative approaches to quantify pore water transport other than molecular diffusion. Two of the approaches compute site-specific depth distributions of solute mixing intensities, but they differ fundamentally in the type of input data. One approach is based on chemical concentration and rate measurements, the other uses ecological data on the infaunal community. Despite their differences, both approaches yield comparable bioirrigation intensities.

In the third approach, measured benthic oxygen uptake fluxes across a wide variety of oceanic environments are used to derive global relationships for enhanced solute transport rates in sediments. This last approach bridges the gap between site-specific studies of pore water irrigation and regional to global assessments of the role of benthic-pelagic coupling in ocean biogeochemistry. The estimates of enhanced solute transport intensities clearly demonstrate that bioirrigation has a major global impact on solute exchanges between the water column and sediments.

Next, the fate of particulate matter in bioturbated sediments is modeled using a stochastic Lagrangian approach. Individual particle histories are explicitly computed from probability density functions that embody the nature of particle transport by bioturbation. The analysis of the results provides insight into the emergence and variability of particle properties relevant for the interpretation of the sedimentary record. In particular, the effect of bioturbation on the oxygen exposure time (OET) of unreactive and reactive particles is investigated.

Finally, two advanced modeling environments for early diagenesis are presented. In the first one, a flexible reaction network simulator is coupled to one-dimensional (1D) transport descriptions. As the reaction network is easily modified and adapted by the user, it is ideally suited to explore biogeochemical reaction systems of increasing complexity. The 1D forward reaction-transport model is further combined with local and global optimization algorithms to enhance model parameterization based on observational data. The second model environment is a preliminary version of a multidimensional reactive transport code for early diagenetic applications.



## **SAMENVATTING**

De laatste decennia zijn er spectaculaire ontwikkelingen geweest in experimentele en analytische technieken op het gebied van de biogeochemie. Deze stellen geochemici en biologen in staat steeds meer gedetailleerde gegevens te verkrijgen over aquatische sedimenten. De gegevens zijn meestal een combinatie van chemische metingen in hoge resolutie, inclusief de bepaling van reactiesnelheden, en informatie over de aanwezige biologische gemeenschappen en hun activiteit. Deze rijkdom aan gegevens heeft geleid tot de vraag naar nieuwe diagnostische modellen die rekening houden met de complexe interacties die in veld- en laboratoriummetingen worden vastgesteld. Vroeg diagenetische modellen zijn noodzakelijk om de kennis te integreren van een breed scala aan wetenschapsgebieden, van transporttheorie en chemie, tot moleculaire biologie en bentische ecologie. Alleen door een zinvolle implementatie van de dominante processen, kan met deze modellen de wisselwerking van reactieve transportprocessen van lokaal tot regionaal en uiteindelijk mondiaal niveau worden opgeschaald.

Dit proefschrift richt zich op de kwantitatieve beschrijving van (1) biologisch-geïnduceerde transportprocessen en (2) de koppeling van reactie en transportprocessen. Het presenteert 3 innovatieve methoden om poriewatertransport, anders dan door moleculaire diffusie, te kwantificeren. Twee van de methoden berekenen locatie-specifieke diepteverdelingen van de intensiteit van vloeistofmenging, maar verschillen fundamenteel in de wijze van invoer van gegevens. De eerste aanpak is gebaseerd op chemische concentraties en metingen van snelheid, de tweede gebruikt ecologische gegevens van de faunagemeenschap. Ondanks de verschillen, leveren beide methoden vergelijkbare bio-irrigatieintensiteiten.

In de derde methode worden gemeten bentische zuurstofopnamefluxen van verschillende oceanbodems gebruikt om mondiale relaties af te leiden voor transportsnelheden van opgeloste stoffen. Deze laatste aanpak slaat een brug tussen de locatie-specifieke studie van poriewaterirrigatie en de regionale tot mondiale rol van bentisch-pelagische koppelingen in de biogeochemie van de oceaan. De schatting van de verhoogde transportintensiteit laat duidelijk zien dat bio-irrigatie een belangrijke mondiale invloed heeft op de uitwisseling van opgeloste stoffen tussen de waterkolom en het sediment.

Vervolgens is het lot van vaste stof deeltjes in gebioturbeerde sedimenten gemodelleerd door middel van een stochastische Lagrangian methode. De geschiedenis van individuele deeltjes is expliciet berekend aan de hand van dichtheidsfuncties om het deeltjes-transport door bioturbatie vorm te geven. De analyse van de resultaten biedt inzicht in het voorkomen en de variabiliteit van sedimentkarakteristieken die relevant zijn voor de interpretatie van de geschiedenis van het sediment. In het bijzonder is het effect onderzocht van bioturbatie op de tijd van blootstelling aan zuurstof van niet-reactieve en reactieve deeltjes.

Tenslotte worden twee geavanceerde modelsystemen voor vroege diagenese gepresenteerd. In de eerste wordt een flexibel reactienetwerk gekoppeld aan een-dimensionale (1D) transportbeschrijvingen. Het reactienetwerk kan eenvoudig door de gebruiker gemodificeerd en aangepast worden en is daarom uitermate geschikt om biogeochemische reactiesystemen met een toenemende complexiteit te onderzoeken. Het 1D-voorwaarts reactief-transportmodel is verder gecombineerd met lokale en globale optimalisatie-algoritmes om modelparameterisatie op basis van gemeten gegevens mogelijk te maken. Het tweede modelsysteem is een voorlopige versie van een multi-dimensionaal reactieve transportcode voor vroege diagenese.

## **CHAPTER 1: Introduction**

Elemental cycling in aquatic sediments results from the interplay of transport and reaction processes. Both types of processes can be purely abiotic or directly driven by the activities of biological organisms. Hence, models of early diagenesis, the sum of processes acting upon sedimentary matter after deposition (literally "stone formation"), have to integrate knowledge from different scientific fields, from physics and chemistry to molecular biology and ecology. Relevant spatial scales extend from molecular (chemical reactions) via micrometer (bacteria), centimeter (benthic fauna) to kilometer and larger scales (global biogeochemical cycles). Similarly, reactive timescales ranging from less than one second (acid-base reactions) to, say, glacial-interglacial variations of organic matter rain rate may have to be considered.

Quantitative assessment of early diagenetic processes at different scales is the topic of this thesis. Theoretical and observational aspects of different scientific disciplines are incorporated in modeling approaches designed to span spatial dimensions ranging from the micro-scale to the entire globe. In particular, the effects of transport induced by benthic fauna on early diagenesis are investigated, with the aim of incorporating ecological information and knowledge into model representations of early diagenesis.

Mathematical models are abstract, scale- and context-dependent approximations of our perception of the world, meant to reflect the determining factors and relevant processes. Because of the implementation of simplifying assumptions, which do not fully reflect the complex nature of aquatic sediments, and also because of inherent analytical uncertainty, there will never be a perfect match between model results and measurements. Hence, model results are supposed to identify patterns and trends, rather than being exact mirrors of reality. However, model validation is typically linked to field data. This thesis incorporates approaches that either explicitly take into account measurement uncertainty, provide probabilistic estimates of natural variability, or statistically compare competing model structures. As such, it aims at a fundamental and quantitative integration of modeling efforts with experimental work and field observations.

In this introduction, first a brief description of aquatic sediments and their importance in biogeochemical cycling are given. In section "Models of early diagenesis" the modeling framework is discussed and, finally, in the section "Overview and organization of the thesis", the topics treated in the individual chapters are introduced and the connections between them are highlighted.

### **Marine sediments**

Marine sediments cover about 75% of the Earth's surface and are arguably one of the world's most prominent bioreactors. They constitute an environment where a dense aggregation of life inhabits a rich diversity of (geo-)ecological niches. Because of a continuous supply of chemical energy, mostly under the form of organic matter, sharp compositional gradients exist below the sediment-water interface (SWI). Deposited particulate matter and pore waters are maintained in a state of non-equilibrium, which creates the opportunity for a multitude of transformation processes, some purely abiotic while others are carried out directly by organisms.

Marine sediments vary significantly in composition, depending on the sources of particulate matter accumulating at the seafloor. They may be dominated by biogenic constituents, such as siliceous and calcareous oozes, or by lithogenic matter as, for instance, deltaic deposits.

However, organic matter deposition and bottom water oxygen concentration are by far the dominant controls on benthic biological activity and early diagenetic transformations. In the modern oceans, with the exception of oxygen minimum zones and stratified basins, bottom waters are well-oxygenated. Hence, differences in early diagenetic environments are primarily the result of differences in the supply flux and reactivity of organic matter reaching the SWI (e.g., (JØRGENSEN, 1983; TROMPET al., 1995)).

Physical transport processes are typically orders of magnitude slower in sediments compared to the overlying turbulent water column. This results in longer residence times of chemical constituents in the sediments and accumulation of energy rich substrates such as settling particulate organic matter, fueling biochemical activity. Thus, a reaction process, which plays a minor role in the water column, may have a large effect on the distribution of a given chemical constituent in the sediment. In general, the representation of chemical transformations in models of early diagenesis depends on the relative time scales of reaction and transport processes. For example, proton exchange reactions are often sufficiently fast, relative to solute and particulate transport rates, that they can be implemented assuming local equilibrium between the acid and base species. However, many reactions in aquatic sediments exhibit longer characteristic time scales and, therefore, require kinetic expressions (Figure 1). For a complete description of chemical cycles in sediments, the equilibrium or kinetic representations of chemical transformations must be coupled to transport equations for all independent constituents (STEEFEL and MACQUARRIE, 1996).

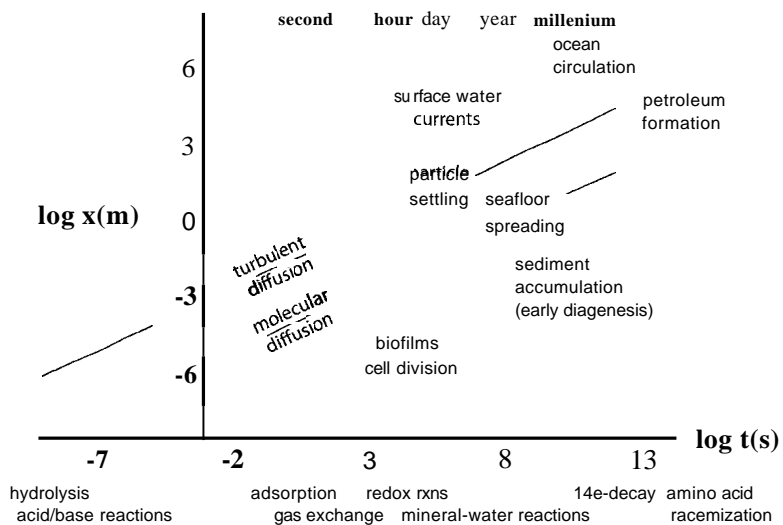


Figure 1. Characteristic time and length scales occurring in aquatic environments. Diffusive time and length scales are calculated as  $t = x^2/2D$ , with a molecular diffusion coefficient of  $10^{-5} \text{ cm}^2 \text{ s}^{-1}$  and an eddy diffusion coefficient of  $1 \text{ cm}^2 \text{ s}^{-1}$ , respectively.

Early diagenetic sequences have been studied extensively in the deep-sea (e.g. (FROELICH et al., 1979)). Because only a small fraction of net primary production in the surface ocean reaches the seafloor (e.g. (SCHLESINGER, 1997)), sediment respiration rates and benthic solute

exchange fluxes are low. As these sediments exhibit a predictable vertical succession of well-separated redox zones, they are often viewed as stable, near-steady state systems. More detailed studies over the past few decades have revealed quite the contrary, however. Rapid transfer of biogenic material from the surface ocean to the seafloor results in a strong benthic-pelagic coupling than previously recognized and even at water depths exceeding several kilometers, benthic biological activity and early diagenetic sequences are found to record seasonal and interannual variations in surface primary production (e.g., (RABUILLE et al., 2001; SOETAERT et al., 1996a)).

When considering coastal sediments, spatial and temporal heterogeneity experiences a quantum leap compared to deep-sea sediments. This presents formidable challenges, both in terms of data acquisition and modeling. Nonetheless, a quantitative understanding of early diagenesis in near shore sediments is crucial, in order to predict the impact on the coastal ocean of the rapidly growing human populations along the coastlines (NOAA, 1999; VER et al., 1999). Of particular concern is the role of sediments in coastal eutrophication (ROWE et al., 1975).

Increased input of biodegradable organic matter modifies the benthic regeneration of nutrients (N and P) and may lead to enhanced release of gaseous constituents, such as CH<sub>4</sub> and N<sub>2</sub>O. Eutrophication also affects benthic infauna, which are especially abundant in coastal sediments. Increased primary production may initially stimulate growth of the benthic faunal community, because of a higher food supply (JOSEFSON, 1990). With advancing eutrophication, however, hypoxia may eliminate species and cause shifts in the benthic community structure (ROSENBERG, 2001), which in turn affects the coupling between sediment and water column processes (THOMPSON and SCHAFFNER, 2001).

Activities of benthic fauna, including particle ingestion, excretion, grazing, burrowing and flushing, have major impact on geochemical conditions and gradients in sediments (HEIP et al., 2001) and references therein). They also affect sediment stability (DE DECKERE et al., 2001), particle size distributions (GIANGRANDE et al., 2002), microbial community structure (MARINELLI et al., 2002), chemical heterogeneity and organic matter preservation (JAHNKE, 1985; MAYER et al., 1995), and benthic exchange fluxes (ALLER et al., 1998; GRAF and ROSENBERG, 1997). Burrowing macrofauna in particular influence pore water distributions (BULL and TAILLEFERT, 2001) and solute fluxes across the SWI (ARCHER and DEVOL, 1992). Flushing intensities of 10-100 ml hr<sup>-1</sup> have been reported for burrowing organisms (KRISTENSEN, 2001). For a typical density of, say, 100 organisms m<sup>-2</sup> in a coastal setting, this corresponds to 1-10 liters of water exchanged per hour and per m<sup>2</sup> between the upper sediment layer and the overlying water column. Yet, despite the obvious importance of burrowing activity for sediment biogeochemistry and elemental mass balances, existing models of early diagenesis do not include explicit representations of the abundance, morphology and flushing intensity of burrows, or they do so only in a highly simplified manner.

## Models of early diagenesis

A quantitative description of biogeochemical cycles in sediments requires identification and measurement of the relevant transformation and transport processes. Given the relatively large number of processes, a fundamental understanding of early diagenesis requires the integration of diverse data sets and information. This is most efficiently done through the formulation of quantitative models, which combine reasoning (common sense) with observational constraints.

The selection of processes and their representation in a model depend on data availability and modeling objectives. The latter may diverge from one model application to another and may include, for instance, data interpretation, hypothesis building and testing, identification of dominant external forcings and system properties, or design of field experiments. Model complexity also depends on the spatio-temporal scale of interest. For example, rapid transport of solutes through individual burrows (KRISTENSEN et al., 1991) does not need to be resolved explicitly if the effects of seasonal changes in organic matter rain rate on benthic fluxes are investigated across an entire ocean basin (RABOUILLE et al., 2001). On the other hand, such a level of detail is necessary if the goal is to explain the coexistence of physiologically distinct groups of microorganisms within the upper few centimeters of a sediment (KORETSKY et al., 2003). In general, with increasing spatial and temporal scales, early diagenetic models tend to become increasingly simplified, with mechanistic process formulations progressively giving way to empirical parameterizations.

### Mathematical model

In the natural sciences, a conceptual model is often translated into a mathematical description. Doing so increases the clarity of formulation and gives access to a very powerful formalism with which the implications of the model can be investigated. The most common modeling approach for early diagenesis is based on conservation of mass and discretization of the resulting equations for numerical solution. However, other model types such as learning approaches (neural networks, e.g., (BARCIELA et al., 1999) or rule-based cellular approaches (GUINOT, 2002) can be used. The focus on mass conservation also reflects the paucity of measurements related to momentum and energy transformation in sediments. On the contrary, chemical mass related properties (concentrations) are routinely determined in early diagenetic studies.

The change in mass in a given volume of sediment results from in- and outflows, together with local sources and sinks. Mathematically, this can be represented as

$$\frac{d}{dt} \int_V C dV = - \int_S F dS + \int_V H dV \quad (1)$$

where  $C$  is concentration of a given constituent in units of mass per unit volume,  $S$  and  $V$  are the surface area and volume of the domain, respectively,  $F$  is the flux of the constituent across the volume's surface, and  $H$  is the sink/source term. Choosing a representative elementary volume in which  $C$  is approximately constant and assuming continuous fields (differentiability), Eq. 1 can be reformulated into a system of coupled partial differential equations (PDEs), one for each chemical constituent of interest:

$$\frac{\partial C_i}{\partial t} = -\nabla F_i + H \quad (2)$$

In sediments, molecular diffusion has long been recognized as an important solute transport process. Additionally, imposed pore fluid flow or the moving reference frame (due to accumulation or erosion of sediment at the SWI, Berner 1980) give rise to advective transport of pore water. For solutes in a saturated porous medium with constant fluid density, Eq. 2 can hence be rewritten as

$$\frac{\partial \phi C_i}{\partial t} = \nabla (D_i \phi \nabla C_i - \omega \phi C_i) + \sum R + T_{b,o'} \quad (3)$$

where  $D_i$  is the effective in situ diffusion coefficient,  $\phi$  is porosity.  $C$  is in mass per fluid volume,  $\omega$  is an advection velocity,  $\mathcal{R}$  represents all the reactions acting upon species  $i$ , and

$T_{bio}$  is related to the activity of organisms in the sediment (see below). Eq. 3 highlights that transport and reaction processes are inherently coupled. It has been used extensively in the last 3 decades in studies of coupled elemental cycles in aquatic sediments (e.g., (BERNER, 1980; BOULDIN, 1968; WANG and VAN CAPPELLEN, 1996)).

The mass conservation equations for the chemical constituents are not independent from each other, but coupled through both transport and reaction terms. Taking into account both chemical and electrical forces, and maintaining macroscopic electroneutrality, the diffusive flux  $F_i^{diff}$  is given by (VAN CAPPELLEN and GAILLARD, 1996):

$$F_i^{diff} = -D_i \left[ \nabla C_i + C_i \nabla \ln a_i - \sum_j \frac{z_i C_i}{z_j C_j} \sum_k z_k D_k \left( C_k \nabla \ln a_k + \nabla C_k \right) \right] \quad (4)$$

where  $D_i$ ,  $a$  and  $z$  are tracer diffusion coefficient, activity coefficient and charge,  $n$  is the number of constituents and  $i$ ,  $j$  and  $k$  are species indices. Hence, in a Fickian diffusion description, where  $F_i^{diff} = -D_i \nabla C_i$ , the diffusion coefficient is not constant but depends on the composition of the fluid. However, Eq. 4 reduces to a simple Fickian form for small concentration  $C_i$  or constant background electrolyte (VAN CAPPELLEN and GAILLARD, 1996). Therefore, the coupling through multi-component diffusion is typically of minor importance in marine sediments.

Strong coupling between the individual mass conservation equations arises through the interaction of chemical species undergoing reaction. For example, the rate of homogeneous oxygenation of dissolved  $Fe^{2+}$ ,  $Fe^{2+} + \frac{1}{4} O_2 + \frac{5}{2} H_2O \rightarrow Fe(OH)_3(S) + 2H^+$ ,

can be described as  $R = k \cdot [Fe^{2+}] \cdot [O_2]$ , where  $k$  is an apparent, pH dependent, rate constant (STUMM and MORGAN, 1996). The reaction term,  $R$ , appears in the conservation equations of  $O_2$ ,  $Fe^{2+}$ , protons and iron oxide. Multicomponent reaction coupling requires the simultaneous solution of the set of partial differential equations (PDEs) describing mass conservation of the various constituents.

As most reactions involve different chemical constituents and due to the large number of reactions relevant in early diagenesis, the coupling between constituents through the reaction term tends to be quite strong, and requires simultaneous solution of the set of PDEs.

### Including benthic fauna

Early diagenetic modeling has historically recognized benthic fauna mainly as transport agents of solid and dissolved constituents. Therefore,  $T_{bio}$  (Eq. 3) was identified as a transport process, represented by diffusive, advective or non-local descriptions. Focusing on the primarily vertical changes in chemical composition and reaction rates in the top centimeters, the corresponding expressions for biologically induced solute transport are:

$$T_{bio} = - \frac{\partial}{\partial x} \left( \phi \cdot D_{bio} \cdot \frac{\partial C}{\partial x} \right), \quad (5a)$$

where  $D_{bio}$  is a biological diffusion coefficient (GOLDHABER et al., 1977)

$$T_{bio} = - \frac{\partial}{\partial x} \left( \phi \cdot v_{bio} \cdot C \right), \quad (5b)$$

where  $v_{bio}$  is a biological advection velocity (HAMMOND et al., 1977), and

$$T_{bio} = \phi \cdot \alpha \cdot (C - C_0), \quad (5c)$$

where  $a$  is a non-local exchange coefficient,  $C_0$  is the concentration at the SWI and  $x$  is depth below the SWI (EMERSON et al., 1984; MARTIN and BANTA, 1992).

It has long been recognized that the simplified representations (Eqs. 5a-c) have several, potentially significant, drawbacks (for a review and theoretical improvements see (MEYSMAN, 2001)). For example, the validity of a diffusive description strongly depends on the length scale and frequency of matter displacement (BOUDREAU, 1986; BOUDREAU and IMBODEN, 1987; MEYSMAN et al., 2003, accepted-a), as it results from a statistical aggregation of small random movements in analogy to Brownian motion. Effective diffusive patterns can still be approached in the presence of a diverse benthic faunal population (MEYSMAN et al., 2003, accepted-b), even if individual displacement distances exceeds the characteristic tracer scale (BOUDREAU and IMBODEN, 1987). However, such a description provides no insight into the mechanism of the disturbance caused by organisms. It is also likely to fail to describe time-dependent episodic events which may have a greater impact on early diagenesis than average faunal activities. Furthermore, in Eqs. 5a-c, the organisms causing the transport are not represented at all. By only considering their effect, they are treated as a "hidden phase", even though benthic fauna can contribute up to 50% to total sediment respiration (HEIP et al., 2001).

The use of the non-local exchange formulation for solute transport (Eq. 5c) owes its popularity to its simplicity, its theoretical similarity to the general exchange function approach (BOUDREAU and IMBODEN, 1987), and its equivalence to Aller's tube model (BOUDREAU, 1984). In the tube model, cylindrically shaped, equidistant burrows are continuously flushed with overlying water (ALLER, 1980). As irrigation activity of burrowing organisms is not continuous and burrow structures may be much more complex, Aller's tube model has been extended to include non-continuous flushing (MARINELLI and BOUDREAU, 1996) and changing burrow surface areas with depth (fURUKAWA et al., 2001). Similarly, the direct effect of burrowing organisms on sedimentary respiration has recently been incorporated (fURUKAWA, 2001).

However, feeding strategies may not be reflected by any of the descriptions given by Eq. 5. For example, the resident fauna's response to the arrival of freshly deposited organic matter may be rapid sequestration and translocation below the SWI (LEVIN et al., 1997). Therefore, solid phase displacement has also been modeled as a non-local process involving transition probabilities (JUMARS et al., 1981; SHULL, 2001; TRAUTH, 1998), taking into account selective feeding (SHULL and YASUDA, 2001). In addition, the presence, motility and selective feeding of benthic organisms have been represented in the cellular automata description of benthic organisms (CHOI et al., 2002). As this approach is rule- and individual-based, and hence strongly linked to the ecology of the organisms, it may also become possible to include the effect of benthic life cycles and shifts in communities (RHOADS et al., 1978).

## **Overview and organization of the thesis**

This thesis covers two main topics: (1) the quantitative description of biologically-induced transport processes and (2) the interplay between transport and reaction processes. In the first part of the thesis, three novel approaches are presented to quantify pore water transport other than molecular diffusion. Two of the approaches yield site specific distributions of mixing intensities, but they differ fundamentally in the type of input data. One approach is based on chemical concentration and rate data, while the other uses ecological data about the faunal community. The third approach aims at estimating enhanced solute transport rates at a global

scale. As such it fills the gap between site-specific studies of irrigation and regional to global assessments of the role of benthic-pelagic coupling in ocean biogeochemistry.

Next, the fate of particulate matter in bioturbated sediments is examined using a stochastic Lagrangian approach. **In** this approach, individual particle histories are explicitly computed from probability density functions that embody the statistical nature of particle transport by bioturbation. The analysis of the results provides insight into the emergence of the average transport properties, which are typically implemented in early diagenetic continuum models.

Two advanced modeling environments for early diagenesis are then presented. **In** the first one, a flexible reaction network simulator is coupled to one-dimensional (1 D) transport equations. The reaction network is easily modified and adapted by the user, allowing her to explore progressively more complex biogeochemical systems. The 1 D forward reaction-transport model has also been combined with optimization algorithms to enhance the integration of available measurements in the modeling effort. Finally, a preliminary version of a multidimensional (2 D and 3 D) representation of early diagenetic environments is described. As an application, chemical concentration fields around a flushed burrow are calculated. With the rapid increase in high resolution, multidimensional data sets, the demand for the type of multidimensional modeling tools developed here will undoubtedly continue to rise.

## Transport processes

Direct measurement of transport rates induced by benthic fauna is difficult. **In** order to determine the effect on benthic fluxes, core incubations have been performed with and without elimination of macrofauna by sieving, freezing, poisoning or asphyxiation. All these treatments impact sediment structure and metabolism, however (HAESE, 2002). As an alternative, modeling approaches have been used to interpret tracer profiles and to detangle the contribution of macrofauna to solid phase and solute transport.

The approaches presented here for the determination of transport intensities of solutes in aquatic sediments differ in their scope, complexity, and applicability. As a complete mechanistic understanding of the resident benthic fauna is currently not available, the organisms are treated as a hidden phase, i.e. only their functional effect is assessed. Hence, the various approaches are all, in part, of empirical nature and based on simplified descriptions of the driving forces.

Solute mixing is quantified at different scales, ranging from the global scale to that of individual burrows. This huge span is associated with mathematical formulations that differ in their sophistication, and are based on different types of data sets. The dimensionality of the data used decreases with increasing spatial scale. Global estimates of enhanced solute mixing are based on an analysis of O<sub>2</sub>-fluxes across the SWI (**Chapter 2**), measured with benthic chambers and obtained from microelectrode profiles. These flux measurements are combined with a simple reactive transport model in order to deduce mixing intensities. Combining global estimates of exchange fluxes and an empirical analysis of diffusive vs. total sediment O<sub>2</sub> uptake, global relationships for enhanced solute transport intensities are derived.

Site specific depth distributions of enhanced transport intensities are obtained using measured concentration and rate profiles of chemical constituents (**Chapter 3**). The method involves the optimization mixing profiles together with a statistical comparison of mixing profiles of different complexity. It explicitly accounts for the uncertainty of the measurements and leads



to the simplest parameterization of biologically induced mixing consistent with the available concentration and rate data.

**In Chapter 4**, solute transport coefficients are derived from ecological data, which includes information on the composition of the resident benthic faunal community and their respective burrowing behavior. Mixing intensities are deduced from the morphometry of burrowing networks by recognizing the central role of burrow walls as areas of exchange between domains associated with distinct transport timescales. Rather than calculating a unique value of transport intensity, this method takes into account the natural variability of infaunal ecology, leading to a quantification of the expected range of solute transport in a given environment.

The inverse approach based on chemical data and the stochastic model based on ecological information focus on the same spatial scale. Despite the fundamental differences between the global, inverse, and stochastic models in terms of complexity and type of input data, results for sites with sufficient data to obtain estimates of biologically induced transport intensities using all three approaches are of amazingly similar (Fig. 2). This implies that some of the fundamental characteristics of bioirrigation have been captured when translating benthic ecological data into transport intensities.

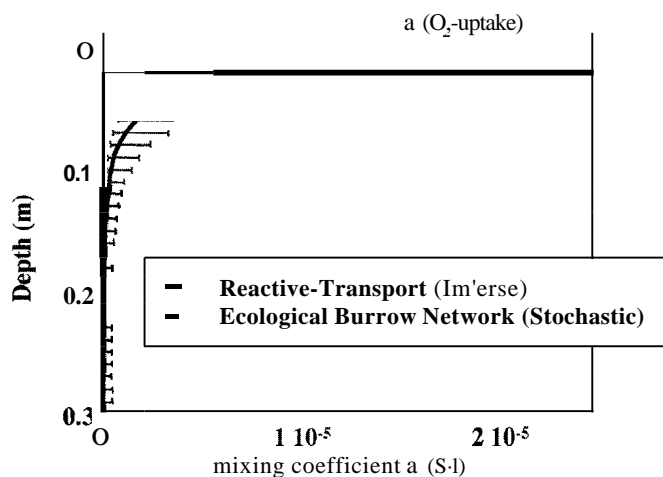


Figure 2. Comparison of enhanced solute transport coefficient ( $a$ ) from inverse, stochastic and global approaches for a study site in a creek bank sediment of a salt marsh on Sapelo Island, Georgia, USA. The origin of the depth axis corresponds to the sediment-water interface. Similar  $a$ -profiles are obtained by inverse and stochastic modeling (Koretsky et al., 2002). The model-derived  $a$ -values at the sediment surface agree closely with flux-based estimates in the oxygenated zone  $\ll$  0.5 cm near the sediment-water interface (Melle and Van Cappellen, 2003).

Bioturbation is often the dominant transport process for solids in surface sediments. This can be illustrated by comparing sediment accumulation to diffusional transport,  $Pe = w \cdot x_{mix} / Db$  where  $Pe$  is the Péclet number,  $w$  is the sedimentation velocity,  $Db$  the bioturbation coefficient and  $x_{mix}$  the average mixing depth of 10 cm (BOUDREAU, 1994). Estimating  $w$  and  $Db$  from global relationships (MIDDELBURG et al., 1997), this results in Péclet numbers  $\ll$  1 under nearly all "average" marine conditions.

Therefore, the analysis of solute transport is complemented by an investigation of time scales relevant for solid phase particles (**Chapter 6**). As the residence time of organic matter in the surficial oxic layer of sediments has been proposed to govern organic matter preservation, particle residence times, ages and their variabilities are determined for settings representative of the coastal ocean, shelf, and deep-sea. The effect of bioturbation on solid phase cycling is evaluated using a stochastic Lagrangian description of particle displacement, which leads to improved estimates of the exposure time of particles to specific environmental conditions such as the oxic zone.

### Coupling transport and reaction

Not only biologically induced transport, but also the biogeochemical reaction network as a whole, and the implementation of the chemically or microbially driven processes are associated with large uncertainties. These uncertainties stem from both a non-unique selection and description of the relevant processes, and their parameterization. The most commonly used reactive transport models of early diagenesis (BOUDREAU, 1996; HENSEN et al., 1997; SOETAERT et al., 1996b; WANG and VAN CAPPELLEN, 1996) do not address the uncertainty of model parameterization explicitly and/or lack the flexibility to change process descriptions in an intuitive way. In **Chapter 7**, such a flexible modeling environment that includes parameter estimation from measurements is presented.

Burrowing organisms also cause significant lateral heterogeneity in surface sediments (Fig. 3), which cannot be captured by 1D models. Therefore, a high resolution 3D model of early diagenesis (**Chapter 5**) has been developed with which the effect of heterogeneous features on early diagenetic processes can be evaluated. As such, it is to my knowledge the first early diagenetic model incorporating simulation of both fluid flow and reaction networks in a heterogeneous, non-symmetrical environment. Future work will include a description of solid phase displacement, extension of the governing equation for flow in the burrow, and relating driving forces for burrow flushing to ecological parameters. Implementation of random heterogeneous features together with the study of scaling influences on average properties may ultimately lead to a better understanding of the link between both laboratory and field data and provides a sound basis for upscaling from the mm to dm scale.

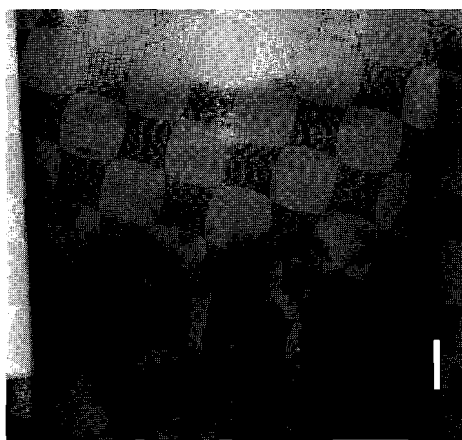


*Figure 3. Infaunal burrows as heterogeneous structures in surface sediment, seen through the plexi-glass lining of a sediment core liner. Oxidized burrow structures (light grayish areas) from the sediment-water interface downwards. The vertical white bar represents 1 cm; picture courtesy S. loye.*

## References

- Aller R. C. (1980) Quantifying solute distributions in the bioturbated zone of marine sediments by defining an average microenvironment. *Geochimica et Cosmochimica Acta* 44, 1955-1965.
- Aller R. C., Hall P. O. J., Rude P. d., and Aller J. Y. (1998) Biogeochemical heterogeneity and suboxic diagenesis in hemipelagic sediments of the Panama Basin. *Deep-Sea Research* 145, 133-165.
- Archer D. and Devol A. (1992) Benthic oxygen fluxes on the Washington shelf and slope: A comparison of in situ microelectrode and chamber flux measurements. *Limnology and Oceanography* 37(3), 614-629.
- Barciela R. M., Garcia E., and Fernandez E. (1999) Modelling primary production in a coastal embayment affected by upwelling using dynamic ecosystem models and artificial neural networks. *Ecological Modelling* 120(2-3), 199-211.
- Berner R. A. (1980) *Early diagenesis. A theoretical approach*. Princeton University Press.
- Boudreau B. P. (1984) On the equivalence of nonlocal and radial-diffusion models for porewater irrigation. *Journal of Marine Research* 42, 731-735.
- Boudreau B. P. (1986) Mathematics of tracer mixing in sediments: II. Nonlocal mixing and biological conveyor-belt phenomena. *American Journal of Science* 286, 199-238.
- Boudreau B. P. (1994) Is burial velocity a master parameter for bioturbation? *Geochimica et Cosmochimica Acta* 58(4), 1243-1249.
- Boudreau B. P. (1996) A method-of-lines code for carbon and nutrient diagenesis in aquatic sediments. *Computers & Geosciences*. 22(5), 479-496.
- Boudreau B. P. and Imboden D. M. (1987) Mathematics of tracer mixing in sediments: III. The Theory of Nonlocal Mixing within Sediments. *American Journal of Science* 287, 693-719.
- Bouldin D. R. (1968) Models for describing the diffusion of oxygen and other mobile constituents across the mud-water interface. *Journal of Ecology* 56, 77-87.
- Bull D. C. and Taillefert M. (2001) Seasonal and topographic variations in proewaters of a southeastern USA salt marsh as revealed by voltarmetric profiling. *Geochemical Transactions* 13, DOI: 10.1039/b1l08493c.
- Choi J., Francois-Carcaillet E., and Boudreau B. P. (2002) Lattice-automaton bioturbation simulator (LABS): implementation for small deposit feeders. *Computers & Geosciences* 28, 212-222.
- de Deckere E. M. G. T., T.J. T., and de Brouwer J. E. C. (2001) Destabilization of cohesive intertidal sediments by infauna. *Estuarine, Coastal and Shelf Science* 53, 665-669.
- Emerson S., Jahnke R., and Heggge D. (1984) Sediment-water exchange in shallow water estuarine sediments. *Journal of Marine Research* 42, 709-730.
- Froelich P. N., Klinkhammer G. P., Bender M. L., Luedke N. A., Heath G. R., Cullen D., Dauphin P., Hammond D., Hartmann B., and Maynard V. (1979) Early oxidation of organic matter in pelagic sediments of eastern equatorial Atlantic: suboxic diagenesis. *Geochimica et Cosmochimica Acta* 43(7), 1075-1090.
- Furukawa Y. (2001) Biogeochemical consequences of macrofauna burrow ventilation. *Geochemical Transactions* 11, DOI: 10.1039/b108381c.
- Furukawa Y., Bentley S. J., and Lavoie D. L. (2001) Bioirrigation modeling in experimental benthic mesocosms. *Journal of Marine Research* 59, 417-452.
- Giangrande A., Montresor M., Cavallo A., and Licciano M. (2002) Influence of Naineris laevigata (Polychaeta: Orbiniidae) on vertical grain size distribution, and dinoflagellate resting stages in the sediment. *Journal of Sea Research* 42(2), 97-108.
- Goldhaber M. B., Aller R. C., Cochran J. K., Rosenfeld J. K., Martens C. S., and Berner R. A. (1977) Sulfate reduction diffusion and bioturbation in Long Island Sound sediments: Report of the FOAM group. *American Journal of Science* 277, 193-237.
- Graf G. and Rosenberg R. (1997) Bioresuspension and biodeposition: a review. *Journal of Marine Systems* 11, 269-278.
- Guinot V. (2002) Modelling using stochastic, finite state cellular automata: rule inference from continuum models. *Applied Mathematical Modelling* 26(6), 701-714.
- Haese R. R. (2002) Macrobenthic activity and its effects on biogeochemical reactions and fluxes. In *Ocean Margin Systems* (ed. G. Wefer, D. Billett, D. Hebbeln, B. B. M. Schluter, and T. Van Weering), pp. 219-234. Springer-Verlag.
- Hammond D. E., Simpson H. J., and Mathieu G. (1977) Radon 222 distribution and transport across the sediment-water interface in the Hudson River estuary. *J. Geophysical Research* 82(27), 3913-3920.
- Heip C. H. R., Duineveld G., Flach E., Graf G., Helder W., Herman P. M. J., Lavaleye M., Middelburg J. J., **pfannkuche O., Soetaert K., Soltwedel T., de Stigter H., Thomsen L., Vanaverbeke J., and de Wilde P.**

- (2001) The role of the benthic biota in sedimentary metabolism and sediment-water exchange processes in the Goban Spur area (NE Atlantic). *Deep-Sea Research II* 48,3223-3243.
- Hensen C., Landenberger H., Zabel M., Gundersen J. K., Glud R. N., and Schulz H. D. (1997) Simulation of early diagenetic processes in continental slope sediments off southwest Africa: the computer model CoTAM tested. *Marine Geology* 144, 191-210.
- Jahnke R. (1985) A model of microenvironments in deep-sea sediments: Formation and effects on porewater profiles. *Limnol. Oceanogr.* 30(5), 956-965.
- Jørgensen B. B. (1983) Processes at the sediment-water interface. In *The major biogeochemical cycles and their interactions* (ed. B. Bolin and R. B. Cook), pp. 477-509. SCOPE.
- Josefson A. B. (1990) Increase of benthic biomass in the Skagerrak-Kattegat during the 1970s and 1980s - effects of organic enrichment? *Marine Ecology Progress Series* 66, 117-130.
- Jumars P. A., Nowell A. R. M., and Self R. F. L. (1981) A simple model of low-sediment-organism interaction. *Marine Geology* 42, 155-172.
- Koretsky C. M., Meile C., and Van Cappellen P. (2002) Quantifying bioirrigation using ecological parameters: A stochastic approach. *Marine Ecology Progress Series* 235, 17 - 30.
- Koretsky C. M., Moore eM., Lowe K. L., Meile C., DiChristina T. L., and Van Cappellen P. (2003) Seasonal Oscillation of Microbial Iron and Sulfate Reduction in Saltmarsh Sediments. *Biogeochemistry*.
- Kristensen E. (2001) Impact of polychaetes (*Nereis* spp. and *Arenicola marina*) on carbon biogeochemistry in coastal marine sediments. *Marine Ecology Progress Series* 212, DOI: 10.1039/b108114d.
- Kristensen E., Jensen M. H., and Aller R. C. (1991) Direct measurement of dissolved inorganic nitrogen exchange and denitrification in individual polychaete (*Nereis virens*) burrows. *Journal of Marine Research* 49(2), 355-377.
- Levin L. A., Blair N., DeMaster D., Plaia G., Fornes W., Martin C., and Thomas C. (1997) Rapid subduction of organic matter by maldivid polychaetes on the North Carolina slope. *Journal of Marine Research* 55(3), 595-611.
- Marinelli R. L. and Boudreau B. P. (1996) An experimental modeling study of pH and related solutes in an anoxic coastal sediment. *Journal of Marine Research* 54, 939-966.
- Marinelli R. L., Lovell C. R., Wakeham S. G., Ringelberg D. B., and White D. C. (2002) Experimental investigation of the control of bacterial community composition in macrofaunal burrows. *Marine Ecology Progress Series* 235, 1-13.
- Martin W. R. and Banta G. T. (1992) The measurement of sediment irrigation rates: A comparison of the tracer and  $^{222}\text{Rn}/^{226}\text{Ra}$  disequilibrium techniques. *Journal of Marine Research* 50, 125-154.
- Mayer M. S., Schaffner L., and Kemp W. M. (1995) Nitrification potentials of benthic macrofaunal tubes and burrow walls: effects of sediment  $\text{NH}_4^+$  and animal irrigation behavior. *Marine Ecology Progress Series* 121, 157-169.
- Meile C. and Van Cappellen P. (2003) Global estimates of enhanced solute transport in marine sediments. *Limnology and Oceanography* 48(2), 777-786.
- Meysman F. (2001) Modelling the influence of ecological interactions on reactive transport processes in sediments. Ph.D., Gent University.
- Meysman F. J. R., Boudreau B. P., and Middelburg J. J. (2003, accepted-a) Relations between local, non-local, discrete and continuous models of bioturbation. *Journal of Marine Research*.
- Meysman F. J. R., Boudreau B. P., and Middelburg J. J. (2003, accepted-b) Why does biological resemble Fickian diffusion? *Journal of Marine Research*.
- Middelburg J. J., Soetaert K., and Herman P. M. (1997) Empirical relationships for use in global diagenetic models. *Deep-Sea Research* 44(2), 327-344.
- NOAA. (1999) <http://spo.nos.noaa.gov/projects/population/population.html>.
- Rabouille C., Witbaard R., and Duineveld G. C. A. (2001) Annual and interannual variability of sedimentary recycling in the North Atlantic Ocean (BENGAL site) studied with a non-steady-state model. *Progress in Oceanography* 50, 147-170.
- Rhoads D. C., McCall P. L., and Yingst J. Y. (1978) Disturbance and production on the estuarine seafloor. *American Scientist* 66, 577-586.
- Rosenberg R. (2001) Marine benthic faunal successional stages and related sedimentary activity. *Scientia Marina* 65(Suppl. 2), 107-119.
- Rowe G. T., Clifford C. H., Smith K. L. J., and P. L. (1975) Benthic nutrient regeneration and its coupling to primary production in coastal waters. *Nature* 255, 215-217.
- Schlesinger W. H. (1997) *Biogeochemistry - An analysis of Global Change*. Academic Press.
- Shull D. H. (2001) Transition-matrix model of bioturbation and radionuclide diagenesis. *Limnology and Oceanography* 46(4), 905-916.
- Shull D. H. and Yasuda M. (2001) Size-selective downward particle transport by cirratulid polychaetes.** *Journal of Marine Research* 59, 453-473.

- Soetaert K., Herman P. M. J., and Middelburg J. J. (1996a) Dynamic response of deep-sea sediments to seasonal variations: A model. *Limnology and Oceanography* 41(8), 1651-1668.
- Soetaert K., Herman P. M. J., and Middelburg J. J. (1996b) A model of early diagenetic processes from the shelf to abyssal depths. *Geochimica et Cosmochimica Acta* 60(6), 1019-1040.
- Steeffé C. I. and MacQuarrie K. T. B. (1996) Approaches to modeling of reactive transport in porous media. In *Reactive transport in porous media*, Vol. 34 (ed. P. C. Lichtner, C. I. Steefel, and E. H. Oelkers), pp. 83-130. Mineralogical Society of America.
- Stumm W. and Morgan J. J. (1996) *Aquatic Chemistry*, pp. 1022. John Wiley & Sons, Inc.
- Thompson M. L. and Schaffner L. C. (2001) Population biology and secondary production of the suspension feeding polychaete *Chaetopterus* cf. *variopedatus*: Implications for benthic-pelagic coupling in lower Chesapeake Bay. *Limnology and Oceanography* 46(8), 1899-1907.
- Trauth M. H. (1998) Turbo: A dynamic-probabilistic simulation to study the effects of bioturbation on paleoceanographic time series. *Computers & Geosciences* 24(5), 433-441.
- Tromp T. K., Van Cappellen P., and Key R. M. (1995) A global model for the early diagenesis of organic carbon and organic phosphorus in marine sediments. *Geochimica et Cosmochimica Acta* 59(7), 1259-1284.
- Van Cappellen P. and Gaillard J.-F. (1996) Biogeochemical dynamics in aquatic sediments. In *Reactive transport in porous media*, Vol. 34 (ed. P. C. Lichtner, C. I. Steefel, and E. H. Oelkers), pp. 335-376. Mineralogical Society of America.
- Ver L. M. B., MacKenzie F. T., and Lerman A. (1999) Carbon cycle in the coastal zone: effects of global perturbations and change in the past three centuries. *Chemical Geology* 159, 283-304.
- Wang Y. and Van Cappellen P. (1996) A multicomponent reactive transport model of early diagenesis: Application to redox cycling in coastal marine sediments. *Geochimica et Cosmochimica Acta* 60(16), 2993-3014.

## **CHAPTER 2: Global estimates of enhanced solute transport in marine sediments <sup>1</sup>**

### **Abstract**

Pore water solute transport processes acting in addition to molecular diffusion affect sediment biogeochemistry and benthic exchange fluxes. Given the relatively few direct measurements of enhanced transport intensities, there is a need for predictive relationships to calculate enhanced transport parameters from more readily available information. Here, enhanced diffusion coefficients and nonlocal mass transfer coefficients are obtained by comparing total and molecular diffusion fluxes of oxygen across the sediment-water interface. Semi-empirical relationships for these coefficients are derived as functions of benthic oxygen uptake. According to these relationships, enhanced solute transport significantly impacts sediment - water column exchanges in regions with large benthic oxygen fluxes, typically on the continental shelves. On a global scale, enhanced transport contributes approximately one third of the total benthic flux of oxygen and more than half of that of phosphate.

### **Introduction**

The sediment-water interface (SWI) constitutes a natural boundary in the oceans across which the transport regimes of both solids and solutes change dramatically (Boudreau and 2001). For solutes, open water turbulence gives way to molecular diffusion through the porous medium of the sediment. In the uppermost layers of marine sediments, however, biologically-induced solute transport (bioirrigation) may exceed transport due to molecular diffusion (Archer and Devol, 1992; Meile et al., 2001). Pore water advection driven by pressure changes as a result of wave or tide action, may also contribute significantly to solute transport fluxes in permeable sandy sediments in nearshore environments (Ziebis et al., 1996; Boudreau et al., 2001). Quantitative estimates of enhanced transport intensities are thus important in order to constrain benthic fluxes of dissolved nutrients or oxygen uptake at the seafloor.

Pore water concentrations change significantly over depth scales of mm to dm and give rise to a typical vertical zonation of porewater chemistry. The concentration gradients are the result of a multitude of different reaction and transport processes acting simultaneously, which complicates identification of the individual processes. Concentration profiles are therefore complemented by direct measurements of reaction and transport rates. Mathematical models that explicitly couple the reaction network to the transport processes further help with the interpretation of the observational data. From model simulations it is then possible to estimate reaction rates and fluxes which may be difficult to measure directly (Soetaert et al., 1996b; Van Cappellen and Wang, 1996). However, because detailed information is generally required as input, such models tend to be applied only at sites where extensive data sets have been collected, although the underlying mathematical description is generally valid.

---

<sup>1</sup> Meile, C. and Van Cappellen, P. (2003). *Limnology and Oceanography* 48(2); 777-786.

Acknowledgments. We thank F. for providing a data set in advance of publication and D. Archer for a compilation of his data. Insightful comments from two anonymous reviewers helped us improve the manuscript. This study was funded in part by the Netherlands Organisation for Scientific Research (NWO-Pionier Programme).

To overcome the scarcity of comprehensive, site specific data sets, global relationships for various reaction and transport parameters have been developed. Such relationships estimate crucial model parameters from easily obtainable site characteristics. Although of an empirical nature, these relationships provide simple parameterizations that capture the combined effects of multiple factors and processes. Examples are global expressions relating particle mixing intensities plus depths of the bioturbated layer (Boudreau, 1994, 1997), organic carbon degradation rates (Tromp et al., 1995) or fluxes of organic carbon and oxidants at the SWI (Middelburg et al., 1997) to water depth or sedimentation rate. Global relationships are particularly useful when averaging over relatively large spatial scales, as it is the case in ocean models of coupled sediment and water column biogeochemistry (Soetaert et al., 2000; Archer et al., 2002)

While enhanced solute exchange fluxes and associated transport intensities have been estimated at individual study sites (e.g., (Smethie et al., 1981; Martin and Banta, 1992; Meile et al., 2001)), little has been presented in terms of a global synthesis. Jahnke (2001), however, reported a systematic trend in the relative importance of enhanced solute transport and molecular diffusion, as a function of the total  $O_2$  uptake by sediments. At low  $O_2$  uptake fluxes, typical for the deep-sea, total and diffusive  $O_2$  fluxes across the SWI are of the same order of magnitude. At high  $O_2$  uptake fluxes, such as encountered in coastal environments, a large fraction of the total uptake of  $O_2$  cannot be accounted for by molecular diffusion.

In this paper, we use measured  $O_2$  fluxes across the SWI and pore water  $O_2$  gradients to derive global relationships for enhanced solute transport (i.e. transport not due to molecular diffusion) in marine surface sediments. Parameterizations are proposed for both diffusional and nonlocal transport descriptions. To illustrate the impact of enhanced solute transport, the global effects of enhanced transport on oxygen and phosphate fluxes at the seafloor are estimated.

## Data and Methods

To separate the contributions of molecular diffusion and enhanced transport to total solute fluxes across the SWI, we compare benthic fluxes obtained with different experimental approaches. Benthic fluxes due to molecular diffusion ( $F_{diff}$ ) are estimated from vertical high-resolution pore water concentration profiles (microprofiles) and molecular diffusion coefficients under in situ conditions (Reimers et al., 2001). Total solute fluxes ( $F_{tot}$ ), i.e. combining the contributions of molecular diffusion and enhanced transport, are estimated from in situ benthic chamber experiments. From the difference between  $F_{diff}$  and  $F_{tot}$ , enhanced transport parameters are deduced. Because of the relatively large available database, the analysis presented is based on  $O_2$  microprofiles and  $O_2$  benthic flux measurements.

### Data set

Data sources for  $F_{diff}$  and  $F_{tot}$  are summarized in Table 1. Total exchange fluxes calculated from concentration changes measured in benthic chambers currently provide the most direct measurements of total solute fluxes across the SWI (Martin and Sayles, 1994). To minimize the effect of spatial heterogeneity, only fluxes from the same station are compared. To avoid sampling artifacts, e.g., due to changing temperature and pressure during sample recovery (Glud et al., 1994), only benthic fluxes measured in situ are used here (Table 1). Solute fluxes may also vary significantly as a function of time: sediment  $O_2$  uptake, for example, depends strongly on the delivery of organic matter and thence may exhibit seasonal variability (Sayles et al., 1994; Soetaert et al., 1996a). Therefore, we only compare  $F_{tot}$  and  $F_{diff}$  values determined at the same time.

The effect of small-scale topography on diffusive exchange fluxes calculated from one-dimensional concentration profiles and Revsbech, 1985; et al. 2002) is expected to be negligible in the selected data set, because gradients (where specified) were mainly measured across the diffusive boundary layer, just above the sediment surface. Thus, diffusive fluxes are used directly as reported in the studies listed in Table 1.

Table 1: Data description, sources and references

O <sub>2</sub> flux across the SWI	
• Coastal (Skagerrak and German Bight)	(Forster et al., 1999)
• Continental shelf (Washington)	(Archer and Devol, 1992)
	(Devol and Christensen, 1993)
• Arctic (Svalbard)	(Glud et al., 1998)
• Continental slope and rise (off Central California)	(Reimers et al., 1992)
• Deep sea (South Atlantic)	(Glud et al., 1994)
• Deep Sea (South Atlantic)	and Glud, 2002)
• Deep sea (Northeast Pacific)	(Cai and Reimers, 1995)
• Bottom water O <sub>2</sub> , temperature and salinity Values from the water depth closest to the sea floor. Depth resolution ranges from 10 m near the sea surface to 500 m below 2000 m, with a resolution of 1 by 1 degree between 60° N and 60° S	(Levitus and Boyer, 1994), available via <a href="http://ingrid.ldgo.columbia.edu">http://ingrid.ldgo.columbia.edu</a>
• Topography ETOP05 5x5 minutes U.S. Navy database sampled on a 1 by 1 degree grid between 60° N and 60° S to match the Levitus data set or taken for the entire globe to determine ocean floor area per water depth interval	(National Geophysical Data Center, 1988), available via <a href="http://ingrid.ldgo.columbia.edu">http://ingrid.ldgo.columbia.edu</a>
• P04-gradients Compilation of pore water phosphate gradients at the SWI. See original references for details.	(Colman and Holland, 2000), available via <a href="http://www.ngdc.noaa.gov/mgg/sepml">http://www.ngdc.noaa.gov/mgg/sepml</a> archive/

## Empirical relationships

Comparison of measured total and diffusive benthic exchange fluxes directly quantifies the flux caused by processes other than molecular diffusion ( $F_{xs} = F_{tot} - F_{diff}$ ). However, often only an estimate of the total O<sub>2</sub> sediment uptake is available. We therefore estimate molecular diffusion fluxes from total fluxes using an empirical fitting function. As constraints we impose that  $F_{diff} \rightarrow F_{tot}$  when  $F_{tot} \rightarrow 0$ , while at all values of the O<sub>2</sub> uptake,  $F_{diff} \leq F_{tot}$ .

Here, we use the following relationship:

$$F_{diff} = \frac{500 \cdot F_{tot}}{646 + F_{tot}} \quad (1)$$

where the numerical values are obtained from the best fit to the data set (Fig. 1;  $r^2 = 0.79$ ), with both  $F_{diff}$  and  $F_{tot}$  in units of  $\mu\text{mol cm}^{-2} \text{ yr}^{-1}$ . Other functions that give more weight to low O<sub>2</sub> fluxes were also tested. They result in similar predicted values of  $F_{diff}$  (Fig. 1).

In order to quantify the contribution of enhanced transport to O<sub>2</sub> exchange across the SWI on a global scale, total benthic O<sub>2</sub> exchange must also be estimated at sites without direct nux measurements. To this end we use a relationship proposed by Wijsman (2000), which relates benthic O<sub>2</sub> uptake to water depth:



$$F_{tot} = 23.22 \cdot e^{-0.017z} + 3.78 \cdot e^{-0.00047z} \quad (2)$$

where  $z$  is water depth (m) and  $F_{tot}$  the benthic  $O_2$  flux in units of  $\text{mmol } O_2 \text{ m}^{-2} \text{ d}^{-1}$ . Equation 2 is based on 528 flux estimates using a variety of measurement techniques ( $r^2=0.71$ ) and predicted  $O_2$  fluxes for water depths between 9000 and 20 m range from 10 to  $1000 \mu\text{mol em}^{-2} \text{ yr}^{-1}$ . For a detailed discussion of the data and their analysis, see Chapter 2 in (Wijnsman, 2000).

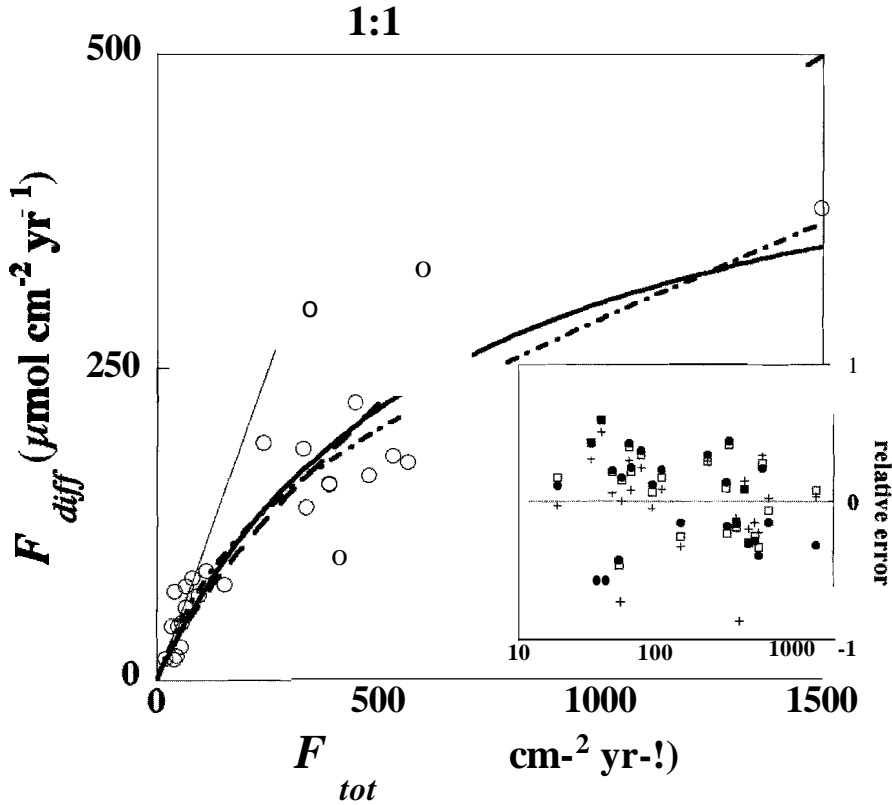


Figure 1. Diffusive benthic  $O_2$  fluxes derived from microprojiles vs. total sediment-water  $O_2$  exchange fluxes measured with benthic chambers. Circles represent the measured values and curved lines are three empirical fitting equations. all explaining about 80% of the measured values of  $F_{diff}$ . The thick line is Eq. 1 (squares in inset), the dashed line is a fit after log transformation of the fluxes,  $10\log(F_{diff}+1) = (17.969 \cdot 10\log(F_{tot} + 1)) / (17.969 + 10\log(F_{tot} + 1))$  (circles in inset), and the dashed-dotted line (crosses in inset) is  $\log(F_{diff} / F_{tot}) = -0.839 \cdot F_{tot} / (562.28 + F_{tot})$ . The inset shows the relative residual errors, defined as  $(F_{diff}^{calc} - F_{diff}^{meas}) / F_{diff}^{meas}$  in percent. The relative error on  $F_{diff}$ , when estimated from  $F_{tot}$ , is about 30%.

## Representations of enhanced transport

Enhanced transport has been described as a diffusive (e.g., (Goldhaber et al., 1977; Matisoff and Wang, 1998)), advective (e.g., (Hammond et al., 1977; McCaffrey et al., 1980)) or

nonlocal process (e.g., (Emerson et al., 1984; Meile et al., 2001). Here, we consider two commonly used representations of enhanced transport, based on diffusive and nonlocal parameterizations, whose applicability depend on the physical processes causing mixing as well as frequency and length scale of mixing events (Boudreau, 1986a, 1986b, Boudreau and Imboden 1987). The following equations relate the transport coefficients to the enhanced transport flux:

$$\text{Diffusive: } F_{xs} = - D_{enh} \phi \left. \frac{\partial C}{\partial x} \right|_{SWR} \quad (3)$$

$$\text{Nonlocal: } F_{xs} = \int_{SWR} \alpha \phi (C_0 - C) dx \quad (4)$$

where  $D_{enh}$  is the enhanced diffusion coefficient,  $\alpha$  the nonlocal transport coefficient (in units of inverse time),  $\phi$  porosity,  $C_0$  the solute concentration at the SWI, and  $x$  depth below the SWI.

### Model assumptions

Equations 3 and 4 show that to determine the diffusive and nonlocal enhanced solute exchange coefficients, the concentration profile of the solute in the sediment must be known. Because we have a global coverage of the seafloor, i.e. also including sites where no measured  $O_2$  profiles are available, pore water  $O_2$  concentrations must be calculated. In order to do so, we assume that porosity gradients and the effects of sedimentation and compaction are negligible. Additionally, the following assumptions underlie the model approach.

1. The  $O_2$  concentration profile is at steady state. This is an appropriate assumption for the derivation of global ocean relationships, which do not account for transient, site-specific effects.

2. Benthic primary production is negligible, which excludes shallow clear water sites from our analysis. The total benthic flux of oxygen is therefore related to the rate of  $O_2$  consumption in the sediment,  $R$ , by

$$F_{tot} = \phi \int_{SWR} R dx. \quad (5)$$

3. The rate of  $O_2$  consumption is constant over the depth interval of  $O_2$  penetration. Thus,  $R$  equals the input flux of  $O_2$  into the oxic zone, divided by  $\phi$  and the  $O_2$  penetration depth,  $L$ . Quasi-0<sup>th</sup> order rate profiles of net  $O_2$  consumption have been reported in a number of studies (Berg et al., 1998; Glud et al., 1998), and are attributed to significant oxygenation of reduced inorganic species at the bottom of the aerobic surface layer. Nonetheless, other rate distributions have been reported and the impact of assuming a constant  $O_2$  consumption rate with depth on enhanced solute transport parameters is therefore evaluated below.

### Enhanced transport parameters

For a diffusive description of enhanced solute transport, the governing mass balance equation is

$$0 = (D_{sed} + D_{enh}) \frac{\partial^2 C}{\partial x^2} - R \quad (6)$$

with  $R = \frac{F_{tot}}{\phi L}$ , where the enhanced diffusion coefficient is, for the sake of simplicity, assumed constant within the depth interval of  $O_2$  penetration. The effective molecular diffusion coefficient,  $D_{sed}$ , is corrected for tortuosity using  $D_{sed} = \frac{D_{sol}(Z, sat)}{1 - \ln(\phi)}$ , where  $D_{sol}$

is the molecular diffusion coefficient in solution, at in situ temperature ( $T$ ) and salinity ( $sal$ ) (Boudreau, 1997). The conditions to be fulfilled by Eq. 6 are:

$$C|_{x=0} = C_0, C|_{x=L} = 0, \left. \frac{\partial C}{\partial x} \right|_{x=L} = 0 \quad (7)$$

Equation 6 is solved for two endmember cases. **In** the first case, the O<sub>2</sub> penetration depth is assumed to be unaffected by enhanced O<sub>2</sub> delivery across the SWI, i.e.  $L = L_{diff}$  where  $L_{diff}$  is the O<sub>2</sub> penetration depth when molecular diffusion is the only transport process ( $D_{enh} = 0$ ). **In** this case, enhanced transport results in an increase in the O<sub>2</sub> consumption rate,  $R$ , and Eq. 6 yields

$$L = L_{diff} = \frac{2\phi C_0 D_{sed}}{F_{diff}} \quad (8)$$

**In** the second endmember case,  $R$  is assumed to only reflect the reactivity and abundance of reduced substances. Therefore, enhanced influx of O<sub>2</sub> into the sediment does not affect the magnitude of  $R$ , but only increases the depth of O<sub>2</sub> penetration, so that

$$L = L_{diff} \frac{F_{tot}}{F_{diff}} = \frac{2\phi C_0 D_{sed}}{F_{diff}^2} F_{tot} \quad (9)$$

The two endmember estimates of  $L$ , Eq. 8 and Eq. 9, are compared to measured values in Fig. 2. Not unexpectedly, Eq. 8 tends to systematically underestimate the measured values, while Eq. 9 overestimates the depth of O<sub>2</sub> penetration. The arithmetic average of both equations,  $L$ , however, provides a remarkably robust predictor of the O<sub>2</sub> penetration depth (Fig. 2). Equation 6 is therefore solved for  $D_{enh}$  with  $L$  as lower boundary depth. The following relationship is obtained:

$$D_{enh} = \frac{1}{2} \left\{ D_{sed} \left( \frac{F_{tot}}{F_{diff}} - 1 \right) + D_{sed} \left( \frac{F_{tot}}{F_{diff}} - 1 \right) \right\} \quad (10)$$

where the first term on the right hand side results from  $L = L_{diff}$  (Eq. 8), whereas the second term originates from assuming  $L = L_{diff} \frac{F_{tot}}{F_{diff}}$  (Eq.9).

**In** contrast to the diffusive description, under nonlocal transport, O<sub>2</sub> can be delivered below the aerobic surface layer (Eq. 4), with O<sub>2</sub> being reduced along burrow walls in the otherwise anoxic sediment. Based on an analysis of  $a$ -profiles from a variety of sites, Meile et al. (2001) concluded that only about 10-20% of the total benthic O<sub>2</sub> flux is delivered to the aerobic zone. Thus, for a quantification of enhanced solute mixing intensities the entire  $a$ -profile below the O<sub>2</sub> penetration depth must be known.

The driving force for enhanced transport is inherently connected to the sediment-water interface, e.g. through wave action or burrowing organisms. Hence, decreasing transport coefficients with depth are often assumed (e.g. Martin and Banta 1992). Here, we consider a simple linear decrease of  $a$  from the SWI to  $x_{mix}$ , the solute mixing depth. The latter is assumed to coincide with the solid phase mixing depth, which, based mainly on an analysis of 210Pb profiles, has been proposed to be on the order of 10 cm across a wide range of marine sediments (Boudreau, 1994). Together with a parabolic approximation of the O<sub>2</sub> profile between the SWI and  $L$ ,  $C(x) = C_0 - C_0 \left( \frac{x^2}{L^2} - \frac{2xL}{L^2} + \frac{L^2}{L^2} \right)$ , the average value of  $a$  in the oxic zone.  $\alpha$  is then obtained from Eq. 4:

$$a = \begin{cases} \frac{12x_{mix} - 6L}{L^2 - 4Lx_{mix} + 6x_{mix}^2} \frac{F_{xs}}{\phi C_0} & \text{for } L \leq x_{mix} \\ \frac{6L}{x_{mix}(4L - x_{mix})} \frac{F_{xs}}{\phi C_0} & \text{for } L > x_{mix} \end{cases} \quad (11)$$

where  $x_{mix}$  is set to 10 em. The assumption of a linear  $a$  depth-distribution is evaluated below.

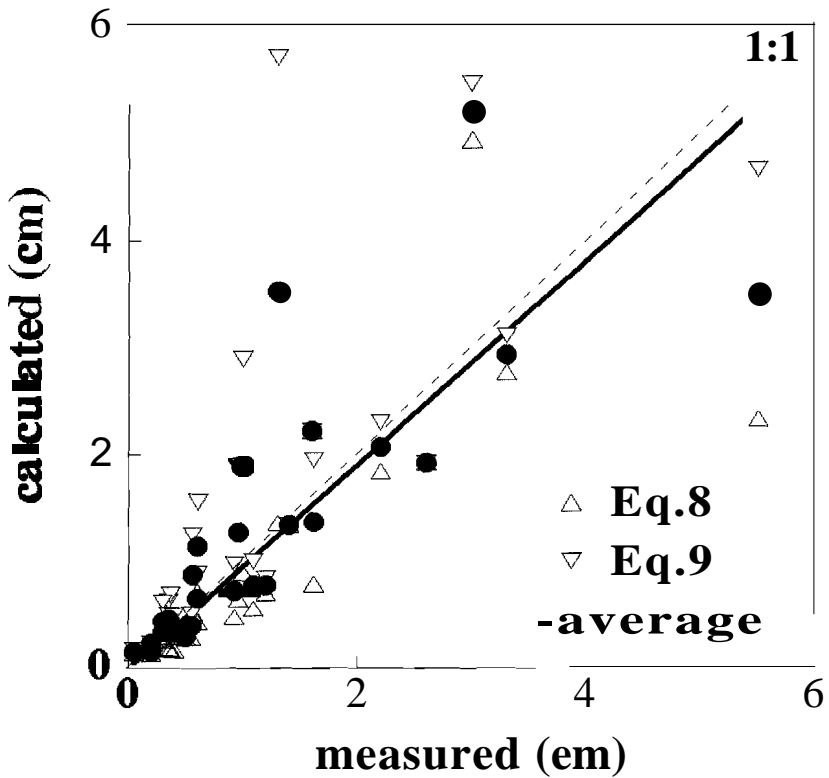


Figure 2. Calculated and measured  $O_2$  penetration depths. The thick line is the regression through the  $O_2$  penetration depths obtained by averaging Eqs. 8 and 9 ( $r^2 = 0.64$ ). The calculated  $O_2$  penetration depths are based on measured values of  $F_{tot}$  and  $F_{diff}$ . See text for discussion.

## Uncertainty analysis

Several assumptions in the mathematical framework outlined above may impact the magnitude of the derived enhanced solute transport coefficients. Furthermore, uncertainties associated with the oxygen fluxes  $F_{tot}$  and  $F_{diff}$  also propagate into the estimated enhanced transport coefficients.

*Rate profile.* The rate of O<sub>2</sub> consumption may deviate from the proposed 0th order kinetics. However, with the condition that the depth-integrated rate of consumption must match the delivery of O<sub>2</sub> to the oxic layer, the O<sub>2</sub> profile and the O<sub>2</sub> penetration depth depend only weakly on the shape of the net rate profile. Relative to the constant rate scenario, a linearly increasing rate with depth ( $R = k \cdot x$  for  $0 \leq x < L$  and  $R=0$  for  $x \geq L$ ) results in an approximately 25% smaller  $L$ , while an exponentially decreasing rate ( $R = k \cdot e^{-x/L}$  for  $0 \leq x < L$  and  $R=0$  for  $x \geq L$ ) increases the O<sub>2</sub> penetration depth by about 20%. Thus, rate profiles deviating significantly from the proposed 0th order kinetics produce O<sub>2</sub> penetration depths that lie within the range of the two endmembers used to estimate the O<sub>2</sub> penetration depth (Eqs. 8 and 9). Furthermore,  $L$  and the concentration gradients at the SWI differ between the different rate descriptions in such a way that  $Denh$  is unaffected by the selection of the rate profile, when the conditions given by 6 and 7 are fulfilled.

*O<sub>2</sub> penetration depth.* While the estimate of  $\alpha$  is only weakly dependent on  $L$ , which is easily seen by substituting various values of  $L$  in Eq. 11, an erroneous estimate of  $L$  impacts  $Denh$ . Comparison of  $Denh$  values calculated using  $L=L_{diff}$  (Eq. 8) and  $L = L_{diff} \frac{F_{tot}}{F_{diff}}$  (Eq. 9) as lower and upper limits for  $L$ , and using Eq. 11 to predict  $F_{diff}$  shows a  $\pm 50\%$  variation of  $Denh$ -values around the best estimates obtained with Eq. 10.

*Nonlocal mixing profile.* In order to evaluate the effect of the shape of the  $\alpha$ -profile on the estimated average  $\alpha$ -value in the aerobic layer, Eq. 11 is compared to (1) an  $\alpha$ -profile constant down to  $x_{mix}$  and 0 below, (2) a constant  $\alpha$  down to  $L$  and linearly decreasing below  $L$  to reach 0 at  $x_{mix}$ , and (3) an exponentially decreasing  $\alpha$  with 95% of the mixing intensity taking place above  $x_{mix}$ . All  $\alpha$ -cases are based on a parabolic concentration profile and conservation of mass for O<sub>2</sub>. The resulting  $\bar{\alpha}$ -values in the oxic zone are given by:

$$\bar{\alpha} = \frac{\frac{3L^2}{-x_{lim}^3 + 3x_{lim}^2 L + 3L^2 x_{mix} - 3L^2 x_{lim}} \cdot \frac{F_{xs}}{\phi C_0}}{-4L^3 - BLx_{mix} + 9x_{mix}^2 - 3x_{lim}^2 + 12Lx_{lim} - 6x_{mix}x_{lim}} \cdot \frac{F_{xs}}{\phi C_0} \quad (12)$$

$$\frac{6(x_{mix} - L)}{p2L(e^{PL/x_{mix}} - 1)} \cdot \frac{F_{xs}}{\phi C_0}$$

$$\frac{2x_{mix}^2 (e^{PL/x_{mix}} - 1) - 2x_{mix}PL - p2L^2 e^{-P}}{\phi C_0}$$

for the three respective  $\alpha$ -profile shapes, with  $x_{lim} = \min(x_{mix}, L)$  and  $p = \ln(1 - 0.95)$ . Although the calculated  $\bar{\alpha}$ -values differ significantly among the various scenarios, the relative difference in  $\bar{\alpha}$  between the linear and the other profile shapes is less than 60%, and the linearly decreasing  $\alpha$ -profile gives  $\bar{\alpha}$ -values intermediate between the other scenarios.

*Mixing depth.* The mixing depth,  $x_{mix}$ , may vary from site to site, and mixing depths are not necessarily equal for solids and solutes, as transport processes may differ. Thus, the sensitivity of the average value of  $\alpha$  in the oxic layer towards  $x_{mix}$  is evaluated. Ignoring covariances, the uncertainty ( $\sigma_P$ ) associated with a parameter  $P$  can be expressed as

$$\sigma_P = \sum_i \left( \frac{\partial P}{\partial X_i} \right)^2 \sigma_{X_i}^2 \quad (13)$$

where  $\sigma_X$  is the uncertainty associated with the independent parameter  $X$ . Identifying  $P$  as  $\alpha$  (Eq. 11) and  $X$  as  $x_{mix}$ , the relative error in  $\alpha$  for  $L < x_{mix}$  is equal to

$$\frac{2(L^2 - 6Lx_{mix} + 6x_{mix}^2)}{(L^2 - 4Lx_{mix} + 6x_{mix}^2)(2x_{mix} - L)} \sigma_{x_{mix}}$$

and 1.1 times the relative error in  $x_{mix}$ ,  $\frac{\sigma_{x_{mix}}}{x_{mix}}$ . This may be significant at any individual study site, but is rather small when considering global relationships.

*O<sub>2</sub> fluxes.* While the general trend of  $F_{diff}$  vs.  $F_{tot}$  is captured by Eq. 1, the considerable uncertainties on predicted  $F_{diff}$  values (Fig. 1, inset) lead to significant uncertainties in the calculated transport parameters. Because some of the independent variables ( $X$ , Eq. 13), such as the molecular diffusion coefficient,  $C_0$  or  $\phi$ , are either experimentally accessible and/or remain fairly constant, the uncertainty in  $D_{enh}$  or  $\bar{\alpha}$  ( $\sigma_P$ , Eq. 13) reflects mostly the uncertainty on the fluxes ( $F_{tot}$ ,  $F_{diff}$ ). Expressing  $F_{diff}$  as a function of  $F_{tot}$  (Eq. 1), an approximate measure for the uncertainties associated with the predicted enhanced transport parameters is obtained when substituting  $P$  in Eq. 13 by Eq. 10 and  $\Pi$ , respectively. This analysis indicates that, within the conceptual framework developed above, estimates of  $D_{enh}$  are more sensitive to errors in  $F_{tot}$  and  $F_{diff}$  than estimates of  $\bar{\alpha}$  (Fig. 3).

Figure 3 also shows that for both diffusive and nonlocal description, the uncertainties of the predicted transport coefficients are in a reasonable range when the total sediment O<sub>2</sub> uptake is known (the relative error in the prediction of  $F_{diff}$  from  $F_{tot}$ ,  $\frac{\sigma_{F_{diff}}}{F_{diff}}$ , is on the order

of 30%, Fig. 1, inset). However, when  $F_{tot}$  is estimated from, say, water depth, the relative error in  $F_{tot}$  may easily be 50%, which increases the uncertainty of transport parameter estimates considerably. The predicted transport coefficients are more error prone at low total O<sub>2</sub> uptake (Fig. 3), which typically corresponds to greater water depths and lower enhanced transport intensities.

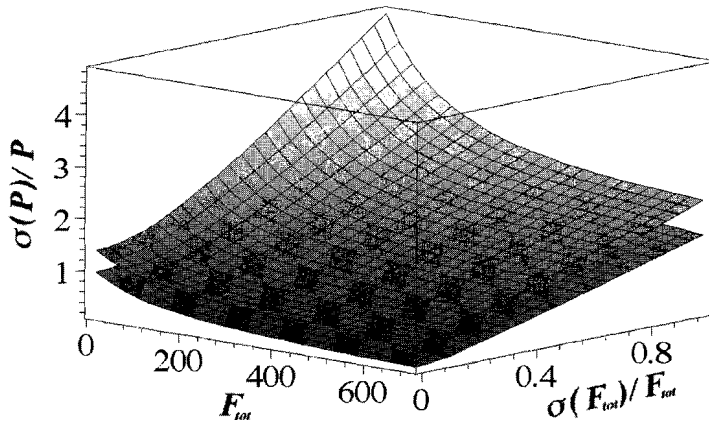


Figure 3. Relative error on the enhanced transport coefficients as a function of  $F_{tot}$  (in units of  $\mu\text{mol cm}^2 \text{ yr}^{-1}$ ) and the relative uncertainty on  $F_{tot}$ . The upper and lower surfaces correspond to enhanced diffusion and nonlocal transport, respectively. For the calculations,  $F_{diff}$  is estimated from  $F_{tot}$  by Eq. 1,  $\sigma_{F_{diff}}/F_{diff}$  is set to 30% (Fig. 1), porosity is 0.8,  $D_{sed}$  is  $20 \text{ cm}^2 \text{ yr}^{-1}$ , and the O<sub>2</sub> concentration in the overlying water is assumed to be  $100 \mu\text{M}$ .

## Results and Discussion

### Enhanced O<sub>2</sub> uptake at the seafloor

The global contribution of enhanced solute transport to benthic O<sub>2</sub> exchange fluxes is estimated using the relationship between  $F_{diff}$  and  $F_{tot}$  (Eq. 1). Benthic O<sub>2</sub> fluxes are calculated as a function of water depth (Eq. 2, water depths > 20 m, the depth cutoff is chosen to exclude areas with a major contribution of benthic primary production). Total sediment O<sub>2</sub> uptake is then obtained through multiplication with the corresponding ocean floor surface areas, calculated from the ETOP bathymetric map on a 1 by 1 degree grid (Table 1). This analysis suggests that more than 40% of the total mass of O<sub>2</sub> is taken up by sediments located at water depths shallower than 300 m. A significant portion, about a third of the total O<sub>2</sub> uptake at the entire seafloor, is estimated to be due to enhanced transport. This fraction drops by about 10% when considering only water depths greater than 100 m rather than 20 m.

Such a significant contribution of enhanced benthic O<sub>2</sub> uptake in continental margin environments implies a pronounced impact on the early diagenetic pathways of organic matter degradation. For example, enhanced supply of O<sub>2</sub> may substantially promote the reoxidation of reduced inorganic species, such as sulfide, thereby sustaining sulfate availability and high sulfate reduction rates (Ferdelman et al., 1999; Fossing et al., 2000; Koretsky et al., in prep.), and preventing methanogenesis.

### Patterns in enhanced transport

To assess enhanced transport on a global scale, transport coefficients are calculated for the ocean between 60°N and 60°S on a 1 by 1 degree grid. This resolution is dictated by the availability of O<sub>2</sub>, temperature and salinity data (Levitus data set, Table 1), which are used to obtain  $C_0$  and  $D_{sed}(O_2)$  for each grid point. Porosity near the SWI is typically between 0.75 and 1, and for the global simulations is assumed to be 0.8. Enhanced transport coefficients are calculated from estimates of total O<sub>2</sub> solute exchange fluxes (Eq. 2, with water depth based on the ETOP map), estimating  $F_{diff}$  from  $F_{tot}$  (Fig. 1), and using Eqs. 10 and 11, respectively.

In addition to the transport coefficients obtained on the 1 by 1 degree grid, results from the individual study sites listed in Table 1, based on measured values of  $L$ ,  $F_{tot}$ ,  $F_{diff}$  and  $C_0$ , are shown in Figure 4. The two enhanced solute transport representations,  $D_{enh}$  and  $\bar{a}$ , derived from the global ocean grid show similar patterns with depth or total benthic O<sub>2</sub> flux. As expected, enhanced transport coefficients are high relative to diffusive exchange at high total benthic O<sub>2</sub> fluxes, where  $F_{xs}$  becomes significant (Fig. 1). Model results suggest that at total O<sub>2</sub> fluxes smaller than about 100 to 150  $\mu\text{mol cm}^{-2} \text{yr}^{-1}$ , which according to Eq. 2 roughly correspond to water depths greater than 250-400 m, molecular diffusion is the dominant transport mechanism (Fig. 4A). Results from site-specific calculations show a somewhat larger range of  $F_{tot}$  where coefficients of molecular diffusion and enhanced diffusion are of similar magnitude (about 50-250  $\mu\text{mol cm}^{-2} \text{yr}^{-1}$ , Fig. 4A). The solid phase mixing coefficient  $D_b$ , estimated from water depth (Middelburg et al. 1997), is systematically smaller than either the molecular or the enhanced diffusion coefficient (by an order of magnitude or more, not shown), indicating that solid phase mixing has, globally, a minor effect on solute transport in marine sediments.

Generally, poorer agreement exists between the global grid and the site-specific estimates of enhanced transport coefficients at low benthic O<sub>2</sub> uptake fluxes (Fig. 4). This reflects the large (relative) uncertainties associated with estimates of enhanced transport coefficients at low  $F_{tot}$  (Fig. 3) and thus low  $F_{xs}$ . However, under these conditions, characteristic for the deep-sea, enhanced transport tends to play a minor role in benthic solute

fluxes. At benthic uptake fluxes  $F_{tot} > 100 \mu\text{mol cm}^2 \text{yr}^{-1}$ , site-specific enhanced transport parameters show increasing trends with  $F_{tot}$ , similar to those observed for the global grid results.

## Global relationships

When the benthic  $\text{O}_2$  flux,  $F_{tot}$ , is known at a given site, enhanced transport coefficients can be calculated by combining an estimate of  $D_{diff}$  derived from  $F_{tot}$  (Fig. 1) with Eq. 10 ( $D_{enh}$ ) or Eq. 11 ( $\bar{\alpha}$ ). For sites where the benthic  $\text{O}_2$  flux has not been measured, we recommend to estimate  $F_{tot}$ , for example, from the total organic carbon mineralization rate. In both cases, site-specific values of the other input parameters,  $D_{sed}(\text{O}_2)$ ,  $\phi$ ,  $L$  and  $C_0$ , should be used preferably.

When not all the necessary site-specific information is available, or when simple parameterizations are needed for use in biogeochemical models of the whole ocean, the following empirical equations can be used. These equations are derived by fitting the entire set of transport coefficients calculated for the global ocean grid (Fig. 4):

$$D_{enh} = (7.6375 - 7.4465 \cdot e^{-0.00089603 \cdot F_{tot}(\text{O}_2)}) \cdot D_{sed}(\text{O}_2) \quad (r^2 = 0.99) \quad (14)$$

$$\bar{\alpha} = (-73.071 + 71.912 \cdot e^{-0.0013846 \cdot F_{tot}(\text{O}_2)}) \cdot C_0^{-1} \quad (r^2 = 0.99) \quad (15)$$

$$D_{enh} = 48133 - 48089 \cdot e^{-0.000046764 \cdot F_{tot}(\text{O}_2)} \quad (r^2 = 0.94) \quad (16)$$

$$\bar{\alpha} = -1591.7 + 1580.8 \cdot e^{-0.00055127 \cdot F_{tot}(\text{O}_2)} \quad (r^2 = 0.21) \quad (17)$$

where the units are  $\text{cm}^2 \text{yr}^{-1}$  for  $D_{enh}$  and  $D_{sed}(\text{O}_2)$ ,  $\mu\text{mol cm}^{-2} \text{yr}^{-1}$  for  $F_{tot}(\text{O}_2)$ ,  $\text{yr}^{-1}$  for  $\bar{\alpha}$ , mM for the  $\text{O}_2$  bottom water concentration,  $C_0$ , and the  $r^2$  values refer to the fit to the global grid rather than the site-specific results.

Comparison of the  $r^2$  values reveals that  $\bar{\alpha}$  cannot be predicted accurately from  $F_{tot}$  alone (Eq. 17);  $\bar{\alpha} \cdot C_0$ , however, strongly correlates with  $F_{tot}$  (Eq. 15). The globally-predicted  $\bar{\alpha} \cdot C_0$  values also agree well with the site-specific values (Fig. 4B). Use of the nonlocal transport description therefore requires knowledge of the  $\text{O}_2$  bottom water concentration. For  $D_{enh}$ , only a moderate increase in  $r^2$  is observed when variations in  $D_{sed}$  are taken into account. However, the good fit of Eq. 16 to the global grid parameter values partially reflects the correlation between bottom water temperature and water depth (see analysis of the Levitus data set in (Tromp et al., 1995), together with the fact that  $F_{tot}$  is estimated from water depth (Eq. 2). Therefore, we recommend use of Eq. 14 when salinity and temperature (and, possibly, porosity) values are available to estimate  $D_{sed}$ .

Equations 15 and 14 or 16 allow one to predict enhanced transport coefficients from the benthic uptake flux. Alternatively, the parameters can be obtained from water depth,  $z$ , by substituting Eq. 2 into Eqs. 14-16. This increases the uncertainty on the parameter values, however, because of the propagation of errors associated with estimating  $F_{tot}$  from  $z$  (Fig. 3).



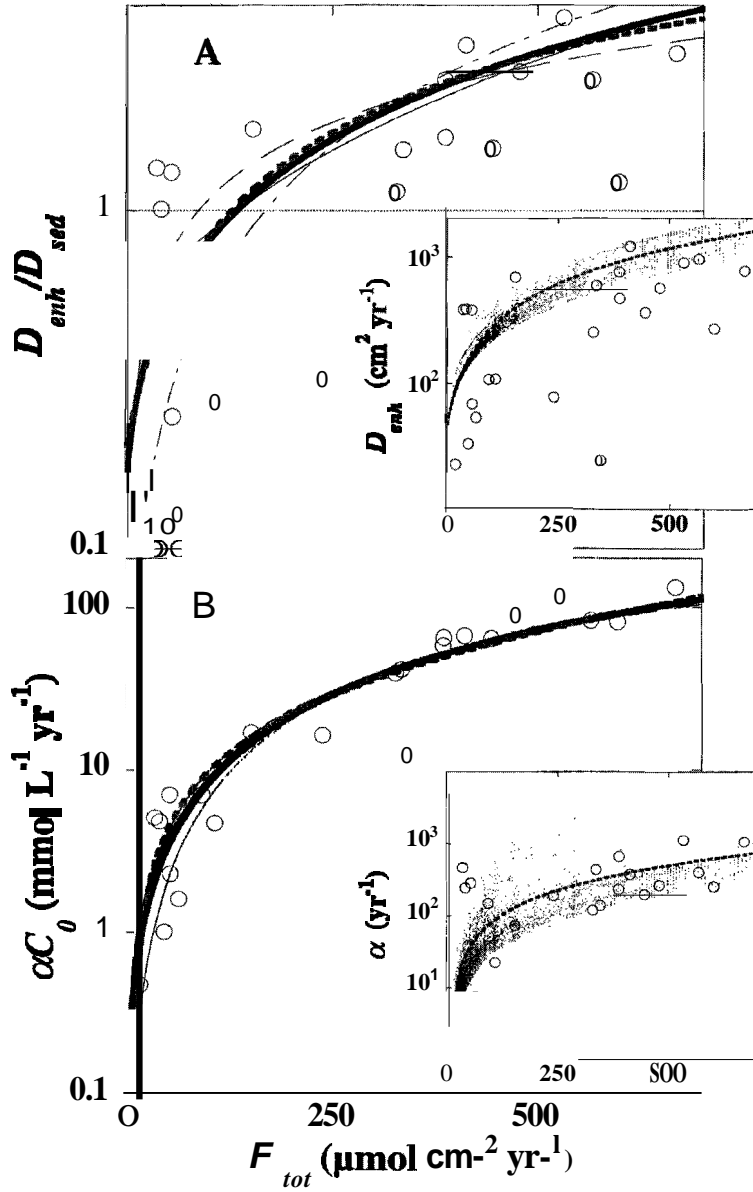


Figure 4. Enhanced solute transport coefficients (Panel A: diffusional, Panel B: nonlocal) as a function of the total benthic  $O_2$  uptake flux. Circles denote site-specific estimates (Table 1), dots are the coefficients estimated for the global grid. The thin lines in panels A and B correspond to the predicted parameter values using the three different empirical equations to estimate  $F_{diff}$  from (Fig. 1). The line patterns are the same as in Fig. 1. The thick lines in panels A and B correspond to the predicted parameter values using the arithmetic mean of the three empirical equations to estimate  $F_{diff}$ . The thick dashed lines represent the functions obtained by curve fitting the global grid estimates (panel A: Eq. 14; inset: Eq. 16; panel B: Eq. 15; inset: Eq. 17). For plotting purposes, when the measured  $F_{diff}$  exceeds transport coefficients are set to the arbitrarily chosen minimum value of the y-axis.

## Comparison to other studies

The finding that enhanced transport is significant in near shore and continental shelf environments, is supported by studies at individual sites, e.g. (Archer and Devol, 1992), and enhanced diffusion coefficients in shallow North Sea sediments are several times higher than molecular diffusion coefficients (Vanderborght et al., 1977). The model prediction that enhanced solute mixing tends to be less important in deep-sea sediments also agrees with experimental studies (Reimers and Smith, 1986). Our estimates of enhanced diffusion coefficients fall in the range reported in (Berg et al. 2001), where it was shown that solute mixing coefficients exceed solid phase  $D_b$ -values by a factor of 15-20 at a near-shore site. Our results thus support that enhanced solute diffusion coefficients cannot be adequately approximated by solid phase mixing parameters.

Nonlocal transport coefficients agree well with results from independent modeling approaches. In shallow-water carbonate sediments of Dry Tortugas, Florida, both early diagenetic and stochastic modeling approaches give  $\bar{a}$ -values near the SWI between  $3.10 \cdot 10^{-6}$  (Furukawa et al., 2000) and  $4.6 \cdot 10^{-6}$  s<sup>-1</sup> (Koretsky et al., 2002). The  $\bar{a}$ -value calculated here,  $2.7 \cdot 10^{-6}$  s<sup>-1</sup>, is in excellent agreement with these studies ( $F_{IOP} = 96 \mu\text{mol cm}^{-2} \text{ yr}^{-1}$ ,  $F_{diff} = 61 \mu\text{mol cm}^{-2} \text{ yr}^{-1}$ ,  $L = 0.26 \text{ cm}$ ,  $C_0 = 141 \mu\text{M}$ ,  $\phi = 0.58$ ; data from (Furukawa et al., 2000)). Predicted  $\bar{a}$ -coefficients in the oxic zone of three sediments of the Skagerrak agree with the values in (Wang and Van Cappellen, 1996) to within 7-25%, if their modeled  $\text{O}_2$  fluxes are used to calculate  $\bar{a}$ . If Eq. 1 is applied to estimate  $F_{diff}$ , the values are still within 7 - 35% of each other ( $4.1\text{-}9.4 \cdot 10^{-6}$  s<sup>-1</sup> calculated here vs.  $5.6\text{-}7.9 \cdot 10^{-6}$  s<sup>-1</sup> used in (Wang and Van Cappellen, 1996), respectively). On the Washington shelf,  $\bar{a}$ -values obtained based on total  $\text{O}_2$  fluxes from (Christensen et al., 1984) at two sites are  $5.1 \cdot 10^{-6}$  s<sup>-1</sup> and  $9.5 \cdot 10^{-6}$  s<sup>-1</sup>, respectively. This compares favorably to inverse modeling results based on radon and sulfate profiles, which lead to values of  $3.7 \cdot 10^{-6}$  s<sup>-1</sup> and  $6.2 \cdot 10^{-6}$  s<sup>-1</sup>, respectively (Meile et al., 2001).

## Benthic phosphate fluxes

Colman and Holland (2000) have recently assessed the efflux of nutrient phosphate from marine sediments on a global scale. Based on 193 measured pore water phosphate gradients (Table 1), they calculated benthic phosphate fluxes taking into account molecular diffusion but assuming a negligible contribution from enhanced solute transport. Here, we examine the potential impact of enhanced transport on benthic regeneration of phosphate using the enhanced diffusion approach. The latter can be directly applied to the pore water gradients compiled by Colman and Holland.

For many of their sites, Colman and Holland provide organic carbon deposition and burial fluxes. We use the difference between these fluxes as a measure of the total organic carbon oxidation rate and hence of the total benthic  $\text{O}_2$  uptake flux,  $F_{tot}(\text{O}_2)$ . For each site, the diffusion flux,  $F_{diff}(\text{O}_2)$ , is obtained from  $F_{tot}(\text{O}_2)$  by taking the average of the three fitting functions shown in Fig. 1. A value of  $D_{eff}$  can then be calculated with Eq. (10). This value, together with the measured phosphate gradient, porosity and molecular diffusion coefficient of phosphate given in Colman and Holland (2000), allows us to estimate the benthic flux of phosphate at the site.

In their global budget, Colman and Holland divided the ocean in two provinces, the Shelf-Slope and the Rise-Deep Sea, each characterized by an average sedimentation rate,  $\omega$ .

Following the same approach, we estimate the average benthic phosphate flux in each province from the empirical relationship between the benthic phosphate flux and  $\omega$  obtained for the entire set of sites. The total flux of phosphate from the seafloor in each province is then estimated by multiplying the average flux by the corresponding surface area of the

province (Fig. 5). A more detailed calculation, based on a greater number of water depth intervals derived from the ETOP map (Table 1) and using a global relationship between  $\omega$  and water depth (Middelburg et al., 1997), results in essentially the same global benthic flux of phosphate (less than 5% difference).

The results in Fig. 5 indicate a large effect of enhanced transport on the flux of phosphate from the seafloor. This effect is particularly pronounced along the ocean margins, where enhanced transport dominates the benthic exchange of phosphate. While the diffusion model may not be the most appropriate representation of enhanced transport of pore water phosphate on a global scale, a preliminary analysis of pore water profiles using the non-local model shows a similarly large contribution of enhanced transport on the benthic efflux of phosphate (results not shown). Thus, ignoring enhanced pore water transport may introduce significant errors when estimating benthic fluxes of phosphate and, most likely, of other dissolved nutrients.

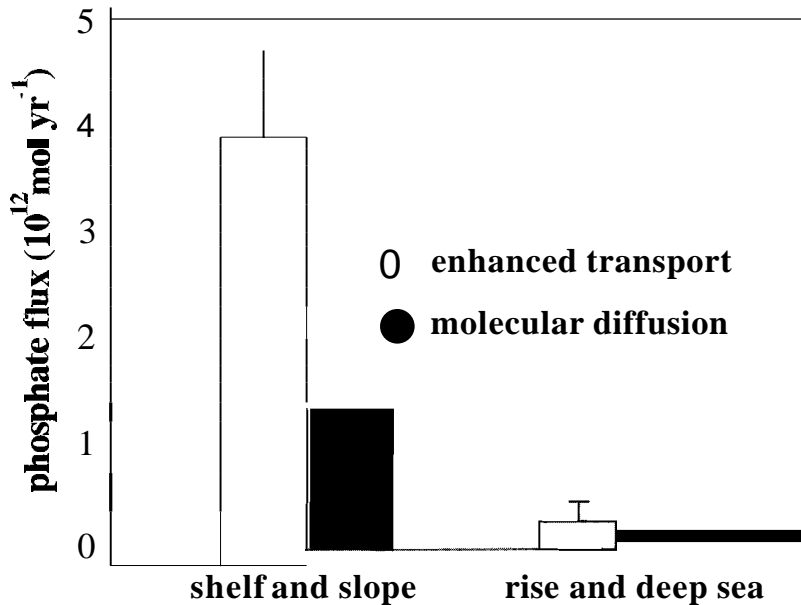


Figure 5. Global benthic phosphate fluxes. The figure illustrates the large relative contribution of enhanced transport in continental margin sediments. Error bars give standard deviations originating from the different estimates of  $F_{diff}(O_2)$  from (Fig. 1). Actual uncertainties on the absolute fluxes are significantly larger (see in particular Fig. 2A in (Colman and Holland, 2000)).

## Synthesis and perspectives

The proposed global relationships for enhanced transport parameters are derived by combining an empirical relationship between the diffusive and total exchange flux of  $O_2$  across the sediment-water interface (SWI) with physical models of diffusive and non-local solute transport in sediments. The choice of  $O_2$  as enhanced transport tracer is dictated by the rapidly growing body of  $O_2$  microprofile data and benthic chamber flux measurements. An added advantage is the high reactivity of  $O_2$  which causes the benthic flux and profile of  $O_2$  to rapidly adjust to changes in external forcings, for example the deposition flux of organic matter. Thus, the proposed approach may also be suited to quantify seasonal variations in enhanced transport intensity.

The impact of enhanced transport on sediment-water column exchanges is most pronounced in coastal marine environments, where the oxic zone tends to be very thin. Oxygen pore water profiles therefore mainly contain information on enhanced transport properties close to the SWI, although irrigation may affect pore water chemistry well below the oxic surface layer (e.g., Furukawa et al., 2000). In addition, the enhanced transport parameters of different chemical species may differ, because of differences in diffusive properties and reactive length scales around macrofaunal burrows (e.g., Aller, 2001; Koretsky et al., 2002).

In shallow-water permeable sediments, wave-induced pressure fluctuations cause advective solute transport (e.g., Huettel and Webster, 2001), a mechanism not explicitly considered here. Frequently, these sediments are also inhabited by active populations of macrofauna, hence, several mechanisms can contribute simultaneously to enhanced pore water transport (D'Andrea et al., 2002). In nearshore environments, the end-member transport models used here may thus no longer offer reliable ways to estimate benthic exchange fluxes. Furthermore, the simple interpretation of  $O_2$  pore water profiles, which assumes  $O_2$  is only consumed (Eq. 5), is not valid when benthic photosynthesis becomes significant (e.g., Jahnke et al., 2000).

The above points to the need for further work on enhanced transport in coastal sediments. In particular, efforts should focus on better constraining the uncertainties associated with the transfer of enhanced transport properties determined for  $O_2$  to other chemical species, and developing more advanced models for the complex solute transport dynamics in nearshore sediments. Future studies could also integrate the predictive relationships of enhanced pore water transport presented here in regional ocean studies, e.g., using GIS modeling tools (e.g. Schliiter et al., 2000). Such studies could then account for region-specific effects on sediment-water column exchanges related to, for instance, the bottom water oxygen distribution and organic matter deposition flux.

## References

- Aller, R. C. 2001. Transport and reactions in the bioirrigated zone, p.269-301. In B. P. Boudreau and B. B. Jørgensen [eds.], *The benthic boundary layer*. Oxford University Press.
- Archer, D., and A. Devol. 1992. Benthic oxygen fluxes on the Washington shelf and slope: A comparison of in situ microelectrode and chamber flux measurements. *Umnol. Oceanogr.* 37: 614-629.
- Archer, D. E., J. L. Morford, and S. R. Emerson. 2002. A model of suboxic sedimentary diagenesis suitable for automatic running and gridded global domains. *Global Biogeochem. Cycles* 16: 1288-1333.
- Berg, P., N. Risgaard-Petersen, and S. Rysgaard. 1998. Interpretation of measured concentration profiles in sediment pore water. *Umnol. Oceanogr.* 43: 1500-1510.
- Berg, P., S. Rysgaard, P. Funch, and M. K. Sejr. 2001. Effects of bioturbation on solutes and solids in marine sediments. *Aquat. Microb. Ecol.* 26: 81-94.
- Boudreau, B., M. Huettel, S. Forster, R. A. Jahnke, A. McLachlan, J. J. Middelburg, P. Nielsen, F. Sansone, G. Taghon, W. Van Raaphorst, I. Webster, J. M. Weslawski, P. Wiberg, and B. Sundby. 2001. Permeable marine sediments: Overturning an old paradigm. *EOS* 82: 133-136.
- Boudreau, B., and B. B. Jørgensen. 2001. *The benthic boundary layer*. Oxford University Press.
- Boudreau, B. P. 1984. On the equivalence of nonlocal and radial-diffusion models for porewater irrigation. *J. Mar. Res.* 42: 731-735.
- Boudreau, B. P. 1986a. Mathematics of tracer mixing in sediments: I. Spatially-dependent, diffusive mixing. *Amer. Jour. Sci.* 286: 161-198.
- Boudreau, B. P. 1986b. Mathematics of tracer mixing in sediments: II. Nonlocal mixing and biological conveyor-belt phenomena. *Amer. Jour. Sci.* 286: 199-238.
- Boudreau, B. P., and D. Imboden. 1987. Mathematics of tracer mixing in sediments: III. The theory of nonlocal mixing within sediments. *Amer. Jour. Sci.* 287: 693-719.
- Boudreau, B. P. 1994. Is burial velocity a master parameter for bioturbation? *Geochim. Cosmochim. Acta* 58: 1243-1249.
- Boudreau, B. P. 1997. *Diagenetic models and their implementation*. Springer.
- Cai, W.-J., and C. E. Reimers. 1995. Benthic oxygen flux, bottom water oxygen concentration and core top organic carbon content in the deep northeast Pacific Ocean. *Deep-Sea Res.* 42: 1681-1699.
- Christensen, J. P., A. H. Devol, and W. M. Smethie. 1984. Biological enhancement of solute exchange between sediments and bottom water on the Washington continental shelf. *Cont. Shelf Res.* 3: 9-23.
- Colman, A. S., and H. D. Holland. 2000. The global diagenetic flux of phosphorus from marine sediments to the oceans: Redox sensitivity and the control of atmospheric oxygen levels, p. 53-75. In C. R. Glenn, L. Prevot-Lucas, and J. Lucas [eds.], *Marine authigenesis: From global to microbial*. SEPM Special Publication No. 64, Society of Sedimentary Geology.
- D'Andrea, A. F., R. C. Aller, and G. R. Lopez. 2002. Organic matter flux and reactivity on a South Carolina sandflat: The impacts of porewater advection and macrobiological structures. *Limnol. Oceanogr.* 47: 1056-1070.
- Devol, A. H., and J. P. Christensen. 1993. Benthic fluxes and nitrogen cycling in sediments of the continental margin of eastern North Pacific. *J. Mar. Res.* 51: 345-372.
- Emerson, S., R. Jahnke, and D. Heggie. 1984. Sediment-water exchange in shallow water estuarine sediments. *J. Mar. Res.* 42: 709-730.
- Ferdelman, T. G., H. Fossing, and K. Neumann. 1999. Sulfate reduction in surface sediments of the southeast Atlantic continental margin between 15°38'S and 27°57'S (Angola and Namibia). *Limnol. Oceanogr.* 44: 650-661.
- Forster, S., R. N. Glud, J. K. Gundersen, and M. Huettel. 1999. In situ study of bromide tracer and oxygen flux in coastal sediments. *Estuar. Coast. Shelf Sci.* 49: 813-827.
- Fossing, H., T. G. Ferdelman, and P. Berg. 2000. Sulfate reduction and methane oxidation in continental margin sediments influenced by irrigation (South-East Atlantic off Namibia). *Geochim. Cosmochim. Acta* 64: 897-910.
- Furukawa, Y., S. Bentley, A. Shiller, D. Lavoie, and P. Van Cappellen. 2000. The role of biologically-enhanced pore water transport in early diagenesis: An example from carbonate sediments in the vicinity of North Key Harbor, Dry Tortugas National Park, Florida. *J. Mar. Res.* 58: 493-522.
- Glud, R. N., J. K. Gundersen, and B. B. Jørgensen. 1994. Diffusive and total oxygen uptake of deep-sea sediments in the eastern South Atlantic Ocean: in situ and laboratory measurements. *Deep-Sea Res.* 41: 1767-1788.
- Glud, R. N., O. Holby, F. Hoffmann, and D. Canfield. 1998. Benthic mineralisation and exchange in Arctic sediments (Svalbard, Norway). *Mar. Ecol. Prog. Ser.* 173: 237-251.

- Goldhaber, M. B., R. C. Aller, J. K. Cochran, J. K. Rosenfeld, C. S. Martens, and R. A. Berner. 1977. Sulfate reduction diffusion and bioturbation in Long Island Sound sediments: Report of the FOAM group. *Amer. Jour. Sci.* 277: 193-237.
- Hammond, D. E., H. J. Simpson, and G. Mathieu. 1977. Radon-222 distribution and transport across the sediment-water interface in the Hudson River estuary. *J. Geophys. Res.* 82: 3913-3920.
- Huellel, M., and I. T. Webster. 2001. Porewater flow in permeable sediments, p. 144-179. In B. P. Boudreau and B. B. Jørgensen [eds.], *The benthic boundary layer*. Oxford University Press.
- Jahnke, R. A., J. R. Nelson, R. L. Marinelli and I. E. Eckman. 2000. Benthic flux of biogenic elements on the Southeastern US continental shelf: influence of pore water advective transport and benthic microalgae. *Cont. Shelf Res.* 20: 109-127.
- Jahnke, R. A. 2001. Constraining organic matter cycling with benthic fluxes, p. 302-319. In B. P. Boudreau and B. B. Jørgensen [eds.], *The benthic boundary layer*. Oxford University Press.
- Jørgensen, B. B., and N. P. Revsbech. 1985. Diffusive boundary layers and the oxygen uptake of sediments and detritus. *Limnol. Oceanogr.* 30: 111-122.
- Koretsky, C. M., C. Meile, and P. Van Cappellen. 2002. Quantifying bioirrigation using ecological parameters: A stochastic approach. *Geochem. Trans.* 3: 17-30.
- Levitus, S., and T. Boyer. 1994. *World Ocean Atlas*. NOAA Atlas NESDIS, U.S. Department of Commerce.
- Martin, W. R., and G. T. Banta. 1992. The measurement of sediment irrigation rates: A comparison of the Br<sup>-</sup> tracer and <sup>222</sup>Rn/<sup>226</sup>Ra disequilibrium techniques. *J. Mar. Res.* 50: 125-154.
- Martin, W. R., and F. L. Sayles. 1994. Seafloor diagenetic fluxes, p. 143-163. In Board on Earth Sciences and Resources Commission on Geosciences, Environment, and Resources: National Resource Council [ed.], *Material fluxes on the surface of the Earth*. National Academy Press.
- Matisoff, G., and X. Wang. 1998. Solute transport in sediments by freshwater infaunal bioirrigators. *Limnol. Oceanogr.* 43: 1487-1499.
- McCaffrey, R. J., A. C. Myers, E. Davey, G. Morrison, M. Bender, N. Luedtke, D. Cullen, P. Froelich, and G. Klinkhammer. 1980. The relation between pore water chemistry and benthic fluxes of nutrients and manganese in Narragansett Bay, Rhode Island. *Limnol. Oceanogr.* 25: 31-44.
- Meile, C., C. Koretsky, and P. Van Cappellen. 2001. Quantifying bioirrigation in aquatic sediments: An inverse modeling approach. *Limnol. Oceanogr.* 46: 164-177.
- Middelburg, J. J., K. Soetaert, and P. M. Herman. 1997. Empirical relationships for use in global diagenetic models. *Deep-Sea Res.* 44: 327-344.
- National Geophysical Data Center. 1988. Digital relief of the surface of the Earth (ETOP05). Data Announcement 88-MGG-02. NOAA.
- Reimers, C. E., R. A. Jahnke, and D. C. McCorkle. 1992. Carbon fluxes and burial rates over the continental slope and rise off Central California with implications for the global carbon cycle. *Global Biogeochem. Cycles* 6: 199-224.
- Reimers, C. E., R. A. Jahnke, and L. Thomsen. 2001. In situ sampling in the benthic boundary layer, p. 245-268. In B. P. Boudreau and B. B. Jørgensen [eds.], *The benthic boundary layer*. Oxford University Press.
- Reimers, C. E., and K. L. J. Smith. 1986. Reconciling measured and predicted fluxes of oxygen across the deep sea sediment-water interface. *Limnol. Oceanogr.* 31: 305-318.
- Røy, H., M. Huetel, and B. B. Jørgensen. 2002. The role of small-scale topography for oxygen flux across the diffusive boundary layer. *Limnol. Oceanogr.* 47: 837-847.
- Sayles, F. L., W. R. Martin, and W. G. Deuser. 1994. Response of benthic oxygen demand to particulate organic carbon supply in the deep sea near Bermuda. *Nature* 371: 686-689.
- Schlüter M., E. J. Sauter, A. Schafer, and W. Ritzrau. 2000. Spatial budget of organic carbon flux to the seafloor of the northern North Atlantic (60°N - 80°N). *Global Biogeochem. Cycles* 14: 329-340.
- Smethie, W. M. I., C. A. Nittrouer, and R. F. L. Self. 1981. The use of Radon-222 as a tracer of sediment irrigation and mixing on the Washington continental shelf. *Mar. Geol.* 42: 173-200.
- Soetaert, K., P. M. J. Herman, and J. J. Middelburg. 1996a. Dynamic response of deep-sea sediments to seasonal variations: A model. *Limnol. Oceanogr.* 41: 1651-1668.
- Soetaert, K., P. M. J. Herman, and J. J. Middelburg. 1996b. A model of early diagenetic processes from the shelf to abyssal depths. *Geochim. Cosmochim. Acta* 60: 1019-1040.
- Soetaert, K., J. J. Middelburg, P. M. J. Herman, and K. Buis. 2000. On the coupling of benthic and pelagic biogeochemical models. *Earth-Sci. Rev.* 51: 173-201.
- Tromp, T. K., P. Van Cappellen, and R. M. Key. 1995. A global model for the early diagenesis of organic carbon and organic phosphorus in marine sediments. *Geochim. Cosmochim. Acta* 59: 1259-1284.
- Van Cappellen, P., and Y. Wang. 1996. Cycling of iron and manganese in surface sediments: A general theory for the coupled transport and reaction of carbon, oxygen, nitrogen, sulfur, iron and manganese. *Amer. Jour. Sci.* 296: 197-243.

- Vanderborght, I. P., R. Wollast, and G. Billen. 1977. Kinetic models of diagenesis in disturbed sediments. Part I. Iron transfer properties and silica diagenesis. *Limnol. Oceanogr.* 22: 787-793.
- Wang, Y., and P. Van Cappellen. 1996. A multicomponent reactive transport model of early diagenesis: Application to redox cycling in coastal marine sediments. *Geochim. Cosmochim. Acta* 60: 2993-3014.
- Wang, Y., F., and R. Glud. 2002. Benthic carbon mineralization in the Atlantic Ocean: A synthesis based on in situ data from the 1990s decade. *Deep-Sea Res. I* (in press).
- Wijsman, J. 2000. Early diagenetic processes in Northwestem Black Sea sediments. Ph.D. Thesis, Groningen University, The Netherlands. Available at <http://www.ub.rug.nl/eldoc/dis/science/j.w.m.wijsman/>.
- Ziebis, W., M. Huettel, and S. Forster. 1996. Impact of biogenic sediment topography on oxygen fluxes in permeable seabeds. *Mar. Ecol. Prog. Ser.* 135: 227-237.

## **CHAPTER 3: Quantifying bioirrigation in aquatic sediments: An inverse modeling approach <sup>2</sup>**

### **Abstract**

An inverse model was developed to quantify the depth distributions of bioirrigation intensities in sediments based on measured solute concentration and reaction rate profiles. The model computes statistically-optimal bioirrigation coefficient profiles, that is, profiles which best represent measured data with the least number of adjustable parameters. A parameter reduction routine weighs the goodness-of-fit of calculated concentration profiles against the number of adjustable parameters by performing statistical F-tests, while Monte Carlo simulations reduce the effects of spatial correlation and help avoid local minima encountered by the downhill simplex optimization algorithm. A quality function allows identification of depth intervals where bioirrigation coefficients are not well constrained. The inverse model was applied to four different depositional environments (Sapelo Island, Georgia; Buzzards Bay, Massachusetts; Washington Shelf; Svalbard, Norway) using total CO<sub>2</sub> production, sulfate reduction and <sup>222</sup>Rn/<sup>226</sup>Ra disequilibrium data. Calculated bioirrigation coefficients generally decreased rapidly as a function of depth, but distinct subsurface maxima were observed for sites in Buzzards Bay and along the Washington Shelf. Irrigation fluxes of O<sub>2</sub> computed with the model-derived bioirrigation coefficients were in good agreement with those obtained by difference between total benthic O<sub>2</sub> fluxes measured with benthic chambers and diffusive fluxes calculated from O<sub>2</sub> microprofiles.

### **Introduction**

Biogeochemical cycles in aquatic sediments depend on coupled reaction and transport processes. The latter include diffusion, advection and biologically induced transport. Benthic macrofaunal activity may enhance solute transport through the passive or active flushing of infaunal burrow networks with water originating from the sediment-water interface (bioirrigation). In sediments with dense macrofaunal populations, bioirrigation may increase solute exchange fluxes across the sediment-water interface to such an extent that measured benthic fluxes are due primarily to bioirrigation, rather than diffusion (e.g. Hammond and Fuller 1979; Archer and Devol 1992). In heavily bioturbated sediments, enhanced biological transport may increase the return of nutrients to the overlying water. Such benthic nutrient release promotes benthic-pelagic coupling and contributes to the high primary productivity of nearshore marine environments (Rowe et al. 1975).

Bioirrigation also has a significant impact on the spatial distribution of early diagenetic processes in aquatic sediments. Flushing of burrow networks removes metabolites and reduced species from the bulk pore waters. At the same time, the introduction of oxidants via burrows to depths at which bulk conditions are highly reducing promotes reoxidation reactions near burrow walls (Aller and Aller 1998). Zonation in sediment redox conditions near burrow walls may significantly affect the microbial ecology at depth by increasing the variety of potential microbial niches (Aller et al. 1983; Mayer et al. 1995; Lowe et al. 2000). In addition, if solute transport rates are rapid relative to reaction rates, as is often the case in sediments with intense bioirrigation, it may become difficult to infer dominant microbial

<sup>2</sup> Meile, C., Koretsky, C.M., and Van Cappellen, P. (2002). *Limnology and Oceanography* 46(1): 164-177.

Acknowledgments. We thank 1. Kostka for providing sulfate reduction rate measurements from the Sapelo Island salt marsh site in advance of publication. E. Viollier, K. Hunter and S. Joye are thanked for valuable discussions. This work was supported financially by the Office of Naval Research (Grant no. N00014-98-1-0203).



organic carbon degradation pathways directly from pore water concentration gradients (e.g. Berner 1985; Fossing et al. 2000; Furukawa et al. 2000).

In this study, an inverse model is used to estimate the magnitude and the depth dependence of bioirrigation in aquatic sediments from measured concentration and reaction rate profiles. Bioirrigation has been represented previously in early diagenetic models as a non-local transport process, in which the bioirrigation intensity with depth is quantified by a mass transfer, or bioirrigation, coefficient (Boudreau 1984; Emerson et al. 1984). In contrast to previous studies (e.g. Martin and Sayles 1987), the inverse approach presented here does not require an a priori, and hence subjective, assignment of the functional depth-dependence of the bioirrigation coefficient profile. The inverse approach is also advantageous because measurement uncertainties can be accounted for explicitly in the model calculations, thus limiting the overinterpretation of measured data. Furthermore, constraints may be applied to parameter values, allowing knowledge regarding the system to be incorporated into the model.

The procedure presented in this study is similar to that of Berg et al. (1998), who used an inverse approach to identify reaction rate profiles in sediments with known transport rates. In particular, our model shares a similar (but not identical) approach with respect to the reduction of adjustable parameters, which leads to a statistically-optimal description of bioirrigation as a function of depth. However, the work presented here differs significantly from that of Berg et al. (1998) in a number of ways. First, Berg et al. (1998) used the inverse approach to solve for reaction rate profiles, whereas in this study the focus is on quantifying biologically induced solute transport. Second, the procedure presented here explicitly accounts for measurement uncertainties, and it allows model results to be constrained using a priori information about bioirrigation intensities in a given environment. Third, our model includes Monte Carlo simulations, in order to address shortcomings of the optimization and parameter reduction algorithms. In particular, a quality function is developed which identifies depth regions where the procedure does not lead to meaningful results. Finally, with the model presented, bioirrigation coefficient profiles can be determined from simultaneous analysis of multiple chemical constituents.

## Model Development

### Early diagenetic equation and boundary conditions

Biologically induced solute exchange, or bioirrigation, can be incorporated in the general early diagenetic equation of a solute species by combining it with terms representing diffusion, advection, and reaction:

$$\frac{\partial(\phi C)}{\partial t} = \frac{\partial}{\partial z} \left( D \phi \left( \frac{\partial C}{\partial z} \right) \right) - \frac{\partial(v \phi C)}{\partial z} + \alpha \phi (C_{flush} - C) + R \quad (1)$$

where  $D$  is the diffusion coefficient of the solute species corrected for tortuosity, temperature, salinity and pressure (Ullman and Aller 1982),  $v$  is the advection velocity relative to the sediment-water interface (neglecting  $\phi C \frac{\partial \omega}{\partial z}$  where  $\omega$  is the burial velocity),  $R$  is the net rate

of production of the solute at depth  $z$ ,  $\alpha$  the bioirrigation coefficient (in units of inverse time),  $\phi$  the porosity,  $C$  the solute concentration in the bulk sediment, and  $C_{flush}$  the flushing concentration of the solute, generally approximated as the concentration in the bottom water. Use of the relatively simple, non-local formulation of bioirrigation given in Equation (1) is justified by its structural similarity to a general exchange function approach (Boudreau 1987),

and its mathematical equivalence to a 3-D description of continuously flushed vertical tube-shaped burrows (Aller 1980; Boudreau 1984).

Equation (I) is solved numerically at steady state using a blended finite difference scheme (Fiadeiro and Veronis 1977; Boudreau 1997). In advection-dominated systems this blended scheme becomes a backward difference formula, whereas in diffusion-dominated systems it becomes a central difference scheme, thus balancing stability and accuracy of the numerical scheme. Discretization transforms the bioirrigation coefficient profile into a stepfunction and therefore  $\alpha$ -values for each depth segment are required.

Several options for defining upper and lower boundary conditions are included in the model. Fixed concentration or constant flux boundaries may be assigned, or mass balance considerations may be used to determine the solute concentration at either the upper or lower boundary. In the mass balance approach, the consumption or production of the solute species is integrated between the upper and lower boundary and combined with the calculated fluxes of the species into or out of the sediment via diffusion and bioirrigation. The solute concentration in either the top or bottom depth segment is then adjusted until mass balance is satisfied. In all of the simulations described below, the option of fixed concentrations is used for both the upper and lower boundary conditions.

### Inverse optimization routine

Using measured concentration and reaction rate profiles at steady state, it is possible to solve the discretized form of Equation (I) directly for the bioirrigation coefficient profile. However, this type of approach often yields oscillating values of  $\alpha(z)$ , as described for reaction rate profiles by Berg et al. (1998). In addition, the direct method does not allow bioirrigation coefficients to be constrained to physically meaningful values. For example, negative values of the mass transfer coefficient are not physically reasonable, but often result from a simple forward application of Equation (1). In addition to eliminating physically unreasonable solutions, the inverse approach also allows uncertainties and constraints to be incorporated directly into the model, and it does not require an arbitrary choice for the depth-dependence of the bioirrigation coefficients.

In the algorithm developed in this study (Figure 1), an initial guess of the bioirrigation coefficient depth profile is systematically altered using a modified downhill simplex method (Press et al. 1989) to find a profile that reproduces measured concentration profiles within specified limits of uncertainty. The downhill simplex algorithm is an iterative procedure to minimize an objective function which reflects the quality of a calculated solution. The iterative optimization of the objective function is repeated until convergence between the calculated and measured concentration profiles, within a given uncertainty, is achieved at all depths, or until a specified number of iterations (typically > 1000) are completed.

The objective function (OF) accounts for the fit to the data, via the sum of the weighted least square differences between the measured and calculated concentrations at each depth in the profile, modified by penalty functions. The latter increase the value of the objective function when values of  $\alpha(i)$  either violate the parameter constraints or result in calculated concentrations that are less than a defined limiting value (typically 0). Mathematically,

$$OF = \sum_{i=1}^n \left( \frac{C_{meas,i} - C_{calc,i}}{\sigma_{C,i}} \right)^2 + t \sum_{i=1}^n \left( \frac{C_{lim,calc,i} - C_{calc,i}}{CFC,i} \right)^2 + c \sum_{i=1}^n \left( \frac{C_{um,i} - C_{calc,i}}{\sigma_{C,i}} \right)^2 \quad (2)$$

where  $\sigma_{C,i}$  is the uncertainty of the measured concentration,  $n$  is the number of depth segments, chosen to reflect the resolution of the measurements. The weighting parameters,  $t$  and  $c$ , are set to 0 if no violations of the constraints on parameters or concentrations occur; otherwise they are assigned values  $\geq 0$ . In the simulations shown here,  $t$  and  $c$  are both set to 10 when violations occur, but other values can be assigned by the user if necessary.  $C_{meas}$ ,

$C_{\text{calc}}$  and  $C_{\text{lim}}$  are the measured, calculated and limit concentrations (e.g.,  $C_{\text{lim}} = 0$ ; forcing modeled concentrations to 0), respectively;  $C(\alpha_{\text{lim}})$  is the concentration calculated using the constraining value of  $\alpha$  (e.g.,  $\alpha_{\text{lim}} = 0$ ) at the depths where  $\alpha$  violates the constraints.

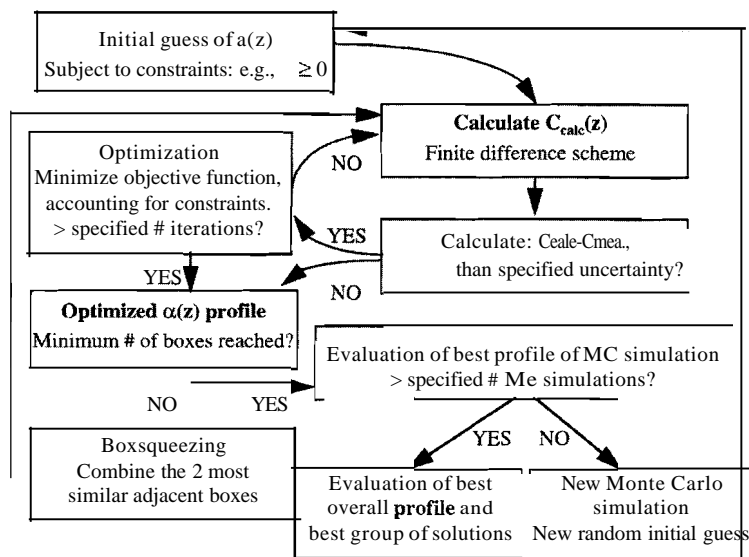


Figure 1. Flow-chart of the inverse modeling approach.

## Reduction of independent parameters and statistical quality of fit

The optimization procedure described above leads to a solution that is consistent with both the measured data and the applied constraints. However, adjacent depth segments may have very similar bioirrigation coefficient values, so that the profile could be simplified (i.e., the number of fitting parameters reduced) without a significant loss in the quality of the fit between the measured and calculated concentration profiles. Therefore, a 'boxsqueezing' algorithm was developed to systematically reduce the number of fitting parameters. In this algorithm, the depth discretization of the profile is changed by combining the two adjacent depth segments with the most similar parameter values into a single segment. After the two segments are 'squeezed' together, the optimization routine is repeated using the new discretization. This process is continued until a pre-specified minimum number of parameters is reached.

The statistically-optimal depth discretization is determined using two criteria. The primary criterion is that the calculated concentration at each depth in the initial discretization must lie within the uncertainty of the measured data (i.e., convergence is required at each depth). If more than one discretization of the parameter profile meets this criterion, then the quality of the fit associated with each discretization is weighted against the simplicity of the bioirrigation coefficient profile by performing a series of F-tests at a 95% confidence level (for details on the test statistics see Kleinbaum et al. 1988, and Berg et al. 1998). In this way, the 'boxsqueezing' routine allows the objective determination of the simplest parameter profile which describes the measured data.

## Monte Carlo simulations

The most severe limitation of the downhill simplex algorithm used to optimize the parameter profile is that it may yield solutions associated with a local, rather than global, minimum of the objective function. Therefore, in the presence of local minima, the optimized parameter value depends on the initial guess of that value. This limitation of the downhill simplex optimization method is overcome by performing a series of Monte Carlo simulations with initial guesses of the parameter profile chosen at random from a specified range of values. In the model presented here, the range of initial parameter values at each depth may either be specified explicitly or may be constrained by calculating, at each depth, the maximum and minimum parameter value (subject to specified constraints) which yields a calculated concentration consistent with the measured concentration and its associated uncertainty. Each Monte Carlo simulation yields a single, statistically-optimal parameter profile, based on the criteria described in the previous section.

Optimized profiles resulting from the individual Monte Carlo simulations are compared and ranked according to the same criteria used to determine the best discretization of the parameter profile. Ranks are first assigned to profiles based on convergence. That is, profiles with greater numbers of converged depths (using the original depth discretization) are ranked above profiles with fewer converged depths. Within a group of profiles with the same number of converged segments, each profile is rated as better or worse than each of the other profiles. For two profiles with different numbers of adjustable parameters, this rating is based on an F-test, which determines whether the additional adjustable parameters significantly improve the fit of the calculated concentration profiles to the measured ones. For two profiles with the same number of adjustable parameters, the profile with the lower objective function value receives the higher ranking. The overall rank of a given profile is then based on the number of times it ranked better than other profiles in the pool. This procedure leads to the selection of the "best" individual bioirrigation coefficient profile.

In the parameter reduction scheme used in this study, the combination of depth segments is non-reversible. Thus, if depth segments are combined in a way that does not correctly reflect the underlying process, subsequent optimization of the profile will be biased. However, inappropriate combination of two depth segments as an artifact of the optimization routine will likely result in a profile ranked lower than others produced by the Monte Carlo simulations. This is because it will either result in a worse fit or it will prevent the further reduction of the numbers of adjustable parameters because the convergence criterion cannot be met.

The variability of the bioirrigation coefficient profiles produced by the Monte Carlo simulations serves as a qualitative indicator of how well the  $\alpha$ -values can be constrained at any given depth. Part of the variability, however, results from spatial correlation, that is, coupling between adjacent spatial nodes. Because diffusion tends to smooth concentration profiles, an overprediction of the 'true' (unknown) irrigation coefficient coupled to an underpredicted value in an adjacent depth segment may yield a good fit to the measured data. Decreasing the number of adjustable parameters generally lessens spatial coupling by broadening the depth segments with constant parameter values. However, if  $\alpha$  changes significantly over a small depth interval, the parameter reduction may instead induce spatial coupling. The effects of spatial coupling are greatly reduced by averaging results from multiple Monte Carlo simulations. Thus, the average irrigation coefficient profile calculated from the individual parameter profiles of the Monte Carlo simulations may lead to a solution closer to the true value of  $\alpha$  (see section Model performance). However, care must be taken to include in the averaging only those solutions which belong to the global minimum. Based

on test runs with model scenarios (see below), it was found that between 100 to 500 Monte Carlo simulations were sufficient to obtain reproducible results.

### Quality function

To assess the quality of the model results, a quantitative quality measure ( $Q$ ) was developed, which reflects the sensitivity of the concentration profile to changes in the parameter profile (i.e., the irrigation coefficient), as well as on the goodness of the fit between the measured and calculated concentration profiles. It is defined, at any given depth  $z$ , as

$$Q = \left| 8 \frac{\alpha_{avg}}{\Delta C} \right| \quad (3)$$

where  $\Delta C$ , the difference between measured and calculated concentrations at depth  $z$ , accounts for the goodness of fit. The sensitivity (8) is evaluated by perturbing the optimized a-profile at depth  $z$  while leaving the rest of the profile unchanged. The value of 8 is then equal to the difference in concentration between the optimized and perturbed a-profile at depth  $z$ , divided by the difference in the optimized and perturbed value of  $\alpha$  at this depth.

Multiplication by a scaling factor  $\alpha_{avg}$ , the average value of the bioirrigation coefficient over the entire core depth, results in a dimensionless value of  $Q$ . This allows comparison of the quality of model results for environments with different bioirrigation intensities.

The limit value of  $Q$ , below which model results become meaningless, was established empirically by applying the model to a number of synthetic scenarios with known bioirrigation coefficient profiles (see section Model performance). In Figure 2, deviations between calculated and imposed irrigation coefficients from a variety of model scenarios are plotted against  $Q_{min}$ , the lowest value of  $Q(z)$  over the whole depth profile. The absolute deviation of  $\alpha$  at the depth where  $Q$  equals  $Q_{min}$  and the relative error at this depth both increase significantly below a value of  $Q_{min} \approx 0.4$ . The largest absolute error in  $\alpha$  is generally found at the depth where  $Q$  equals  $Q_{min}$ . In what follows, the bioirrigation coefficient is deemed well-constrained for depth intervals where  $Q \geq 0.4$ .

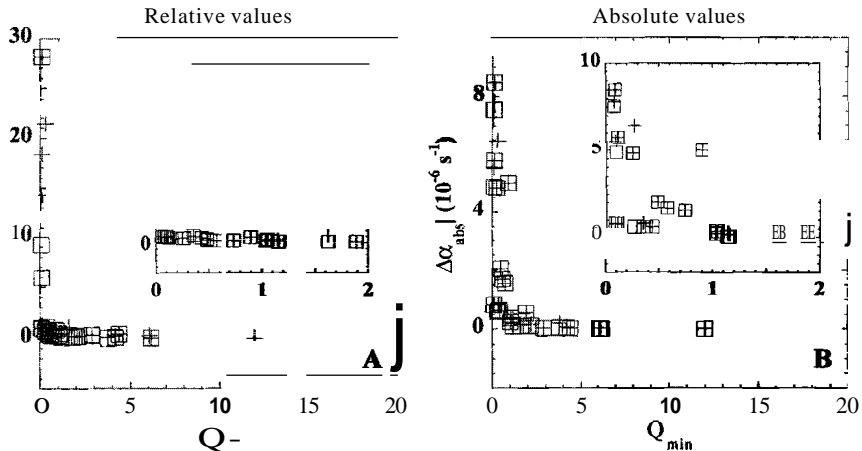


Figure 2. (A) Relative and (B) absolute deviations between calculated and 'true' irrigation coefficients plotted against the minimum value of the quality function for the entire depth profile. Data are from a variety of synthetic model simulations (see text). Open squares represent the absolute error at the depth at which  $Q$  reaches its minimum value; crosses depict the maximum absolute error in the entire profile. See text for detailed discussion.

To increase computational efficiency, the quality function is only evaluated for the statistically-best Monte Carlo simulation profile and for a limited number of averaged profiles. To select the profiles to be averaged, the statistically-best profiles from the individual Monte Carlo simulations are ranked as described in the previous section. Averaged profiles are then calculated from these profiles, using those with a rank better than 1, 2, 5, 10, 25, 50 and 100% of the total number of Monte Carlo simulations. Of these averaged profiles, that which produced the highest value of  $Q_{min}$  is taken as the best representation of  $\alpha(z)$ . The selected individual profiles are used to calculate standard deviations about the best estimate of  $\alpha(z)$ .

### Non-unique nature of solutions

It is sometimes assumed (erroneously) that models which provide a good fit to measured data are 'correct'. In fact, for natural systems, the available quality or quantity of data often cannot provide unique solutions to modeled problems. In other words, model solutions may yield an excellent fit to measured data without correctly representing the underlying process(es). For example, it may not be possible to determine unique values of  $\alpha$  with Equation (1), particularly when the flushing concentration lies within the uncertainty of the measured pore water concentrations. In such a case, high values of  $\alpha$  simply shift the calculated concentration closer towards the value of the flushing concentration. Thus, an irrigation coefficient profile might be found which reproduces measured concentrations, but which does not accurately represent the in situ exchange intensity.

To minimize such problems,  $\alpha$  is extrapolated from adjacent depth segments if (1) the flushing concentration lies within the uncertainty of the measured value and the calculated concentration is closer to the flushing concentration than to the measured one (indicating a likely overestimate of  $\alpha$ ), or (2) the flushing concentration is very close to the calculated concentration (difference smaller than 10% of the uncertainty at that depth) and the corresponding irrigation coefficient is very large (e.g.  $> 10^{-3}$  sol). In the top and bottom depth segments, where fixed concentration boundary conditions apply,  $\alpha$  is undefined and is therefore set equal to the value in the adjacent depth segment.

### Multicomponent optimization

A more robust quantification of solute exchange may be obtained by using independent data sets for multiple chemical constituents. Such an approach assumes that the same irrigation coefficient applies to the different constituents. This is likely to hold true if the solute species have similar physico-chemical properties or if the frequency of burrow flushing is slow enough to allow equilibration of the chemical composition of pore waters and burrow solution (Hammond et al. 1985). In the case of continuous flushing of burrows, however,  $\alpha$  is related both to the diffusion coefficient and the diffusive pathlength (Boudreau 1984). The latter is influenced by the reactivity of a chemical (Marinelli and Boudreau 1996) and, hence, differences in irrigation coefficients may be expected for different chemical species.

In a multicomponent calculation, the objective function (OF) should reflect all the constituents involved in the calculation of  $\alpha$ . Thus, it is defined as the sum of the contributions from the different chemical constituents. In the multicomponent simulations shown below, the objective function was modified slightly, so that only depth segments lacking convergence contributed to the value of OF. This leads to stronger dependence on convergence than for the standard definition of OF given by Equation 2. Irrigation coefficient profiles are ranked according to the same criteria as in the one component case. However, the quality of fit is determined separately for each concentration profile and the sum of ranks from this evaluation is used as the decision variable for the overall quality of an irrigation

coefficient profile.  $Q(z)$  is assigned the average value of all profiles at a given depth. Hence, high values of  $Q(z)$  indicate that the irrigation coefficient is well defined by all of the chemical species used in the calculation. Values of  $Q$  are likely to be lower in the multicomponent approach, however, because the resulting bioirrigation coefficient profile must provide a good fit to all species involved in the optimization.

## Model Performance

Before the model was applied to data from natural systems, it was first tested using a series of simulations designed to analyze the performance of the three primary model components: the downhill simplex optimization, the reduction of adjustable parameters ('boxsqueezing') and the Monte Carlo simulations. The finite difference scheme has been thoroughly tested previously (Meile 1999).

A set of synthetic rate and irrigation coefficient profiles was used with specified fixed concentration boundary conditions, in order to calculate corresponding concentration profiles. From these rate and concentration profiles, with uncertainties specified for each concentration, the irrigation coefficient profiles were back-calculated with the inverse model. In this way, model performance was assessed for a variety of hypothetical environmental scenarios.

## Model scenarios

Model performance is illustrated in Figure 3. The 'baseline scenario' is representative of a highly productive coastal-estuarine environment, with the rate and concentration profile corresponding to, for example, profiles of the net rate of sulfate reduction and the sulfate concentration.

The calculated profiles shown in Figure 3A demonstrate that both the single, statistically-best profile and the average profile reproduce the true bioirrigation coefficient profile very well at most depths. The single best profile, however, fails to reproduce some of the fine-structure of the true bioirrigation coefficient profile. In particular, the high value of  $\alpha$  is underestimated at 1 cm depth. Simplification of the modeled profiles through 'boxsqueezing' (from 19 initial to 5 final depth segments) of the statistically-best profile prevents the steep decrease of the true bioirrigation coefficients at the top of the profile from being simulated exactly (Figure 3A). The lower values of the quality function near the top of the profile (Figure 3E) reflect the lower sensitivity just below the water-sediment interface, which is due to the small value of the bioirrigation driving force ( $C_{fluSh-C}(Z)$ ).

Simulation results shown in Figure 3B and F were calculated using the same reaction rate and bioirrigation profiles as in the baseline scenario, but the uncertainty associated with the measured concentration profile was increased from 1 to 5%. Due to the larger uncertainties, the number of depth segments with distinct values of  $\alpha$  is reduced to just three in the statistically-best irrigation coefficient profile. Although the calculated bioirrigation coefficient profile matches the imposed solution quite well, the range of possible  $\alpha$ -profiles leading to converged concentration profiles is considerably larger than for the case above. The maximum value increases to as much as  $10^{-4} \text{ s}^{-1}$  near the sediment-water interface. Thus, as expected, the quality of the model results is directly influenced by the quality of the data.

Results shown in Figure 3C were calculated using the baseline scenario, but with an imposed solute consumption rate equal to zero, as would be the case for an unreactive species. The main difference to the previous scenarios is a lower sensitivity of the concentration values to the calculated irrigation coefficient profile, and hence lower values of  $Q$ . Nonetheless, good fits to the true concentration and irrigation coefficient profiles are still obtained (Figure 3C and G). The lower sensitivity, particularly in the upper cm of sediment, reflects the fact that

non-zero rates increase the difference between the flushing concentration and the pore water concentration, which, in turn, facilitates identification of the true bioirrigation coefficient profile.

For the simulation results shown in Figure 3D and H, a bioirrigation profile with a step function depth-dependence was imposed. This corresponds qualitatively to the irrigation regime resulting from the activity of certain polychaetes (e.g. Craig and Lopez 1996). The model results fit the imposed profile extremely well, giving rise to values of  $Q$  that are generally much higher than in simulations for which a steeply decreasing bioirrigation coefficient profile was used. Thus, the inverse approach appears to be capable of identifying regions of markedly different irrigation intensities within the sediment column.

To illustrate spatial correlation,  $a$ -values were interpolated linearly from the values at the center of the depth segments to the depths of the interface of two adjacent boxes. The oscillating values in the enveloping minimum and maximum of  $a$ -values (Figs 3A-3D) reflect spatial coupling in the underlying individual profiles. These profiles, which are also consistent with the data available and their uncertainties, are ranked low in the statistical comparison due to the larger number of fitting parameters.

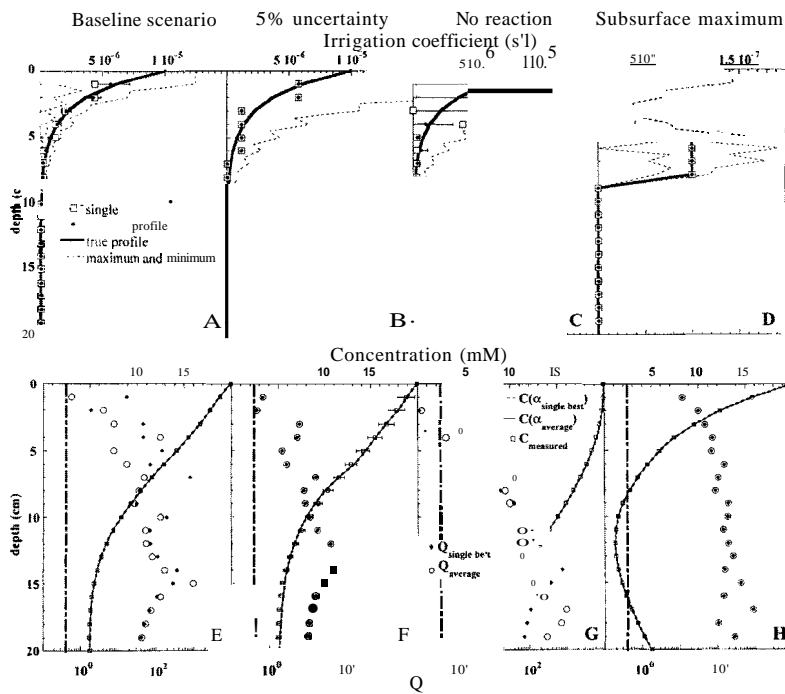


Figure 3. Model results using imposed depth profiles of rate and bioirrigation coefficient. (A) Single best and averaged irrigation coefficient profiles, and minimum and maximum values of  $a$  for all converged simulations, in the 'baseline scenario' which is defined by an exponentially decreasing solute consumption rate ( $R$  ( $\text{mM s}^{-1}$ ) =  $0.5 \exp(-15 * z(\text{cm}))$ ), a steeply decreasing bioirrigation coefficient profile, a 1% uncertainty in the concentrations, and concentration boundary conditions. (B) Symbols and simulations are identical to (A) except that the uncertainties on concentrations are assigned a value of 5% (C) same as (A), except that the reaction rate is set to 0 at all depth. (D) same as (A), except that the bioirrigation depth-dependency is defined by a step function. (E)-(H) Concentration and quality function profiles for the simulations described in panels (A)-(D), respectively. The vertical dashed line shows the value of  $Q = 0.4$ , below which model results are no longer well-constrained.



## Model Application

The inverse model was used to quantify bioirrigation coefficient values with depth in a variety of marine environments using measured data for three different chemical constituents (Table 1). Diffusion coefficients were either calculated as a function of temperature, salinity and pressure and corrected for tortuosity (Ullman and Aller 1982), or they were taken directly from the studies to which our model results are compared. Pore water advection through the bulk sediment was neglected, while rapid, preferential flow through burrows was accounted for by the bioirrigation coefficient. The advective transport due to sedimentation was also neglected, because at all study sites sedimentation rates are less than 10 mm yr<sup>-1</sup> (Howarth and Giblin 1983; Christensen et al. 1984; Tromp et al. 1995, Glud et al. 1998), which is insignificant compared to diffusion and bioirrigation rates. Measured porosity, concentration and rate profiles were interpolated to the depths of the gridpoints using a weighted distance relationship. Input data resolution was set to 1 cm. For the Rn/Ra disequilibrium data, the reaction term included a first order term accounting for the decay of pore water Rn, while the production of Rn through decay of Ra was accounted for using a zero order rate based on the measured Rn secular equilibrium activity ( $\lambda_{Rn} \phi Rn_{\text{porewater}}$  and  $\lambda_{Rn} \phi Rn_{\text{equilibrium}}$ , respectively, with  $\lambda_{Rn}$  being the <sup>222</sup>Rn decay constant of 3.824 dol). Constraints were applied to exclude negative values of the irrigation coefficients and calculated concentrations.

*Table 1. Study sites, input data and summary of model results. The irrigation transfer velocity (V) is calculated by integrating the bioirrigation coefficient over the whole core depth; z<sub>90</sub> is the depth at which the depth-integrated bioirrigation coefficient reaches 90% of the total transfer velocity.*

site	water depth	data used	V (cm yr <sup>-1</sup> )	z <sub>90</sub> (cm)
Malangen (Sv-1: 69° 29.4'N 18° 07.5'W)	329m	DIC, pH, Rem	4267 ± 982	14.5
Storefjorden (Sv-5: 77° 33.0'N 19° 05.0'W)	175 m	DIC, pH, Rem	1742 ± 300	14.5
Sapelo Is. (June, 31° 22'N 81° 14'W)	intertidal	SO <sub>4</sub> <sup>2-</sup> , SRR	1841 ± 349	4
Sapelo Is. (August, 31° 22'N 81° 14'W)	intertidal	SO <sub>4</sub> <sup>2-</sup> , SRR	29127 ± 28479	4
Buzzards Bay (near Weepeeket Is.)	15m	Rn/Ra	138	18
Washington Shelf, core 2A (MSSD-1, Aug)	86m	SO <sub>4</sub> <sup>2-</sup> , SRR	341	28.5
		Rn/Ra	1708 ± 88	23.5
		Rn/Ra and SO <sub>4</sub> <sup>2-</sup> , SRR	959 ± 446	23.5
Washington Shelf, core 3A (MSSD-2, Aug)	86m	SO <sub>4</sub> <sup>2-</sup> , SRR	1607 ± 828	24.5
		Rn/Ra	898 ± 200	21.5
		Rn/Ra and SO <sub>4</sub> <sup>2-</sup> , SRR	809 ± 172	24.5

### Subtidal estuary, Buzzards Bay, Massachusetts

<sup>222</sup>Rn/<sup>226</sup>Ra disequilibrium has been used to study mixing processes in sediments (e.g. Hammond et al. 1977; Key et al. 1979; Gruebel and Martens 1984). Due to the large difference in the half lives of parent and daughter isotope, any deviation of the measured Rn activity at a given depth in the sediment from its value at secular equilibrium may be attributed to transport processes. Martin and Banta (1992) used Rn/Ra disequilibrium data to quantify bioirrigation at a subtidal estuarine site at Buzzards Bay (Table 1). Bioirrigation coefficients calculated using the inverse model developed in this study could be directly compared to those of Martin and Banta (1992).

To apply the inverse model, Rn activities, porosity and diffusivity data were taken directly from Figure 2 and Table 2 in Martin and Banta (1992). As in the latter study, it was assumed that the activity of Rn in the overlying water equals 0, and that the Rn profile represents

steady state conditions. However, unlike in Martin and Banta's study, the lower boundary condition was set to a fixed Rn value, instead of applying an open system condition. In agreement with Martin and Banta (1992), inverse model results indicate that solute transport in the top 5 cm of the sediment is diffusion-dominated, whereas below 5 cm depth both studies suggest that transport via bioirrigation is substantial compared to transport via diffusion. In addition, the depth-integrated value of  $\alpha$  obtained with the inverse model (Table 1), which can be interpreted as a transfer velocity across the sediment-water interface and gives a measure for the overall intensity of bioirrigation at a given site, differs by less than a factor of 2 from Martin and Banta (1992). However, in the upper diffusion-dominated portion of the sediment, values of  $Q$  are quite low (Figure 4B), indicating that bioirrigation coefficients in this portion of the profile are not well constrained. Although the depth-integrated irrigation coefficients found in the two studies are similar, the depth-dependence of the irrigation coefficient obtained by the inverse method is quite different from that presented by Martin and Banta (1992). This is because Martin and Banta (1992) imposed an exponential shape of the irrigation coefficient profile in order to fit the measured Rn profile. With the inverse model, no a priori shape of the irrigation coefficient is assumed. According to the results of the inverse model, the irrigation coefficient exhibits a distinct subsurface maximum between 10 and 14 cm sediment depth, rather than a monotonic change with depth (Figure 4A). Such a subsurface maximum in the bioirrigation coefficient profile could reflect the activity of deposit feeders such as *Nephtys*, which have been reported by Martin and Banta (1992) at the study site. The same authors also observed a subsurface maximum in an excess bromide profile in one of the cores collected at the site.

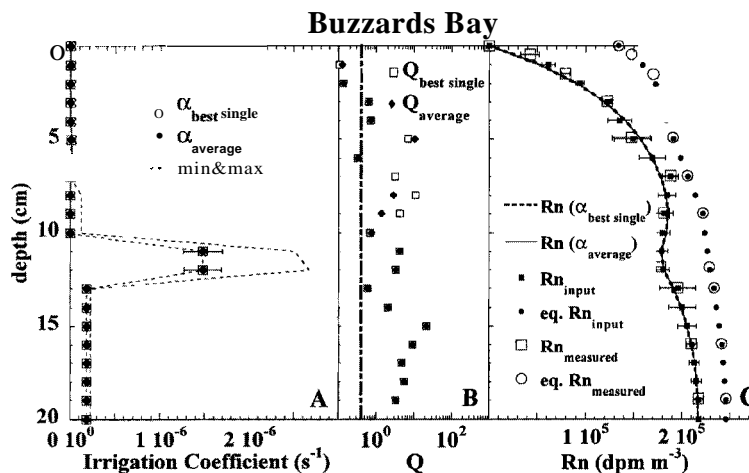


Figure 4. Bioirrigation at Buzzards Bay. (A) The single, statistically-best irrigation coefficient profile, and the averaged irrigation coefficient profile, together with maximum and minimum values of the profiles with the least number of non-covered boxes. (B) Quality function profile for the single, statistically-best solution and the averaged solution. The dashed line shows the limit value of  $Q = 0.4$ . (C) Measured, interpolated and calculated Rn pore water activities as well as measured and interpolated secular equilibrium activity of Rn.

## Washington continental shelf

Bioirrigation has been quantified previously on the Washington Shelf using forward calculations based on Rn/RA disequilibrium data and sulfate concentration plus reduction rate data (Smethie et al. 1981; Christensen et al. 1984). Bioirrigation coefficient profiles were calculated in this study by applying the inverse model to two sites on the Washington Shelf (Table 1) based on sulfate and Rn data alone, as well as from simultaneous optimization of both data sets.

Inverse model results obtained using either Rn or  $SO_4^{2-}$  profiles alone, or both species simultaneously, indicate significant bioirrigation to a depth of approximately 30 cm at both sites and high irrigation coefficients in core 3A near the sediment-water interface (Figures 5A and 6A). The main difference in the bioirrigation profiles for the individual species occurs near the sediment-water interface in core 2A, where results obtained using the sulfate profiles alone give no indication of the intense irrigation suggested by the Rn profile (Figure 5A). The results obtained for cores 2A and 3A using Rn, sulfate or both suggest a subsurface maximum in irrigation at approximately 11 and 19 cm depth, respectively (Figure 5A and 6A).

From the difference in Rn and  $SO_4^{2-}$  diffusion coefficients, it might be expected that the bioirrigation coefficient values obtained from Rn data should be higher than those obtained using  $SO_4^{2-}$  data, possibly by as much as a factor of 2. Such a difference in the magnitude of the irrigation coefficients is observed for the lower portion of core 2A, but not for core 3A. The lack of a systematic difference in bioirrigation coefficients between the two species justifies the simultaneous optimization of Rn and  $SO_4^{2-}$  profiles. In core 3A, simultaneous optimization of sulfate and Rn profiles shows high values of  $Q$  near the sediment-water interface and significant irrigation down to 30 cm depth, as found from the sulfate and Rn profiles alone (Figure 6A). The multicomponent optimization in core 2A leads, not surprisingly, to intermediate values of  $Q$  near the water-sediment interface, compared to the two single-species analyses, but the visually poor fit to the sulfate concentration as well as the low values of  $Q$  indicate the relatively low reliability of the model results in the upper few centimeters (Figure 5B and C). It is difficult to determine the coefficients precisely over a large portion of the profile as indicated by the large error bars associated with the irrigation coefficient profile. Nonetheless, it appears that the irrigation coefficients are relatively high near the top and bottom of the cores at both sites. Overall, the results obtained for both sites diverge significantly from the exponential decrease of  $Q$  which is often assumed in early diagenetic models (Martin and Sayles 1987; Schluter et al. 2000; Wang and Van Cappellen 1996).

The inverse model results compare favorably to the findings of Christensen et al. (1984), who also found significant irrigation to a depth of 30 cm. However, Christensen et al. (1984) suggested the presence of a subsurface maximum in the bioirrigation coefficient at about 5 cm based on the  $SO_4^{2-}$  profiles. Such a subsurface maximum was not observed in any of the profiles calculated here using the inverse model.

Independent evidence supports the validity of the bioirrigation  $Q$  calculated by the inverse model, at least with respect to depth-dependence. The subsurface maximum in the irrigation coefficients found in core 2A between 10 and 11 cm using the inverse method matches the depth of a worm burrow reported in core 2A by Smethie et al. (1981). This subsurface peak is apparent in profiles calculated with the inverse model using the sulfate or Rn data alone, or using a combination of the two (Figures 5), but is not apparent in any of the calculated profiles reported by Christensen et al. (1984).

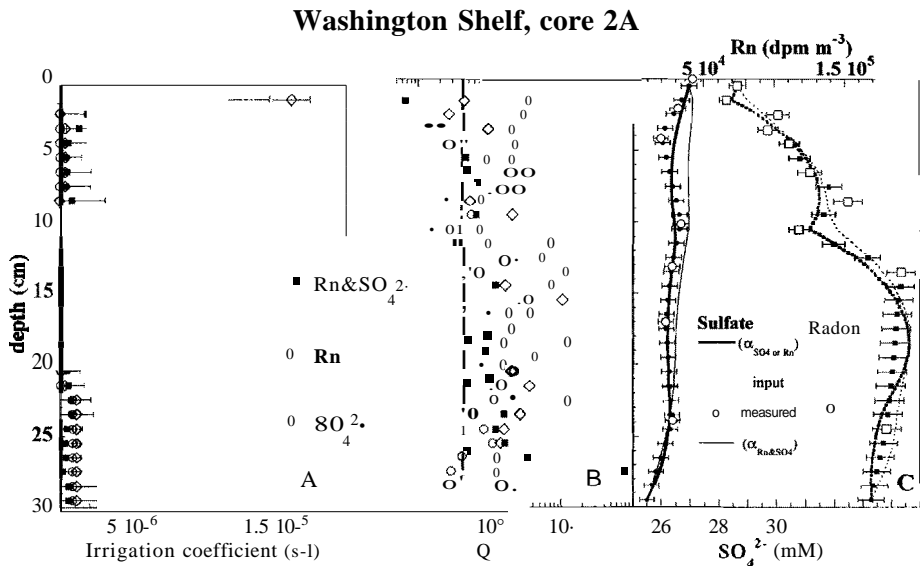
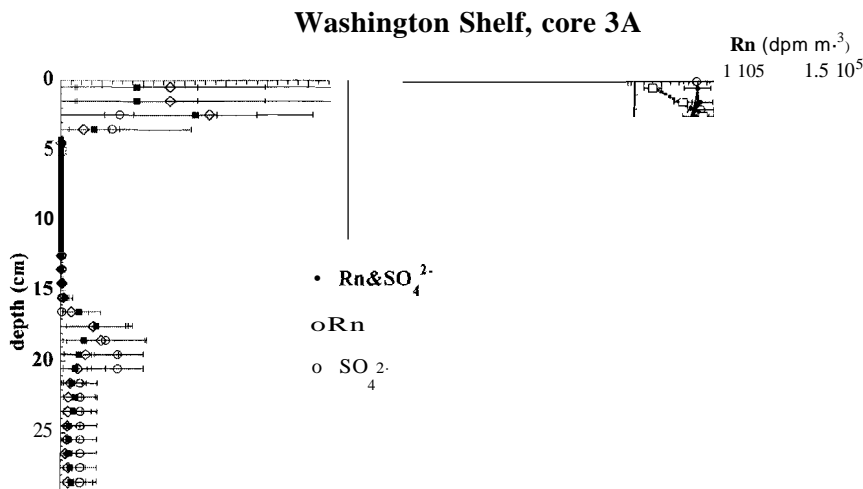


Figure 5. Bioirrigation on the Washington Shelf, core 2A. (A) Average bioirrigation coefficient profile and (B) quality function obtained from simulations using Rn and sulfate data alone, as well as simultaneous optimization, respectively. (C) Calculated and measured sulfate concentrations and pore water radon activities, respectively. Sulfate reduction rates and Rn equilibrium activities used in these simulations (not shown) are from Christensen et al. 1984, their Figure 2, and Smethie et al. 1981, their Table 1.



The deep, rapid solute transport implied by the high bioirrigation coefficients found near the bottom of the cores also helps to explain the observed departure of measured pore water Rn activities from secular equilibrium values. Smethie et al. (1981) attributed this difference to analytical overestimation of the equilibrium Rn activity. However, model simulations using corrected equilibrium activities proposed by Smethie et al. (1981) fail to produce enhanced bioirrigation coefficients at the depth of the reported burrow. This suggests that the difference in Rn activities may not be due to analytical artifacts, but rather to solute transport induced by deep intense bioirrigation.

To further evaluate the bioirrigation coefficients predicted by the inverse model, Oz irrigation fluxes across the sediment-water interface at the Washington Shelf sites were estimated, assuming that the bioirrigation coefficients derived from the sulfate and Rn data apply to Oz. If this assumption is violated, the calculated Oz irrigation fluxes will tend to be underestimates, because the high reactivity of Oz would give rise to steep concentration gradients which would accelerate diffusional transport of Oz across burrow walls (Marinelli and Boudreau 1996). To calculate the Oz irrigation fluxes, the sediment concentration was assumed to be negligible, and the Oz flushing concentration was set to 130  $\mu\text{mol l}^{-1}$  as cited by Christensen et al. (1984). This leads to calculated irrigation fluxes of  $2 \pm 1.0$  and  $1.6 \pm 0.4$   $\text{mmol O}_2 \text{ m}^{-2} \text{ d}^{-1}$  at sites MSSD-1 and -2, respectively, which is similar to the values of 1.2 and 2.5  $\text{mmol O}_2 \text{ m}^{-2} \text{ d}^{-1}$ , respectively, calculated by Christensen et al. (1984). Archer and Devol (1992) determined O<sub>2</sub> irrigation fluxes on the Washington Shelf from the difference between total solute fluxes measured with benthic chambers and diffusive fluxes calculated from high resolution pore water O<sub>2</sub> profiles. The O<sub>2</sub> irrigation fluxes reported by these authors near the study area range from 1.4-6.3  $\text{mmol m}^{-2} \text{ d}^{-1}$  which is of the same order of magnitude as the fluxes calculated using the inverse model results.

### **Arctic environment, Svalbard, Norway**

Bioirrigation coefficient profiles were calculated for two sites near Svalbard, Norway, one at Malangen Fjord and the other at Storefjorden (Sv-1 and Sv-5, respectively, Table 1). The bioirrigation profiles were optimized using profiles of dissolved inorganic carbon concentration (DIC), DIC production rate (Reoz) and pH for the two sites described in Kostka et al. (1999). The diffusion coefficient for DIC was calculated from the diffusivities of the different carbonate species, weighted according to their relative contribution to DIC based on the measured pH values.

Calculated bioirrigation coefficient profiles at both sites show very high depth-integrated values of  $\alpha$  (Table 1) and a distinct decrease of  $\alpha$  with depth (Figure 7A and C). The quality function has high values over the entire profile (Figure 7B and D), and the calculated concentrations are within the uncertainties of the interpolated measurements (not shown). This provides a high level of confidence that the calculated bioirrigation coefficient profiles are meaningful and implies a very active benthic macroinfauna in these Arctic environments.

To assess the inverse model results, calculated Oz irrigation fluxes were compared to the difference between measured benthic oxygen fluxes and diffusive fluxes calculated from O<sub>2</sub> microelectrode profiles measured at the Storefjorden site (Glud et al. 1998). Irrigation fluxes were calculated using the measured bottom water Oz concentration of 328  $\mu\text{mol l}^{-1}$  as the flushing concentration and, because the Oz penetration depth is approximately 1 cm and the concentration decreases approximately linearly with depth (Glud et al. 1998), the Oz concentration was assumed to be half the flushing concentration in the top centimeter of sediment and 0 below. This calculation results in an estimated irrigation flux of approximately 10  $\text{mmol Oz m}^{-2} \text{ d}^{-1}$ , which is 2.5 times greater than the difference between the

measured benthic and diffusive fluxes of  $3.9 \pm 1.5 \text{ mmol } O_2 \text{ m}^{-2} \text{ dol}$ . The irrigation flux of DIC calculated from the irrigation coefficient profile also exceeds the difference between measured benthic and diffusive fluxes (Glud et al. 1998) by about a factor of 2.5. At present, the reason for the discrepancy between calculated and measured irrigation fluxes is unclear.

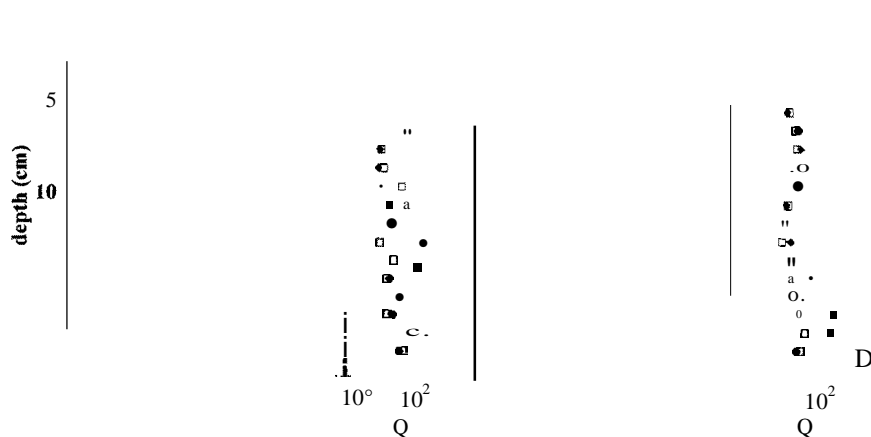


Figure 7. Bioirrigation in the Svalbard region, based on DIC,  $R_{CO_2}$  and pH profiles. Symbols and panels in panels (A) and (C), and (B) and (D) are the same as in Figure 4, panels (A) and (B), respectively. DIC concentrations and DIC production rates used in these simulations (not shown) are from Kostka et al. 1999, their Figures 2 and 6.

### Salt marsh environment, Sapelo Island, Georgia

Salt marsh sediments are densely populated by macrofauna including fiddler crabs, mud crabs, polychaete worms and shrimp, all of which may build extensive burrow networks (e.g. Teal 1958; Basan and Frey 1977). Therefore, bioirrigation is likely to be an important solute transport process in salt marsh sediments. Nonetheless, few attempts have been made to quantify bioirrigation in these environments. Here, the inverse model was applied to data collected at an unvegetated creek bank site at Sapelo Island, a barrier island ~8 km off the coast of Georgia, USA (Table 1).

Sulfate concentrations were measured on pore waters collected using diffusion equilibrators (Koretsky et al., in prep), and sulfate reduction rates were determined by adding trace quantities of  $^{35}SO_4^{2-}$  to sediments (Kostka et al. 1978) and incubating them for 2 hours (Kostka et al., submitted). To derive irrigation coefficients using the inverse model, net rates of sulfate consumption are required. Thus, if in situ reoxidation of reduced sulfur is significantly higher than during the 2 hour laboratory incubation, then this would lead to an overestimation of the calculated irrigation coefficients. This might occur, for example, because  $O_2$  is entirely excluded in the laboratory experiment, whereas in the field  $O_2$  may be introduced into the sediment via bioirrigation.

Calculated irrigation profiles might also be biased because sulfate concentration profiles measured using diffusion equilibrators represent pore water concentrations averaged over several days to weeks, whereas the sulfate reduction rates represent instantaneous rates. This difference in timescales may influence model results significantly if the sulfate pore water concentrations, sulfate flushing concentrations or the sulfate reduction rates fluctuated greatly

during the three week deployment period of the diffusion equilibrators. Furthermore, the time resolution of the concentration and reduction rate data does not allow potential non-steady state effects on the measured profiles to be addressed. Thus, the data were assumed to represent seasonal quasi-steady states, in spite of the fact that salt marshes are clearly dynamic ecosystems.

The bioirrigation coefficients calculated from the sulfate concentration and reduction rate profiles are high in the uppermost 5 cm of the sediment column, both for June and August (Figure 8A). However, low values of  $Q$  in August near the sediment-water interface, indicate that the bioirrigation coefficients are not well constrained (Figure 8B). This is because the sulfate flushing concentration lies within the uncertainty interval of the measured sulfate concentrations near the sediment-water interface (Figure 8C). Thus, the irrigation coefficient is likely to be overpredicted in the uppermost 4 cm.

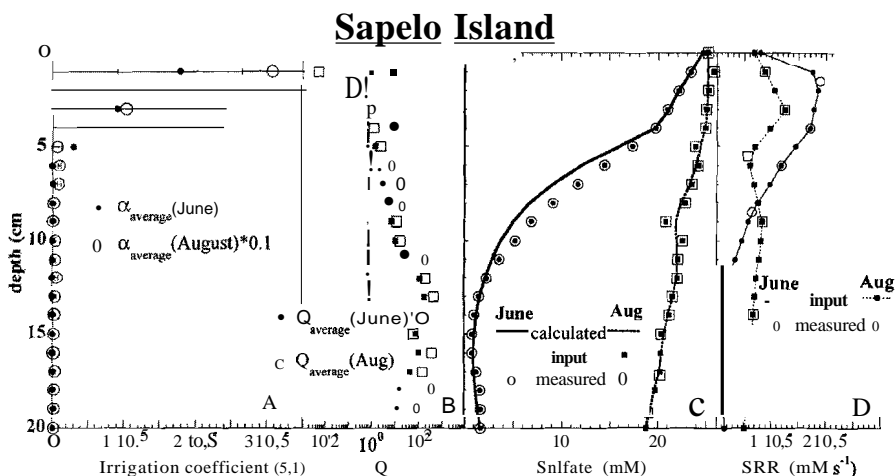


Figure 8. Bioirrigation at Sapelo Island in June 1998 and August 1997, based on sulfate profiles and sulfate reduction rates (Koretsky et al., in prep).

As for the Svalbard and Washington Shelf sites, the  $O_2$  irrigation flux across the sediment-water interface was calculated using the bioirrigation coefficient profiles. To calculate the  $O_2$  flux due to irrigation, the bulk sediment was assumed to have negligible  $O_2$  concentrations at all depths.  $O_2$  flushing concentrations of 211  $\mu\text{M}$  in June and 193  $\mu\text{M}$  in August were set by assuming saturation with respect to atmospheric  $O_2$  (at 25 and 30°C, Kostka et al., submitted). These assumptions, combined with the calculated bioirrigation coefficient yield estimated bioirrigation  $O_2$  fluxes of  $8.1 \pm 1.1$  and  $117 \pm 115$  mmol  $O_2$  m<sup>-2</sup> d<sup>-1</sup> in June and August, respectively.

Oxygen uptake by a salt marsh sediment at Sapelo Island was estimated by Teal and Kanwisher (1961) to be approximately 17 mmol m<sup>-2</sup> d<sup>-1</sup>, but their data do not allow the relative contribution of diffusion to the total flux to be calculated. The overall  $O_2$  benthic flux reported by Teal and Kanwisher (1961) and the calculated  $O_2$  irrigation flux for June from this study are at least qualitatively consistent, but the measured  $O_2$  benthic flux suggests that the irrigation flux calculated here for August is too high. The implication that the August irrigation coefficients are overestimated is perhaps not surprising, given the low values of  $Q$  and the large error bars associated with the extremely high irrigation coefficients calculated near the sediment-water interface.

Results of this study support previous findings that sulfate reduction rates cannot always be inferred directly from sulfate concentration gradients in heavily bioturbated sediments (e.g. Berner 1985; Fossing et al. 2000; Furukawa et al. 2000). In addition, the high irrigation intensities found for the Sapelo Island sediment imply that biologically induced transport efficiently counters sulfate depletion and thereby helps sustain high sulfate reduction rates. Thus, intense macrofaunal activity, by supporting high fluxes of sulfate and O<sub>2</sub>, helps explain low emissions of methane from highly productive salt marshes (Howarth and Giblin 1983).

## **Conclusions**

In many natural sediments, the quality and quantity of available data are such that many different bioirrigation coefficient profiles can fit measured data within the limits of uncertainty. Therefore, it may not be possible to uniquely determine the true irrigation coefficient profiles. Nonetheless, as shown here, it is possible to rank potential solutions according to objective criteria, and to judge the meaningfulness of results using algorithms such as the quality function developed in this study. The proposed quality function reflects both the sensitivity of concentration profiles to changes in the bioirrigation coefficient and the goodness of the fit between calculated and measured concentration profiles.

The inverse model was used in this study to calculate bioirrigation coefficient profiles in four different marine sedimentary environments. The model results indicate the existence of subsurface maxima in bioirrigation intensity at sites in Buzzards Bay and on the Washington Shelf. Previous studies failed to reveal these features at these sites. The model results highlight one of the primary advantages of using the inverse approach, namely, that it does not require an a priori, and therefore biased, definition of the depth-dependence of the irrigation coefficient.

Bioirrigation coefficient profiles obtained with the inverse model were used to estimate irrigation O<sub>2</sub> fluxes across the sediment-water interface. These estimates were compared to irrigation fluxes derived from the difference between measured benthic and calculated diffusive fluxes at sites with available data. In most cases, the O<sub>2</sub> fluxes estimated from the calculated irrigation coefficient profiles were of the same order of magnitude as measured fluxes. The worst agreement was found between measured and calculated irrigation fluxes for the August data from the Sapelo Island salt marsh site. However, the calculated irrigation coefficient profile was also characterized by very low values of the quality function. Thus, the poor reliability of the calculated irrigation coefficients would have been established even without comparison to an independent data set.

The inclusion of non-local solute transport in early diagenetic reactive transport models (e.g. Boudreau 1996; Wang and Van Cappellen 1996) creates the need for an objective parameterization of bioirrigation coefficients. The model presented provides a new tool for the unbiased interpretation of data collected in a variety of aquatic sediments. The model is available compiled for Macintosh PowerPCs by contacting the first author (meile@geo.uu.nl). It can be used not only to determine bioirrigation coefficient profiles, but also to determine reaction rate profiles (i.e., zones of consumption or production) for environments in which transport processes are known.



## References

- Aller, R. C. 1980. Quantifying solute distributions in the bioturbated zone of marine sediments by defining an average microenvironment. *Geochim. Cosmochim. Acta* 44: L955-1965.
- Aller, R. C., and J. Y. Aller. 1998. The effect of biogenic irrigation intensity and solute exchange on diagenetic reaction rates in marine sediments. *J. Mar. Res.* 56: 905-936.
- Aller, R. C., J. Y. Yingst, and W. J. Ullman. 1983. Comparative biogeochemistry of water in intertidal *Onuphis* (polychaeta) and *Upogebia* (crustacea) burrows: temporal patterns and causes. *J. Mar. Res.* 41: 571-604.
- Archer, D., and A. Devol. 1992. Benthic oxygen fluxes on the Washington shelf and slope: A comparison of in situ microelectrode and chamber flux measurements. *Limnol. Oceanogr.* 37: 614-629.
- Basan, P. B., and R. W. Frey. 1977. Actual-palaeontology and neoichnology of salt marshes near Sapelo Island, Georgia, p.41-70. In T. P. Crimes, and J. C. Harper [eds.], *Trace Fossils 2*. Steel House Press.
- Berg, P., N. Risgaard-Petersen, and S. Rysgaard. 1998. Interpretation of measured concentration profiles in sediment pore water. *Limnol. Oceanogr.* 43: 1500-1510.
- Berner, R. A. 1985. Sulphate reduction, organic matter decomposition and pyrite formation. *Phil. Trans. R. Soc. Lond.* A315: 25-38.
- Boudreau, B. P. 1984. On the equivalence of nonlocal and radial-diffusion models for porewater irrigation. *J. Mar. Res.* 42: 731-735.
- Boudreau, B. P. 1987. Mathematics of tracer mixing in sediments: III. The theory of nonlocal mixing within sediments. *Am. J. Sci.* 287: 693-719.
- Boudreau, B. P. 1996. A method-of-lines code for carbon and nutrient diagenesis in aquatic sediments. *Computers Geosci.* 22: 479-496.
- Boudreau, B. P. 1997. *Diagenetic models and their implementation*. Springer.
- Christensen, J. P., A. H. Devol, and W. M. Smethie. 1984. Biological enhancement of solute exchange between sediments and bottom water on the Washington continental shelf. *Continental Shelf Res.* 3: 9-23.
- Craig, N. I. and G. R. Lopez. 1996. Reactive and nonreactive particle dynamics in dense assemblages of the head down deposit feeder *Clymenella torquata*, p.30. In S. A. Woodin, D. M. Allen, S. E. Stancyk, J. Williams-Howze, R. J. Feller, D. S. Wethey, N. D. Pentcheff, G. T. Chandler, A. W. Decho, and B. C. Coull [eds.], *24th Annual Benthic Ecology Meeting*, Columbia, South Carolina, March 7-10, 1996.
- Emerson, S., R. Jahnke, and D. Heggie. 1984. Sediment-water exchange in shallow water estuarine sediments. *J. Mar. Res.* 42: 709-730.
- Fiadeiro, M. E., and G. Veronis. 1977. On weighted-mean schemes for the finite-difference approximation to the advection-diffusion equation. *Tellus* 29: 512-522.
- Fossing, H., T.G. Ferdelman, and P. Berg. 2000. Sulfate reduction and methane oxidation in continental margin sediments influenced by irrigation (South-East Atlantic off Namibia). *Geochim. Cosmochim. Acta* 64: 897-910.
- Furukawa, Y., S. Bentley, A. Shiller, D. Lavoie, and P. Van Cappellen. 2000. The role of biologically-enhanced pore water transport in early diagenesis: An example from carbonate sediments in the vicinity of North Key Harbor, Dry Tortugas National Park, Florida. *J. Mar. Res.* 58: 493-522.
- Glud, R. N., O. Holby, F. Hoffmann, and D. Canfield. 1998. Benthic mineralisation and exchange in Arctic sediments (Svalbard, Norway). *Mar. Ecol. Prog. Ser.* 173: 237-251.
- Gruebel, K. A., and C. S. Martens. 1984. Radon-222 tracing of sediment-water chemical transport in an estuarine sediment. *Limnol. Oceanogr.* 29: 587-597.
- Hammond, D. E., and C. Fuller. 1979. The use of Radon-222 to estimate benthic exchange and atmospheric exchanges in San Francisco Bay, p.213-230. In T. J. Conomos [ed.], *San Francisco Bay, The Urbanized Estuary*. Amer. Assoc. Adv. Sci.
- Hammond, D. E., C. Fuller, D. Harmon, B. Hartman, M. Korosec, L. G. Miller, R. Rea, S. Warren, W. Berelson, and S. Hager. 1985. Benthic fluxes in San Francisco Bay. *Hydrobiologia* 129: 69-90.
- Hammond, D. E., H. J. Simpson, and G. Mathieu. 1977. Radon-222 distribution and transport across the sediment-water interface in the Hudson River estuary. *J. Geophys. Res.* 82: 3913-3920.
- Howarth, R. W., and A. Gibling. 1983. Sulfate reduction in the salt marshes at Sapelo Island, Georgia. *Limnol. Oceanogr.* 28: 70-82.
- B. B. 1978. A comparison of methods for the quantification of bacterial sulfate reduction in coastal marine sediments. I. Measurement with radiotracer methods. *Geomicrobiology* 1: 11-27.
- Key, R. M., N. L. J. Guinasso, and D. R. Schink. 1979. Emanation of Radon-222 from marine sediments. *Mar. Chem.* 7: 221-250.

- Kleinbaum, D.G., L.L. Kupper, and K.E. Muller. 1988. Applied regression analysis and other multivariate methods, 2nd ed. PWS-KENT.
- Kostka, J. E., B. Thamdrup, R. N. Glud, and D. E. Canfield. 1999. Rates and pathways of carbon oxidation in permanently cold arctic sediments. *Mar. Ecol. Prog. Ser.* 180: 7-21.
- Lowe, K.L., T.J. DiChristina, A. Roychoudhury, and P. Van Cappellen. 2000. Microbiological and geochemical characterization of microbial Fe(III) reduction in salt marsh sediments. *Geomicrobiol. J.* 17: 163-178.
- Marinelli, R. L. and Boudreau, B. P. 1996. An experimental and modeling study of pH and related solutes in an irrigated anoxic coastal sediment. *J. Mar. Res.* 54: 939-966.
- Martin, W. R., and G. T. Banta. 1992. The measurement of sediment irrigation rates: A comparison of the Br<sup>-</sup> tracer and <sup>222</sup>Rn/<sup>226</sup>Ra disequilibrium techniques. *J. Mar. Res.* 50: 125-154.
- Martin, W. R., and F. L. Sayles. 1987. Seasonal cycles of particle and solute transport processes in nearshore sediments: <sup>222</sup>Rn/<sup>226</sup>Ra and <sup>234</sup>Th/<sup>238</sup>U disequilibrium at a site in Buzzards Bay, MA. *Geochim. Cosmochim. Acta* 51: 927-943.
- Mayer, M. S., L. Schaffner, and W. M. Kemp. 1995. Nitrification potentials of benthic macrofaunal tubes and burrow walls: effects of sediment NH<sub>4</sub><sup>+</sup> and animal irrigation behavior. *Mar. Ecol. Prog. Ser.* 121: 157-169.
- Meile, C. 1999. An inverse model for reactive transport in biogeochemical systems: Application to biologically-enhanced pore water transport (irrigation) in aquatic sediments. MSc thesis, Georgia Institute of Technology.
- Press, W. H., B. P. Flannery, S. A. Teukolsky, and W. T. Vetterling. 1989. Numerical Recipes (Fortran Version). Cambridge University Press.
- Rowe, G. T., C. H. Clifford, K. L. J. Smith, and P. L. Hamilton. 1975. Benthic nutrient regeneration and its coupling to primary production in coastal waters. *Nature* 255: 215-217.
- Schlüter, M., E. Sauter, H.-P. Hansen, and E. Suess. 2000. Seasonal variations of bioirrigation in coastal sediments: Modelling of field data. *Geochim. Cosmochim. Acta* 64: 821-834.
- Smethie, W. M. J., C. A. Nittrouer, and R. F. L. Self. 1981. The use of Radon-222 as a tracer of sediment irrigation and mixing on the Washington continental shelf. *Mar. Geol.* 42: 173-200.
- Teal, J. M. 1958. Distribution of fiddler crabs in Georgia salt marshes. *Ecology* 39: 185-193.
- Teal, J. M., and J. Kanwisher 1961. Gas exchange in a Georgia salt marsh. *Limnol. Oceanogr.* 6: 388-399.
- Tromp, T. K., P. Van Cappellen, and R. M. Key. 1995. A global model for the early diagenesis of organic carbon and organic phosphorus in marine sediments. *Geochim. Cosmochim. Acta* 59: 1259-1284.
- Ullman, W. I., and R. C. Aller. 1982. Diffusion coefficients in nearshore marine sediments. *limnol. Oceanogr.* 27: 552-556.
- Wang, Y., and P. Van Cappellen. 1996. A multicomponent reactive transport model of early diagenesis: Application to redox cycling in coastal marine sediments. *Geochim. Cosmochim. Acta* 60: 2993-3014.

## CHAPTER 4: bioirrigation using ecological parameters: A stochastic approach

### Abstract

Irrigation by benthic macrofauna has a major influence on the biogeochemistry and microbial community structure of sediments. Existing quantitative models of bioirrigation rely primarily on chemical, rather than ecological, information and the depth-dependence of bioirrigation intensity is either imposed or constrained through a data fitting procedure. In this study, stochastic simulations of 3D burrow networks are used to calculate mean densities, volumes and wall surface areas of burrows, as well as their variabilities, as a function of sediment depth. Burrow networks of the following model organisms are considered: the polychaete worms *Nereis diversicolor* and *Schizocardium sp.*, the shrimp *Callinassa subterranea*, the echiuran worm *Maxmuelleria lankesteri*, the fiddler crabs *Uca minax*, *U. pugnax* and *U. pugilator*, and the mud crabs *Sesarma reticulatulll* and *Eurytiulll limosum*. Consortia of these model organisms are then used to predict burrow networks in a shallow water carbonate sediment at Dry Tortugas, FL, and in two intertidal saltmarsh sites at Sapelo Island, GA. Solute-specific nonlocal bioirrigation coefficients are calculated from the depth-dependent burrow surface areas and the radial diffusive length scale around the burrows. Bioirrigation coefficients for sulfate obtained from network simulations, with the diffusive length scales constrained by sulfate reduction rate profiles, agree with independent estimates of bioirrigation coefficients based on pore water chemistry. Bioirrigation coefficients for O<sub>2</sub> derived from the stochastic model, with the diffusion length scales constrained by O<sub>2</sub> microprofiles measured at the sediment-water interface, are larger than irrigation coefficients based on vertical pore water chemical profiles. This reflects, in part, the rapid attenuation with depth of the O<sub>2</sub> concentration within the burrows, which reduces the driving force for chemical transfer across the burrow walls. Correction for the depletion of O<sub>2</sub> in the burrows results in closer agreement between stochastically-derived and chemically-derived irrigation coefficient profiles.

### Introduction

Nearshore sediments support large populations of burrowing macroinfauna, such as polychaete worms, shrimps and crabs. These organisms build extensive burrow networks within the upper 10 to 100 cm of the sediment column, which are either passively or actively flushed with water from the overlying sediment-water interface (SWI). Differences in solute concentrations between water flushed through burrows and pore water in the surrounding bulk sediment provide the driving force for enhanced solute mass transfer, called bioirrigation<sup>1,3</sup>. Bioirrigation not only enhances solute fluxes<sup>4,5</sup>, but also influences the microbial community structure<sup>6,9</sup>, as well as sediment and pore water composition<sup>10-15</sup>. Mathematical one-dimensional (1D) models of bioirrigation have been developed that treat bioirrigation variously as a diffusive, advective or nonlocal process. Diffusive models of

<sup>3</sup> Koretsky, C.M., Meile, C. and Van Cappellen, P. (2002) *Geochemical Transactions* 3(3): 17-30. DOI: 10.1039/b1I0459d

Acknowledgements. We would especially like to thank Yoko Furukawa, Dawn Lavoie and Sam Bentley for discussions of the work presented here and for providing us with benthic mesocosm data. The comments of two anonymous reviewers are appreciated and helped to improve this manuscript. This research was supported by Office of Naval Research grants N00014-98-1-0203 and N00014-01-0599 and the Netherlands Organisation of Scientific Research (NWO-Pionier programme).

bioirrigation use increased diffusion coefficients to account for enhanced solute transport due to macrofaunal activity within a defined mixing zone<sup>16,20</sup>. A diffusive representation implies that biological solute mixing is rapid and occurs on a spatial scale much smaller than the characteristic length scale of chemical pore water gradients<sup>21</sup>. Less common are advective models of bioirrigation, in which an enhanced advection velocity accounts for increased vertical pore water transport<sup>11,22,23</sup>. Boudreau<sup>24</sup> and Boudreau and Imboden<sup>25</sup> have argued that a more appropriate description of bioirrigation is based on a nonlocal transport description. The most common approach employs a mass transfer coefficient or bioirrigation coefficient,  $\alpha$ , to describe the rate of exchange between overlying water and pore waters at depth<sup>12,26,27</sup>. None of the ID bioirrigation models, however, include an explicit representation of the burrow networks constructed by the resident macrofaunal populations.

An important step in bridging the gap between chemical transport modeling of bioirrigation and benthic ecology was the development of the 3-dimensional (3D) radial diffusion model by Aller<sup>1</sup>. In this approach, burrows are represented as continuously flushed, evenly spaced cylindrical burrows of constant diameter and depth. Solutes are transported diffusively across the burrow walls in response to concentration gradients between bulk pore waters and waters flushed into burrows from the overlying SWI. Boudreau and Marinelli extended the 3D burrow model to describe discontinuous flushing of burrows, as well as variations in animal population (distance between burrows) and organism sizes (burrow radii)<sup>5</sup>. Boudreau further showed that the ID nonlocal description of inigation is equivalent to the 3D model of continuously flushed vertical cylinders; the ID nonlocal equation is simply the radially integrated form of the 3D model<sup>28</sup>. The equivalence between the 3D burrow model and the ID nonlocal model implies that the magnitude of bioirrigation at a given depth depends critically on the burrow wall surface area at that depth.

In all of the above models (diffusive, advective, nonlocal and cylindrical burrow) assumptions are made regarding the depth dependence of the intensity of bioirrigation. Bioirrigation intensity is either assumed to be constant over a discrete interval, or a functional depth-dependence is assigned to enhanced diffusion coefficients or nonlocal exchange coefficients<sup>12,13,29,30</sup>. Values of irrigation coefficients are generally derived by fitting chemical profiles, rather than by relying on ecological information. However, in principle, the latter could be used to determine the depth dependence of bioirrigation intensity directly. In addition, the models discussed so far are strictly deterministic and provide no information concerning the spatial or temporal variability of irrigation.

In this study, a stochastic model of bioirrigation based on benthic ecological data is presented. Information on burrow sizes and shapes for a variety of representative macrofaunal organisms is used to calculate stochastic realizations of 3D burrow networks. By generating a large number of burrow networks it then becomes possible to determine both average burrow surface areas and their variability as a function of depth. Benthic ecologists have characterized the structures of burrows using methods such as resin casting and X-radiography; these detailed measurements can be used to calculate the depth-dependence of burrow surface areas without implementing a stochastic approach. However, the stochastic model presented here is advantageous because it can also be used to provide estimates of surface area variability. Surface areas from the stochastic model provide an independent method for constraining the depth dependence of irrigation coefficients used in ID nonlocal models of bioirrigation. The stochastic model also provides a method to assess the uncertainty associated with irrigation coefficients in sediments.

## Model

### The Stochastic Burrow Network

In the stochastic model, the sediment is represented as a 3D grid over which burrows are distributed. Burrows are modeled using ten endmember shapes commonly observed in macrofaunal burrow networks (Figure 1). The following input parameters, with corresponding standard deviations and probability distributions where appropriate, are user-specified: (1) total burrow density (burrows per  $m^2$ ), (2) probability of occurrence for each of the 10 possible burrow shapes, and (3) radius and lengths of segments associated with each burrow shape. For example, V-shaped burrows require specifications for vertical and horizontal segment lengths; Y-shaped burrows require specifications for lengths of inclined upper branches and for the horizontal stem.

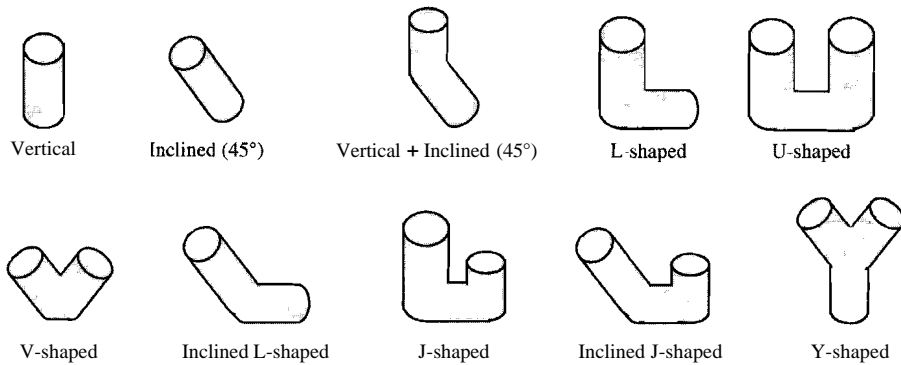


Figure 1. Endmember shapes used in stochastic burrow network simulation.

With the specified input parameters, burrows are distributed over the grid as follows. For each realization of the network a total burrow density is chosen randomly from the user-specified probability distribution of the total burrow density. The total burrow density is partitioned among the different burrow shapes based on the user-specified probabilities of occurrence of the ten possible burrow shapes. For each burrow, the lengths of the burrow segments and the radius of the burrow are selected similarly using the corresponding probability distributions. For nonvertical burrow orientations, the direction of the horizontal or inclined burrow section is selected randomly as north, south, east or west, with equal probability for each direction.

After all of the burrow parameters have been calculated, the burrow is placed into the 3D network of grid blocks. Each block either contains bulk sediment or is part of a burrow. The location of the burrow is determined by generating random coordinates for the burrow exit at the top surface of the grid (i.e., at the SWI). For each burrow type, the user specifies whether the burrow is allowed to intersect with other burrows. [If the calculated exit coordinates cause the burrow to intersect with another burrow, and no intersection is allowed, the exit coordinates are recalculated until the burrow can be located in the grid, or until a large number of attempts (specified by the user) is exceeded, ending the simulation. To eliminate edge effects, burrows that exit the grid sides are continued at the opposite edge (i.e., a periodic boundary condition is imposed). For all stochastically generated parameters, either a Rayleigh or Gaussian probability distribution function may be selected, or the parameter may be specified deterministically for use in all simulations.

For each stochastic realization of the burrow network (Fig. 2), the burrow volume, density and burrow wall surface area are calculated within each depth interval of the 3D grid. To calculate surface areas, all burrows are treated as cylindrical tubes. The surface area ( $S_h$ ) per unit sediment depth of vertical or horizontal burrows is therefore equal to

$$s_{\substack{v \\ h}} = \begin{cases} \beta < 45^\circ : \frac{2\pi r_l}{\cos \beta} \\ \beta \geq 45^\circ : \frac{2\pi r_l}{\sin \beta} \end{cases} \quad (1)$$

where  $r_l$  is the burrow radius,  $\beta$  is the angle of the burrow with respect to the vertical, and the subscript  $h$  indicates that the surface area within the depth interval is normalized to the uniform grid spacing,  $h$ . The total burrow surface area per unit sediment depth,  $S_h$ , at any given depth is then obtained by:

$$S_h = \sum s_h \quad (2)$$

where summation is carried out over all the burrows in the given depth interval. For simplicity, in the case of intersecting burrows, the surface area at the grid point of intersection is that calculated for the last burrow placed in the grid block. Because burrows are placed into the grid randomly and many networks are simulated, this results in an averaging of intersecting large and small surface area burrows. The mean values and standard deviations of the burrow density and burrow surface area are calculated as a function of depth by performing a large number of successive burrow network simulations (default 10,000 simulations).

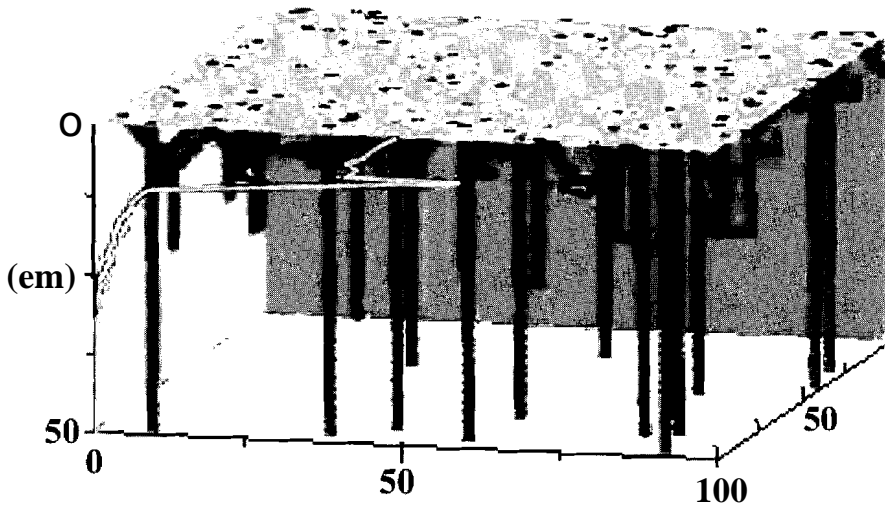


Figure 2. Sample 3D stochastic network simulation of burrows and corresponding burrow surface area per volume (line in front plane) as a function of depth.

## Burrow Networks and Nonlocal Exchange Coefficients

### *Derivation of nonlocal exchange coefficients from burrow surface areas*

Bioirrigation occurs because burrows provide conduits for solute mass transport that is rapid relative to diffusion through the bulk sediment. The burrow network therefore significantly influences biogeochemical cycling in the sediment. This is especially true in nearshore environments, where biologically mediated transport is often the dominant solute transport mechanism in surface sediments<sup>31</sup>. Studies that attempt to link observed pore water profiles with the underlying process dynamics thus require a mathematical description of solute exchange due to bioirrigation. One such model is the nonlocal exchange coefficient description of bioirrigation<sup>26</sup>, where the rate at which a solute is added or removed by bioirrigation (Inl) at a given depth in the sediment is given by

$$I_{nl}(x) = \alpha_i \phi (C_0 - C_{avg}) \quad (3)$$

where  $\phi$  is the sediment porosity, and the bioirrigation coefficient,  $\alpha_i$ , in units of inverse time, denotes the nonlocal exchange coefficient describing mass transfer of a given solute,  $i$ , between the overlying water and the bulk sediment;  $C_0$  and  $C_{avg}$  are the solute concentrations in the overlying water and in the bulk sediment, respectively.

Boudreau has demonstrated that the nonlocal exchange coefficient description of bioirrigation is equivalent to the continuously flushed radial tube model of bioirrigation developed by Aller<sup>28</sup>. He proposes the following equation:

$$J_{nl} = - \frac{2 D_i \phi}{r_2^2 - r_1^2} \bar{r}_i \left. \frac{\partial C}{\partial r} \right|_{r_1} \quad (4)$$

where  $D_i$  is the molecular diffusion coefficient of the  $i$ -th species corrected for tortuosity,  $r_1$  the radius of the vertical, cylindrical burrows,  $r_2$  the half-distance between burrows, and  $(\partial C / \partial r)$  the concentration gradient of solute  $i$  extending from the burrow wall into the bulk sediment. In the idealized radial tube model, the term  $\bar{r}_i$  corresponds to the burrow surface area per volume of sediment surrounding an individual burrow ( $s_v$ ). The main difficulty in applying Eqn. (4) resides in estimating  $(\partial C / \partial r)$ . If we approximate the concentration gradient by a truncated Taylor series expansion, then

$$\left. \frac{\partial C}{\partial r} \right|_{r_1} = \frac{C_{avg} - C_b}{\bar{r}_i - r_1} \quad (5)$$

where  $\bar{r}_i$  is the (time averaged) distance from the burrow wall at which the solute concentration reaches the radially averaged concentration,  $C_{avg}$ , for the bulk sediment at a given depth and  $C_b$  is the (time averaged) concentration in the burrow.

If the total burrow volume is relatively small (i.e.  $r_1 \ll r_2$ ), the volume of bulk sediment surrounding an individual burrow at a given depth is approximately equal to the total sediment volume divided by the number of burrows at that depth. Therefore,  $s_v \approx S_v$ , where  $S_v$  is the burrow surface area summed over all burrows divided by the total volume of sediment modeled within a given depth interval. At the sites assessed in this study (Dry Tortugas, FL and Sapelo Island, GA), the contribution of burrows to total sediment porosity is small ( $\ll 5\%$ ), justifying this simplification. If we assume that the solute concentrations within burrows are similar to the concentrations in the overlying water ( $C_b \approx C_0$ ) then, using Eqns. (3-5), it follows that

$$\alpha_{i,0} = \frac{2D_i r_i}{(r_i^2 - r_i^2) \cdot (C_0 - C_{avg})} \left. \frac{\partial C}{\partial r} \right|_r \quad (6)$$

$$\frac{DiSv}{(C_0 - C_{avg})} \left. \frac{\partial C}{\partial r} \right|_r \approx D \frac{Sv}{r_i - r_i}$$

Equation (6) is derived for the idealized model of evenly spaced, identical vertical burrows. In this study, we assume that, within each horizontal slice of the 3D sediment grid, Eqn. (6) provides a good approximation for the relationship between the bioirrigation intensity and the size and density of burrows. The stochastic burrow network can then be used to calculate mean values of burrow surface areas and radii, which can be implemented in Eqn. (6). While the assumption underlying the equivalence between ID nonlocal irrigation coefficients and idealized 3D cylindrical burrows is not strictly met for complex burrow geometries, the approach provides a means to estimate the depth-dependence of  $\alpha$ , which is otherwise poorly constrained.

The equivalent burrow radius  $r_l(x)$  is calculated from the total burrow surface area per unit sediment depth according to

$$r_l(x) = \frac{Sh(X)}{2\pi \cdot ntot(x)}, \quad (7)$$

where  $ntot(x)$  is the total number of burrows encountered in the depth interval over which  $Sh$  is determined. Both  $ntot$  and  $Sh$  are calculated from the stochastic realizations of the 3D burrow network. Equation (7) accounts for the fact that inclination of the burrows with respect to the vertical increases the surface area available for exchange between burrows and bulk sediment<sup>31,32</sup>. The average half-distance between burrows may be required for estimation of  $\bar{r}_i$  (see below). It is obtained by analogy with an ideal closest packing arrangement of vertical burrows, i.e. burrows (and the cylindrical packet of sediment surrounding each burrow) are assumed to be distributed evenly over the grid. The average half-distance between burrows at a given depth  $x$ , is then given by

$$r_2(x) = \frac{1}{2\sqrt{3}} \cdot \frac{A_0}{ntot(x)} \quad (8)$$

where  $ntot(x)$  is the mean total number of burrows encountered in the sediment slab, and  $A_0$  is the horizontal surface area of the 3D grid.

### Diffusion length scales

From Eqn. (6) it is evident that the irrigation coefficient may depend on the chemical species, not only through the species-specific diffusion coefficient, but also through a characteristic radial diffusion length scale,  $L_r = \bar{r}_i - r_i$ . In theory, the latter can be obtained by direct measurements of chemical microprofiles across at the burrow-sediment interface (BSI). Such data, however, are rarely available. Alternatively, vertical microprofiles recorded at the sediment-water interface (SWI) may be used as analogs for the gradients at the BSI, or the radial diffusion length scales may be estimated from simplified reaction-transport models.

If vertical diffusion at the SWI is considered analogous to radial diffusion at the BSI, the measured vertical length scale of the concentration change at the SWI ( $L_v'$ ) must be corrected to convert from the planar geometry of the SWI to the radial geometry of the BSI. If we assume that the net rate of consumption (production) of the solute of interest is similar in the vicinity of the SWI and the BSI, then we can equate the planar and cylindrical volumes in which the solute is consumed (produced). Specifically, at the SWI, the ratio of a volume of a unit area of surface extending to depth  $L_v'$ , divided by the surface area of the sediment is



$L_i'$ . This must be equal to the ratio of sediment volume associated with an individual burrow to the surface area,

$$L_i = \frac{\int_0^{r_i} 2\pi r dr}{2\pi r_1} \quad (9)$$

which yields,

$$\bar{r}_i = \sqrt{r_1^2(x) + 2r_1(x)L_i} \quad (10)$$

The radial diffusion length scale  $\bar{r}_i$  predicted by Eqn. (10) is strictly speaking only valid near the SWI, where  $L_i'$  reflects the local production or consumption of the solute. As the production (consumption) rate changes with depth, so will the value of  $\bar{r}_i$ .

When measurements of rates of consumption or production of the solute in the bulk sediment are known, it is possible to estimate values of  $L_i$  by assuming that in close proximity of burrows solute transport is dominated by irrigation (i.e., vertical diffusion can be ignored). From the vertical profiles of solute concentration and net rate of production/consumption  $\alpha$  can be determined by balancing the flux across the burrow walls with the reaction taking place in the surrounding sediment,

$$-D_i \phi \frac{\partial C}{\partial r} \Big|_{r_n} \cdot 2\pi r_1 = \int_0^{r_i} \phi R_i \cdot 2\pi r dr \quad (11)$$

Using the approximation of Eqn. (5), and assuming  $C_0$ , the corresponding length scale at the BSI for  $r_2 \gg r_1$  is then

$$L_i = 2D_i \frac{r_1}{r_2} \left( \frac{C_0 - C_{avg}}{r_2^2 R_i} \right) \quad (12)$$

where  $R_i$  is the net rate of production/consumption in the bulk sediment expressed per unit pore water volume.

Estimates of length scales and bioirrigation coefficients can also be obtained if the reaction kinetics are known and the governing mass balance equation is solved at steady state, with the average concentration defined as

$$C_{avg} = \frac{\int_0^{r_2} rC(r)dr + \int_0^{r_1} rCodrJ}{\int_0^{r_2} rCodrJ} \quad (13)$$

Subsequently,  $\bar{r}_i$  can be determined using the condition  $C(\bar{r}_i) = C_{avg}$ . For example, for zeroth order kinetics,

$$0 = \frac{D_i}{r} \frac{\partial}{\partial r} \left( r \frac{\partial C}{\partial r} \right) - R_i \quad (14)$$

With the boundary conditions  $C(r) = C_0$  and  $(\partial C / \partial r) = 0$  at  $r = 0$ , the radial concentration profile is given by

$$C(r) = C_b + \frac{R_i}{4D_i} (r_1^2 - r^2) + \frac{R_i r_2^2}{2D_i} \ln \left( \frac{r}{r_1} \right) \quad (15)$$

Solving for  $\bar{r}_i$  leads to

$$\bar{r} = \exp \left( \frac{-i(x) - \beta}{2} + \frac{\gamma}{4} \right) + \frac{r_1^2}{2r_2^2} - \frac{r_1^4}{4r_2^4} \quad (16a)$$

$$x = -r_2^2 \exp(y),$$

$$y = (-r_2^4 (10.5r; - 2r_2^4 \ln(r_2) - r_1^4 r_1^2 + a.5r_1^4))$$

where  $f(x)$  fulfills  $f(x) \cdot \exp(X) = x$ . For  $|x| < 0.3$ ,  $f(x)$ , the Lambert W function, can be expressed with a relative error  $< 1\%$  in a series expansion,

$$f(x) \approx x - x^2 + \frac{3x^3}{2} - \frac{8x^4}{3} + \frac{125x^5}{24} - \frac{154x^6}{5} + \frac{16807x^7}{720} - \frac{16384x^8}{315} + \frac{1531441x^9}{4480} \quad (16b)$$

From Eqn. (16) it is apparent that for zeroth order kinetics,  $\bar{r}_i$  depends only on the burrow size and spacing, not on the reaction rate or diffusion coefficient. Thus, the expected species specificity of  $\alpha$  only results from the species dependence of the effective diffusion coefficient. For other reaction kinetics!, numerical methods are required to determine  $\bar{r}_i$ .

### Burrow flushing efficiency

Nonlocal transport models of irrigation generally assume perfectly efficient flushing of burrows, that is  $C_b = C_o$  (Eqns. 3, 6). If perfect flushing does not occur, then depletion (or accumulation) of the solute within the burrow will cause the nonlocal irrigation coefficient,  $\alpha_{i,b}(x)$  to deviate from the apparent irrigation coefficient,  $\alpha_{i,0}(x)$  defined by Eqn. (3). The relationship between the true irrigation coefficient ( $\alpha_{i,b}$ ) and the apparent coefficient is

$$a_{i,b} \approx \frac{D_i S_v}{(C_o - C_{avg})} \left. \frac{\partial C}{\partial r} \right|_{r_i} \approx D_i \frac{S_v}{(C_o - C_{avg})} \frac{(C_b - C_{avg})}{(r_i - r_1)} = \alpha_{i,0} \frac{(C_b - C_{avg})}{(C_o - C_{avg})} \quad (17)$$

For highly reactive species, or small burrows, this effect may significantly affect bioirrigation coefficient profiles. From Eqn. (17), it can be seen that the bioirrigation intensity is species-specific, because  $C_b$  and  $C$ , and therefore the ratio of  $(C_b - C)/(C_o - C)$ , depend on the reactivity and diffusion coefficient of the individual solute species.

To assess the significance of concentration changes in burrows, the steady state concentration profile within a burrow can be estimated. Balancing the net delivery of the solute to a given depth, by flushing of a vertical burrow with radial exchange across the burrow wall gives

$$Q \frac{\partial C_b}{\partial x} = 2\pi r_i \cdot D_i \phi \left. \frac{\partial C}{\partial r} \right|_{r_i} \quad (18)$$

where  $Q$  is the volumetric flux of water flushing through the burrow.  $Q$  is obtained either by direct measurement or is estimated iteratively using the depth-integrated irrigation coefficient profile. Advective water velocity in the burrow is related to the mass flux of water by  $u = Q/(\pi r_i)$ . If the average concentration of the solute in the bulk sediment remains approximately constant (e.g., in the case of  $O_2$  which is rapidly depleted near the SWI, so that  $C_{avg} \approx 0$  over most of the depth range of interest), then the radial derivative in Eqn. (18) can be expressed according to Eqn. (5), or

$$\frac{\partial C_b}{\partial x} = - \frac{2D_i \phi}{r_i u L_i} (C_b - C_{avg}) \quad (19)$$

Solving Eqn. (17) for the boundary condition  $C_b(0) = C_o$  gives

$$C_b(x) = (C_o - C_{avg}) e^{-\frac{2D_i \phi x}{r_i u L_i}} + C_{avg} \quad (20)$$

which shows, as expected, that deviation from perfectly flushed burrows is favored by narrow burrows (small  $r_i$ ), slow water exchange (small  $u$ ) and high solute reactivity (small  $L_i$ ).

The flushing efficiency is related to the residence time of water in the burrows,  $\tau_{res} = (V_b/Q)$  where  $V_b$  is the burrow volume. If we assume, for simplicity, that  $\alpha$  is constant with depth then

$$\tau_{res} = \frac{nOV_b}{A \int_0^r \alpha dx} \approx \frac{f_j^2}{f^2 \alpha} \quad (21)$$

Therefore, it is possible to obtain estimates of irrigation coefficients based on flushing frequencies ( $\tau_{res}^{-1}$ ), burrow thickness ( $r$ ) and abundance ( $f$ ). Although the specific form of Eqn. (21) is only valid in the limited case of  $\alpha$  constant with depth, nonetheless, this equation highlights the potential use of data on burrow flushing frequencies of benthic organisms to constrain bioirrigation intensities.

## Results and Discussion

### Model Organisms

The burrows of a variety of macrofauna, especially those inhabiting intertidal and shallow subtidal environments, have been characterized by resin casting<sup>34</sup>. Resin casts are obtained by pouring a dense epoxy directly into sediments or mesocosms; after hardening, casts are removed and cleaned. This technique is widely used to study burrow morphology and to obtain estimates of burrow surface areas and volumes. However, it can be difficult to obtain casts of deep-burrowing macrofauna<sup>35</sup> and to distinguish burrows of different types of macrofauna. For example, initial resin cast studies of the echiuran worm *Maxmuelleria lankesteri* suggested that burrows have a single entrance at the surface<sup>36,37</sup>. However, subsequent studies of sediment intake and ejection have demonstrated the presence of a second connection to the surface. The second entrance was likely not found in initial resin cast studies because the presence of the large echiuran worms within inhabited burrows blocked the flow of resin<sup>35</sup> and because second openings are often occluded by sediment<sup>38</sup>.

X-radiography of sediment slabs from box cores has also been used to estimate burrow shapes and burrow wall surface areas<sup>32,39,40</sup>. Burrows of organisms in deeper environments have been studied using underwater television and remote photography<sup>6,41-43</sup>, and through mesocosm experiments conducted with organisms collected from sediments<sup>44,45</sup>.

It should be noted that portions of the burrow structure of some organisms may not be irrigated. Therefore, relying solely on resin casting or X-radiography to determine burrow surface areas of exchange may lead to overestimates of irrigation intensity, particularly for deep burrows. This highlights the importance of obtaining detailed information concerning the burrowing and irrigating activities of individual organisms in constructing more representative, ecology-based bioirrigation models.

Table 1 Parameterization of burrows. Cumulative distribution junctions are Gaussian. Ve = vertical burrow parameter; VY = upper branches of Y-shaped burrow parameter; SY = stem of V-shaped burrow parameter; I = 45° inclined burrow parameter; V = V-shaped burrow parameter; Y = Y-shaped burrow parameter, L = L-shaped burrow parameter

Organism	Density distribution/m <sup>-2</sup>	Shape	Depth/rn (min/max)	Length/m (min/max)	J-shape Up-look length/m	Radius/m (min/max)	Refs
<i>Callianassa subterranea</i>	150.0 ± 15	U-shape	0.103 ± 0.037 (0.0810.23)	0.21 ± 0.076 (0.0110.60)	N/A	0.00425 ± 0.0005 (0.000110.10)	45,47
	North Sea	50% V-shape	0.103 ± 0.037 (UY)	0.21 ± 0.076	N/A	0.00425 ± 0.0005 (0.0001/0.10)	45,49
	150.0 ± 15	50% U-shape	0.50 ± 0.05 (SY)	0.0110.601			
	Scottish Loch & Davies Reef		0.103 ± 0.37 (I) (0.0810.90)	0.60 ± 0.02 (0.0110.90)	N/A	0.006 ± 0.0002 (0.000110.10)	46,47, 48
	3.0 ± 2	50% I-shape	0.45 ± 0.17 (Ve)				
	Scottish	50% vert + 45°	0.10 ± 0.05 (I) (0.08/0.80)				
<i>Maxmuelleria lankesteri</i>	2 ± 0.5	50% U-shape	0.42 ± 0.13	0.77 ± 2.4 (0.10/1.5)	N/A	0.015 ± 0.005 (0.00110.10)	36,37, 38
		Loch	12.5% V-shape 12.5% V-shape + 45° 12.5% inclined 12.5% inclined L-shape	0.166 ± 0.254 ± 0.045 (I) (0.30/1.0)			
			100% Y	0.08 ± 0.01 (UY) 0.08 ± 0.01 (SY) (0.0110.30)	N/A	N/A	0.001 ± 0.0003 (0.00001/0.01)
<i>Uca pugilator</i>	52 ± 10	25% L-shape 25% inclined L-shape 25% J-shape 25% inclined J-shape	0.15 ± 0.10 (0.10/0.30)	0.04 ± 0.01 (0.01/1.5)	0.02 ± 0.005	0.0175 ± 0.0025 (0.000110.10)	55,56, 60,61, 65
<i>Ucapugnax</i>	13 ± 4	25% L-shape 25% inclined L-shape 25% J-shape 25% inclined J-shape	0.20 ± 0.025 (0.10/0.40)	0.14 ± 0.01 (0.1/1.5)	0.02 ± 0.005	0.0075 ± 0.0025 (0.000110.10)	55,56, 57

### Decapoda: Thalassinidae: *Callianassa subterranea*

Thalassinid shrimp are extremely common, inhabiting intertidal, shallow subtidal and possibly deep-sea sedimentary environments<sup>46,47</sup>. Their burrows, which are used by the organisms for shelter, feeding and reproduction, are deep (sometimes exceeding 2m depth) and typically have quite complex morphologies. Burrow morphologies may vary for a single species, depending on the sedimentary environment. For example, *Callianassa subterranea* burrow morphologies are much more complex in sandy<sup>44,45</sup> than in muddy sediments<sup>46,48</sup>. Mesocosm studies of *C. subterranea* collected from sandy North Sea sediments suggest that these shrimp construct burrows with 5.9±1.6 openings<sup>45</sup> at the sediment-water interface connecting to a lattice of nearly horizontal chambers<sup>45</sup>. This complex morphology is approximated in this study by treating each burrow as a combination of three intersecting U-shaped burrows (Table 1). This results in a distinct subsurface maximum in burrow wall surface area at approximately 10cm depth (Fig. 3A).

However, *C. subterranea* burrows do not always resemble intersecting U-shapes. Nickell and Atkinson report several *C. subterranea* burrow casts from muddy Scottish Loch sediments with single, nearly vertical shafts extending downward from a lattice of horizontal tunnels<sup>48</sup>. Tudhope and Scoffin found even more complex *C. subterranea* burrow networks that had 5 or more downward-inclined chambers radiating from a central V-shaped burrow<sup>9</sup>. To account for the presence of the deep shafts found in these studies, *C. subterranea* burrows are modeled using a combination of 50% V-shaped and 50% Y-shaped burrows (Fig. 3B). The addition of Y-shaped burrows representing deeply penetrating shafts results in the persistence of significant burrow surface area to depths of greater than 80cm, compared to less than 25cm in simulations using only V-shaped burrows (Figs. 3A,B). However, the deeper portions of Y-shaped *Callianassa* burrows may be irrigated only

infrequently, so that without consideration of flushing frequency the model may lead to overestimates of the bioirrigation intensity at depth.

In muddy subtidal sediments from the west coast of Scotland, Atkinson and Nash found only one *C. subterranea* burrow, out of 17 casts, that had more than a single inhalent shaft opening to the surface<sup>46</sup>. However, Nickell and Atkinson found that most burrows from this environment had an additional, much smaller exhalent shaft that opened or partially opened at the sediment surface, perhaps facilitating flow of water through the burrows<sup>48</sup>. Reported organism densities in these sediments are much lower than estimates from North Sea sites, and burrow depths are considerably greater. To examine the potential differences in surface area resulting from the extremes of reported burrow morphologies, these Scottish Loch burrows are modeled here assuming only a single connection to the surface, by using 50% L-shaped and 50% vertical/45° inclined burrow shapes. This results in a distinct increase in burrow wall surface area at approximately 10cm, which is not dissimilar from the subsurface maxima resulting from simulations using V- and Y-shaped burrows (Fig. 3C). Thus, *C. subterranea* is likely to promote deep bioirrigation in all of these settings, with a subsurface maximum in burrow surface area at depths of 10cm or greater.

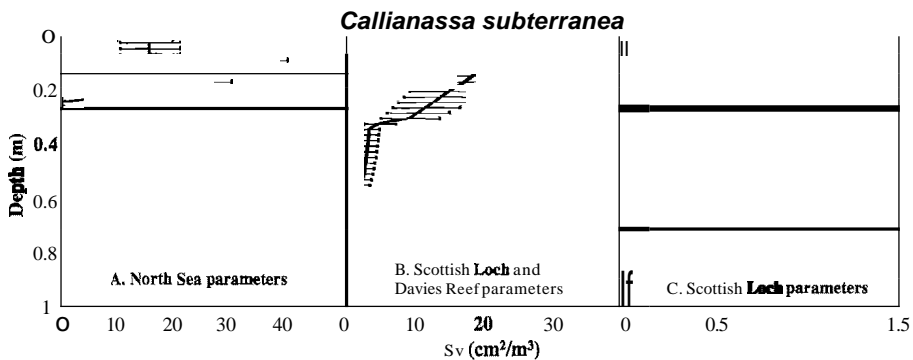


Figure 3. Burrow wall surface area per unit sediment volume,  $S_v$ , as a function of depth for burrow network simulations of the Thalassid shrimp *Callianassa subterranea* using (A) U-shaped burrows (North Sea site parameters), (B) U- and Y-shaped burrows (North Sea & Davies Reef site parameters) or (C) L-shaped and vertical+45° inclined shapes (Scottish Loch site parameters). See Table 1 for data used for all calculations.

#### *Echiura: Bonellidae: lankesteri*

The echiuran worm *Maxmuelleria lankesteri* has been recognized as an important bioturbator because, unlike many other burrowing macrofauna, it builds extremely deep, temporally persistent burrows. Single burrows have been observed to remain in place for at least 15 months and are suspected to persist in a single location for years<sup>37,38</sup>. Although *M. lankesteri* is found from the west coast of Scotland to the Skagerrak, its burrows have been studied particularly in Irish Sea sediments, where the organism is thought to promote deep, rapid mixing of radionuclide contaminants into the

There has been some controversy surrounding the morphology of *M. lankesteri* burrows<sup>35,38</sup>. In this study, simulations of *M. lankesteri* burrows were made using V-shaped burrows, single shaft (L-shaped, inclined L-shaped, 45° inclined, vertical/45° inclined), or mixtures of V-shaped and single shaft burrows. Surface areas as a function of depth are similar for all morphologies; results for mixtures of V-shaped and single shaft burrows are shown in Fig. 4. The simulated burrow surface area profile suggests that *M. lankesteri* promotes bioirrigation to depths of up to 1m. However, as seen in Fig. 4, a very high variability in irrigation intensity can be expected below 30cm.

*Nereididacea: Nereididae: Nereis diversicolor*

The polychaete worm *Nereis diversicolor* inhabits estuarine, intertidal sediments throughout Europe<sup>40,50,51,52</sup>. Very high population densities (2000-4000 individuals·m<sup>-2</sup>) are common, suggesting that in many estuaries these polychaetes contribute significant bioirrigation intensity. Burrow morphologies have been studied in laboratory mesocosms and field settings using resin casting and X-radiography<sup>40,53</sup>. Although burrows have frequently been described as having a simple V-shape, Davey has shown that in mesocosms *N. diversicolor* burrows initiate in a V-shape, but soon exhibit more complex morphologies<sup>40</sup>. After several hours, burrows are extended to form a Y-shape, and after several days have complex morphologies including multiple openings at the sediment-water interface. The morphology of *N. diversicolor* burrows in natural sediments may depend on animal population densities; U-shaped burrows of *N. virens* are constructed at low animal densities, but in dense populations burrows may be 1-, L- or Y-shaped<sup>54</sup>. Although Gerino and Stora describe *N. diversicolor* burrows in their study as V-shaped<sup>53</sup>, X-radiographs of these burrows shown in their Figure 1 suggest that they are Y-shaped. X-radiographs of burrows shown in Davey and Gerino and Stora are used to estimate the depths and horizontal extent of burrows (Table 1)<sup>40,53</sup>. The resulting surface area depth profile agrees closely with burrow wall surface areas measured by Gerino and Stora<sup>53</sup> using resin casts of 4 individual *N. diversicolor* burrows from a mesocosm study (Fig. 5).

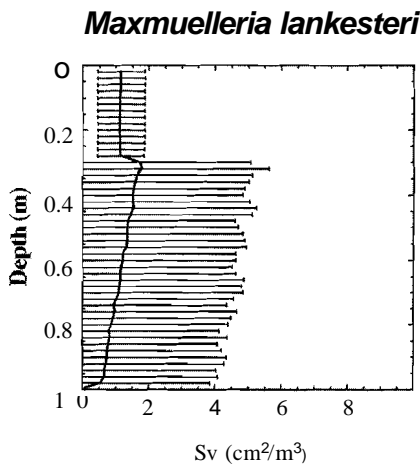


Figure 4.  $S_v$  as a function of depth for burrow network simulations of the Echiuran worm *Maxmuelleria lankesteri*. Parameters are given in Table 1.

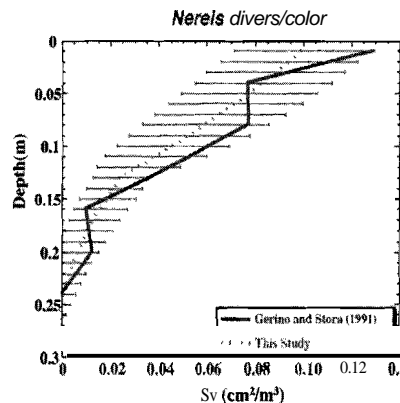


Figure 5. Comparison of  $S_v$  for four individual *Nereis diversicolor* from Gerino and Stora<sup>53</sup> (solid thick line) and from this study (dotted thin line). Error bars show one standard deviation calculated from stochastic network simulations.

*Decapoda: Ocypodidae: Uca minax, Uca pugnax, and Uca pugilator*

Fiddler crabs, including the sand fiddler (*Uca pugilator*), the mud fiddler (*Uca pugnax*) and the brackish water fiddler (*Uca minax*) are among the most numerous and conspicuous of burrowing macrofauna in intertidal mangrove and saltmarsh sediments<sup>55,56,57,58</sup>. Estimates of fiddler crab densities in a saltmarsh at Sapelo Island, GA are as high as 205±46m<sup>-2</sup> and bUwS have been reported to penetrate to depths of up to 65cm<sup>57,59</sup>. However, unlike other burrowing macrofauna, fiddler crabs do not permanently inhabit or actively irrigate their burrows. In fact, some fiddler crabs plug their burrow entrances to prevent flooding during tidal inundation<sup>55,60,61</sup>. Fiddler crab burrows are nonetheless likely to contribute to solute

transport, because of the abundance of abandoned burrows that are passively flushed by tidal inundation. However, most studies of fiddler crabs report only aperture or organism densities, making an assessment of flushed burrow density difficult.

Burrow network simulations suggest that *U. minax* burrows, because of their large size (Table 1), will contribute most to irrigation, especially at depths greater than 30cm (Fig. 6C). Simulated burrow wall surface area profiles for *U. pugilator* and *U. pugnax* both exhibit a subsurface maximum at approximately 10cm depth (Fig. 6A,B), with few burrows extending deeper than 20-25cm into the sediment.

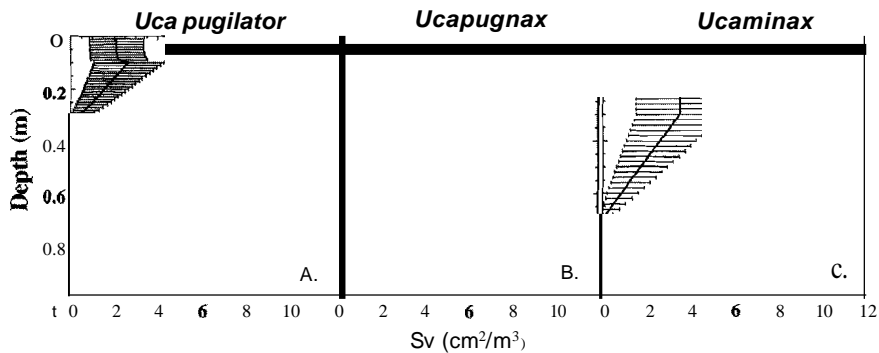


Figure 6.  $S_v$ s as a function of depth for fiddler crabs including (A) *Uca pugilator*, (B) *Uca pugnax*, and (C) *Uca minax*. Parameters are given in Table 1.

#### Decapoda: Grapsidae: *Sesarma reticulatum* and *Eurytium limosum*

The marsh crab *Sesarma reticulatum* occurs in a variety of intertidal marsh environments<sup>55, 57, 62</sup>. Reported population densities range from 30/m<sup>2</sup> in levee marshes with tall-form *Spartina alterniflora* to just 1/m<sup>2</sup> in unvegetated creek banks<sup>55</sup>. Burrows are extensive and, especially near the sediment surface, have complex morphologies. Typical burrows have several entrances attaching a shallowly sloping initial tunnel several cm long to the surface. This initial tunnel network is connected to a single vertical shaft of 2-5cm diameter that descends into the sediment to depths averaging 13-30cm, although depths of up to 75cm have been reported<sup>56, 62</sup>. *S. reticulatum* burrow networks were simulated in greatly simplified form as single vertical shafts (Table 1). This results in a burrow surface area profile that decays gradually with depth (Fig. 7A).

Another crab species found frequently in both vegetated and unvegetated intertidal saltmarshes is *Eurytium limosum*<sup>55, 57</sup>. *E. limosum* burrows are typically composed of two or more shallow tunnels that extend laterally for 60-70cm; a single inclined shaft joins the long, shallow tunnels and descends to 20-30cm depth to create a broadly Y-shaped burrow<sup>57</sup>. *E. limosum* burrows were simulated in this study by treating each burrow as a combination of two shallow, intersecting L-shaped and one deep 45°-inclined burrows. The presence of just a few *E. limosum* burrows greatly enhances burrow surface areas in the upper few centimeters of the sediment column (Fig. 7B).

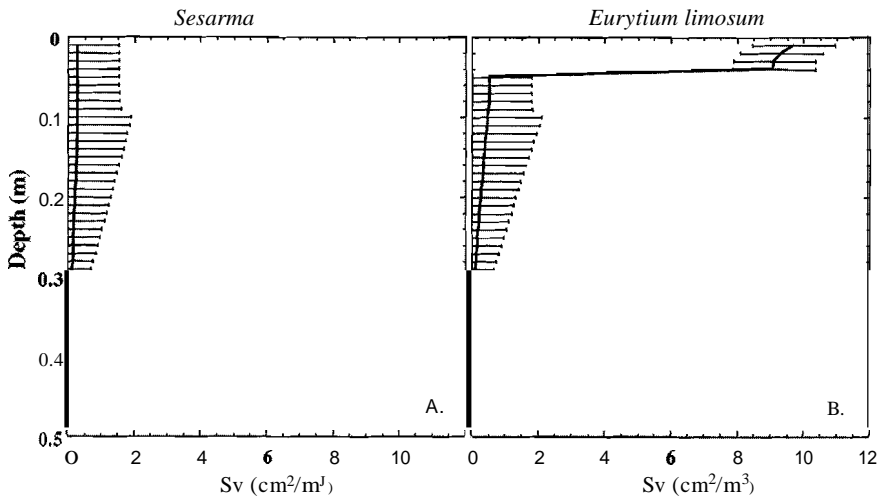


Figure 7.  $S_v$  as a function of depth for the mud crabs (A) *Sesarma reticulatum* and (B) *Eurytium limosum*. Parameters are given in Table 1.

*Enteropreusta: Spengelidae: Schizocardium sp.*

Laboratory mesocosms have been used to assess the role of the funnel-feeding acorn worm *Schizocardium sp.* in promoting bioirrigation of shallow, near-shore sediments in St. Louis Bay, Mississippi Sound<sup>32</sup>. X-radiographs of mesocosm sediment slabs suggest that *Schizocardium sp.* build approximately U- or V-shaped burrows penetrating to a maximum of 9cm depth. Burrow networks were simulated in this study assuming that all burrows are approximately V-shaped. The resulting surface area profiles decrease continuously with depth (Fig. 8A).

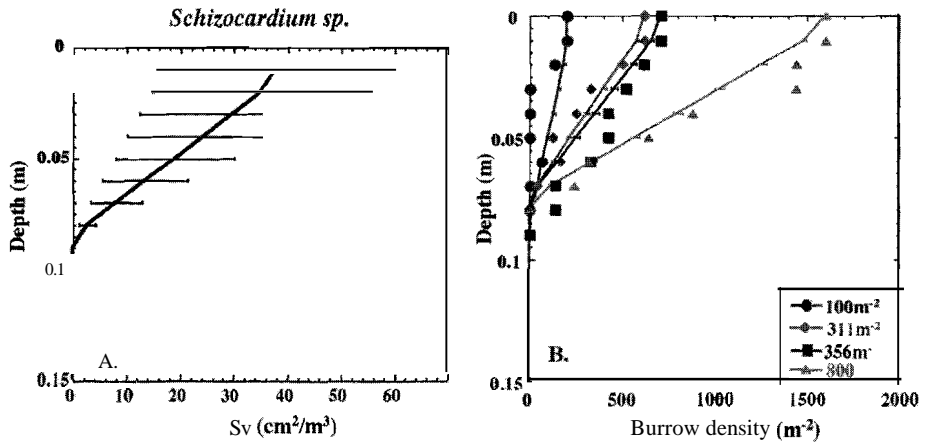


Figure 8. (A)  $S_v$  as a function of depth for the acorn worm *Schizocardium sp.* with mean animal density of  $50 \text{ am}^{-2}$ . (B) Burrow densities for populations of  $100 \text{ m}^{-2}$ ,  $311 \text{ m}^{-2}$ ,  $356 \text{ m}^{-2}$  and  $800 \text{ m}^{-2}$ . Lines are burrow densities from this study; symbols represent number of active burrows reported from X-radiography of mesocosm slabs<sup>32</sup>. Error bars represent  $\pm 1$  standard deviation in burrow density.



X-radiography of sediment slabs has been used to directly determine *Schizocardium* burrow densities as a function of depth in four mesocosms<sup>32</sup>. The expected depth-dependence of *Schizocardium* burrow density, given the animal densities in the various mesocosms (100, 311, 356, 800) is calculated with the stochastic model with parameters given in Table 1 (Fig. 8B). Because total animal densities are known and therefore are kept invariant in the stochastic model, standard deviations shown in Fig. 8B are relatively small. In all four cases, burrow density profiles calculated using the stochastic model are in very good agreement with reported densities from X-radiography of sediment slabs.

## Dry Tortugas, Florida, USA

### *Macrofaunal consortia*

The consortium of bioturbating macrofauna present in shallow-water carbonate reef sediments at Dry Tortugas, FL has been described by D'Andrea and Lopez<sup>63</sup>. Of the deeply (>4cm) bioturbating organisms, D'Andrea and Lopez suggest that the polychaete worm *Notomastus* sp. (density=113.2m<sup>-2</sup>) and the burrowing shrimp *Callianassa* sp. (density=40.8m<sup>-2</sup>) are dominant<sup>63</sup>. *Notomastus*, a deep deposit feeding capitellid polychaete, was commonly found at depths greater than 15cm, most often occurring at 25-30cm depth<sup>63</sup>.

To simulate burrow networks at Dry Tortugas, only the dominant deep bioturbators *Notomastus* and *Callianassa* are considered here. *Notomastus* burrows are assumed to be similar in morphology to those of the polychaete *Nereis diversicolor*, with penetration depths of 20±2.5cm for *Notomastus*. In fact, this is a great simplification; *Notomastus* burrows have been reported to resemble complex spirals (D'Andrea and Lopez, personal communication), thus, *Notomastus* burrows may contribute a greater surface area of exchange than is considered here. *Callianassa* sp. are assumed to build burrows with morphology similar to those reported for Great Barrier Reef Sediments<sup>49</sup> and are therefore modeled using the U- and Y-shaped *Callianassa* burrow parameters given in Table 1. The presence of these two organisms alone leads to a burrow surface area profile with three distinct regions; in the upper 6cm surface areas are high and essentially constant with depth, from 6-12cm they decrease rapidly and then more gradually in the depth interval 12 to 90cm (Fig.9A).

### *Bioirrigation coefficients*

From the surface area profiles shown in Fig. 9A, bioirrigation coefficients are calculated using Eqns. (6) and (10).  $D_i$  is calculated using porosity and molecular diffusion coefficient data given in Furukawa et al.<sup>15</sup> and  $r_l$  is calculated using Eqn. (7) with surface areas and burrow densities obtained from the stochastic network simulations. The  $O_2$  penetration depth at the SWI ( $L_{O_2}$ ) is set to 2.6mm, based on vertical microelectrode profiles measured by Furukawa et al.<sup>15</sup>, and is used to calculate  $\bar{r}_{O_2}$  according to Eqn. (10); values vary from 4.8 to 6.4mm. At the SWI, this results in predicted irrigation coefficients that are approximately twice as high as the values estimated by Furukawa et al. from diagenetic modeling of chemical data<sup>15</sup> (Fig. 9B), perhaps reflecting the use of  $L_{O_2}$  measured at the SWI, rather than at the BSI. The predicted irrigation coefficients also exhibit a less pronounced decrease with depth than the coefficients obtained by Furukawa et al.<sup>32</sup>. The higher irrigation coefficients estimated in this study may be due, at least in part, to imperfect burrow flushing. Eqns. (17) and (20) are used to assess this possibility. This correction leads to lower irrigation coefficients, with mean values within a factor of 2 of estimates from Furukawa et al.<sup>15</sup>. Nonetheless, the results suggest that  $O_2$  gradients measured at the SWI may not yield accurate estimates of radial diffusion length scales at the BSI at depths greater than a few mm.

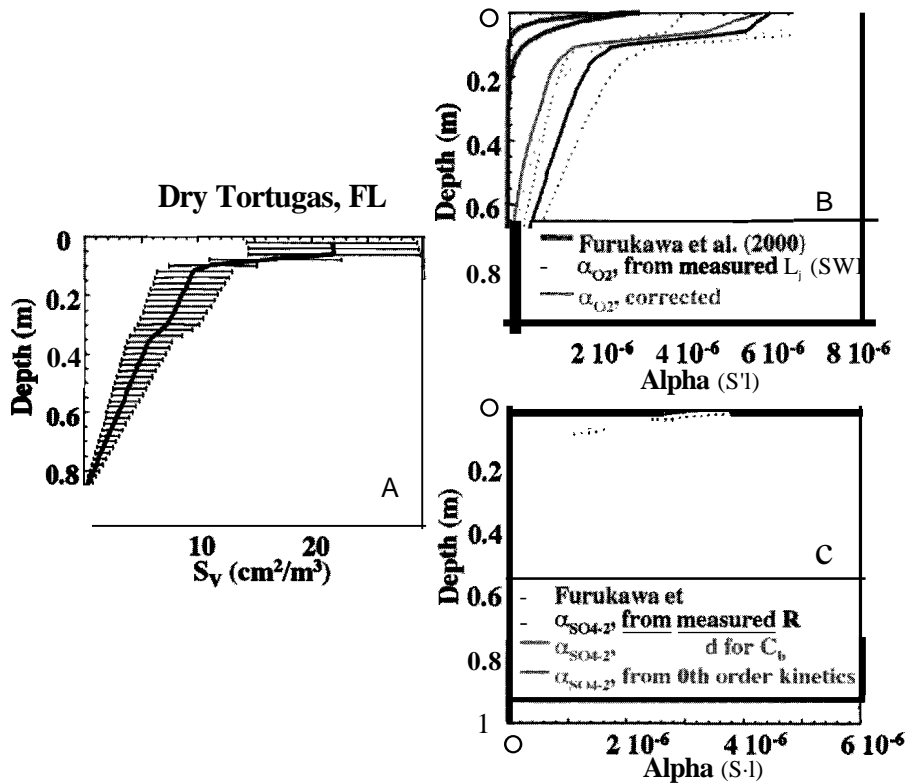


Figure 9. (A)  $S_v$  as a function of depth in shallow carbonate sediment at Dry Tortugas, FL, USA, from simulations using a consortium of the polychaete worm *Notomastus* sp. and the shrimp *Callinassa* sp. (B) Bioirrigation coefficients (S<sup>-1</sup>) as a function of depth for Dry Tortugas, FL derived by fitting an early diagenetic model to measured pore water profiles (Furukawa et al.<sup>32</sup>; the 2 curves exponentially decreasing with depth), and estimated from the burrow network in this model.  $\alpha_{O_2}$  was calculated using  $L = 2.6$  mm from Furukawa et al.<sup>15</sup>, with Eqn. (5), assuming  $C_b = C_0$ .  $\alpha_{O_2}$  was corrected for  $C_b$  using Eqns. (17) and (20). (C) Bioirrigation coefficients (s<sup>-1</sup>) as a function of depth from Furukawa et al.<sup>32</sup> (2 exponentially decreasing curves) and estimated from the burrow network in this model. The dark line with highest  $a$ -values at the SWI indicates  $a_{SO_4-2}$  calculated using sulfate concentration and reduction rate profiles from Furukawa et al.<sup>12</sup>; the light gray line almost coinciding with it indicates  $a_{SO_4-2}$  corrected for  $C_b$  using Eqns. (17) and (20). The solid line with low  $a$ -values at the SWI indicates bioirrigation coefficient profile calculated using Eqn. (16), assuming 0th order kinetics for sulfate reduction. Dotted lines indicate irrigation coefficient profiles calculated using  $\pm 1$  standard deviation of the stochastic model burrow densities and surface areas.

Bioirrigation coefficients are also calculated by combining the stochastic burrow network simulations with sulfate concentration and reduction rate profiles taken from Furukawa et al.<sup>15</sup>. The resulting irrigation coefficients predicted using Eqns. (6) and (12) are only slightly larger than those predicted by Furukawa et al.<sup>15</sup> and exhibit a similar depth-dependence (Fig. 9C). Because sulfate is a less reactive solute than O<sub>2</sub>, correction of this profile for inefficient flushing using Eqns. (17) and (20) has negligible effect (Fig. 9C). Both the corrected and uncorrected sulfate bioirrigation coefficient values are significantly smaller than those calculated for O<sub>2</sub>. This is primarily because of the much larger radial diffusion length scales

calculated for S04.2. Sulfate reactive length scales are also large relative to those obtained from O<sub>2</sub> microprofiles, because they are calculated from bulk sulfate reduction rates that decrease rapidly with depth, reflecting changing reactivity with depth.

Bioirrigation coefficient profiles are also calculated here completely independently from data in Furukawa et al.<sup>15</sup>, by assuming zero order kinetics for sulfate reduction and using Eqn. (16). In this case, the irrigation coefficients, which depend only on the burrow sizes and spacings, are approximately a factor of 3 lower than those calculated by Furukawa et al.<sup>15</sup> right at the SWI (Fig. 9C). Below a few mm, however, good agreement between the two independent approaches is observed.

## Sapelo Island, GA, USA: Unvegetated Creek Bank

### Macrofaunal consortia

Intertidal saltmarshes at Sapelo Island, GA are populated by diverse, abundant burrowing macrofauna<sup>55,57,59,64,66</sup>. Basan and Frey report 1040 burrow apertures·m<sup>2</sup> in an unvegetated creek bank at Sapelo Island<sup>57</sup>, and suggest that the majority of these apertures are due to polychaete worms including *Nereis succinea* and *Heteromastus filiformis*. Other burrows are attributed to fiddler crabs, especially *Uca pugilator*, burrowing shrimp including *Upogebia affinis* and predatory mud crabs such as *Panopeus herbsti*, which share the burrows of *Sesarma reticulatum*<sup>56</sup>. Teal also inventoried burrowing macrofauna at an unvegetated creek bank on Sapelo Island, GA and found *Uca pugilator* (52m<sup>2</sup>), *Uca pugnax* (13m<sup>2</sup>), *Sesarma reticulatum* (1m,2) and *Eurytium limosum* (6m,2)<sup>55</sup>.

A simulated burrow network for an unvegetated creek bank at Sapelo Island, GA was completed using *U. pugilator*, *U. pugnax* and *E. limosum* densities taken directly from Teal<sup>55</sup>, while for *S. reticulatum* and *P. herbsti* averages of data given for *S. reticulatum* by Teal and for *P. herbsti* by Basan and Frey are used<sup>55,57</sup>. *Upogebia affinis* shrimp burrows are assumed to be similar in morphology to *Callinassa* shrimp. A polychaete density of 450±50m<sup>2</sup> is derived by assuming a total aperture density of ~1000m<sup>2</sup> of which are due to organisms other than polychaetes.

Burrow wall surface areas for polychaetes, shrimp and fiddler crabs only are highest near the sediment-water interface and decay gradually to a depth of approximately 30cm (Fig. 10A). The addition of *E. limosum*/*P. herbsti* burrows results in much higher burrow wall surface areas in the upper few cm of sediment and a more rapid decay of the burrow surface areas with depth (Fig. 10B).

### Bioirrigation coefficients

As for the Dry Tortugas site, the stochastic model-derived surface areas shown in Fig. 10B are used with Eqns. (6) and (10) to derive a bioirrigation coefficient profile. A porosity of 76%<sup>67</sup> is used to obtain D<sub>O<sub>2</sub></sub>, and  $\tau_l$  is calculated using Eqn. (7). Using a measured O<sub>2</sub> flux of 68-89 mmol O<sub>2</sub> m<sup>2</sup> d<sup>-1</sup> yields O<sub>2</sub> penetration depth (L<sub>O<sub>2</sub></sub>) values between approximately 0.2mm and 1.0mm<sup>72</sup>. Given that the marsh sediments are periodically exposed to the atmosphere, an L<sub>O<sub>2</sub></sub> value of 1.0mm is used in this study, which results in  $\bar{\tau}_{O_2}$  values that vary from 4.1 to 17.0mm. The resulting bioirrigation coefficient profile, shown in Fig. 10C, is compared to that of Meile et al.<sup>68</sup> who used an inverse modeling approach to obtain a bioirrigation coefficient profiles from sulfate concentration and reduction rate measurements. In the upper 5 cm of sediment, bioirrigation coefficients from this study are approximately a factor of 2 greater than those of Meile et al.<sup>68</sup>, and the bioirrigation coefficient profile from this study does not decay as rapidly with depth. Eqns. (17) and (20) are used to correct the

profile for the effects of imperfect burrow flushing. The resulting profile still suggests more intense irrigation throughout the sediment than the of Meile et al.<sup>68</sup>.

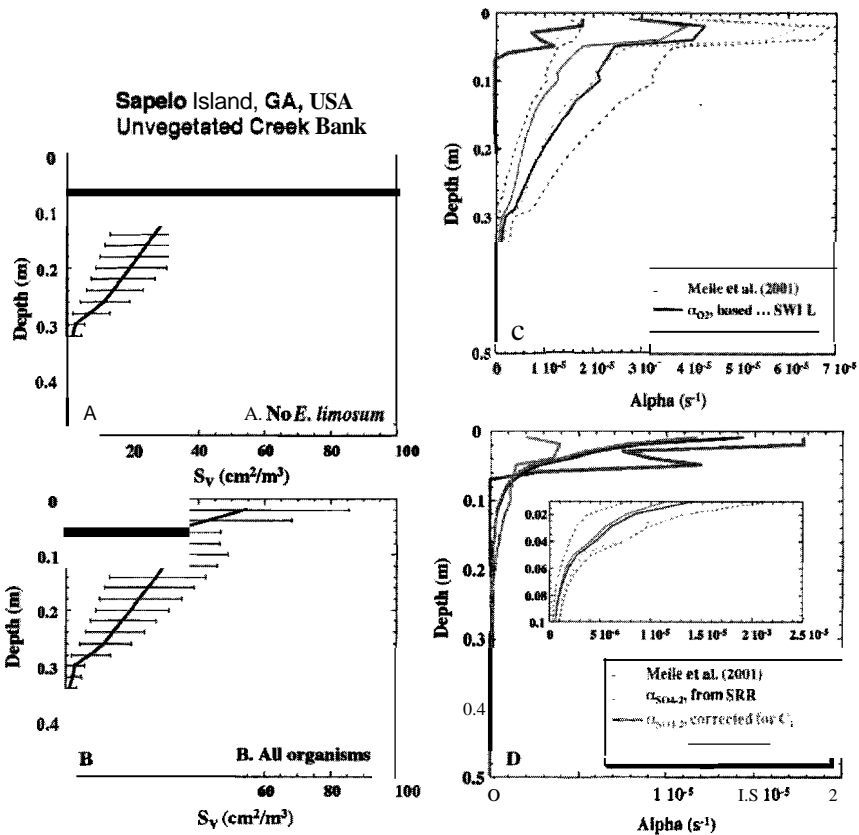


Figure 10. (A)  $S_v$  as a function of depth in an unvegetated saltmarsh creekbank at Sapelo Island, GA, USA including polychaete worms, fiddler crabs and the mudcrabs *Sesarma reticulatum* and *Panopeus herbsterei*. (B)  $S_v$  (cm<sup>2</sup>/m<sup>2</sup>) with all of the organisms included in (A) as well as *Eurytium limosum*. (C) Bioirrigation coefficients (s<sup>-1</sup>) as a function of depth calculated using inverse modeling of chemical data (dark solid line) and  $\alpha_{O_2}$  estimated from the burrow network in this model using  $L=1.0$ mm with Eqn. (6), assuming  $C_b=C_0$  (dark solid line, right) and with correction for depletion of  $O_2$  in burrows (light gray solid line). (D)  $\alpha_{504.2}$  bioirrigation coefficients calculated using the stochastic network model with measured sulfate reduction rates, without correction for  $C_b$  (smooth solid line) and with correction for  $C_b$  (smooth light gray line). The light gray line with low values near the SWI indicates bioirrigation coefficient profile calculated with the stochastic network, assuming zero order kinetics for sulfate reduction (Eqn. 16). Dotted lines indicate irrigation coefficients calculated using  $\pm 1$  standard deviation of the burrow density and surface area profiles.

The lower irrigation values given by Meile et al.<sup>68</sup> may reflect differences in solute-specific irrigation coefficients. Therefore, irrigation coefficients for sulfate are calculated here using sulfate concentration and reduction rate profiles<sup>67, 68</sup> and Eqns. (6) and (12). The resulting irrigation coefficient profile (Fig. 10D) is in excellent agreement with the profile given by Meile et al.<sup>68</sup>. Correction of the stochastically-derived bioirrigation coefficients for the effects of imperfect flushing using Eqns. (17) and (20) does not significantly change the profile.

Bioirrigation coefficients are also calculated assuming zero order kinetics for sulfate reduction. The resulting profile, which depends only on the burrow sizes and spacings, and which is completely independent from the sulfate concentration and reduction rate profiles used by Meile et al.<sup>68</sup>, is also shown in Fig. 10D. The resulting bioirrigation coefficients are somewhat smaller than those of Meile et al.<sup>68</sup>. Overall, the results for the creek bank sites indicate that it is possible to obtain meaningful irrigation coefficients from the stochastically simulated burrow network.

## Sapelo Island, GA, USA: Vegetated Pondered Marsh

### *Macrofaunal consortia*

The abundance and composition of macrofaunal communities present in saltmarsh environments shows significant spatial zonation, with community composition depending on length of tidal inundation, presence or absence of vegetation and sediment composition<sup>57</sup>. Thus, areas of the marsh with dense, diverse macrofaunal populations, such as the unvegetated creek bank discussed above, are likely to have deeper, more intense bioirrigation than regions of the marsh with fewer organisms. For example, pondered marsh regions are much more sparsely populated with macrofauna than creek bank sites. At Sapelo Island, GA, Basan and Frey report burrow apertures  $m^{-2}$  in the pondered marsh<sup>57</sup>, compared to  $1040m^{-2}$  at the unvegetated creek bank. Teal found only two types of crab in the pondered marsh, the fiddler crab *Uca pugnax* ( $27 \pm 7m^{-2}$ ) and the mud crab *Eurytium limosum* ( $4 \pm 1m^{-2}$ )<sup>55</sup>. All other burrow apertures ( $\sim 280 m^{-2}$ ) are likely due to the polychaete worm *Nereis succinea*. Basan and Frey report that burrow depths are typically shorter in the densely vegetated pondered marsh<sup>57</sup>, and that burrow shapes are typically less complex. In simulations, *Uca pugnax* burrows at the pondered marsh were assumed to reach a mean depth of only 15 cm, compared to 20 cm at the creek bank. The lower density of organisms inhabiting the pondered marsh leads to lower surface areas as a function of depth compared to the creek bank site (Fig. 11A).

### *Bioirrigation coefficients*

Bioirrigation profiles at the pondered marsh are calculated for both dissolved  $O_2$  and  $SO_4^{2-}$ .  $O_2$  irrigation coefficient profiles are calculated using a vertical diffusion length scale of 1.0 cm, as for the creek bank site. Diffusion coefficients were corrected using the porosity of 85% reported by Kostka et al.<sup>67</sup>. Dissolved  $SO_4^{2-}$  irrigation coefficient profiles are calculated using measured sulfate concentration and reduction rate profiles<sup>67,69</sup>. Correction for inefficient burrow results in slightly lower  $O_2$  irrigation coefficients, but has no significant impact on  $SO_4^{2-}$  irrigation coefficients (Fig. 11B, C). The intensity of irrigation, especially as indicated by the  $O_2$  irrigation coefficient profiles is somewhat less than at the creek bank site. The depth of irrigation is also somewhat shallower at the pondered marsh, because of the lower density of deep-burrowing infauna and because infauna in pondered marsh areas tend to build shallower burrows than in creek bank sediments<sup>57</sup>. Because of shallower irrigation, the pondered marsh sediments have a more compressed redox stratification, with more reducing conditions closer to the sediment surface, compared to the more intensely irrigated creek bank sediments<sup>69</sup>.

## Comparison of Diagenetic and Stochastic Irrigation Models

Model results obtained at Dry Tortugas, FL and Sapelo Island, GA demonstrate that the ecologically-based stochastic model yields bioirrigation coefficients that are comparable to those obtained independently via inverse modeling or by use of multicomponent early diagenetic reactive transport models. The latter do not require information concerning the benthic organisms responsible for irrigation, rather, bioirrigation coefficients are inferred from model simulations fitting measured chemical and/or reaction rate profiles (Meile et al., 2001). In contrast, the stochastic model presented here explicitly uses ecological data to calculate irrigation intensities. Pore water profiles are not *per se* required, although the radial diffusive length scale ( $L$ ) across the burrow-sediment interface must be specified. As few direct measurements of  $L$  are currently available,  $L$  values are constrained here using other available chemical data.

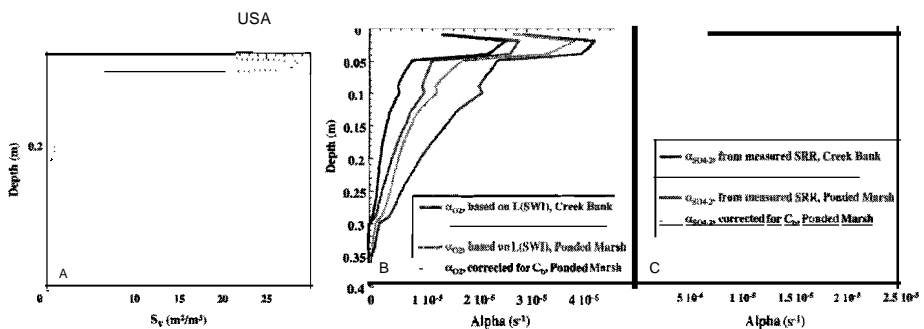


Figure 11. (A)  $S_{\nu}$  as a function of depth for the ponded marsh (solid line) and creek bank (dotted lines) at Sapelo Island, GA with dotted lines indicating  $\pm 1$  standard deviation of the surface area. (B) Bioirrigation coefficients ( $S'$ ) as a function of depth at Sapelo Island calculated for dissolved O<sub>2</sub> at the creek bank (dark gray, rightmost curve) or ponded marsh (medium gray, 2<sup>nd</sup> from the left) with correction for solute depletion within burrows and without correction for solute depletion at the creek bank (light gray) and ponded marsh (black). (C) Bioirrigation coefficients as a function of depth at Sapelo Island calculated for dissolved SO<sub>4</sub><sup>2-</sup> with correction for solute depletion within burrows at the creek bank (light gray) or ponded marsh (black) and without correction for solute depletion at the creek bank (dark gray) and ponded marsh (medium gray). Corrected  $\alpha$ -values are similar to the uncorrected ones.

An important strength of the stochastic model is that uncertainties associated with calculated bioirrigation intensities can be evaluated. The uncertainties derive from the probability density functions describing the burrow network, which in turn are based on statistical information about the ecological variables (animal density, burrow size and geometry). Thus, the model-calculated uncertainties on the bioirrigation coefficients reflect the natural variation in abundance and burrowing activity of the benthic macrofauna.

The stochastic model is not intended to replace early reactive transport models of early diagenesis. Rather, it is an additional tool to constrain irrigation coefficients, which can then be used in early diagenetic modeling. Independent estimates of transport parameters significantly enhance the reliability of reactive transport calculations applied to the complex biogeochemical dynamics of sediments.

## Conclusions

Aquatic sediments are typically redox stratified, with increasingly reducing conditions encountered at depth. However, burrow networks built by macroinfauna create a complex 3-dimensional patchwork of relatively more oxidized or reduced sediment compartments. The resulting increase in interfacial area separating zones with disparate redox characteristics enhances diffusive exchange and creates ecological and geochemical microzones that affect sediment biogeochemical dynamics.

In this study, the spatial distribution of distinct sediment zones due to burrowing macroinfauna are quantified by simulating 3D burrow networks for a variety of model organisms and for consortia of organisms in shallow carbonate and intertidal saltmarsh sediments. The conceptual approach provides a link between the ecological characteristics of burrowing macroinfauna and the resulting biogeochemical consequence on solute transport and biogeochemical cycling. The impact on diffusional exchange of solutes between burrow water and bulk sediment is addressed, and quantitative estimates for nonlocal transport parameters are proposed. This is of particular importance, because a quantitative description of biogeochemical dynamics in sediments, for example based on the interpretation of chemical profiles, requires the quantification of transport intensities.

The approach outlined here allows an independent, ecologically-based, assessment of the depth-dependence of bioirrigation coefficient profiles. Burrow network simulations of even relatively simple model organisms are found to result in depth-dependent burrow wall surface areas that are neither constant nor exponentially decreasing over a given interval, as is commonly assumed in bioirrigation models. Network simulations of the burrowing shrimp *Callinassa subterranea*, the echiuran worm *Maxmuelleria lankesteri*, and the fiddler crab *Uca pugilator* all result in burrow wall surface areas characterized by a subsurface maximum. These maxima are similar to subsurface maxima in bioirrigation intensity reported in chemically-based studies that have not imposed *a priori* restrictions on the depth-dependence of bioirrigation. Furthermore, model simulations demonstrate that relatively rare organisms may have a disproportionate influence on solute transport in sediments. For example, burrow wall surface area profiles calculated for an unvegetated saltmarsh creek bank site at Sapelo Island, GA with and without the mud crab *E. limosum* are quite distinct (Fig. 11A,B), in spite of the fact that *E. limosum*, is responsible for only 6 out of ~1000 apertures·m<sup>-2</sup>.

Burrow network simulations provide estimates of burrow surface areas as a function of depth, which are used to derive nonlocal bioirrigation coefficients. In carbonate reef sediments at Dry Tortugas, O<sub>2</sub> based bioirrigation coefficients calculated using the stochastic model are somewhat larger than values found through diagenetic modeling<sup>15</sup>. However, if the irrigation coefficients are corrected for inefficient flushing, using an estimate of the time-averaged value of C<sub>b</sub>, the agreement is better.

Sulfate bioirrigation coefficient profiles calculated using the stochastic model for an unvegetated intertidal saltmarsh creek bank site are in good agreement with nonlocal bioirrigation coefficient profiles determined by Meile et al.<sup>68</sup> using an inverse modeling approach. Calculated irrigation coefficients for an adjacent ponded marsh site are somewhat lower. This lower mixing intensity may contribute to the more compressed vertical redox zonation observed in chemical pore water profiles at the ponded marsh compared to the creek bank<sup>69</sup>.

To go beyond the model presented here, further information is required regarding the depth-dependence of solute concentrations within burrows, as well as the temporal variation of solute concentrations within burrows. Nonetheless, the current model provides an extremely useful link between benthic macrofaunal ecology and a quantitative description of chemical transport by bioirrigation.

## References

1. RC. Aller, Quantifying solute distributions in the bioturbated zone of marine sediments by defining an average microenvironment, 1980, *Geochimica et Cosmochimica Acta*, 44, 1955-1965.
2. Re. Aller, The importance of relict burrow structures and burrow irrigation in controlling sedimentary solute distributions, 1984, *Geochimica et Cosmochimica Acta*, 48, 1929-1934.
3. Re. Aller and J.Y. Aller, The effect of biogenic irrigation intensity and solute exchange on diagenetic reaction rates in marine sediments. 1998, *Journal of Marine Research*, 56, 905-936.
4. G. Matisoff, IB. Fisher and S. Matis, Effects of benthic macroinvertebrates on the exchange of solutes between sediments and freshwater, 1985, *Hydrobiologia*. 122, 19-33.
5. B.P. Boudreau and RL. Marinelli, A modeling study of discontinuous biological irrigation. 1994, *Journal of Marine Research*, 52, 947-968.
6. Re. Aller. I Y. Yingst and W.J. Ullman, Comparative biogeochemistry of water in intertidal *Onuphis* (polychaeta) and *Upogebia* (crustacea) burrows: temporal patterns and causes, 1983, *Journal of Marine Research*. 41, 5671-604.
7. D.M. Alongi, Microbes, meiofauna, and bacterial productivity on tubes constructed by the polychaete *Capitella capitata*, 1985. *Marine Ecology Progress Series*, 23, 207-208.
8. G.M. Branch and A. Pringle. The impact of the sand prawn *Callinassa kraussi* Stebbing on sediment turnover and on bacteria, meiofauna, and benthic microflora, 1987, *Journal of Experimental Marine Biology and Ecology*, 107,219-235.
9. F.e. Dobbs and J.B. Guckert, *Callinassa trilobata* (Crustacea: Thalassinidea) influences abundance of meiofauna and biomass, composition, and physiologic state of microbial communities within its burrow, 1988. *Marine Ecology Progress Series*, 45, 69-79.
10. N.P. Revsbech, J. T.H. Blackburn and IP. Lomholt, Distribution of oxygen in marine sediments measured with microelectrodes, 1980, *Limnology and Oceanography*, 25, 403-411.
11. W.M. Smethie, Jr., C.A. Nittrouer, and R.F.L. Self, The use of radon-222 as a tracer of sediment irrigation and mixing on the Washington Continental Shelf, 1981, *Marine Geology*, 42, 173-200.
12. D.E. Hammond. e. Fuller, D. Harmon, B. Hartman. M. Korosc. L.G. Miller. R. Rea. S. Warren, W. Berelson and S.W. Hager, Benthic fluxes in San Francisco Bay. 1985. *Hydrobiologia*. 129,69-90.
13. Y. Wang and P. Van Cappellen, A multicomponent reactive transport model of early diagenesis: application to redox cycling in coastal marine sediments, 1996, *Geochimica et Cosmochimica Acta*, 60, 2993-3014.
14. H. Fossing, T.G. Ferdelman. and P. Berg, Sulfate reduction and methane oxidation in continental margin sediments influenced by irrigation (South-East Atlantic off Namibia). 2000, *Geochimica et Cosmochimica Acta*. 64, 897-910.
15. Y. Furukawa, S.J. Bentley. A.M. Shiller, D.L. Lavoie and P. Van Cappellen, The role of biologically-enhanced pore water transport in early diagenesis: an example from carbonate sediments in the vicinity of North Key Harbor, Dry Tortugas National Park. Florida, 2000, *Journal of Research*, 58, 493-522.
16. M.B. Goldhaber, R.e. Aller, IK. Cochran, J.K. Rosenfeld, C.S. Martens and R.A. Berner, Sulfate reduction, diffusion, and bioturbation in Long Island Sound sediments: report of the FOAM group, 1977. *American Journal of Science*, 277, 193-237.
17. D.R Schink and IN.L. Guinasso. Effects of bioturbation on sediment-seawater interaction, 1977, *Marine Geology*. 23, 133-154.
18. D.R Schink and J.N.L. Guinasso, Redistribution of dissolved and adsorbed materials in abyssal marine sediments undergoing biological stirring, 1978. *American Journal of Science*, 278, 687-702.
19. R.e. Aller. The effects of animal-sediment interactions on geochemical processes near the sediment-water interface, in *Estuarine Interactions*. ed. M.L. Wiley. Academic Press, 1978. pp. 157-172.
20. G. Matisoff and X. Wang, Solute transport in sediments by freshwater infaunal bioirrigators, 1998, *Limnology and Oceanography*, 43, 1487-1499.
21. B.P. Boudreau, Mathematics of tracer mixing in sediments: I. Spatially-dependent, diffusive mixing, 1986, *American Journal of Science*, 286. 161-198.
22. D.E. Hammond and C. Fuller, The use of radon-222 to estimate benthic exchange and atmospheric exchanges in San Francisco Bay, ed. T.J. Conomos. *San Francisco Bay: the Urbanized Estuary*, Pacific Div. Am. Ass. Adv. Sci, San Francisco. 1979, pp. 213-230.
23. R.J. McCaffrey, A.C. Myers. E. Davey. G. Morrison, M. Bender, N. Luedte, D. Cullen. P. Froelich and G. Klinkhammer, The relation between pore water chemistry and benthic fluxes of nutrients and manganese in Narragansett Bay, Rhode Island, 1980. *Limnology and Oceanography*, 25, 31-44.



24. B.P. Boudreau, Mathematics of tracer mixing in sediments: II. Nonlocal mixing and biological conveyor-belt phenomena, 1986, American Journal of Science, 286, 199-238.
25. B.P. Boudreau and D.M. Imboden, Mathematics of tracer mixing in sediments: III. The theory of nonlocal mixing within sediments, 1986, American Journal of Science, 286, 693-719.
26. S. Emerson, R. Jahnke and D. Heggie, Sediment-water exchange in shallow water estuarine sediments, 1984, Journal of Marine Research, 42, 709-730.
27. I.P. Christensen, A.H. Devol, and W.M. Smethie, Jr., Biological enhancement of solute exchange between sediments and bottom water on the Washington continental shelf, 1984, Continental Shelf Research, 3, 9-23.
28. B.P. Boudreau, On the equivalence on nonlocal and radial-diffusion models for porewater irrigation, 1984, Journal of Marine Research, 42, 731-735.
29. W.R. Martin and G.T. Banta, The measurement of sediment irrigation rates: a comparison of the Br<sup>-</sup> tracer and <sup>222</sup>Rn/<sup>226</sup>Ra disequilibrium techniques, 1992, Journal of Marine Research, 50, 125-154.
30. M. Schlüter, E. Sauter, H.-P. Hansen and E. Suess, Modelling seasonal variations of bioirrigation in coastal sediments, 2000, Geochimica et Cosmochimica Acta, 64, 821-834.
31. P. Van Cappellen and I.-F. Gaillard, Biogeochemical dynamics in aquatic sediments, in Reactive transport in porous media, P. c. Lichtner, C. I. Steefel, and E.H. Oelkers, Editors. 1996, Mineralogy Society of America: Washington D.C. p. 335-376.
32. Y. Furukawa, S. I. Bentley and D.L. Lavoie, Bioirrigation modeling in experimental benthic mesocosms. 2001, Journal of Marine Research, 59, 417-452.
33. R.C. Aller and J.Y. Yingst, Effects of the marine deposit-feeders *Heteromastix filiformis* (Polychaeta), *Macoma balthica* (Bivalvia), and *Tellina texana* (Bivalvia) on averaged sedimentary solute transport, reaction rates, and microbial distribution, Journal of Marine Research, 1985, 43, 615-645.
34. E.A. Shinn, Burrowing in recent lime sediments of Florida and the Bahamas, 1968, Journal of Paleontology, 42, 879-894.
35. D. I. Hughes, A.D. Ansell and R. I.A. Atkinson, Sediment bioturbation by the echiuran worm *Maxmuelleria lankesteri* (Herdman) and its consequences for radionuclide dispersal in Irish Sea sediments, 1996, Journal of Experimental Marine Biology and Ecology, 195, 203-220.
36. D.J. Hughes, A.D. Ansell, R. I.A. Atkinson and L. A., Underwater television observations of surface activity of the echiuran worm *Maxmuelleria lankesteri* (Echiura: Bonelliidae), 1993, Journal of Natural History, 27, 219-248.
37. L. A. Nickell, R. I.A. Atkinson, D.J. Hughes, A.D. Ansell and C. I Smith, Burrow morphology of the echiuran worm *Maxmuelleria lankesteri* (Echiura: Bonelliidae), and a brief review of burrow structure and related ecology of the Echiura, 1994, Journal of Natural History, 29, 871-885.
38. D.J. Hughes, R.J.A. Atkinson and A.D. Ansell. The annual cycle of sediment turnover by the echiuran worm *Maxmuelleria lankesteri* (Herdman) in a Scottish sea loch, 1999, Journal of Experimental Marine Biology and Ecology, 238, 209-223.
39. I.D. Howard, X-ray radiography for examination of burrowing in sediments by marine invertebrate organisms, 1969, Sedimentology, 11, 249-258.
40. J.T. Davey, The architecture of the burrow of *Nereis diversicolor* and its quantification in relation to sediment-water exchange, 1994, Journal of Experimental Marine Biology and Ecology, 179, 115-129.
41. R.J.A. Atkinson and R.D.M. Nash, Burrows and their inhabitants, 1985, Progress in Underwater Science, 10, 109-115.
42. R.J.A. Atkinson, Mud-burrowing megafauna of the Clyde Sea Area, 1986, Proceedings of the Royal Society of Edinburgh, 90B, 351-361.
43. D.J. Hughes and R.J.A. Atkinson, A towed video survey of megafaunal bioturbation in the north-eastern Irish Sea, 1997, Journal of the Marine Biological Association of the United Kingdom, 77, 635-653.
44. R. Witbaard and G.C.A. Duineveld, Some aspects of the biology and ecology of the burrowing shrimp *Callinassa subterranea* (Montagu) (Thalassinidea) from the southern North Sea, 1989, Sarsia, 74, 209-219.
45. A. A Rowden and M.B. Jones, The burrow structure of the mud shrimp *Callinassa subterranea* (Decapoda: Thalassinidea), 1995, Journal of Natural History, 29, 1155-1165.
46. R.J.A. Atkinson and R.D.M. Nash, Some preliminary observations on the burrows of *Callinassa subterranea* (Montagu) (Decapoda: Thalassinidea) from the west coast of Scotland, 1990, Journal of Natural History, 24, 403-413.
47. R.B. Griffis and T.H. Suchanek, A model of burrow architecture and trophic modes in thalassinidean shrimp (Decapoda: Thalassinidea), 1991, Marine Ecology Progress Series, 79, 171-183.

48. L.A Nickell, D.I Hughes and R.I.A Atkinson, Megafaunal bioturbation in organically enriched Scottish sea lochs, 1995, *Biology and Ecology of Shallow Coastal Waters: Proceedings of the 28th European Marine Biology Symposium, Herakleion, Greece.*
49. A.W. Tudhope and T.P. Scoffin, The effects of *Callianassa* bioturbation on the preservation of carbonate grains in Davies Reef Lagoon, Great Barrier Reef, Australia, 1984, *Journal of Sedimentary Petrology*, 54, 1091-1096.
50. E. Kristensen, Life cycle, growth and production in estuarine populations of the polychaetes *Nereis virens* and *N. diversicolor*, 1984, *Holarctic Ecology*, 7, 249-256.
51. I.T. Davey and c.L. George. Factors in the distribution of intertidal. estuarine polychaetes: a field experiment with *Nereis* (*Hediste*) *diversicolor* and *Nephtys hombergi* in the Tamar at Plymouth, 1986, *Estuarine, Coastal and Shelf Science*. 22,603-618.
52. M. Nithart. Population dynamics and secondary production of *Nereis diversicolor* in a north Norfolk saltmarsh (UK), 1998, *Journal of the Marine Biological Association of the United Kingdom*, 78, 131-143.
53. M. Gerino and G. Stora, Analyse quantitative in vitro de la bioturbation induite par la polychete *Nereis diversicolor*, 1991, *Comptes Rendus Acad. Sci. Paris*, 313, 489-494.
54. G. Miron, G. Desrosiers, C. Retiere and R Lambert. Evolution spatio-temporelle du reseau de galleries chez le polychete *Nereis virens* (Sars) en relation avec la densite, 1991, *Canadian Journal of Zoology*, 69,39-42.
55. I.M. Teal, Distribution of fiddler crabs in Georgia salt marshes. 1958, *Ecology*, 39,185-193.
56. E.A Allen and H.A Curran. Biogenic sedimentary structures produced by crabs in lagoon margin and salt marsh environments near Beaufort, North Carolina, 1974, *Journal of Sedimentary Petrology*, 44, 538-548.
57. P.B. Basan and R. W. Frey, Actual-paleontology and neoichnology of salt marshes near Sapelo Island, Georgia. in *Trace Fossils 2*, ed. T. P. Crimes and J. C. Harper, Steel House Press, London, 1977, pp. 41-70.
58. D.M. Alongi, Mangroves and salt marshes, in *Coastal Ecosystem Processes*, CRC Press. New York, 1998, pp. 43-92.
59. P.L. Wolf, S.F. Shanholtzer and R.I. Reimold, Population estimates for *Decapoda pugna* (Smith. 1870) on the Duplin Estuary Marsh, Georgia, U.S.A (*Decapoda Bracyura, Ocypodidae*), 1975, *Crustaceana*, 91, 79-91
60. J.B. Dembowski, Notes on the behavior of the fiddler crab. 1926, *Biological Bulletin*, 50, 179-201.
61. J.H. Christy, Burrow structure and use in the sand fiddler crab. *Decapoda pugilator* (Bose), 1982, *Animal Behavior*, 30, 687-694.
62. O.W. Crichton. Marsh crab: Intertidal tunnel-maker and grass-eater, 1960, *Estuarine Bulletin*, 5, 3-10.
63. A.F. D'Andrea and G.R. Lopez. Benthic macrofauna in a shallow water carbonate sediment: major bioturbators at the Dry Tortugas, 1997, *Geo-Marine Letters*, 17,276-282.
64. J.M. Teal, Energy flow in the salt marsh ecosystem of Georgia, 1962, *Ecology*, 43, 614-624
65. R.W. Frey and T.V. Mayou, Decapod burrows in Holocene Barrier Island Beaches and Washover Fans, Georgia, 1971, *Senckenbergiana maritima*. 3, 53-77.
66. c.L. Montague, The influence of fiddler crab burrows and burrowing on metabolic proceses in salt marsh sediments, in *Estuarine Comparisons*. ed. V.S. Kennedy, 1982, Academic Press, New York, pp. 283-301.
67. J.E. Kostka. A. Roychoudhury and P. Van Cappellen, Rates and controls of anaerobic microbial respiration across spatial and temporal gradients in saltmarsh sediments, 2001, *Biogeochemistry*, in press.
68. C. Meile, C.M. Koretsky and P. Van Cappellen, Quantifying bioirrigation in aquatic sediments: an inverse modeling approach, 2001, *Limnology and Oceanography*. 46, 164-177.
69. C.M. Koretsky, P. Van Cappellen, T.I. DiChristina, J.E. Kostka, K.L. Lowe, C. Moore, A.N. Roychoudhury and E. Viollier, Contrasting geochemical and microbial structures of saltmarsh sediments: seasonal and spatial trends at Sapelo Island (Georgia, USA), in preparation.
70. M. Emmerson, Remedial habitat creation: does *Nereis diversicolor* play a confounding role in the colonisation and establishment of the pioneering saltmarsh plant, *Spartina anglica*?, 2000, *Helgolander Marine Research*, 54, 110-116.
71. V.F. Clavero. E.X. Niell, and I.A Fernandez, Effects of *Nereis diversicolor* O.F. Muller abundance on the dissolved phosphate exchange between sediment and overlying water in Palmones River Estuary (Southern Spain), 1991, *Estuarine, Coastal and Shelf Science*, 33, 193-202.
72. W.J. Cai, L.R Pomeroy, M.A Moran and Y. Wang, Oxygen and carbon dioxide mass balance for the estuarine-intertidal marsh complex of five rivers in the southeastern U.S.. 1999, *Limnology and Oceanography*, 44, 639-649.

## **CHAPTER 5: Explicit representation of spatial heterogeneity in reactive transport models: Application to bioirrigated sediments <sup>4</sup>**

### **Abstract**

Existing reactive transport models represent aquatic sediments as one-dimensional systems. These models account for the predominantly vertical chemical gradients recorded by traditional pore water and solid sediment sampling techniques (e.g., cores, dialysis samplers). However, advances in sampling techniques, including the rapid development of in situ microprofilers, are providing increasingly detailed data sets, which highlight the laterally heterogeneous nature of the water - sediment interface. In particular, coastal sediments inhabited by macrofauna exhibit large horizontal gradients in chemical composition and microbial communities. The availability of comprehensive and multidimensional data sets, along with our growing conceptual understanding of the complex biogeochemical dynamics in sediments, require more sophisticated reactive transport models that explicitly account for the heterogeneity of aquatic sediments. Here, we present a model that explicitly calculates the effect of flushing of macrofaunal burrows on dissolved chemical species distributions.

### **Introduction**

The sediment-water interface separates the transport regime of the water column, dominated by turbulent mixing and fast particle settling, from that of the sediments, dominated by molecular diffusion and sediment accumulation. The resulting increase in residence times of reactive chemical species allows early diagenetic processes to significantly alter both the amount and composition of solid material being buried in the sedimentary record.

Because the input of organic matter is the main energy source for the resident heterotrophic microbial populations, microbial activity tends to be highest near the sediment-water interface. However, the top few centimeters of sediment are also influenced by the presence of macrofauna. The flushing activity of burrowing macrofauna, which maintains O<sub>2</sub> levels and avoids the accumulation of toxins such as free sulfide results in enhanced solute transport, whereas feeding and burrow excavation induces solid phase transport.

Particularly in coastal ocean sediments, enhanced solute transport by macrofauna can exceed transport via molecular diffusion (Archer and Devol, 1992; Meile and Van Cappellen, in press). Enhanced transport increases recycling of dissolved nutrients to the water column and hence contributes to sustain high primary productivity in nearshore environments. To resolve the impact on both early diagenesis and water column processes, enhanced solute transport has to be accounted for in the model formulation. Coupling of reaction and transport processes in heterogeneous, burrowed surface sediments requires a numerical approach.

Here, we address the effect of flushed burrow networks on the distribution of dissolved chemical constituents. Burrows act as conduits for preferential solute transport, leading to spatially heterogeneous distributions of chemicals. By rapidly redistributing solutes, oxidants can be delivered to depths where the bulk sediment is anoxic. As a result, the chemical redox structure of the sediment deviates from the simple I-D vertical redox zonation, typical for deep sea sediments (Froelich et al., 1979), where molecular diffusion represents the major transport process replenishing electron acceptors (O<sub>2</sub>, NO<sub>3</sub><sup>-</sup>, SO<sub>4</sub><sup>2-</sup>).

<sup>4</sup> C. Meile, Tuncay and P. Van Cappellen (2003). Journal of Geochemical Exploration 78-79:231-234.

## Method

The interplay of reaction and transport is simulated with a 3-dimensional finite element code, solving for both flow and chemical species distribution. The flow equation for an incompressible fluid is

$$\frac{\partial \phi}{\partial t} = - \left( \frac{k}{\mu} (\nabla p - \rho g) \right)$$

where  $\rho$ ,  $\phi$ ,  $\mu$ ,  $k$ ,  $p$ ,  $g$  and  $t$  are density, porosity, viscosity, permeability, pressure, gravitational acceleration and time, respectively. The fluid velocity ( $q$ ) is related to the pressure field by

$$q = \phi v = - \frac{k}{\mu} (\nabla p - \rho g)$$

The distribution of a dissolved chemical species obeys

$$\frac{\partial \phi C_m}{\partial t} = \nabla \cdot (D \nabla C_m) - \nabla \cdot (\phi v C_m) + \phi R_m$$

where  $C_m$  is the mass of species  $m$  per unit volume porewater,  $D$  the diffusion tensor and  $R_m$  the sum of all reaction rates acting upon  $C_m$ . The elements ( $i,j$ ) of the diffusion tensor are given by

$$D_{ij} = \phi D^m \delta_{ij} + (\alpha_L - \alpha_T) \frac{z_i z_j}{|q|} + \alpha_T |q| \delta_{ij},$$

where  $D^m$ ,  $\delta_{ij}$ ,  $\alpha_L$ ,  $\alpha_T$  are the molecular diffusion coefficient, Kronecker delta, and longitudinal and transverse dispersivities, respectively.

We have developed a Galerkin finite element program that can simulate coupled fluid flow and solute transport for 1-D, 2-D (both plane and cylindrical symmetry) and 3-D problems. We adopted an explicit time stepping scheme to ease addition and/or elimination of solute species in the reaction network. During each timestep, advection velocities are calculated first, followed by the concentration fields with explicit formulation of the reaction rates. The program allows users to choose from a substantial set of variations of conjugate gradient and preconditioner techniques and direct solvers.

## Application to a coastal ocean site

Simulations representative for a coastal ocean site are performed based on a study by (Furukawa et al., 2001). The following chemical species are considered:  $O_2$ ,  $NO_3^-$ ,  $NH_4^+$ , total sulfide ( $TS = H_2S + HS^- + S_2$ ), and sulfate. The reactions taken into account are degradation of organic matter by aerobic respiration, denitrification and dissimilatory sulfate reduction, as well as oxidation of sulfide and nitrification (Table 1).

Within the modeling framework used here, this minimum set of early diagenetic reactions can easily be expanded if desired (Furukawa et al., 2000; Wang and Van Cappellen, 1996). Because the present study focuses on the impact of burrowing macrofauna on solute transport (bioirrigation), only dissolved species are modeled explicitly. The formulation of the rate of organic matter degradation does not contain an explicit dependency on organic carbon ( $C_{org}$ ), but assumes that within the zone of bioturbation  $C_{org}$  is well mixed. Hence, the maximum rates of respiration,  $R_{oc}$  and  $R_{OCAn}$ , are assumed to be constant. To reflect more efficient aerobic degradation, respiration rates under oxic conditions exceed those under anoxic conditions ( $R_{oc} > R_{OCAn}$ ).

Table 1: Reaction rate and rate laws.  $C_{org}$  represents organic carbon of the form  $(CH_2O)_x(NH_3)_y$ . Using Redfield ratio gives  $x=106$   $y=16$ . Rate laws and constants are taken from (Furukawa et al., 2001)

Reaction	Rate expression
aerobic respiration: $C_{org} + (x + 2y) \cdot O_2 + y \cdot HCO_3^- \rightarrow$ $y \cdot NO_3^- + (x + y)CO_2 + (x + 2y)H_2O$	$R_1 = \frac{R_{OCAn}}{X} \cdot \frac{O_2}{K_m^{O_2} + O_2}$
denitrification: $C_{org} + \frac{4x}{5} NO_3^- \rightarrow \frac{2x}{5} N_2$ $+ \frac{x}{5} CO_2 + \frac{3y}{5} HCO_3^- + \frac{3x+6y}{5} H_2O$	$R_2 = \frac{R_{OCAn}}{x} \cdot \frac{NO_3^-}{K_m^{NO_3^-} + NO_3^-}$ $\frac{K_{inh}^{O_2}}{K_{inh}^{O_2} + O_2}$
sulfate reduction: $C_{org} + \frac{x}{2} \cdot SO_4^{2-} + y \cdot CO_2 + y \cdot H_2O \rightarrow$ $\frac{x}{2} \cdot H_2S + y \cdot NH_4^+ + (x + y)HCO_3^-$	$R_3 = \frac{R_{OCAn}}{X} \cdot \frac{SO_4^{2-}}{K_m^{SO_4^{2-}} + SO_4^{2-}}$ $\frac{K_{inh}^{NO_3^-}}{K_{inh}^{NO_3^-} + NO_3^-} \cdot \frac{K_{inh}^{O_2}}{K_{inh}^{O_2} + O_2}$
nitrification: $NH_4^+ + 2O_2 \rightarrow NO_3^- + H_2O + 2H^+$	$R_4 = k_{nitri} \cdot NH_4^+$
sulfide oxidation: $HS^- + 2O_2 \rightarrow SO_4^{2-} + H^+$	$R_5 = k_{sox} \cdot TS \cdot O_2$

Rate parameters:

$$R_{OCAn} = 6.9 \cdot 10^5 \text{ mol m}^{-3} \text{ s}^{-1}, R_{OCAn} = 2.5 \cdot 10^6 \text{ mol m}^{-3} \text{ s}^{-1}$$

$$K_m^{O_2} = 20 \mu\text{M}, K_m^{NO_3^-} = 5 \mu\text{M}, K_m^{SO_4^{2-}} = 1.6 \text{ mM}$$

$$K_{inh}^{O_2} = K_m^{O_2}, K_{inh}^{NO_3^-} = K_m^{NO_3^-}$$

$$k_{nitri} = 1.6 \cdot 10^3 \text{ mor}^{-1} \text{ m}^3 \text{ s}^{-1}, k_{sox} = 5.07 \cdot 10^6 \text{ mor}^{-1} \text{ m}^3 \text{ s}^{-1}$$

Simulations are carried out for a planar 10 by 10 cm domain, i.e. the model extends only 1 element into the third, horizontal, dimension to speed up the computations. A U-shaped burrow with a side-gallery (Fig. 1) is considered and a continuous flow of  $0.1 \text{ g m}^{-1} \text{ s}^{-1}$  is imposed at the inlet of the burrow. The latter value is comparable to time integrated flushing intensities estimated by Mayer et al. (1995) for burrows in coastal sediments. The porosity of the unburrowed sediment is taken as 0.5, and lateral and longitudinal dispersivities are set to zero. Initial solute concentrations throughout the computational domain are set to the values at the upper boundary ( $O_2 = 228 \mu\text{M}$ ,  $NO_3^- = 15 \mu\text{M}$ ,  $SO_4^{2-} = 13 \text{ mM}$ ,  $NH_4^+ = 14 \mu\text{M}$ ,  $TS = 0 \mu\text{M}$ ; Furukawa et al., 2001). A periodic boundary condition is imposed at the sides and no flow at the bottom of the domain. Shown here are results after 7 days, when steady state conditions are reached (Fig. 1).

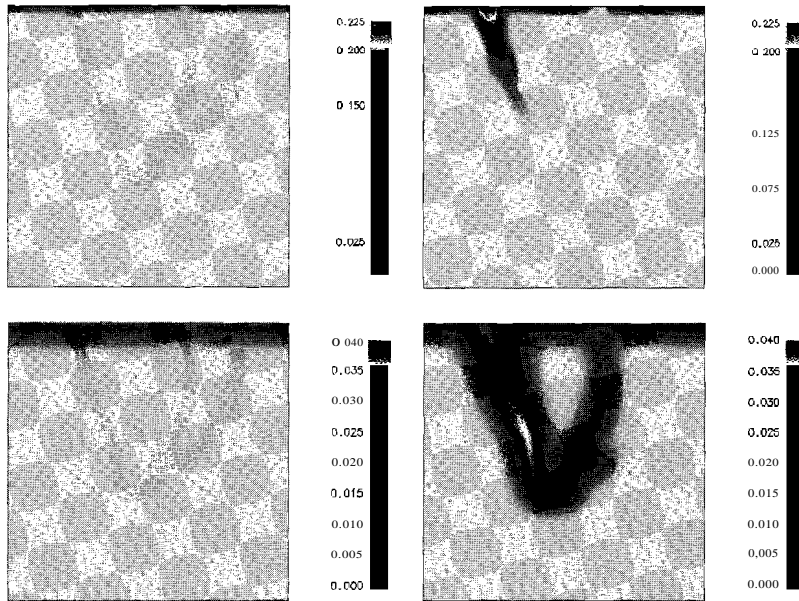


Figure 1. Comparison of model simulations with and without burrow flushing. The upper panels show the  $O_2$ , the lower the  $NO_3^-$  concentration fields (in mM). The left panels depict the non-flushing scenario, with the imposed burrow geometry indicated in gray. The right panels show the results when the burrow is flushed continuously.

Figure 1 illustrates the large impact flushed burrow structures have on the distribution of chemical species within the upper sediment. Without a burrow, the observed pattern follows the traditional vertical redox stratification of sediments, with  $O_2$  rapidly depleted within the upper 5mm, followed by  $NO_3^-$ . The flushed burrow, however, leads to a locally much deeper penetration of  $O_2$  and  $NO_3^-$ . This may help explain the presence of aerobic bacteria at depth in highly anoxic nearshore sediments (e.g., Lowe et al., 2000). Due to nitrification, the nitrate concentration in and near the burrow may exceed the concentration in the overlying water. Bioirrigation may therefore be a major control on the intensity of coupled nitrification - denitrification in sediments. The limited impact of the side gallery on the  $O_2$  and  $NO_3^-$  distributions illustrates that active flushing of burrows by macrofauna is needed to create significant chemical heterogeneity.

## Conclusions

Enhanced transport is typically described as a rapid exchange between overlying water and (average) porewater concentration at depth in the sediment. Our results indicate that this is likely a poor description for reactive solutes, which may exhibit more complex interactions between transport and reaction processes. Traditional models of early diagenesis based on an average representation of the system cannot account for these interactions. Consequently, any quantitative description of early diagenesis based on average properties should be used with caution as they may fail to predict certain critical features of the spatial distribution and temporal dynamics of the microbial populations that drive the transformation of organic matter.

Future work will include the study of the transient nature of burrow flushing, and include formulations of enhanced solid transport. Due to the flexibility of our approach, and the use of a graphical mesh generator interface, the model is also suited for implementation of other types of heterogeneous features, e.g., patchy distribution of reactive solids, such as organic matter or ferric oxyhydroxides.

## References

- Archer, D., Devol, A., 1992. Benthic oxygen fluxes on the Washington shelf and slope: A comparison of in situ microelectrode and chamber flux measurements: *Limnol. Oceanogr.*, 37, 614-629.
- Froelich, P.N., Klinkhammer, G.P., Bender, M.L., Luedke, N.A., Heath, G.R., Cullen, D., Dauphin, P., Hammond, D., Hartmann, B., Maynard, V., 1979. Early oxidation of organic matter in pelagic sediments of eastern equatorial Atlantic: suboxic diagenesis. *Geochim. Cosmochim. Acta*, 43, 1075-1090.
- Furukawa, Y., Bentley, S., Shiller, A., Lavoie, D., Van Cappellen, P., 2000. The role of biologically-enhanced pore water transport in early diagenesis: An example from carbonate sediments in the vicinity of North Key Harbor, Dry Tortugas National Park, Florida. *J. Mar. Res.* 58, 493-522.
- Furukawa, Y., 2001. Biogeochemical consequences of macrofauna burrow ventilation: *Geochem. Trans.*, II, 83-91. DOI: 10.1D39/b108381c
- Lowe, K.L., DiChristina, T.J., Roychoudhury, A., Van Cappellen, P., 2000. Microbiological and geochemical characterization of microbial Fe(III) reduction in salt marsh sediments. *Geomicrobiol. J.* 17, 163-178.
- Mayer, M.S., Schaffner, L., Kemp, W.M., 1995. Nitrification potentials of benthic macrofaunal tubes and burrow walls: effects of sediment  $\text{NH}_4^+$  and animal irrigation behavior. *Mar. Ecol. Prog. Ser.*, 121, 157-169.
- Meile, C., Van Cappellen, P., in press. Global estimates of enhanced solute transport in marine sediments. *Limnol. Oceanogr.*
- Wang, Y., Van Cappellen, P., 1996. A multicomponent reactive transport model of early diagenesis: Application to redox cycling in coastal marine sediments. *Geochim. Cosmochim. Acta*, 60, 2993-3014.

## **CHAPTER 6: Particle age distributions and O<sub>2</sub> exposure times: Time scales in bioturbated sediments <sup>5</sup>**

### **Abstract**

A stochastic particle tracking approach is used to compute particulate age distributions and oxygen exposure times in bioturbated marine sediments. Simulations representative of abyssal plain, continental slope and continental shelf sediments indicate that, within the mixed zone, the variability in particle age is of the same order of magnitude as the average age itself. The spreading of particle age induced by bioturbation is preserved when sediment layers are buried below the mixed layer. Particle reactivity has a major impact on age distributions. Average ages of particle-bound constituents that undergo decay during early diagenesis are smaller than those of inert tracers. The oxygen exposure time (*OEn* of sedimentary organic matter depends on the particle mixing intensity and degradation kinetics. Particularly in bioturbated, deep-sea sediments, where oxygen penetrates deep below the sediment-water interface, *OETs* of deposited organic matter may diverge significantly from simple estimates obtained by dividing the O<sub>2</sub> penetration depth by the linear sedimentation rate.

### **Introduction**

Transport time scales, for example transit or residence times, are fundamental properties of environmental systems. They allow one to compare different environments, and to gauge the relative importance of transport and reaction processes affecting the structure and evolution of ecosystems (CARLETON, 2002; NIXON et al., 1996). In complex transport systems, however, transit times and tracer-age distributions may no longer be related in a simple manner (HOLZER and HALL, 2000). Furthermore, because of dispersive transport processes, particles or solute parcels of different ages are mixed together in a given sample volume (SCHIFFELBEIN, 1985). For reactive substances, for example particulate and dissolved organic matter, this complicates the relationship between average age and apparent reactivity.

Particulate matter arriving at the seafloor experiences a dramatic change in transport regime. Below the sediment-water interface (SWI), a particle moves because of the accumulation of new sediment at the SWI, or it is redistributed through the activity of benthic organisms (BERNER, 1980; VAN CAPPELLEN and GAILLARD, 1996). The latter process, bioturbation, is often the dominant particulate transport process in the uppermost portion of marine sediments (BOUDREAU, 1997; TROMP et al., 1995), and is reflected in rather homogeneous vertical distributions of particle-associated tracers (e.g., (BERGER and JOHNSON, 1978). In contrast to sedimentation, bioturbation may selectively transport particles depending on their composition and age (SMITH et al., 1993).

An important aim of early diagenetic research is to constrain the evolution of the reactivities of organic matter and mineral phases prior to their preservation in the sedimentary record. This evolution depends not only on the initial reactivity of deposited particulates and the transport regime within the sediment, but also on chemical conditions in the pore water medium. It has been proposed, for instance, that the extent of degradation of organic matter is dependent on the amount of time it spends in contact with pore water O<sub>2</sub> (HARTNETI et al.,

---

<sup>5</sup> Christof Meile and Philippe Van Cappellen



1998). The residence time within the oxygenated zone is determined by the particulate transport rates plus the degradation kinetics of the deposited organic matter.

To simulate diffusive spreading of particle age distributions by bioturbation, we use a random walk model to track individual particle histories in depositional settings representative of shelf, continental slope and abyssal plain environments. We explicitly account for the influence of reaction processes on particle age and residence times in the bioturbated sediment. With this approach it becomes possible to calculate both the mean and variance of particle age distributions, as a function of the biogeochemical reactivity of organic or mineral constituents of the sediment. As an application, we examine the influence of bioturbation on the oxygen exposure time (*OET*) and the burial efficiency of organic matter.

## Method

### Governing Equation

In the approach developed here, solid phase transport caused by benthic macrofauna is represented as a diffusion process (BERNER, 1980). Although random diffusion does not capture all the details of the behavior of benthic organisms (MEYSMAN et al., 2003, accepted-a), it has, in many cases, been successful in reproducing the depth distributions of inert tracers and radioisotopes. On a theoretical level, the diffusion representation of bioturbation requires frequent particle displacements over fairly short distances. The diffusion approximation becomes questionable when the mixing length scale is larger than the distance over which the concentration of the tracer is changing significantly, e.g. in the presence of Zoophycos (LEUSCHNER et al., 2002; LOEWEMARK and WERNER, 2001), or when the mixing events are relatively rare (BOUDREAU, 1986; MEYSMAN et al., 2003, accepted-a). For certain types of bioturbation, such as food caching (JUMARS et al., 1990) or conveyor belt feeding (JAHNKE et al., 1986), a non-local transport description may be more appropriate (SHULL, 2001). Furthermore, because of selective mixing (SHULL and YASUDA, 2001), transport intensities may differ from one particle type to another.

Depending on the effect of bioturbation on sediment porosity two diffusive endmember formulations can be distinguished (BOUDREAU, 1997). Mixing without effect on porosity is termed intraphase mixing, while mixing of the whole sediment, or interphase mixing, tends to average out porosity gradients. Current available datasets often do not allow one to distinguish conclusively between these endmembers (MULSOWET et al., 1998). Here, we circumvent this issue by performing simulations where porosity is assumed constant with depth. The governing equation for mass conservation of a solid constituent, including advection, diffusion and reaction, is then

$$\frac{\partial B}{\partial t} = \frac{\partial}{\partial x} \left( D \frac{\partial B}{\partial x} \right) - \frac{\partial (\omega B)}{\partial x} + R \quad (1)$$

where  $D$  is the bioturbation coefficient,  $\omega$  the linear sedimentation velocity,  $R$  the reaction rate,  $x$  depth below the SWI, and  $B$  the activity or concentration of the constituent per unit volume solid sediment.

## Bioturbation coefficients

Estimates of the magnitude of the bioturbation coefficient,  $Db$ , in marine sediments have been derived from fitting tracer distributions, in particular  $^{210}\text{Pb}$  depth profiles (BOUDREAU, 1994; SOETAERT et al., 1996). Based on the analysis of various tracer profiles, empirical correlations have been derived, which relate  $Db$ , the sedimentation rate ( $\omega$ ) and water depth ( $z$ ) (BOUDREAU, 1994; MIDDELBURG et al., 1997; TROMP et al., 1995). Here, we use the empirical relationships of Middelburg et al. (1997):

$$a > (\text{cm yr}^{-1}) = 3.3 \cdot 10^{(-0.87478367 - 0.00043512z)} \quad (2)$$

$$Db(O) (\text{cm}^2 \text{ yr}^{-1}) = 5.2 \cdot 10^{(0.76241122 - 0.00039724z)}$$

where  $z$  is water depth in meters and  $Db(O)$  is the bioturbation coefficient at the SWI.

The thickness of the bioturbated layer is relatively constant over a wide variety of depositional settings in the oceans, with an average mixing depth of approximately 10 cm (BOUDREAU, 1994). A number of mathematical functions describing the depth dependence of  $Db$  in the mixing zone have been proposed. The following expression is used in this study: it offers a flexible description of the commonly reported decrease of  $Db$  with increasing distance from the SWI (NIE et al., 2001):

$$Db(x) = Db(O) \text{erfc} \left[ \frac{x - x_{\text{mix}}}{s} \right] \quad (3)$$

where  $x_{\text{mix}}$  is the depth at which  $Db(x)$  drops to half its value at the SWI. The value of  $s$  controls the steepness with which  $Db$  approaches zero at depth. Based on the relatively limited number of  $Db(x)$  profiles that have been constrained directly by field observations (VAN CAPPELLEN and GAILLARD, 1996), we have selected the values  $x_{\text{mix}} = 8$  cm and  $s = 1$  cm.

## Transport by random walk

Diffusional transport is implemented as a random, one-dimensional movement of particles. In contrast to the deterministic and macroscopic Equation (1), the stochastic approach tracks individual particles whose movements obey a Markovian chain (LABOLLE et al., 1998). The governing equation for the temporal and spatial evolution of the corresponding probability density is the Fokker-Planck or forward Kolmogorov equation (LABOLLE et al., 1998; RISKEN, 1989), on which the random walk procedure is based:

$$\frac{\partial p}{\partial t} = \frac{\partial^2}{\partial x^2} (Kp) - \frac{\partial}{\partial x} (Ap) \quad (4)$$

where  $p$  is the probability density function, and  $A$  and  $K$  describe the mean particle displacement and the increase of the variance per unit time, respectively.

Without the reaction term,  $R$ , Equations (1) and (4) are of similar but not identical form. Assuming that for large numbers of particles, the probability density provides a direct measure of the observed concentration,  $B$ , it follows from Equations (1) and (4) that

$$K = Db \quad \text{and} \quad A = -\frac{\partial Db}{\partial x} + \omega$$

Thus, for spatially varying diffusion coefficients, the mean particle displacement rate equals the linear sedimentation rate corrected by a drift term, which corresponds to the gradient in  $Db$ . The drift term points particles towards regions of intense mixing. Its omission leads to an accumulation of particles in regions of low diffusivity, which is inconsistent with Equation (1) (UFFINK, 1990).

Taking into account the drift term in  $A$ , stochastic particle transport can now be described as the sum of a random displacement due to diffusion, plus the directional movement imposed by sedimentation. In a given time step  $\Delta t$ , a given particle will move over a distance

$$\Delta x = \left( \frac{\partial D_b}{\partial x} + \omega \right) \Delta t + Q \cdot \sigma \quad (5)$$

where  $Q$  is a normal distributed random variable with mean 0 and variance 1, and  $\sigma$  is the diffusional step distance. The next step is to calculate the magnitude of  $\sigma$  for any given values of  $x$  and  $t$ .

The diffusional stepsize is found by considering the moments of the probability density function:

$$N = \frac{M}{M_0} = \frac{\int Jx^n p dx}{\int J p dx} \quad (6)$$

Relating the time derivative of the  $n$ th moment and Equation 4, and stipulating a spatially limited particle concentration, mathematical transformation using integration by part (HUNTER et al., 1993; VISSER, 1997) yields

$$\begin{aligned} \frac{dM^n}{dt} &= \int x^n \left( -\frac{\partial}{\partial x}(Ap) + \frac{\partial}{\partial x} \left( K \frac{\partial p}{\partial x} \right) \right) dx \\ &= n(n-1) \int Db(x) \cdot px, -2dx + n \int \left( \frac{\partial D_b}{\partial x} + \omega \right) \cdot px, -ldx \end{aligned} \quad (7)$$

If at the beginning of a given time step the particle is at position  $x''$  then, using a linear approximation of  $Db$  around  $x''$

$$Db(x) = Db(x_r) + \left. \frac{\partial Db}{\partial x} \right|_{x=x_r} (x - x_r) \quad (8)$$

the time evolution of the  $n$ th moment of the particle is given by

$$\frac{dM^n}{dt} = n(n-1) \iint Db(x_r) + \left. \frac{\partial Db}{\partial x} \right|_{x=x_r} (x-x_r) J P x, -2 dx + n \iint \left( \left. \frac{\partial D_b}{\partial x} \right|_{x=x_r} + \omega \right) p x^{n-1} dx \quad (9)$$

At the start of each time step, the density function associated with the particle is described by a Dirac delta function. Hence, the first and higher order moments are initially equal to 0. Following the approach of Visser (1997), but taking into account the advection term, results in

$$\frac{dN^n}{dt} = n \left( \left. \frac{\partial D_b}{\partial x} \right|_{x=x_r} + \omega \right) N^{n-1} \quad (10)$$

where  $x_r$  is set equal to zero. The first and second normalized moments are related to the movement of the center of mass and the variance, or spreading, around the center of mass, respectively. They are evaluated with Equation (10), together with the following linear approximation, taking into account that the particle is described by a Dirac function at the beginning of the timestep, such that  $N_n(0)=0$  for  $n>0$ :

$$N_n = \int_0^{\Delta t} \frac{dN_n}{dt} dt \approx \frac{dN_n}{dt} \Delta t \quad (11)$$

which yields

$$N_1(\Delta t) \approx \left( \frac{aD_b}{\partial x} + \omega \right) \Delta t$$

$$N_z(\Delta t) \approx \left( 2D_b + 2 \left( 2 \frac{\partial D_b}{\partial x} + \omega \right) N_1^* \right) \Delta t = 2D_b \Delta t + \left( 2 \left( \frac{\partial D_b}{\partial x} \right)^2 + 3\omega \frac{\partial D_b}{\partial x} + \omega^2 \right) \Delta t^2 \quad (12)$$

where  $N_1^*$  is the position of the center of mass after half of the time step has elapsed. The diffusional step size can then be obtained directly from the variance around the center of mass,  $\sigma^2 = N_2 - N_1^2$ :

$$\sigma^2 = 2D_b \Delta t + \left( \left( \frac{\partial D_b}{\partial x} \right)^2 + \omega \frac{\partial D_b}{\partial x} \right) \Delta t^2 \quad (13)$$

If the diffusion coefficient is constant with space, Equation (13) reduces to the well-known diffusional steplength in homogeneous media,  $\sigma = \sqrt{2D_b \Delta t}$ . Equation (13) neglects 3<sup>rd</sup> and higher order moments and, therefore, ignores errors of magnitude  $O(\Delta t^2)$ , which only become relevant at large time steps (ERMAK and NASSTROM, 2(00)).

## Reaction

The stochastic representation of reaction is similar to that described by (KINZELBACH and UFFINK, 1987). It involves calculating the probability that the particle-bound constituent undergoes reaction in a given time interval  $t$  to  $t + \Delta t$ :

$$P_{rxn} = \frac{\int_{t_0}^{t_0 + \Delta t} fR(t) dt}{\int_0^{\infty} fR(t) dt} \quad (14)$$

Normalization by the integral of the rate,  $R$ , from the current time  $t$  to infinity avoids probabilities  $>1$ . Note that such a description implies no memory and evaluates the probability of a particle to react within the next time interval. Reaction takes place if a random variable  $U$ , selected from a uniform distribution in  $(0;1)$ , is smaller than  $P_{rxn}$ . Consider, for example, first-order radioactive decay:

$$R(t) = \frac{dB}{dt} = -k \cdot B(t) \quad (15)$$

where  $k$  is the decay (rate) constant. The reaction probability is then

$$P_{rxn} = 1 - e^{-k\Delta t} \quad (16)$$

Rate equation (15) is also used to represent the degradation kinetics of organic matter (BERNER, 1980). However, in contrast to radioactive decay,  $k$  is not a true kinetic constant but depends, among others, on the age and composition of the organic matter, as well as the availability of electron acceptors. In this case the functional relationship between the rate coefficient  $k(t)$  and time must be known explicitly. However, over a small time interval  $\Delta t$ ,  $k(t)$  may be approximated as a constant, and Equation (16) can still be used during each time step.

## Implementation

Particles are injected at the sediment-water interface (SWI) and followed as they travel through the sediment. The simulation continues until all particles move below a prescribed depth of interest,  $L$ . In the applications described below, 100 particles are tracked and the lower boundary of the model domain is set at  $L = 20$  cm. As a result of random movement, a

particle may return to the SWI; it is, however, prevented from crossing the SWI. That is, apart from the initial injection of particles, the SWI acts as an impermeable boundary. An impermeable upper boundary is not fully consistent with the moment analysis used to derive the diffusional step distance. For the small time steps and jump distances in the applications below, this inconsistency only affects particle behavior just below the SWI. A particle can thus only leave the zone of early diagenesis via the lower boundary. It is assumed that when the particle crosses the lower boundary it enters the sedimentary record.

As particles move within the model domain, reactive constituents associated with them undergo reaction. Here, we restrict ourselves to constituents supplied from the water column, which decay during early diagenesis, for example, radioactive isotopes, organic matter or biogenic silica. At the moment a new particle is injected at the SWI, the constituent under consideration is assigned a weight factor,  $pw$ , equal to one. During a time step when reaction takes place ( $U < P_{rxn}$ ), the corresponding weight of the particle is decreased by a factor  $UIP_{rxn}$ . In this manner, it is not the particle as such which decays, but rather the reactive constituent associated with it. Each individual particle thus represents one transport path or history, integrating a multitude of (random) reaction histories.

The spatial step  $\Delta x$  is chosen so that, within the mixed zone, the linear approximation of the  $Db$  depth profile (Equation 8) is valid. The error associated with neglecting second and higher order terms in the Taylor series expansion for  $Db(x)$  is small when

$$\frac{\left(\frac{\partial^2 D_b}{\partial x^2} \cdot \frac{(\Delta x)^2}{2}\right)}{\left(D_b + \frac{\partial D_b}{\partial x} \cdot \Delta x\right)} < \alpha \quad (17)$$

where  $\alpha$  is arbitrarily set to 0.1, which restricts the relative error to less than 10%. A maximum value is then estimated with Equations (5) and (13), imposing a value  $Q = 3$ , thereby encompassing 99% of the expected random step lengths. In the lower part of the model domain, biodiffusion becomes negligible. In the advection-dominated region, defined by  $\left(D_b + \frac{\partial D_b}{\partial x} \cdot \Delta x\right) < 0.001 \cdot \omega \cdot \Delta$ , the time step is adjusted so that the particle advects less than the ensemble averaging depth interval  $\Delta$  (1 cm, see below). In the computational scheme, the time step is thus a function of the particle position.

The depth distributions of particle ages and transit times are obtained by tracking each particle as a function of time, and recording the time spent in each depth interval  $[x, x+\Delta]$ . The model domain is divided in equally spaced depth intervals of  $\Delta = 1$  cm. Based on a periodic sampling every  $t_s = \Delta/(2\omega)$ , estimators of location and variability within each depth interval are calculated at the end of the simulation. The weighted arithmetic mean (average) age of a particle-bound constituent in a given depth interval is computed as

$$\overline{age}(x < x' \leq x + \Delta) = \frac{\sum_{t,i} (age_t \cdot pw_t \cdot \delta_i^t)}{\sum_{t,i} (pw_t \cdot \delta_i^t)} \quad (18)$$

where  $pw_t^i$  and  $age_t$  are the weight and age of the  $i^{\text{th}}$  particle at time  $t$ , respectively. The Kronecker delta  $\delta_i^t$  equals 1 if the particle resides in depth interval  $[x, x+\Delta]$  at time  $t$ ; otherwise it equals 0. The median age within an interval is identified by first sorting all recorded events ( $age_t, pw_t$ ) according to age. Then, the (sorted) particle weights are summed,

progressing from young to old ages, until half the sum of all particle weights is reached. The corresponding age is the median age.

To characterize the variability of particle ages within a given depth interval, the standard deviation  $\sigma$ , skewness (degree of asymmetry;  $Y_3$ ) and kurtosis (flatness compared to normal distribution;  $Y_4$ ) are calculated as follows.

$$\sigma(x < x' \leq x + \Delta) = \left( \frac{\sum_{i,i'} (age_i' - \overline{age})^2 \cdot (pw_i' \cdot \delta_i')}{\sum_{i,i'} (pw_i' \cdot \delta_i')} \right)^{1/2} \quad (19)$$

$$Y_m(x < x' \leq x + \Delta) = \frac{\sum_{i,i'} \left( \frac{(age_i' - \overline{age})^m}{\sigma^m} \cdot (pw_i' \cdot \delta_i') \right)}{\sum_{i,i'} (pw_i' \cdot \delta_i')}$$

The transit time of a particle is defined as the duration since last contact with the SWI. This concept is frequently used in physical oceanography when tracing water parcels (e.g. DELHEZ et al., 2003). The average transit time and its variance in a given depth interval are calculated using expressions similar to Equations (18) and (19), in which the age of a particle is replaced by its transit time. The transit time distributions can be compared to that of the ideal tracer age,  $\tau_{res}$ , which is given by

$$\frac{\partial \tau_{res}}{\partial t} = \frac{\partial}{\partial x} \left( D \frac{\partial \tau_{res}}{\partial x} \right) - \omega \frac{\partial \tau_{res}}{\partial x} + 1 \quad (20)$$

(KHATIWALA et al., 2001). Equation (20) is solved numerically at steady state, with a fixed transit time boundary condition of 0 at the SWI, and a gradient condition,  $\frac{\partial \tau_{res}}{\partial x} = \frac{1}{\alpha}$ , at the lower boundary,  $x = L$ . Hence,  $\tau_{res}$  represents the ensemble average of the transit time of an inert substance.

The oxygen exposure time, or *OET*, has been defined as the ratio of the  $O_2$  penetration depth ( $L_{O_2}$ ) and sedimentation rate ( $\omega$ ) (HARTNETT et al., 1998). Strictly speaking this definition only applies to a nonreactive species in the absence of diffusive particle transport. Here, *OETs* are computed taking explicitly into account bioturbation and reaction, by keeping track of the total time each particle spends in the oxic zone. The definition of the *OET* follows Equation (18), where *OET* replaces age, and  $\delta_i^t$  is 0 or 1 depending on whether the particle is below or above the oxygen penetration depth  $L_{O_2}$  at a given time  $t$ .

With the above approach it is possible to calculate *OETs* in each depth interval. Of particular interest, however, is the *OET* of particles leaving the early diagenetic domain at depth  $L$ . In the applications discussed below, *OETs* at  $x = L$  are calculated for a range of  $O_2$  penetration depths,  $L_{O_2}$ . Because the  $O_2$  pore water distribution readjusts rapidly after a mixing event, relative to the particle transport time scales (MEHREZ and VAN CAPPELLEN, 2003),  $L_{O_2}$  is kept constant when simulating a set of particle trajectories and fluctuations in  $O_2$  penetration depth are not explicitly accounted for. Note that  $L_{O_2}$  can be shallower or deeper than the average mixing depth of 10 cm. The magnitude of  $L_{O_2}$  depends primarily on the supply of reactive organic matter at the SWI, the intensity of pore water irrigation and the bottom water oxygen concentration.

## Applications

The effects of bioturbation on age-related properties of sediments are evaluated for conditions representative of continental shelf, continental rise and abyssal plain environments. Sedimentation rates and biodiffusion intensities are estimated at the selected water depths of 200, 1000 and 4000 m, using the empirical expressions of Middelburg et al. (1997) (Equation 2). For the conditions considered, bioturbation dominates particle transport in the upper 10 cm of the sediments ( $Db > \omega \cdot x_{mix}$ ).

## Particle ages and transit times

Particle ages for nonreactive constituents are shown in Figure I for the continental rise environment (1000 m water depth). Within the upper 8 to 10 cm, average and median particle ages are fairly uniform, illustrating the efficient mixing of particles by benthic infauna. Below 10 cm, the average and median ages increase with a slope parallel to that of the sedimentation-only age. The general shapes of the average and median particle age distributions at the other water depths (200 and 4000 m) are similar to those in Figure 1.

In all cases tested, the age distributions exhibit large variations. Within the upper mixed zone, standard deviations are of the same order of magnitude as the absolute ages themselves (Figure 1). Skewness and kurtosis are typically around 1.5 and 5, respectively, compared to 0 and 3 for a normal distribution, indicating asymmetric and peaked distributions. This can be seen in the histograms on Figure 1, which present the age frequency distributions in two depth intervals. The distributions are skewed to older ages, resulting in median ages that are systematically younger than the average values. Because the median is less affected by uncharacteristically old particles, it is considered a more meaningful measure of the particle age as a function of depth in the sediment.

The spreading of particle ages induced by bioturbation is preserved when a sediment layer is buried below the mixed layer. The results in Figure I thus imply that bioturbation interferes with paleoenvironmental reconstructions in two distinct ways. First, it limits the stratigraphic resolution of the sedimentary record by vertically homogenizing average and median particle ages. Temporal resolution of the sedimentary record is therefore on the order of  $x_{mix}/\omega$ . Second, it mixes together particles with very different early diagenetic trajectories in the same sedimentary horizon. For reactive constituents, this creates a source of uncertainty when interpreting compositional and isotopic records.

In bioturbated sediments, the transit time of an inert constituent is systematically lower than its average or median particle age (compare Figures I and 2). This indicates that most particles return repeatedly to the SWI before being buried below the mixed surface layer. The transit times of an inert constituent computed with the stochastic particle model agree well with the ideal tracer transit times, obtained from Equation (20) (Figure 2). As the transit time is reset to 0 each time the particle reaches the SWI, there is only little spreading, and the arithmetic mean and median transit time distributions almost coincide.

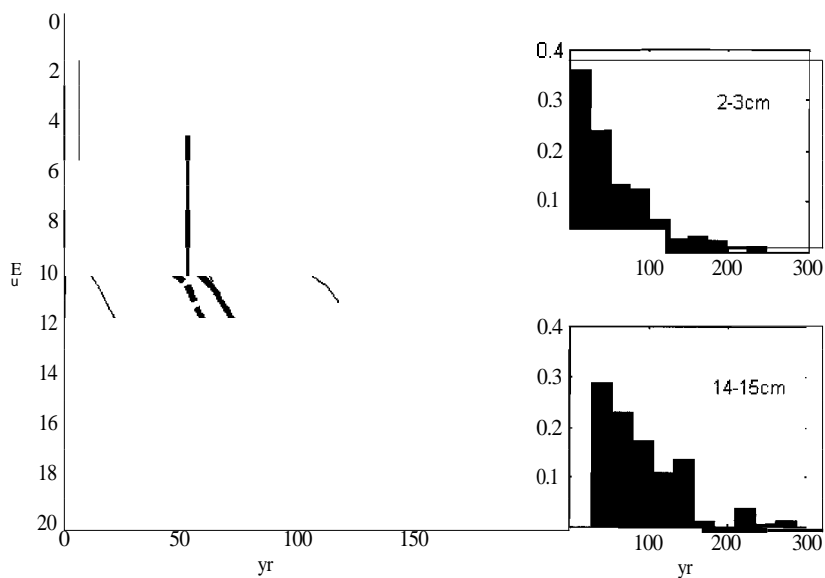


Figure 1. Age distribution of a nonreactive species, plotted versus depth, in the model slope sediment (1000 m water depth). The thick solid line is the average age, the thin lines correspond to  $\pm$  one standard deviation. The dashed line is the median age and the thin dashed-dotted line is the sedimentation-only age ( $\times 10^4$ ). The histograms on the right show relative distribution frequencies of particle ages in two depth intervals.

The average and median ages of reactive particle-bound constituents are lower than the corresponding values for nonreactive constituents (Figure 3). This reflects the greater weight, for reactive constituents, of younger particles that have undergone less decay (Equation 18). The extent to which the age distribution of a reactive constituent deviates from that of a nonreactive tracer varies from one depositional environment to another, as shown by the particle age distributions of  $^{210}\text{Pb}$  (half-life: 22.4 years) in the three model sediments.



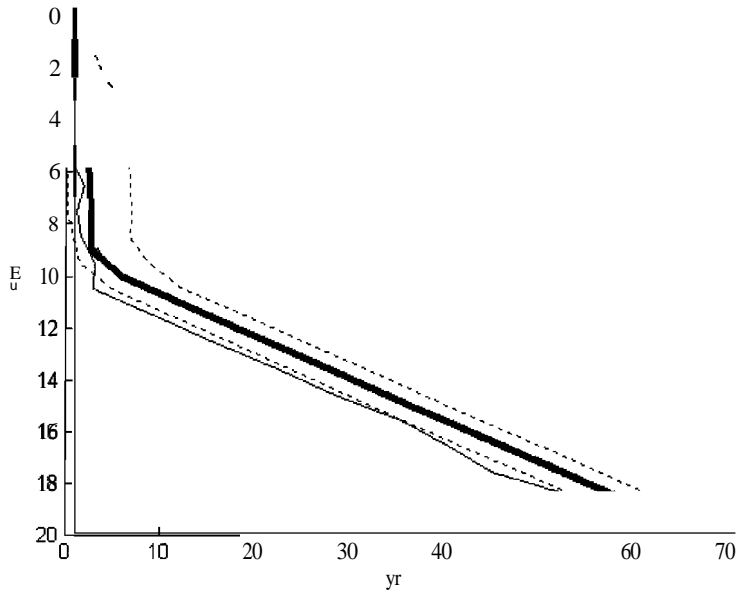


Figure 2. Transit times in the model slope sediment (1000 m water depth), plotted versus depth below the sediment-water. The thick solid line is the solution of Equation (20). Almost coinciding with it, and hence barely visible, are the median values for an inert tracer and  $^{210}\text{Pb}$  (dashed and dashed-dotted thin lines). The surrounding dotted lines indicate the one standard deviation confidence interval around the average. The thin solid line is the transit time for  $^{234}\text{Th}$ .

For the shelf sediment (Figure 3A), the median particle ages of  $^{210}\text{Pb}$  are fairly close to the median ages of nonreactive particles. In the abyssal plain sediment (Figure 3C), however, they approach the transit times of nonreactive particles. This reflects contrasting reaction-transport regimes. For the shelf sediment,  $Db > k \cdot x_{\text{mix}}^2$ , hence, radioactive decay plays a secondary role, relative to bioturbation, in the age distribution of  $^{210}\text{Pb}$ . In the pelagic sediment, however,  $Db < k \cdot x_{\text{mix}}^2$ , so that only those particles with a near-unidirectional downward trajectory have a reasonable probability of surviving passage through the mixed zone. Therefore, the particle age distribution resembles the transit time distribution. For highly reactive  $^{234}\text{Th}$ , with a half-life of only 24 days,  $Db$  is smaller than  $k \cdot x_{\text{mix}}^2$  under all conditions simulated. Consequently, the particle age distribution of  $^{234}\text{Th}$  approaches the transit time distribution in all three environments.

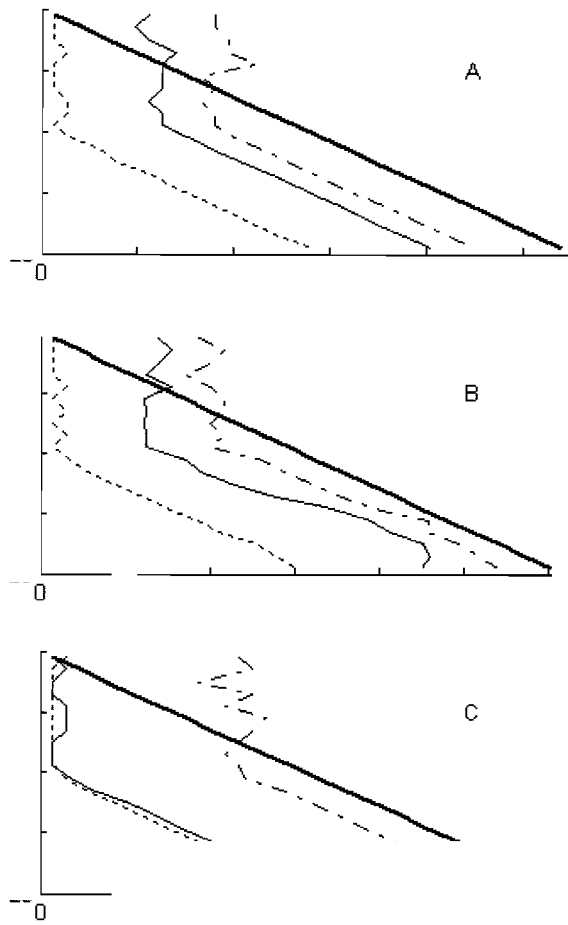


Figure 3. Median ages of reactive and nonreactive substances in different depositional settings, plotted against depth below the sediment-water interface. The dashed-dotted line corresponds to the nonreactive substance, the thin solid line to  $^{210}\text{Pb}$ , the dotted line to  $^{234}\text{Th}$ , and the thick solid line to the sedimentation-only age. Panels A, B and C correspond to the sites at 200 m, 1000 m and 4000 m water depth, respectively. Values of  $D_b$  in A, B and C are 25.06, 12.06 and 0.775  $\text{cm}^2 \text{yr}^{-1}$ ; values of  $\omega$  in A, B and C are 0.36, 0.162 and 0.008  $\text{cm yr}^{-1}$ .

## Oxygen exposure times

For the three depositional environments considered, stochastically computed median *OEYs* of particles being buried in the sedimentary record are generally lower than  $L_{O_2}/\omega$  values (Figure 4). For very small  $L_{O_2}$ , on the order of a few mm or less, mixing may actually result in *OEYs* that exceed  $L_{O_2}/\omega$  (This is barely visible on Figure 4 because of the scale of the  $L_{O_2}$  axis). Like particle age, *OEY* depends on the reactivity of the constituent. For a given oxygen penetration depth, the *OEY* is highest for an inert constituent, and lowest for  $^{234}\text{Th}$ , a proxy for highly reactive particulate constituents. This is due to the fact that only particles with the shortest early diagenetic trajectories still carry highly reactive constituents when exiting the model domain.

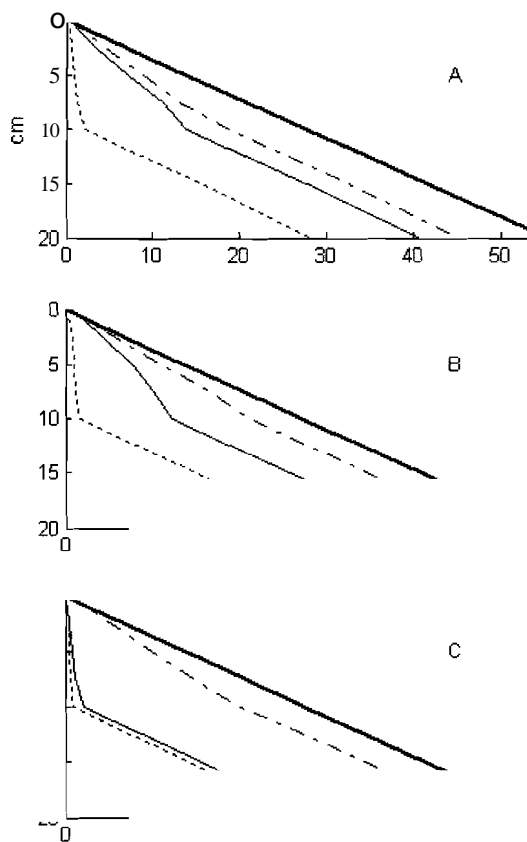


Figure 4. Median OET of reactive and nonreactive substances exiting the lower boundary, plotted as a function of the oxygen penetration depth,  $L_{O_2}$ . The labels are identical to Figure 3, except that the y-axis represents  $O_2$  penetration depth, and the x-axis the OET rather than age.

The probability density functions of the *OETs* have similar features as those of the particle ages described previously: they exhibit a large spreading and are skewed towards high values. Thus, median *OETs*, rather than mean values, provide a more meaningful measure of the typical amount of time a given constituent spends in the oxic surface layer of the sediment. Furthermore, in bioturbated depositional environments, particles having experienced a range of *OETs* are buried together in the sedimentary record.

The oxygen penetration depth is a crucial variable controlling the *OET* (Figure 4). Typically,  $L_{O_2}$  increases with increasing water depth (TROMP et al., 1995). On the continental shelves,  $L_{O_2}$  varies mostly from a few mm to several cm, while in deep-sea sediments dissolved oxygen may persist for several tens of cm or more. Hence, for most marine sediments  $L_{O_2} < x_{mix}$ , except in organic-poor deep-sea sediments. As shown by Figures 4A, 4B and 4C, the offset between the median *OET* of a reactive constituent and the *OET* of an inert tracer increases with increasing  $L_{O_2}$  when  $L_{O_2} < x_{mix}$ . For  $L_{O_2} > x_{mix}$ , the offset remains constant with increasing  $L_{O_2}$  because biodiffusional mixing is now entirely confined to the oxic zone. Below the mixed layer, the median *OET* of both reactive and nonreactive substances increases linearly with depth, due to sedimentation, until the bottom of the oxic zone is reached.

### Organic carbon burial efficiency

The oxygen exposure time (*OET*) approximated by  $L_{O_2}/\omega$  has been suggested to be a master variable determining the extent of organic matter burial into the geologic record (HARTNETT et al., 1998). In the oceans, the sedimentation rate varies over many orders of magnitude, and is a likely determining factor underlying the empirical relationship between burial efficiency and *OET*. However, there is also evidence that oxic conditions may enhance organic matter ( $C_{org}$ ) degradation, e.g. through more efficient degradation of refractory organic materials coupled to aerobic respiration (CANFIELD, 1994; ALLER and ALLER, 1998).

Here, we investigate the impact of  $O_2$  exposure on  $C_{org}$  preservation in the three virtual sediments introduced earlier. Organic matter degradation is assumed to follow first order kinetics with respect to the concentration of  $C_{org}$  (BERNER, 1980). For the baseline scenario, we estimate the oxic and anoxic rate constants (yr.<sup>-1</sup>) of degradation using the global relationships as a function of sedimentation rate (cm yr.<sup>-1</sup>) presented by (TROMP et al., 1995):  $k_{ox} = 2.97\omega^{0.62}$ , and  $k_{anax} = 0.057\omega^{0.94}$ . Typical values of the  $O_2$  penetration depth of 0.3, 2 and 7.5 cm are assigned to the sediments at 200, 1000 and 4000 m water depth, respectively. Burial efficiencies are calculated by monitoring the fraction of organic matter that survives early diagenesis and exits the lower boundary.

The baseline simulations reproduce the overall trend of increasing  $C_{org}$  burial (or preservation) efficiency with decreasing *OETs* (Figure 5, squares). On the figure, the filled squares correspond to *OETs* derived from the stochastic model, while the open squares correspond to  $L_{O_2}/\omega$  values. At the 200 m water depth site, the two approaches yield fairly similar *OET* values. At the deeper sites, however, the two approaches predict significantly different  $O_2$  exposure times for deposited organic matter. This is due to the deeper oxygen penetration depths, which result in a greater offset between the actual *OET* and the sedimentation-only estimate (see Figure 4).

The effect of doubling the  $O_2$  penetration depth at the three sites can be seen by comparing the squares ( $L_m = 0.3, 2$  and  $7.5$  cm) and triangles ( $L_{O_2} = 0.6, 4$  and  $15$  cm) in Figure 5. A major drop in the  $C_{org}$  burial efficiency occurs at the 200 m water depth site. However, the  $OETs$  computed by the stochastic model for the 200 and 1000 m sites are not dramatically altered, because enhanced degradation shifts more weight to younger particles that exit the model domain. This effect is similar to the decrease in  $OET$  with increasing reactivity illustrated in Figure 4. In contrast, at the deep-sea site, oxygen penetration below the mixed layer ( $L_{O_2} = 15$  cm) causes a large shift in  $OET$ , relative to the baseline scenario.

The empirical rate constant estimates based on (TROMP et al., 1995) result in  $k_{ox}/k_{anox}$  ratios of  $200, 575$  and  $3 \cdot 10^4$  at 200, 1000 and 4000 m water depth, respectively. These large differences integrate multiple effects including, not only the difference in intrinsic degradation efficiencies of aerobic and anaerobic microbial populations, but also the progressive decrease in reactivity of organic matter with advancing early diagenesis. Because of the much longer time scales of early diagenesis in the deep-sea, compared to the continental shelves, the relative difference in  $k_{ox}/k_{anox}$  is largest for the simulations at 4000 m water depth.

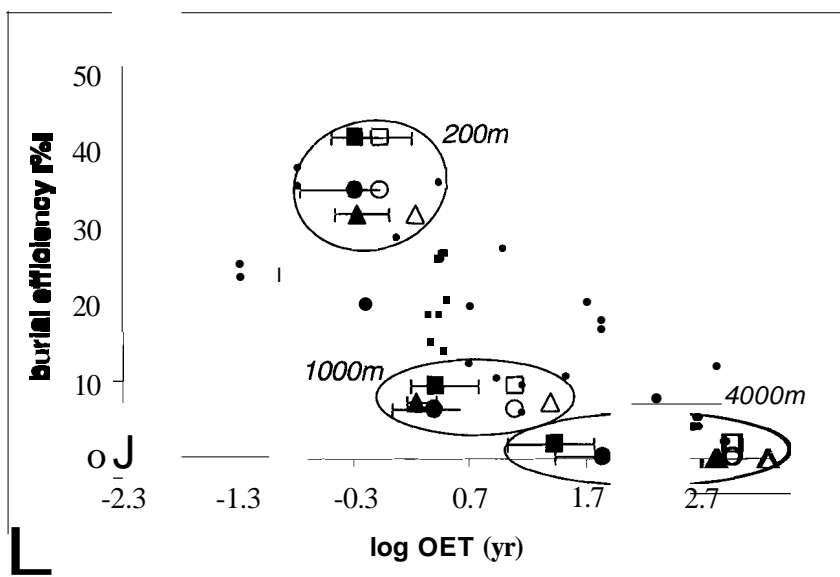


Figure 5.  $OET$  and burial efficiency. Open symbols are based on sedimentation-only estimates of  $OET$ , while filled symbols are based on the median values of stochastically-calculated  $O_2$  exposure times. Error bars for the stochastic  $OETs$  denote the range between 1<sup>st</sup> and 3<sup>rd</sup> quartile. The squares are the baseline scenario with  $L_{O_2} = 0.3, 2$ , and  $7.5$  cm, and  $k_{ox}/k_{anox} = 200, 575$  and  $3 \cdot 10^4$ , at 200, 1000 and 4000 m water depth, respectively. Simulations in which the value of the anoxic rate constant is adjusted to give  $k_{ox}/k_{anox} = 100$  are indicated with circles. Triangles show results after doubling the  $O_2$  penetration depth at the three model sites ( $L_{O_2} = 0.6, 4$  and  $15$  cm). Dots are the data from (HARTNETT et al., 1998), using  $OET = 1..0200$ .

To better constrain the effect of  $k_{ox}/k_{anox}$ , rate constants for aerobic degradation are estimated with the empirical expression,  $k_{ox} = 2.970 \cdot 0.62$ , while  $k_{ox}/k_{anox}$  is assigned a constant value of  $k_{ox}/k_{anox} = 100$  in all three model sediments. At the 200 m water depth site there is a substantial drop in the  $C_{org}$  burial efficiency relative to the baseline scenario (Figure 5, circles), while the changes at the two deeper sites are less pronounced. These results are consistent with the observation that anaerobic decomposition accounts for a major fraction of the organic matter degraded in shelf and coastal sediments, while aerobic degradation dominates in hemipelagic and pelagic sediments (TROMP et al., 1995), and references therein). In the latter environments, the  $C_{org}$  burial efficiency depends primarily on the value of  $k_{ox}$ : increasing  $k_{anox}$ , even by several orders of magnitude, has only a small impact on the burial efficiency.

At the 4000 m water depth site the calculations predict  $C_{org}$  burial efficiencies that approach zero, compared to typical values between 1 and 10% for abyssal plain environments (HENRICHS and REEBURGH, 1987). This reflects the existence of preservation mechanisms that render some organic matter unavailable to bacterial degradation (see (HEDGES and KEIL, 1995) and accompanying articles in the same issue). These mechanisms are not included in the simple first-order degradation model used here, where 100% of the organic matter is assumed to be reactive.

## Conclusions

1. Particle ages, transit times and *OETs* in marine sediments are strongly affected by bioturbation. Biodiffusive mixing leads to large spreading of these temporal properties within sediment layers. The challenge ahead will be to incorporate heterogeneous particle age and *OET* distributions in the description of early diagenetic processes, e.g. the age-dependent degradation of organic matter (MIDDELBURG, 1989).
2. Stochastic simulations, using global parameterizations, demonstrate that actual *OETs* deviate from estimates based on  $L_{O_2}/\omega$ , even for nonreactive species. For reactive chemical constituents, the deviations are even larger. In the model environments studied,  $L_{O_2}/\omega$  ratios overestimate *OETs*, especially at the deepest site.
3. Organic carbon preservation efficiencies are sensitive to the mlxmg regime of the sediment and the degradation kinetics of the organic matter. The simulation results stress the need for a better understanding the mechanisms and factors influencing the reactivity of organic matter. Further progress requires mechanistic (predictive) rate models for organic matter degradation under variable redox conditions.

## References

- Aller R. C. and Aller J. Y. (1998) The effect of biogenic irrigation intensity and solute exchange on diagenetic reaction rates in marine sediments. *Journal of Marine Research* 56(4),905-936.
- Berger W. H. and Johnson R. F. (1978) On the thickness and the <sup>14</sup>C age of the mixed layer in deep-sea carbonates. *Earth and Planetary Science Letters* 41, 223-227.
- Berner R. A. (1980) *Early diagenesis. A theoretical approach*. Princeton University Press.
- Boudreau B. P. (1986) Mathematics of tracer mixing in sediments: I. Spatially-dependent, diffusive mixing. *American Journal of Science* 286,161-198.
- Boudreau B. P. (1994) Is burial velocity a master parameter for bioturbation? *Geochimica et Cosmochimica Acta* 58(4),1243-1249.
- Boudreau B. P. (1997) *Diagenetic Models and Their Implementation*. Springer.
- Canfield D. E. (1994) Factors influencing organic carbon preservation in marine sediments. *Chemical Geology* 114, 315-329.
- Carleton I. N. (2002) Darnkohler number distributions and constituent removal in treatment wetlands. *Ecological Engineering* 19, 233-248.
- Delhez E. I. M., Deleersnijder E., Mouchet A., and Beckers J.-M. (2003) A note on the age of radioactive tracers. *Journal of Marine Systems* 38(3-4), 277-286.
- Ernak D. L. and Nasstrom J. S. (2000) A Lagrangian stochastic diffusion method for inhomogeneous turbulence. *Atmospheric Environment* 34, 1059-1068.
- Hartnett H. E., Keil R. G., Hedges J. I., and Devol A. H. (1998) Influence of oxygen exposure time on organic carbon preservation in continental margin sediments. *Nature* 391,572-574.
- Hedges J. I. and Keil R. G. (1995) Sedimentary organic matter preservation: an assessment and speculative synthesis. *Marine Chemistry* 49,81-115.
- Henrichs S. M. and Reeburgh W. S. (1987) Anaerobic mineralization of marine sediment organic matter: Rates and the role of anaerobic processes in the oceanic carbon economy. *Geomicrobiology Journal* 5(3-4),191-237.
- Holzer M. and Hall T. M. (2000) Transit-time and tracer-age distributions in geophysical flows. *Journal of the Atmospheric Sciences* 57, 3539-3558.
- Hunter J. R., Craig P. D., and Phillips H. E. (1993) On the use of random walk models with spatially variable diffusivity. *Journal of Computational Physics* 106, 366-376.
- Jalmke R. A., Emerson S. R., Cochran J. K., and Heggie D. J. (1986) Fine scale distributions of porosity and particulate excess <sup>210</sup>Pb, organic carbon and CaCO<sub>3</sub> in surface sediments of the deep equatorial Pacific. *Earth and Planetary Science Letters* 77, 59-69.
- Jumars P. A., Mayer L. M., Deming I. W., Baross J. A., and Wheatcroft R. A. (1990) Deep-sea deposit-feeding strategies suggested by environmental and feeding constraints. *Phil. Trans. R. Soc. Lond. A* 331,85-101.
- Khatiwala S., Visbeck M., and Schlosser P. (2001) Age Tracers in an Ocean GeM. *Deep-Sea Research* 48, 1423-1441.
- Kinzelbach W. and Uffink G. I. M. (1987) The random walk method and extensions in groundwater modelling. In *Advances in transport phenomena in porous media*, Vol. 128 (ed. J. Bear and M. Y. Corapcioglu), pp. 761-787. Kluwer Academic Publishers.
- LaBolle E. M., Quastel I., and Fogg G. E. (1998) Diffusion theory for transport in porous media: Transition-probability densities of diffusion processes corresponding to advection-dispersion equations. *Water Resources Research* 34(7), 1685-1693.
- Leuschner D. C., Sirocko F., Grootes P. M., and Erlenkeuser H. (2002) Possible influence of Zoophycos bioturbation on radiocarbon dating and environmental interpretation. *Marine Micropaleontology* 46(1-2), 111-L26.
- Loewemark L. and Werner F. (2001) Dating errors in high-resolution stratigraphy: a <sup>14</sup>C X-ray radiograph and AMS-<sup>14</sup>C study of Zoophycos burrows. *Marine Geology* 177, 191-198.
- Meile C. and Van Cappellen P. (2003) Global estimates of enhanced solute transport in marine sediments. *Limnology and Oceanography* 48(2),777-786.
- Meysman F. J. R., Boudreau B. P., and Middelburg J. J. (2003, accepted-a) Relations between local, non-local, discrete and continuous models of bioturbation. *Journal of Marine Research*.
- Meysman F. J. R., Boudreau B. P., and Middelburg J. J. (2003, accepted-b) Why does biological mixing resemble Fickian diffusion? *Journal of Marine Research*.
- Middelburg J. J. (1989) A simple rate model for organic matter decomposition in marine sediments. *Geochimica et Cosmochimica Acta* 53, 1577-1581.

- Middelburg J. J., Soetaert K., and Herman P. M. (1997) Empirical relationships for use in global diagenetic models. *Deep-Sea Research* 144(2),327-344.
- Mulsow S., Boudreau B. P., and Smith J. N. (1998) Bioturbation and porosity gradients. *Limnology and Oceanography* 43(1),1-9.
- Nie Y., Suayah I. B., Benninger L. K., and Alperin M. J. (2001) Modeling detailed sedimentary <sup>210</sup>Pb and fallout <sup>239,240</sup>Pu profiles to allow episodic events: An application in Chesapeake Bay. *Limnology and Oceanography* 46(6), 1425-1437.
- Nixon S. W., Ammerman J. W., Atkinson L. P., Berounsky V. M., Billen G., Boicourt W. C., Boynton W. R., Church T. M., Ditoro D. M., Elmgren R., Garber J. H., Giblin A. E., Jahnke R. A., Owens N. H. P., Pilson M. E. Q., and Seitzinger S. P. (1996) The fate of nitrogen and phosphorus at the land-sea margin of the North Atlantic Ocean. *Biogeochemistry* 35,141-180.
- Risken H. (1989) *The Fokker-PlanckEquation*. Springer.
- Schiffelbein P. (1985) Extracting the benthic mixing impulse response function: a constrained deconvolution technique. *Marine Geology* 64(3-4), 313-336.
- Shull D. H. (2001) Transition-matrix model of bioturbation and radionuclide diagenesis. *Limnology and Oceanography* 46(4),905-916.
- Shull D. H. and Yasuda M. (2001) Size-selective downward particle transport by cirratullid polychaetes. *Journal of Marine Research* 59, 453-473.
- Smith C. R., Pope R. H., DeMaster D. J., and Magaard L. (1993) Age-dependent mixing in deep-sea sediments. *Geochimica et Cosmochimica Acta* 57,1473-1488.
- Soetaert K., Herman P. M. J., Middelburg J. J., Heip C., deStigter H., van Weering T. E. W., Epping E., and Helder W. (1996) Modelling <sup>210</sup>Pb-derived mixing activity in ocean margin sediments: diffusive versus non-local mixing. *Journal of Marine Research* 54(6),1207-1227.
- Tromp T. K., Van Cappellen P., and Key R. M. (1995) A global model for the early diagenesis of organic carbon and organic phosphorus in marine sediments. *Geochimica et Cosmochimica Acta* 59(7), 1259-1284.
- Uffink G. J. M. (1990) Analysis of dispersion by the random walk method. PhD, Technische Universiteit Delft.
- Van Cappellen P. and Gaillard J.-F. (1996) Biogeochemical dynamics in aquatic sediments. In *Reactive transport in porous media*, Vol. 34 (ed. P. C. Lichtner, C. 1 Steefel, and E. H. Oelkers), pp. 335-376. Mineralogy Society of America.
- Visser A. W. (1997) Using random walk models to simulate the vertical distribution of particles in a turbulent water column. *Marine Ecology Progress Series* 158,275-281.



## **CHAPTER 7: A flexible modeling framework for quantitative and objective analysis of aquatic system dynamics <sup>6</sup>**

### **Introduction**

The cycling of many elements on the Earth's surface result from the coupling between a large number of biogeochemical processes. Their dynamics is controlled by complex reaction networks which tightly couple the fate and behavior of many chemical constituents in natural environments. In their full complexity, the quantitative assessment of these coupled multi-component reaction systems requires the use of advanced mathematical models which can only be solved via numerical simulation.

Mathematical models allow for a quantitative implementation of the processes considered important in a given system, and hence, offer intellectual support for deciphering biogeochemical complexity in natural systems. However, large uncertainties remain when it comes to the selection of the most appropriate reaction network, to the mathematical formulation of the processes included and to the parameterization of these processes. These uncertainties upstream of the process of numerical simulation are often a limiting factor for the quantitative understanding of many problems relevant to the geoscientist.

Modern Reaction-Transport Models (RTM) should therefore

- (i) offer means aiming at a reduction of the uncertainty related to the non-unique model structure;
- (ii) include in some way the uncertainty that presently cannot be reduced.

These objectives guided the development of a new modeling environment, the "Biogeochemical Reaction Network Simulator (BRNS)". The BRNS allows for a flexible process selection and formulation, and offers objective means of parameter estimation. Hence, this modeling environment facilitates comparison of competing model structures, and provides optimal integration of measurements into RTMs.

This chapter describes the current status of the BRNS, with focus on the newly incorporated optimization layer. A continuous update on the work in progress is provided at [http://www.geo.uu.nl/Research/Geochemistry/RTM\\_web/index\\_1.htm](http://www.geo.uu.nl/Research/Geochemistry/RTM_web/index_1.htm).

---

<sup>6</sup> Meile, C. and Regnier, P. We would like to acknowledge D. Aguilera for constructive comments and artistic design of Fig. 2 and P. Jourabchi for the formulation of the deep-sea scenario used in the optimization test case.

## General description of the BRNS

The BRNS is a modeling environment in which RTMs can be constructed in a fully automated way. The flexibility of the approach stems from a procedure which allows constructing the corresponding RTM application for any given biogeochemical reaction network.

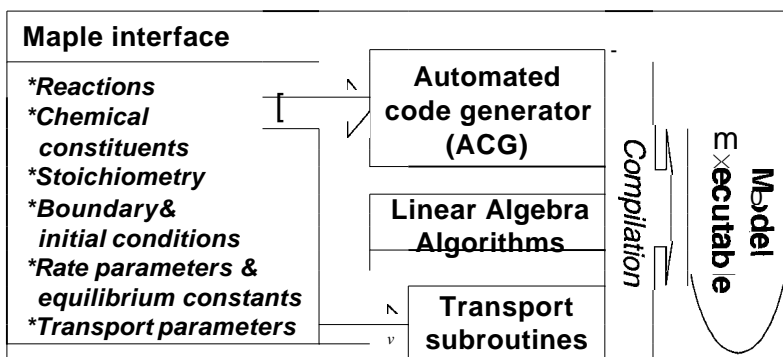


Figure 1. Structure of the BRNS.

The set of equations, which represent the relevant biogeochemical processes included in a reaction network, are defined within the MAPLE symbolic programming environment (CHILAKAPATI, 1995; REGNIER et al., 2002; REGNIER et al., 1997). Within MAPLE, conservation equations for all the chemical constituents pertaining to the reaction network are constructed, and the information necessary for their numerical solution is assembled and processed symbolically. The results, along with additional user-specific information (e.g., parameter values, boundary and initial conditions) are then translated into fully structured FORTRAN code, combined with generic transport routines and linked to standard linear-algebra solvers (Fig. 1). All symbolic programming operations and their translation into FORTRAN have been combined into a MAPLE binary library called ACG (short for Automated Code Generator). Hence, model construction and simulation from within the BRNS requires no prior knowledge of programming or numerical procedures from the user, and therefore facilitates quantitative process oriented studies.

## Objective Data Analysis

Mathematical formulations of biogeochemical reaction rates involve many model parameters that must be constrained experimentally. Examples of such parameters are rate constants, their temperature dependence, and half saturation constants or inhibition functions. Due to inherent difficulties in experimental setup, differences between laboratory and field conditions, or lack of a fundamental understanding of the natural system, model parameters are only known approximately. It may therefore be desirable to constrain these parameters to the maximum extent possible by taking full advantage of the available measured data.

This objective has been achieved using the following strategy (Fig. 2): Forward RTMs produce synthetic data which can be compared to measurements. Using optimization techniques, parameters are then adjusted to systematically improve the fit between modeled and measured data. As the selection of parameters to be optimized is user-selectable from within the BRNS, it takes full advantage of its flexible structure.

A variety of optimization algorithms have been implemented and tested, both with a set of synthetic functions and with a RTM application representative of early diagenesis in deep sea sediments. In what follows, the general structure of the forward RTM is outlined, the optimization procedures are described and the results for the optimization test cases are discussed.

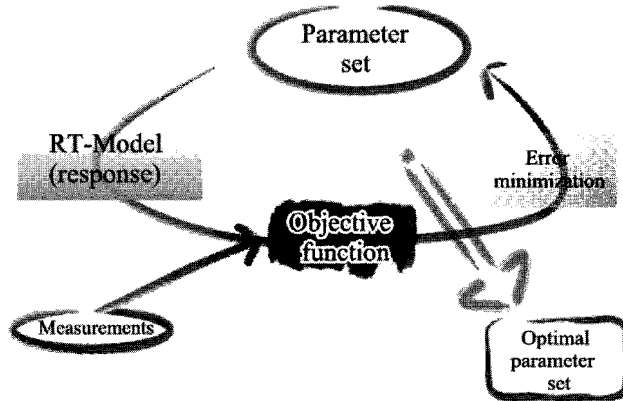


Figure 2. Scheme of the optimization procedure.

### Forward RTM

The temporal and spatial evolution of  $m$  chemical constituents undergoing transport and reaction can be described by a set of conservation equations of the form:

$$\frac{\partial C_j}{\partial t} = T_j + R_j, \quad (j=1, \dots, m) \quad (1)$$

where  $t$  is time,  $T$  is the transport operator and  $R$  represents the sum of reactions affecting a substance  $j$  of concentration  $C$ .

Physical transport in aquatic systems typically encompasses advective and diffusive processes. A general one-dimensional form of  $T$  is written as:

$$T_j = \frac{1}{\xi(x)} \left[ \frac{\partial}{\partial x} \left( D(x) \cdot \xi(x) \cdot \frac{\partial C_j(x,t)}{\partial x} \right) - \frac{\partial}{\partial x} (v(x) \cdot \xi(x) \cdot C_j(x,t)) \right] \quad (2)$$

with

$$\xi(x) = \begin{cases} \text{solids: } (1 - \phi(x)) \cdot A(x) \\ \text{solute: } \phi(x) \cdot A(x) \end{cases}$$

$$D(x) = \begin{cases} \text{solids: } D_b(x) \\ \text{solute: } D_b(x) + D_{di,p}(V(x)) + D_{sed}(\phi(x)) \end{cases}, \text{ and}$$

$$v(x) = \begin{cases} \text{solids: } w(x) \\ \text{solute: } v_{flow}(x) + w(x) \end{cases}$$

In Eq. 2,  $C$  is the concentration of solutes or solids in mass per fluid volume or solid volume, respectively and  $\phi$  is the porosity [-].  $v$  and  $w$  are velocities [ $L T^{-1}$ ]. As  $w$  is a generic

advection velocity acting upon both solids and solutes, it may represent a moving reference frame.  $D_b$ ,  $D_{disp}$  and  $D_{sed}$  all formally represent diffusion coefficients [ $L^2 T^{-1}$ ]. In the current version of the BRNS,  $D_{sed}$  is (internally) defined as  $D_{mol} / (1 - \ln(\phi^2))$ , and  $D_{disp}$  is calculated from flow velocity  $v_{flow}$  and longitudinal dispersivity  $\alpha$  [ $L$ ]:  $D_{disp} = \alpha_L \cdot |v_{flow}|$ .  $A$  is a cross section area [ $L^2$ ], normal to the x-direction, which may change over the spatial domain. The coefficients  $A$ ,  $\phi$ ,  $D_b$ ,  $D_{mol}$ ,  $\alpha_L$ ,  $w$ , and  $v_{flow}$  can all be derived as a function of space.

For a sediment application,  $A$  is set to one,  $D_b$  represents the bioturbation coefficient and  $D_{sed}$  is the in situ molecular diffusion coefficient corrected for tortuosity (BOUDREAU, 1997).  $D_{mol}$  is the molecular diffusion coefficient at in situ temperature and salinity and  $w$  is the sedimentation velocity. In many cases  $v_{flow}$  is close to 0, and setting  $\alpha_L$  to 0 results in ignoring dispersion ( $D_{disp} = 0$ ). Alternatively, in a groundwater flowpath model,  $D_b$  can be set to 0,  $D_{mol}$  may be negligible,  $w$  is 0,  $v_{flow}$  is the fluid flow velocity and  $\alpha_L$  has to be set to the appropriate, scale-dependent value of the dispersivity. In a simulation of an estuary along its longitudinal curvilinear axis,  $A$  is set to 1 and a proper choice of  $A$  and  $v_{flow}$  allows for an implementation of fluid flow. Eddy diffusivities may be implemented through the *Db-term*.

Generally, the reaction term depends on more than one species of the reaction network. Through this coupling, most multi-component problems result therefore in sets of coupled nonlinear PDEs, which have to be solved simultaneously. In most cases, no analytical solutions are available for such problems and one has to resort to discretized approximations of the partial differential equations along a spatio-temporal gridded domain.

## Numerical solvers

The discretized form of Eq. 1 can be expressed with the operators evaluated either at the current time or at the previous time. This is referred to as implicit or explicit solution procedure. Using a Euler time-discretization, one may write

$$\frac{C^{k+1} - C^k}{\Delta t} = \alpha(T^{k+1} + R^{k+1}) + (1 - \alpha)(T^k + R^k), \quad (3)$$

where  $k$  is the time index and  $\alpha$  [0-1] is a weighting parameter, which leads to an implicit ( $\alpha=1$ ), Crank-Nicholson ( $\alpha=0.5$ ) or explicit ( $\alpha=0$ ) formulation of the problem.

## Transient simulations

Reaction networks generally involve coupled, nonlinear rate laws operating over a wide spectrum of time scales. The high degree of stiffness and nonlinearity of the resulting equations generally require implicit numerical schemes for their solution. However, the matrices resulting from the spatio-temporal discretization of the full set of PDEs can become prohibitively large for implicit, simultaneous numerical solution of the transport and reaction operators (YEH and TRIPATHI, 1989). The solution procedure implemented in the BRNS, an alternative to such one-step methods, is Operator splitting (OS), which handles the transport and reaction terms sequentially (STEEFEL and MACQUARRIE, 1996) and hence takes advantage of the additive nature of the operators  $T$  and  $R$ . The separation of  $T$  and  $R$  allows the numerical solution to be tailored to the properties of the individual operators, which can speed up computation significantly.

The formal separation of reaction and transport processes induces error into the solution of the governing equations. Indeed, if transport precedes the reaction step, a substance entering the model domain will be transported during a finite amount of time before it undergoes reaction. The error induced by OS depends therefore on the time step of integration as well as

on the order of the operators (BARRY et al., 1996; KAWARACHCHI and MORSHED, 1995; MORSHED and KALUARACHCHI, 1995). This error may be evaluated for simple problems by comparison with analytical solutions. However, for more complex cases, comparison between different numerical solutions is necessary. This can be done by decreasing the size of the integration time step or by comparing OS results to one-step approaches, which are not subject to this type of error. One may also compare results using different operator splitting strategies. In the BRNS, two operator splitting methods are implemented: The Sequential Non-Iterative Approach (SNIA) and Strang splitting (STEEFEL and MACQUARRIE, 1996). In the former, the transport step precedes reaction, each computed for the entire time step, while in Strang splitting, half a timestep of transport is followed by a full reaction timestep and the remaining half of the transport. Such an embedding of the reaction part into transport is likely to reduce the operator splitting error at a relatively low computational cost, since solving the reaction step is by far the most time consuming operation (see below).

### Transport

The PDEs are essentially uncoupled in the transport operator (see Chapter 1). Hence, they can be solved for each constituent separately, which results in solving  $m$  separate problems of size  $n$ , where  $n$  is the number of spatial nodes. The transport part of Eq. 1,  $\frac{\partial C_j}{\partial t} = T_j$ , is approximated using finite differences. The discretized transport equation for each constituent  $j$  can be recast into matrix form:

$$M \cdot C_j^{new} = d \quad (4)$$

where  $M$  is the tridiagonal transport matrix,  $d$  is a vector depending on the concentration at the previous timestep and  $C_j$  is the concentration vector of a constituent  $j$  extending over the spatial domain. Hence, solving for the new concentration profile only involves inversion of a tridiagonal system (PRESS et al., 1992):

$$C_j^{new} = M^{-1} \cdot d \quad (5)$$

The boundary conditions currently implemented are known concentrations, known concentration gradients or known local (diffusive and advective) fluxes. Further details on the implementation are given in the Appendix.

In order to resolve details in certain parts of the model domain without wasting computational resources, a scheme allowing for a spatially variable grid has been implemented (see Appendix for details). The scheme does not support radically changing grid spacing over short distances. The spatial discretization is preferably done through a coordinate transformation, e.g.  $x' = a_j \sin(a_z + aJx)$ , where  $x'$  and  $x$  are the transformed and the equally spaced grid coordinates and  $\alpha$  are transformation coefficients (NoYE, 1984).

### Reaction

Using OS, the reaction part can also be simplified significantly as reactions can be viewed as local phenomena depending only on the concentrations of chemical species within a given representative elementary volume. The reaction part of the problem can be represented as a series of batch reactors, operating independently at each node of the spatial domain. Therefore, OS reduces to a problem of solving  $n$  times a reaction network of size  $m$ , formulated as a set of coupled ODEs (rather than PDEs). A fully implicit formulation of the reaction part of Eq. 1 leads to the following problem:

$$f_j \equiv R^{k+1} - \frac{C_j^{k+1} - C_j^k}{\Delta t} = 0; j = 1, m \quad (6)$$

This expression defines the function residuals  $f_j$ , a set of functions which have to be zeroed. The task at hand is therefore to find the values of  $C_j^{k+1}$  fulfilling this condition. This is a nonlinear multidimensional root finding problem which can be solved using the Newton-Raphson (NR) method. The NR method makes use of a Taylor Series expansion *off*,

$$if(C + \Delta C) = if(C) + \sum_{i=1}^m \frac{\partial f_i(C)}{\partial C_i} \cdot \Delta C_i + O(\Delta C^2) \quad (7)$$

Neglecting the terms of  $O(\Delta C^2)$ , the reaction problem can be recast into matrix form according to:

$$J \cdot \Delta C = -i \quad (8)$$

where  $i$  is the vector of function residuals of length  $m$  and  $J$  is the Jacobian matrix consisting of the partial differentials of  $i$  with respect to the different chemical components (STEEFEL and MACQUARRIE, 1996):

$$J = \begin{bmatrix} \frac{\partial f_1}{\partial C_1} & \dots & \frac{\partial f_1}{\partial C_m} \\ \vdots & \ddots & \vdots \\ \frac{\partial f_m}{\partial C_1} & \dots & \frac{\partial f_m}{\partial C_m} \end{bmatrix} \quad (9)$$

The update vector  $\Delta C$  is obtained by matrix inversion,  $\Delta C = \Gamma^{-1}(-i)$ , which is implemented as LU-decomposition (PRESS et al., 1992). In an iterative procedure, the concentrations are updated,  $\bar{C}_{new} = \bar{C}_{old} + \Delta \bar{C}$ , where subscripts *new* and *old* are iteration indices, until it is sufficiently close to 0.

The Newton-Raphson root finding method is based on a local linearization of the problem. This is efficient for local searches, but nevertheless may fail depending on the topography of the function(s) for which the root is to be determined (e.g., cyclic non-convergence, shooting off; (PRESS et al., 1992)). When the Newton step  $\Delta \bar{C}$  is large, the local linearization at  $\bar{C}_{old}$  may be a poor approximation after e.g., half of  $\Delta \bar{C}$  has been taken. It is possible that at this point, not only the suggested step size is different, but that the Newton direction may be significantly different. Loosing the advantage of a local linearization due to a changing topography within a single concentration update can be partially remediated by using a relaxation factor, which limits the individual iteration stepsize to a fraction of the Newton step. As an alternative, to take fuller advantage of the local linearization, a combination of the Newton-Raphson with a line search method has been implemented (PRESS et al., 1992). Close to the starting point, the linear approximation points towards lower values of the function residuals, i.e. the direction of the iterative improvement of the solution is locally correct. Therefore, the line search backtracks along the Newton-direction if the full Newton step leads to a position whose functional value is worse than the previous one. Note however that both relaxation and combination with line search can not guarantee the success of the root finding procedure in all cases.

In MAPLE, the function residuals and Jacobian matrix are automatically assembled from the rate expressions (or equilibrium constraints) forming a reaction network. The MAPLE preprocessor combines mixed kinetic and equilibrium expressions into a DAE system using Gauss-Jordan elimination. The advantage of this method is that it minimizes the size of  $\underline{J}$  for a given reaction network. The Jacobian matrix and function residuals required in the Newton algorithm are then translated into fully structured FORTRAN code taking advantage of the MACROFOR package (GOMEZ, 1990). Detailed examples of the automated procedure are given in (REGNIER et al., 2002).

### Steady State Solver

Steady state solutions are often of interest, either because the system is truly at steady state or because an educated guess for unknown initial conditions is required. It is possible to run a transient simulation to a steady state, but this procedure has the disadvantage that the slowest changing component is determining the time it takes to reach steady state. This may lead to long simulation times, which are particularly prohibitive when combined with computationally demanding optimization procedures. To remediate this situation, an approximate, iterative steady state solver has been implemented.

At steady state, the derivative of  $C_j$  with respect to time is zero:  $\frac{\partial C}{\partial t} = 0 = T_j + R_j$  such that

$T_j = -R_j$ . Similar to the transient case, the transport term is recast into a tridiagonal matrix form (Eq. 4). However, in contrast to the transient solver, the reaction term is implemented here in an explicit fashion. The reaction rates are calculated from the known (old) concentrations,  $R_j = R(C_{old})'$  a strategy which avoids the iterative root-finding procedure.

The solution of the resulting system of equation,  $M \cdot C_{j,n,w} = d - R(C_{old})'$  only requires inversion of a tridiagonal matrix for each constituent  $j$ .

The explicit formulation of the reaction term may cause this scheme to fail. An improved approximation of  $R$  at the current iteration therefore proposed:

$$R_{new} \approx R(C_{old}) + \left. \frac{dR}{dC} \right|_{old} (C_{new} - C_{old}) \quad (10)$$

which corresponds to a linear approximation of the rate along the direction of the constituent to be solved for. This approach leads to an improved estimate of  $R$  if the component  $C$  exerts a strong feedback on its own dynamics, but only slightly increases the computational cost. Combining transport and reaction, the new concentration vector can be obtained from inversion of the following tridiagonal system:

$$C_{new} = \left( M + \mathbf{1}, \frac{dR}{dC} \right) \mathbf{I} - \mathbf{I} (R(C_{old}) + \frac{dR}{dC} \cdot C_{old}) \mathbf{I}, \quad (11)$$

where the LHS and the last parenthesis on the RHS are vectors of length  $n$ , and  $\mathbf{I}$  is the identity matrix ( $n \times n$ ). Eq. 11 is solved in sequence for each component and embedded into an iterative loop (Fig. 5). Simulations are run until convergence is achieved, i.e. until  $C^{new} \approx C^{old}$ .

The steady-state solver has been implemented within the ACG, which computes automatically the required rate and derivative information  $(R(C^{old}), \frac{dR}{dC} \big|_{C^{old}})$ . If the derivative

of  $R$  with respect to  $C$  is a function of  $C$ ,  $C^{old}$  is being used. Currently, only kinetic reaction formulations can be used in this procedure. Equilibrium reactions are recast into kinetic expressions using the principle of microscopic reversibility (LASAGA, 1998; STEEFEL and MACQUARRIE, 1996).

## Optimization

The general objective of optimization is to constrain poorly known model parameters by making use of available measurements. To that purpose, an optimization layer, which encapsulates the forward RTM described above, has been implemented (Fig. 2). As parameter optimization is based on a comparison between measured and calculated data - the latter depending on parameter values - many forward RTM runs are required to determine their optimal values. After each forward simulation, the parameters are adjusted and the operation is repeated until the misfit between measurements and calculated data is sufficiently small to meet user-defined convergence criteria.

In general, the number of parameters to be optimized ( $nap$ ) is smaller than the total number of model parameters, either because some are already well known (e.g., molecular diffusion coefficients), or simply because optimization over a large number of parameters is computationally too expensive. The choice of the parameters to be optimized is a matter of experience and is left to the user. This is however a crucial step, as it is a priori difficult to assess whether or not model results vary similarly with changes in different parameters (BRUN et al., 2001).

The quality of the model parameterization is based on a comparison between calculated and measured concentrations. For each forward RTM simulation, the quality of the parameterization is quantified by the scalar objective function,  $OF$ . It consists of a summation of the misfit between calculated and measured values at each time and position where measurements are available and is defined as:

$$OF(\mathbf{p}) = \sum_{x,t,j} \left( \frac{y - y(\mathbf{p})}{\sigma} \right)^2 \quad (12)$$

where  $\mathbf{p}$  is the entire parameter set, including the  $nap$  parameters to be optimized,  $y$  is the measured value and  $y(\mathbf{p})$  is the calculated concentration of species  $j$  at time  $t$  and position  $x$  of measurement. To match the exact location,  $y(\mathbf{p})$  is interpolated with natural splines from the gridded domain to the position of the measurement.  $\sigma$  is the standard deviation associated with a measurement. If no error estimates are available for species  $j$ ,  $\sigma$  can be defined as the average concentration of the species over the whole spatial domain at the time of measurement. Scaling by  $\sigma$  is essential to avoid dominance of the objective function by one single species when species concentrations differ by orders of magnitude.

The parameters subject to optimization and the data files containing the measurements are specified in the MAPLE interface. Hence, this approach takes full advantage of the flexibility of the BRNS and extends its domain of applicability.

### The optimization schemes

There exist many strategies for minimization of the objective function (e.g., (BLIEK et al., 2001; GILL et al., 1981; OSBORNE, 1985)). Here, four methods for unconstrained optimization have been implemented:

- Downhill Simplex (DS)
- Levenberg-Marquardt (LM)
- Simulated Annealing (SA)



- Differential Evolution (DE)

DS and LM are local procedures while SA and DE are global schemes. The fundamental difference between local and global optimization algorithms is that the local schemes may fail in finding a global minimum in the OF if there exists a local minimum near their starting point. Global optimization strategies aim at overcoming this problem, but are computationally more expensive. In what follows, the four optimization procedures are briefly summarized.

### Downhill Simplex

In the Downhill Simplex approach (NELDER and MEAD, 1965), the topography of the  $OF$  is mapped by evaluating its value for  $n_{opt}+1$  parameter sets. The first set  $P_0$  contains, apart from the known parameters, the initial guesses for the  $n_{apt}$  parameters to be optimized. In the other  $n_{opt}$  parameter sets, the adjustable values are slightly perturbed one by one:  $P_i = (1 + \lambda e_i)P_0$ , where  $e_j$  is a unit vector in the  $i^{th}$  direction and  $\lambda$  is a perturbation factor. These  $n_{opt}+1$  sets hence define the initial vertices, which together form a geometrical figure called simplex. During optimization, the simplex is systematically modified to ooze towards a parameter set with a corresponding minimum value of the objective function. It is altered during optimization by reflection (Fig. 4A), reflection and expansion (Fig. 4B), contraction in one dimension (Fig. 4C) and contraction among all dimensions towards the low point (Fig. 4D). Further details are given in (PRESS et al., 1992).

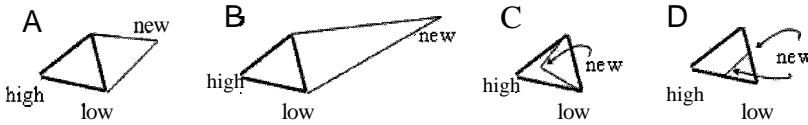


Figure 4. Movements of a two dimensional simplex during minimization. High / low indicates the value of the objective function associated with a vertex.

### Levenberg-Marquardt

The Levenberg-Marquardt algorithm is an iterative nonlinear least-square minimization which combines the Newton procedure with a steepest-descent search (PRESS et al., 1992). In contrast to all other schemes presented here, the minimization process is guided by information on the gradient directions of the  $OF$  with respect to the parameters. This property makes LM the most efficient search method, albeit it may fail if the initial guess is not close enough to the minimum.

LM is based on a quadratic approximation of the objective function (FINSTERLE, 1999):

$$OF(p^{new}) \approx OF(p^{old}) + g^T \Delta p + \frac{1}{2} \Delta p^T H^T \Delta p \quad (13)$$

where  $\Delta p = p^{new} - p^{old}$ .  $g$  is the  $OF$  gradient vector,  $H$  is the Hessian matrix, which contains information on the curvature of the local  $OF$  topography, and the superscript  $T$  indicates transposition.

Combining Eqs. 12 and 13,  $g$  and  $H$  can be written as (FINSTERLE, 1999):

$$g = -2J^T K^{-1} (\tilde{y} - \tilde{y}^J) \quad (14)$$

$$H = 2(J^T K^{-1} J + B)$$

where  $\mathbf{K}$  is the covariance matrix, whose diagonal elements consist of the measurement variances  $\sigma^2$  and is 0 elsewhere.  $\mathbf{J}$  is the Jacobian matrix whose elements are defined as  $j_{ik} = \partial \tilde{y}_i / \partial p_k$ . Hence,  $\mathbf{g}$  depends on the misfit between measurements and calculated values, weighted by the sensitivity of the calculated concentrations towards the adjustable parameters. The matrix  $\mathbf{B}$  is defined as

$$\mathbf{B} = \sum_{meas} \left( \frac{y - \tilde{y}}{\sigma^2} \cdot \nabla^2 \left( \frac{y - \tilde{y}}{\sigma} \right) \right) \quad (15)$$

At the minimum of the  $OF$ , locally approximated by Eq. 13,  $OF(p_{new})$  equals  $OF(p_{old})$ . Hence, gradient and second derivative terms in Eq. 13 must cancel each other (second and third terms on the RHS of Eq.13, respectively). After substitution of Eq. 14 into Eq. 13 one obtains the parameter update vector:

$$\Delta \mathbf{p} = (\mathbf{JTK} - \mathbf{I} + \mathbf{B})^{-1} \mathbf{J}^T \mathbf{K}^{-1} \left( \mathbf{y} - \tilde{\mathbf{y}} \right) \quad (16)$$

The Jacobian matrix can be computed by finite difference approximation using small perturbations of the  $n_{op}$  parameters to be optimized. This requires  $n_{op} + 1$  runs of the forward RTM.

Various gradient-based optimization methods can be derived using different approximation of matrix  $\mathbf{B}$ . For instance, setting  $\mathbf{B} = \mathbf{0}$  results in the Gauss-Newton method, which has quadratic convergence when the parabolic is appropriate (Eq. 13). Alternatively,  $\mathbf{B}$  may be approximated by  $\lambda \cdot \mathbf{I}$ . ( $\mathbf{JTK} - \lambda \mathbf{I}$ ), where  $\lambda$  is a factor which increases diagonal dominance. For  $\lambda \rightarrow \infty$ , the steepest-descent algorithm is obtained. This algorithm is less error prone than the Gauss-Newton method far from the minimum, but exhibits poorer convergence characteristics. In the LM algorithm,  $\lambda$  is dynamically adjusted, adapting the minimization strategy to the progress of the optimization. Figure 5 describes the algorithm implemented (CAVALIER, 2001; PRESS et al., 1992):

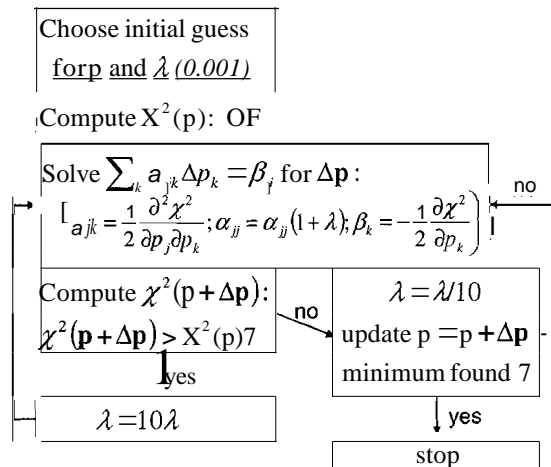


Figure 5. Levenberg-Marquardt algorithm

### *Simulated Annealing*

Simulated Annealing is a global optimization technique which can deal with discontinuous objective functions (METROPOLIS et al., 1953). In SA, the key feature is to occasionally allow for exploration of regions with  $OF$  values larger than the ones encountered so far. Hence, SA is not restricted to the local neighborhood of the starting point and is in theory able to explore the entire solution domain. The implementation of this algorithm requires selection of a probability to accept "uphill moves" and definition of how this probability changes during optimization. By analogy to a slow cooling process in material sciences, these two criteria are referred to as "starting temperature",  $T_0$ , and "cooling schedule", respectively. Intuitively, a high acceptance rate of uphill moves is desirable at the beginning of the optimization in order to minimize the likelihood that only local minima near the starting point are found. As the algorithm explores the solution space further, the probability of accepting parameter sets with higher objective function values than the minimum found so far should decrease to allow for the accurate determination of the minimum.

In the BRNS,  $T_0$  is chosen such that initially about 80% of the uphill moves are accepted (VAN LAARHOVEN and AARTS, 1987). The starting temperature is chosen such that  $e^{-\Delta OF/T_0} = 0.8$ , where  $\Delta OF$  is the average difference between the objective functions corresponding to the unperturbed and the perturbed initial parameter sets, as defined in the DS section above. Using a truncated series expansion of  $e^{-\Delta OF/T_0}$  leads to  $T_0 \approx 5\Delta OF$ . Therefore, the selection of  $T_0$  requires that the user-selectable parameter perturbation  $\lambda$  is large enough to guarantee significant differences in the associated objective function values. This is important to achieve a sufficiently large search space. The probability to accept uphill moves is progressively lowered, in such a way that the algorithm never spends more than a finite amount of time (typically 10% of the maximum allowed iterations) at a given temperature. Here, the new temperature, corresponding to a lower probability of accepting uphill moves, depends on the ratio of the number of function evaluations performed so far ( $it$ ) to the total number of iterations ( $itmx$ ):  $T_{new} = T_{old}(1 - it/itmx)^\alpha$ . The exponent  $\alpha$  determines the cooling speed, and by default is set to 2. Large values of this coefficient lead to slow cooling speed.

Selection of appropriate starting temperature and cooling schedule are subject of debate (e.g., (BOHACHEVSKY et al., 1995; BOHACHEVSKY et al., 1986; CARDOSO et al., 1996; FORBES and JONES, 1990; JONES and FORBES, 1995; PARK and KIM, 1998)). For poor choices of these criteria, SA may not be an efficient technique. Hence, in the BRNS, SA is combined with the Downhill Simplex method, according to the procedure proposed in (PRESS et al., 1992).

### *Differential Evolution*

Differential Evolution is a global optimization algorithm applicable also to nonlinear and non-differentiable continuous functions (STARN and PRICE, 1995). DE belongs to the class of genetic algorithms (GA), which involve random combinations of trial parameter sets. In the terminology of GA, these combinations are named mutation and crossover. Initial parameter sets, called populations, are selected randomly from within a bound range. New parameter sets, forming the next "generation", are obtained by random recombination of the old populations. The procedure can however be biased towards the fittest population (*Phesl*):

$$\mathbf{p}_{i,G+1} = \mathbf{p}_{best,G} + F \cdot \sum (\mathbf{p}_{r_i,G} - \mathbf{p}_{r_{i+1},G})$$

(17)

or

$$\mathbf{P}_{i,G+1} = \mathbf{P}_{i,G} + F \cdot \sum (\mathbf{p}_{r_i,G} - \mathbf{p}_{r_{i+1},G}) + \lambda \cdot (\mathbf{p}_{best,G} - \mathbf{p}_{i,G})$$

where  $\mathbf{P}$  is the parameter set (population),  $G$  is the generation index, "best" indicating the fittest population as measured by the minimum value of the  $OF$ .  $r_i$  is a random variable selecting the populations from which the new generation is created and  $i$  determines the number of populations from which a new population is generated. It is typically set to 1, a value which results in a combination of two or three randomly selected population with the best one.  $F$  is a factor which amplifies the difference between  $\mathbf{p}_{r_i,G}$  and  $\mathbf{p}_{r_{i+1},G}$ , while  $\lambda$  is a greediness factor, which biases the new generation towards the fittest population. To limit the number of control parameters,  $\lambda$  is typically set equal to  $F$ . The new parameter set replaces its predecessor if fitness, measured by the value of the objective function, is improved. Other control settings are number of populations, typically set to 10 times the number of parameters to be optimized, and the number of generations evaluated.

The algorithm exhibits good convergence properties and in many instances is not very sensitive to the user-defined control settings (STORN and PRICE, 1996). In order to be successful, it is however crucial that the global minimum lies within the range of the parameters from which the population vectors are randomly selected. In our case, the range is by default assumed to be within one order of magnitude around the values of the initial parameter profile. Random selection from within this range is based either on a uniform or log-uniform distribution of the parameters.

### Stopping conditions

The optimization process requires the implementation of convergence criteria, which determine when to stop the procedure. Two criteria are proposed here. The first one is related to the progress of the optimization: the process is halted if the difference between best and worst  $OF$  values in the current parameter sets - or current and previous set in the case of LM - is smaller than  $\epsilon_1$ , typically set to  $10^{-6}$ :

$$2 \cdot \frac{|OF_{worst}| - |OF_{best}|}{|OF_{worst}| + |OF_{best}|} < \epsilon_1$$

(18)

The second criterion relates the fit between calculated and measured concentrations to the number of measurements and adjustable parameters. Assuming independent and normally distributed random measurement errors, the  $OF$  follows a  $\chi^2$ -distribution (Eq. 12 with  $\sigma$  as standard deviation). The probability that the observed mismatch between measurements and calculated values for the correct model parameters is less than  $\chi^2$  is given by (CAVALIER, 2001; PRESS et al., 1992):

$$P(\chi^2 | \nu) = \frac{1}{\Gamma(\nu/2)} \int_0^{\chi^2/\nu} e^{-t} t^{\nu/2-1} dt < \epsilon_2$$

(19)

where  $\nu$  represents the degree of freedom, i.e.  $\nu = \text{number of measurements} - \text{number of adjustable parameters}$ . Optimization is stopped when  $P$  is smaller than  $\epsilon_2$ , typically set to  $10^{-3}$ .

## Application of optimization algorithms

### Synthetic objective functions

Performance and possible shortcomings of the optimization algorithms are evaluated by running several test cases of increasing complexity. In order to validate the algorithms, all cases are based on synthetic data. In this section, the objective of the simulations is to determine the accuracy and the potential of the various procedures to find known minima, rather than accurately benchmarking their respective execution speed.

Three test cases involve functions of a single parameter, the fourth one depends on two parameters and the last one consists of a realistic RTM application.

#### *Functions of a single parameter*

The *OF* is defined by the value of the selected functions, i.e.,  $OF = f(x)$ , where  $x$  is the parameter to be optimized. Hence, the *OF* is not based on a comparison between "measured" and calculated data and therefore differs from the *OF* as defined in Eq. 12. For all test cases, each algorithm is executed twice, once starting from the right and once from the left side of the global minimum. The initial guesses  $x_{start}$  are set to 3 and -0.5, respectively. Rather than an initial parameter value, DE requires specification of the range within which to search for the minimum. It is set to  $\pm 10$ .

*Parabola.* The first test case consists of finding the minimum of  $f(x) = (x-2)^2$ . All optimization procedures converge to the minimum value at  $x = 2$ , independent of the starting point.

*Modified Parabola.* The second test case (Fig. 6A) consists of a parabola upon which a sinusoidal perturbation is superimposed:  $f(x) = 0.3x^2 + 3\sin(x)$ . This function has two minima within the range  $\pm 10$ : The global minimum at -1.33 and a local minimum at +3.83. The two local optimization procedures (OS and LM) end up in the local minimum when starting at  $x = 3$ , but successfully reach the global minimum when starting at -0.5. Irrespective of the starting point, both global optimization schemes (SA and DE) find the global minimum.

*Many local minima.* In the third test case (Fig. 6B), the objective function is defined as  $f(x) = x\sin((x-0.7)^{-1})$ . This function exhibits a large number of narrow minima between 0.2 and 1, with the global minimum located at  $x = 0.91$ . When starting from the left of the minima at  $x = -0.5$ , the OS converges to the first minimum encountered near 0.254. When starting from the right side at  $x = 3$ , both DS and LM shoot off towards infinity. In contrast to the local minimization algorithms, DE is able to find the global minimum at  $x = 0.91$  in many instances. However, as this scheme uses random selection, the algorithm occasionally ends up in one of the many local minima between 0.6 and 0.8. Using the default control settings implemented in SA, this algorithm fails to find the global minimum. It either converges to the local minima adjacent to the starting position (i.e.  $x \rightarrow \infty$  and  $x = 0.25$ , as does the DS), or to one of the many local minima between 0.2 and 0.8. However, when the number of iterations is increased and the probability of accepting uphill moves is raised, SA recovers the global minimum.

### Function of two parameters

The fourth test case (Fig. 6C) consists of the Rosenbrock saddle:  $f(x_1, x_2) = 100(x_2 - x_1^2)^2 + (1 - x_1)^2$ . This function requires optimization of the two parameters  $x_1$  and  $x_2$ . The global minimum is located at  $(x_1, x_2) = (1, 1)$ . In addition, this function exhibits also several local minima. The search algorithms are started at  $(2, 2)$ ,  $(2, -2)$ ,  $(-2, 2)$  and  $(-2, -2)$ . DS finds the global minimum from all starting points, while LM never recovers the global minimum. Depending on the starting point, this algorithm ends up at a local minimum near  $(\pm 2, 4)$ . Within the allotted maximum number of iterations, DE only finds the global minimum when the search range for both parameters is restricted between 0 and 2. When this range is increased to  $\pm 10$ , only local minima are recovered. SA finds the global minimum in all instances.

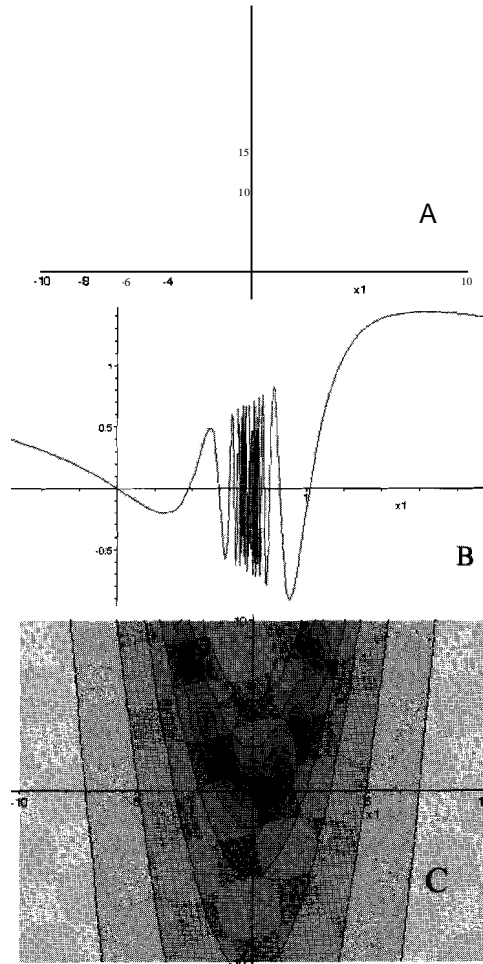


Figure 6. Topography of the synthetic test functions. In panels A and B, the x-axis represents the parameter values and the y-axis the value of the OF. In panel C, parameter values are plotted on the x- and y-axes. The OF value is represented by contour lines and dark colors indicate low values of the function. The function is quite flat, and to better depict the topography of the OF, the logarithm of the function values is used.

Case 2 and 3 reveal that local optimization algorithms may get trapped in local minima. In case 4, DS finds the global minimum because of a fortunate perturbation of the initial parameter profile. However, no general conclusion regarding the properties of the DS algorithm can be drawn from these results. Case 3 demonstrates a shortcoming of the LM algorithm, which falls back onto its starting value if  $x_{start}$  is below 0.04. Below this value, both first and second derivatives of  $f$  with respect to  $x$  are negative which leads to an update vector pointing towards more negative values (Fig. 5). However, the updated position is associated with an increased  $OF$  value, and the trial point is therefore rejected. Subsequently,  $\lambda$  is increased, which results in smaller and smaller step sizes until the stopping criterion is met. This illustrates that the parabolic approximation of the  $OF$  in the LM algorithm may cause the optimization to fail if the starting point is not sufficiently close to the minimum. Cases 3 and 4 show that the success of global schemes may depend on the values of the control parameters tuning the search progress. Nevertheless, DE and SA are the methods of choice for problems with poorly constrained initial parameter guesses or with complex topographies of the  $OF$ .

### RTM application

In this section, the various search algorithms are tested on a multi-component reactive transport problem. This application consists of an early diagenetic model for marine deep-sea sediments. The reaction network involves the species  $O_2$ ,  $NO_3^-$ ,  $HCO_3^-$ ,  $CO_3^{2-}$ ,  $CO_2$ ,  $H^+$ ,  $C_{org}$ ,  $NH_4^+$ ,  $SO_4^{2-}$ ,  $Mn^{2+}$ ,  $MnO_2$ ,  $Fe^{2+}$ ,  $Fe(OH)_2$ ,  $H_2S$  and  $HS^-$ . The reactions considered are degradation of organic matter using  $O_2$ ,  $NO_3^-$ ,  $MnO_2$ ,  $Fe(OH)_2$  or  $SO_4^{2-}$  as terminal electron acceptors. Secondary redox reactions are also implemented following (WANG and VAN CAPPELLEN, 1996). In addition to these kinetic processes, equilibrium expressions (acid-base reactions for dissolved carbonate and sulfide species) are included in the reaction network. In the early diagenetic model, transport is due to burial, molecular diffusion and bioturbation. The conservation equations (Eq. 1) are subject to the following boundary conditions: No concentration gradient at depth for all species and either Dirichlet (fixed solute concentrations) or Robin (fixed solid fluxes) condition at the sediment-water interface (SWI).

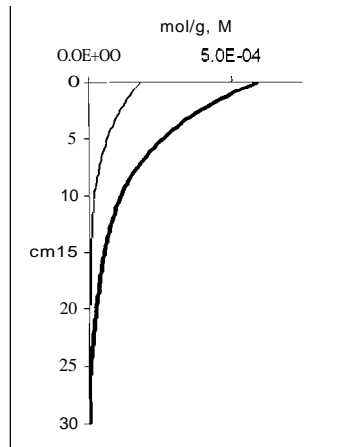


Figure 7.  $O_2$  (thin line) and  $C_{org}$  (thick line) concentration profiles used as proxy for measured data. The profiles are calculated using  $k = 3 \cdot 10^{-3} \text{ yr}^{-1}$  and  $F = 2 \cdot 10^{-6} \text{ mol cm}^{-1} \text{ yr}^{-1}$

The modeled steady state  $O_2$  and  $C_{org}$  depth distributions (Fig. 7) are taken as target profiles for the optimization procedure. These synthetic profiles play the role of the measured data. Two parameters, the first order rate constant for organic carbon degradation  $k$ , and the flux of organic matter at the SWI,  $F$ , are selected as the parameter set to be optimized. The initial parameter guesses in the optimization are set one order of magnitude lower than the values used to construct the target profiles.  $k$  and  $F$  are then optimized to reproduce the synthetic concentration profiles of  $O_2$  and  $C_{org}$ , assuming 5% "measurement error" as an estimate of  $\sigma$ .

All optimization routines converge towards the parameter values used to construct the target profiles. However, they differ in their search progress. The OS algorithm (Fig. 8A) moves quite efficiently towards the minimum, but has difficulties locating its exact value. The LM algorithm (Fig. 8B) is the most efficient search algorithm for this multi-component nonlinear problem. SA (Fig. 8C) first explores the region near the starting point extensively. It is only when uphill moves are accepted less frequently that the search for the minimum becomes more efficient. The OE scheme (Fig. 8D) searches a large parameter space, most of which is outside the range shown.

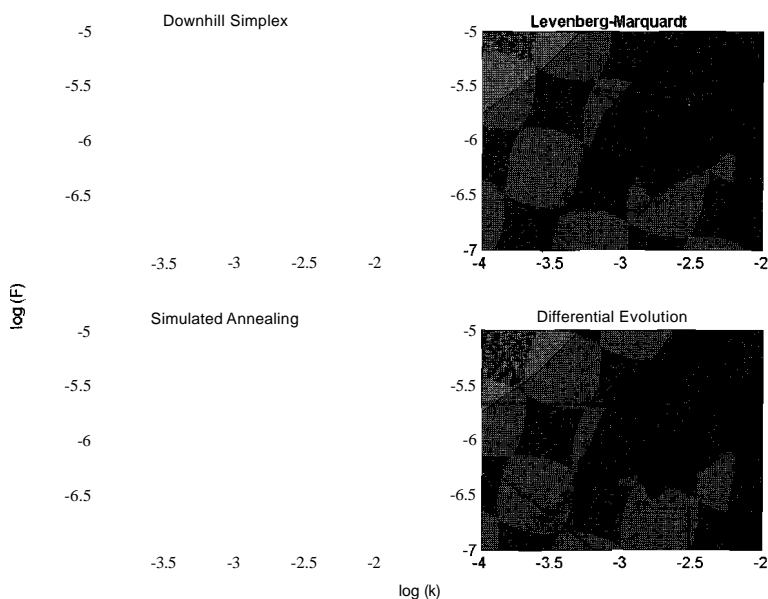


Figure 8. Progress of optimization for different algorithms. Crosses indicate parameter sets at which the objective function has been evaluated. Based on these model runs the topography is estimated. The gray scale gives the value of the objective function (dark color = low values). The lines indicate the path of the optimization. The minimum is located at  $(\log k / \log F) = (-2.52 / -5.68)$  and the starting point at  $(-3.52 / -6.68)$ .

In the particular case studied here, the  $OF$  varies fairly smoothly with both  $k$  and  $F$ . The sampling density of the  $OF$  is indicated by the crosses in Fig. 8. At this sampling scale, the topography does not show any local minima. Hence, there is no obvious advantage to use a global search algorithm. This is why LM is the most efficient search procedure in this case. However, it is important to keep in mind that the  $OF$  topography is not known a priori. Therefore, use of multiple optimization strategies is still recommended.



An important caveat arises when using unconstrained search strategies as they may lead to parameter values that cause inconsistency between model representation and actual system dynamics.

For example, in this application, methanogenesis is not included in the reaction network. Hence, if optimization algorithms generate high values of  $F$ , this will lead to a depletion of all terminal electron acceptors. In this case, the description of organic matter respiration incorporated in the RTM falls short. Similarly, if very low degradation rate constants are generated, the zero gradient condition imposed at the lower boundary of the spatial domain may not represent the natural environment appropriately. Therefore, to guarantee physical meaning of the simulations, the forward RTM should be defined in such a way that it remains a valid representation of reality for all parameter combinations encountered during optimization. In practice, the appropriateness of the RTM may sometimes be difficult to assess. This argues for the use of comprehensive RTMs. As the above example aims at illustrating the capability of the optimization procedures, a throughout analysis has not been performed here.

## **Conclusions**

The various optimization strategies presented here perform well for both synthetic objective functions and the early diagenetic scenario. However, they can all fall short finding the global minimum. In practice, it is therefore recommended to use a combination of optimization algorithms. In well constrained cases, LM is the method of choice due to its efficiency, but when largely unknown parameters are involved, one may need to resort to more general search strategies such as SA or DE.

The BRNS is a modern tool for modeling the dynamics of aquatic systems. The general transport description and flexible implementation of the reaction network allows the use of a single modeling environment for estuaries (REGNIER et al., 1997), aquatic sediments or groundwater systems (REGNIER et al., 2003). The incorporation of a suite of optimization algorithms extends the capabilities of the BRNS significantly. Poorly known model parameters and complex reaction networks are indeed commonly encountered when modeling environmental systems. Therefore, with its new facilities, the BRNS can cope with one of the most pressing issues in the field of biogeochemistry.

## Appendix: Discretization

The governing transport equation

$$\xi(x) \cdot \frac{\partial C(x,t)}{\partial t} = \frac{\partial \left( D(x) \cdot \xi(x) \cdot \frac{\partial C(x,t)}{\partial x} \right)}{\partial x} - \frac{\partial (V(x) \cdot \xi(x) \cdot C(x,t))}{\partial x} \quad (A1)$$

is discretized by calculating the fluxes at faces:

$$\left( \xi_i \frac{\partial C}{\partial t} \right)_i = \frac{\left( D \cdot \xi \cdot \frac{\partial C}{\partial x} \right)_{i+1} - \left( D \cdot \xi \cdot \frac{\partial C}{\partial x} \right)_{i-1}}{x_{i+1} - x_{i-1}} - \frac{(v \cdot \xi \cdot C)_{i+1} - (v \cdot \xi \cdot C)_{i-1}}{x_{i+1} - x_{i-1}} \quad (A2)$$

where  $i$  denotes a spatial node and  $i \pm 1$  are faces (in between nodes). Time is incorporated with an Euler approximation for the temporal derivative and a semi-implicit/explicit description.

$$\xi_i \cdot \frac{C_i^{n+1} - C_i^n}{\Delta t} = \alpha \cdot \frac{D_{i+1} \xi_{i+1} \frac{C_{i+2}^{n+1} - C_{i+1}^{n+1}}{x_{i+2} - x_{i+1}} - D_{i-1} \xi_{i-1} \frac{C_{i+1}^{n+1} - C_{i-2}^{n+1}}{x_i - x_{i-2}}}{x_{i+1} - x_{i-1}} - \frac{v_{i+1} \xi_{i+1} \frac{C_{i+1}^{n+1} - v_{i-1} \xi_{i-1} \frac{C_{i-1}^{n+1}}{i-1}}{x_{i+1} - x_{i-1}}}{x_{i+1} - x_{i-1}} + (1-\alpha) \cdot \frac{D_{i+1} \xi_{i+1} \frac{C_{i+2}^n - C_{i+1}^n}{x_{i+2} - x_{i+1}} - D_{i-1} \xi_{i-1} \frac{C_i^n - C_{i-2}^n}{x_i - x_{i-2}}}{x_{i+1} - x_{i-1}} - \frac{v_{i+1} \xi_{i+1} \frac{C_{i+1}^n - v_{i-1} \xi_{i-1} \frac{C_{i-1}^n}{i-1}}{x_{i+1} - x_{i-1}}}{x_{i+1} - x_{i-1}} \quad (A3)$$

where the superscript  $n$  is a time index. Thus, this scheme varies from explicit ( $\alpha=0$ ) to Crank-Nicholson ( $\alpha=0.5$ ) to implicit ( $\alpha=1$ ).

### Concentrations at faces

Concentrations at the faces can be obtained by linear interpolation from the nodes to the coordinates of the faces:

$$C_{i+1} \approx C_i + \frac{x_{i+1} - x_i}{x_{i+2} - x_i} (C_{i+2} - C_i) \quad \text{and} \quad C_{i-1} \approx C_i - \frac{x_i - x_{i-1}}{x_i - x_{i-2}} (C_i - C_{i-2}) \quad (M)$$

For variable grid spacing, the coordinates of faces are set such that the nodes are midpoints between faces, which can be changed by the user as desired. However, significant differences of the estimated concentration at the faces are only expected in regions with large concentration gradients coinciding with a coarse grid, indicative of a poor choice for the discretization.

### Discretized equation and matrix notation

Substitution of Eq. A4 into Eq. A3, separating terms of old and new concentrations and regrouping gives:

$$\begin{aligned}
 & \frac{a}{(x_{i+1} - x_{i-1})} \cdot \left[ C_i^{n+1} \cdot \left[ \frac{D_{i+1} \xi_{i+1}}{x_{i+2} - x_i} - v_{i+1} \xi_{i+1} \frac{x_{i+1} - x_i}{x_{i+2} - x_i} \right] \right. \\
 & \quad + C_i^{n+1} \cdot \left[ \frac{D_{i+1} \xi_{i+1}}{x_{i+2} - x_i} - \frac{D_{i-1} \xi_{i-1}}{x_i - x_{i-2}} \right. \\
 & \quad \quad \left. \left. - v_{i+1} \xi_{i+1} \left( 1 - \frac{x_{i+1} - x_i}{x_{i+2} - x_i} \right) + v_{i-1} \xi_{i-1} \left( 1 - \frac{x_i - x_{i-1}}{x_i - x_{i-2}} \right) \right] \right] \cdot \left( \frac{\Delta t}{\xi_i} \right) - C_i^{n+1} \\
 & \quad + C_{i-2}^{n+1} \cdot \left[ \frac{D_{i-1} \xi_{i-1}}{x_i - x_{i-2}} + v_{i-1} \xi_{i-1} \frac{x_i - x_{i-1}}{x_i - x_{i-2}} \right] \\
 & \quad \cdot \left( \frac{\Delta t}{\xi_i} \right) - C_i^{n+1} \\
 & \quad \cdot \left[ C_{i+2}^n \cdot \left[ \frac{D_{i+1} \xi_{i+1}}{x_{i+2} - x_i} - v_{i+1} \xi_{i+1} \frac{x_{i+1} - x_i}{x_{i+2} - x_i} \right] \right. \\
 & \quad \quad + C_i^n \cdot \left[ \frac{D_{i+1} \xi_{i+1}}{x_{i+2} - x_i} - \frac{D_{i-1} \xi_{i-1}}{x_i - x_{i-2}} \right. \\
 & \quad \quad \left. \left. - v_{i+1} \xi_{i+1} \left( 1 - \frac{x_{i+1} - x_i}{x_{i+2} - x_i} \right) + v_{i-1} \xi_{i-1} \left( 1 - \frac{x_i - x_{i-1}}{x_i - x_{i-2}} \right) \right] \right] \cdot \left( \frac{\Delta t}{\xi_i} \right) - C_i^n \\
 & \quad + C_{i-2}^n \cdot \left[ \frac{D_{i-1} \xi_{i-1}}{x_i - x_{i-2}} + v_{i-1} \xi_{i-1} \frac{x_i - x_{i-1}}{x_i - x_{i-2}} \right] \\
 & \quad \cdot \left( \frac{\Delta t}{\xi_i} \right) - C_i^n
 \end{aligned} \tag{AS}$$

Eq. AS can be written as  $\alpha C_i^{n+1} + bb_i \cdot C_i^{n+1} + c_i \cdot C_{i+2}^{n+1} = d_i (C_{i-2}^n, C_i^n, C_{i+2}^n)$ , or in matrix form as  $M \cdot C^{n+1} = di(C^n)$  (A6)

Thus, defining  $bb$  as the diagonal of the tridiagonal matrix  $M$ ,  $aa$  the off diagonal below, and  $c$  as the off diagonal above, and multiplying both sides with  $\frac{\xi_i}{\Delta t}$ , the coefficients are:

$$\begin{aligned}
 aa_j &= a \cdot m_a \\
 bb_i &= a' m_b - \frac{\xi_i}{\Delta t} \\
 c_i &= \alpha \cdot m_c \\
 d_i &= (\alpha - 1) (m_a C_{i-2}^n + m_b C_i^n + m_c C_{i+2}^n) - \frac{\xi_i}{\Delta t} \cdot C_i^n
 \end{aligned} \tag{A7}$$

with

$$\begin{aligned}
m_a &= \left[ \frac{D_{i-1} \xi_{i-1}}{x_i - x_{i-2}} + v_{i-1} \xi_{i-1} \frac{x_i - x_{i-1}}{x_i - x_{i-2}} \right] \cdot \frac{1}{(x_{i+1} - x_{i-1})} \\
m_b &= \left[ \frac{D_{i+1} \xi_{i+1}}{x_{i+2} - x_i} - \frac{D_{i-1} \xi_{i-1}}{x_i - x_{i-2}} \right. \\
&\quad \left. - v_{i+1} \xi_{i+1} \left( 1 - \frac{x_{i+1} - x_i}{x_{i+2} - x_i} \right) + v_{i-1} \xi_{i-1} \left( 1 - \frac{x_i - x_{i-1}}{x_i - x_{i-2}} \right) \right] \cdot \frac{1}{(x_{i+1} - x_{i-1})} \\
m_c &= \left[ \frac{D_{i+1} \xi_{i+1}}{x_{i+2} - x_i} - v_{i+1} \xi_{i+1} \frac{x_{i+1} - x_i}{x_{i+2} - x_i} \right] \cdot \frac{1}{(x_{i+1} - x_{i-1})}
\end{aligned} \tag{A8}$$

### Boundary conditions

The coordinate system is defined such that system boundaries are located at nodes rather than faces. Thus, fixing a concentration is straightforward, while defining gradients or fluxes requires approximation of gradients of  $C$ ,  $D$ ,  $v$  or  $\xi$  with respect to  $x$  at the boundaries. The strategy employed here is to estimate the concentration at a point outside the domain based on the (central) finite difference approximation, the concentrations within the domain and the gradient or flux information at the boundary and then solve the governing equation (Eq. A1) at the boundary.

#### Known concentration (Dirichlet)

For a known concentration at a node  $i$ ,  $C_i = C_{known}$  the matrix coefficients are simply:

$$aa_i = 0, bb_i = 1, e_i = 0, d_i = C_{known} \tag{A9}$$

#### Known concentration gradient (Neumann)

The boundary condition is:

$$g = \frac{\partial C}{\partial x} \Big|_{\text{boundary}} = \frac{(X_{i+2} - x_i)}{(x_i - x_{i-2})(X_{i+2} - x_{i-2})} C_{i-2} + \frac{(X_{i+2} - x_i)}{(x_i - x_{i-2})(X_{i+2} - x_i)} C_i + \frac{(X_i - X_{i-2})}{(x_{i+2} - x_i)(X_{i+2} - x_{i-2})} C_{i+2} \tag{A10}$$

In general, the concentration outside the domain ( $C_{out}$ ) can be expressed in terms of the concentration at the boundary ( $C_i$ ) and the one adjacent inside the domain ( $C_{in}$ ):

$$C_{out} = \left[ \frac{-(X_{out} - X_i)}{(X_i - X_{in})(X_{out} - X_{in})} C_i - \frac{(X_{out} - 2x_j + X_{in})}{(X_i - X_{in})(X_{out} - X_i)} C_j \right] \cdot \frac{(X_{out} - X_i)(X_{out} - X_{in})}{(X_i - x_{in})} \tag{A11}$$

After substitution at the boundary and using the form introduced in Eq. A7, one obtains:

$$\begin{aligned}
bb_i &= a' m_b + a \cdot m_a \left[ \frac{(x_{out} - 2x_j + x_{in})}{(x_j - x_{in})} \cdot \frac{(x_{out} - x_{in})}{(x_j - x_{in})} \right] - \frac{\xi_i}{\Delta t} \\
d_i &= (a \cdot I) \left[ m_a \left( \frac{-(X_{out} - 2x_j + x_{in})}{(X_i - x_{in})} \cdot \frac{(X_{out} - x_{in})}{(X_i - x_{in})} \right) C_i^n + m \frac{(X_{out} - x_i)^2}{a (X_i - x_{in})^2} C_{in} \right. \\
&\quad \left. + m \frac{(X_{out} - X_i)(X_{out} - X_{in})}{(X_i - x_{in})} g + m C_i^n + m C_{in}^n \right] \\
&\quad - a \left[ m_a \frac{(X_{out} - x_i)(x_{out} - X_{in})}{(X_i - x_{in})} g \right] - \frac{\xi_i}{\Delta t} C_i^n
\end{aligned} \tag{A12.1}$$

If the gradient is defined at the upper boundary, then

$$aa_i = 0; c_j = a \cdot m_c + a \cdot m_a \left[ \frac{(x_{out} - x_j)^2}{(x_i - x_{in})^2} \right] \tag{A12.2}$$

whereas at the lower boundary

$$aa = a \cdot m_a + a' m_c \left[ \frac{(X_{out} - x_i)^2}{(x_i - x_m)^2} \right]; c_i = 0 \quad (\text{AI2.3})$$

### Known flux condition (Robin)

A known flux at the boundary is described by:

$$F_{known} = - \frac{\partial(D\xi C)}{\partial x} \Big|_i + (v\xi C)_i = -D_i \xi_i \frac{\partial \xi}{\partial x} \Big|_i - D_i C_i \frac{\partial \xi}{\partial x} \Big|_i - C_i \xi_i \frac{\partial D}{\partial x} \Big|_i + v_i \xi_i C_i \quad (\text{AI3})$$

Approximation of the concentration gradient gives

$$\begin{aligned} F_{known} = & C_{1-2} \left[ -D_i \xi_i \frac{-(X_{i+2} - x_i)}{(x_i - x_{i-2})(x_{i+2} - x_{i-2})} \right] \\ & + C_i \left[ -D_i \xi_i \frac{(x_{i+2} - x_i) - (x_i - x_{i-2})}{(x_i - x_{i-2})(x_{i+2} - x_i)} \frac{D}{\partial x} \Big|_i + v_i \xi_i \right] \\ & + C_{i+2} \left[ -D_i \xi_i \frac{(X_i - X_{i+2})}{(X_{i+2} - x_{i-2})} \right] \end{aligned} \quad (\text{AI4})$$

In general terms, the concentration outside is hence

$$c_{out} = \left[ C_i \left[ -D_i \xi_i \frac{(x_{out} - 2x_i + x_m)}{(x_i - x_m)(x_{out} - x_i)} \frac{D}{\partial x} \Big|_i - \xi_i \frac{\partial D}{\partial x} \Big|_i + v_i \xi_i \right] \frac{(x_{out} - x_i)(x_{out} - x_m)}{D_i \xi_i (x_i - x_m)} \right. \\ \left. + C_m \left[ -D_i \xi_i \frac{-(x_{out} - x_i)}{(x_i - x_m)(x_{out} - x_m)} \frac{J-F_{known}}{D_i \xi_i (x_i - x_m)} \right] \right] \quad (\text{AI5})$$

and the resulting matrix coefficients are:

$$\begin{aligned} bb = & a' m_a \left[ -D_i \xi_i \frac{(x_{out} - 2x_i + x_m)}{(x_i - x_m)(x_{out} - x_i)} \frac{D}{\partial x} \Big|_i - \xi_i \frac{\partial D}{\partial x} \Big|_i + v_i \xi_i \right] \frac{(x_{out} - x_i)(x_{out} - x_m)}{D_i \xi_i (x_i - x_m)} \\ & + a' m_b + \frac{\xi_i}{\Delta t} \\ d_i = & (a-1) \left[ m_a \left( -D_i \xi_i \frac{(x_{out} - 2x_i + x_m)}{(x_i - x_m)(x_{out} - x_i)} \frac{D}{\partial x} \Big|_i - \xi_i \frac{\partial D}{\partial x} \Big|_i + v_i \xi_i \right) \frac{(x_{out} - x_i)(x_{out} - x_m)}{D_i \xi_i (x_i - x_m)} C_i^n \right. \\ & \left. + m_a \frac{(x_{out} - x_i)^2}{(x_i - x_m)^2} C_m^n + m_a \left( -\frac{(x_{out} - x_i)(x_{out} - x_m)}{D_i \xi_i (x_i - x_m)} F_{known} \right) + m_b C_i^n + m_c C_m^n \right] \\ & - a' m \left[ -D_i \xi_i \frac{(X_{out} - 2x_i + X_m)}{(X_i - x_m)(X_{out} - x_i)} \frac{D}{\partial x} \Big|_i - \xi_i \frac{\partial D}{\partial x} \Big|_i + v_i \xi_i \right] \frac{(x_{out} - x_i)(x_{out} - x_m)}{D_i \xi_i (X_i - x_m)} \frac{\xi_i}{\Delta t} C_i^n \end{aligned} \quad (\text{AI6.1})$$

If the flux is defined at the upper boundary, then

$$aa = a' c = a \cdot m_c + a' m \left[ \frac{(x_{out} - X_i)}{(x_i - x_m)} \right] \quad (\text{AI6.2})$$

whereas at the lower boundary

$$aa = a \cdot m_a + a' m_c \left[ \frac{(x_{out} - x_i)^2}{(x_i - x_m)^2} \right]; c = 0 \quad (\text{AI6.3})$$

Note that calculation of the derivatives of  $\xi, D, v$  (Eq. AI6.1) with respect to  $x$  involves points outside the domain. By default, the property outside the domain is approximated by linear extrapolation:

$$P_{out} = P_i + \frac{r_m - P_i}{X_{in} - X_i} (x_{out} - X_i) \quad (A17)$$

where  $x_{out}$  is set to the coordinates of the ghost concentration and  $i$  is situated at the boundary. Consistency of the extrapolation is checked by restricting it to physically sensible values such as  $D \geq 0$  and  $1 \geq \phi \geq 0$ . Alternatively, if additional information is available, these coefficients outside the domain can be explicitly defined by the user.

Finally, in advection dominated systems, central difference approximations may not be stable. Hence, the BRNS currently also contains an upwind scheme. Future extensions will incorporate more elaborate transport schemes such as weighted finite differences (BOUDREAU, 1997; FIADREIRO and VERONIS, 1977) or TVD schemes (STEEFEL and MACQUARRIE, 1996). Due to the modular operator splitting approach, the BRNS is well suited for such incremental improvements.

## References

- Barry D. A., Miller C. T., and Culligan-Hensley P. J. (1996) Temporal discretisation errors in non-iterative split-operator approaches to solving chemical reaction/groundwater transport models. *Journal of Contaminant Hydrology* 22, 1-17.
- Bliet C., Spallucci P., Vicente L. N., Neumaier A., Granvilliers L., Monfroy E., Benhamou F., Huens E., Van Hentenryck P., Sam-Haroud D., and Faltings B. (2001) The Coconut Project: Algorithms for Solving Nonlinear Constrained and Optimization Problems: The State of The Art. ILOG, TO Darmstadt, University of Coimbra, University of Viemla, University of Nantes, Catholic University of Louvain, Swiss Federal Institute of Technology.
- Bohachevsky I. O., Honson M. E., and Stein M. L. (1995) Simulated annealing and generalizations. In *Adaption of Simulated Annealing to Chemical Optimization Problems* (ed. J. H. Kalivas), pp. 3-24. Elsevier.
- Bohachevsky I. O., Johnson M. E., and Stein M. L. (1986) Generalized simulated annealing for function optimization. *Technometrics* 28(3), 209-217.
- Boudreau B. P. (1997) *Diagenetic Models and Their Implementation*. Springer.
- Bmn R., Reichert P., and Kiinsch H. R. (2001) Practical identifiability analysis of large environmental simulation models. *Water Resources Research* 37(4), 1015-1030.
- Cardoso M. F., Salcedo R. L., and Feyo de Azevedo S. (1996) The simplex-simulated annealing approach to continuous non-linear optimization. *Computers and Chemical Engineering* 20(9), 1065-1080.
- Cavalier F. (2001) *Le controle global de VIRGO*. Habilitation, Universite Paris-Sud.
- Chilakapati A. (1995) RAFT: a simulator for reactive flow and transport of groundwater contaminants. Pacific Northwest Laboratory.
- Fiadairo M. E. and Veronis G. (1977) On weighted-mean schemes for the finite-difference approximation to the advection-diffusion equation. *Tellus* 29, 512-522.
- Finsterle S. (1999) *iTough2 User's Guide*, pp. 130. Earth Sciences Division, Lawrence Berkeley National Laboratory, University of California.
- Forbes G. W. and Jones A. E. W. (1990) Towards global optimization with adaptive simulated annealing. *International Lens Design Conference*, 144-153.
- Gill P. E., Murray W., and Wright M. H. (1981) *Practical optimization*. Academic Press.
- Gomez C. (1990) MACROFORT: a FORTRAN code generator in MAPLE. INRIA.
- Jones A. E. W. and Forbes G. W. (1995) An adaptive simulated annealing algorithm for global optimization over continuous variables. *Journal of Global Optimization* 6, 1-37.
- Kaluarachchi J. J. and Morshed J. (1995) Critical assessment of the operator-splitting technique in solving the advection-dispersion-reaction equation: 1. First-order reaction. *Advances in Water Resources* 18(2), 89-100.
- Lasaga A. C. (1998) *Kinetic theory in the Earth Sciences*. Princeton University Press.
- Metropolis N., Rosenbluth A., Rosenbluth M., Teller A., and Teller E. (1953) Equation of state calculations by fast computing machines. *Journal of Chemical Physics* 21(6), 1087-1092.

- Morshed J. and Kaluarachchi J. J. (1995) Critical assessment of the operator-splitting technique in solving the advection-dispersion-reaction equation: 2. Monod kinetics and coupled transport. *Advances in Water Resources* 18(2), 101-110.
- Nelder J. A. and Mead R. (1965) A simplex method for function minimization. *Computer Journal* 7, 308-313.
- Noye J. (1984) Finite Difference Techniques for Partial Differential Equations. In *Computational Techniques for Differential Equations*, Vol. 83 (ed. J. Noye), pp. 95-354. Elsevier.
- Osborne M. R. (1985) *Finite Algorithms in Optimization and Data Analysis*. John Wiley&Sons.
- Park M.-W. and Kim Y.-D. (1998) A systematic procedure for setting parameters in simulated annealing algorithms. *Computers & Operations Research* 25(3), 207-217.
- Press W. H., Flannery B. P., Teukolsky S. A., and Vetterling W. T. (1992) *Numerical Recipes (Fortran Version)*. Cambridge University Press.
- Regnier P., Jourabchi P., and Slomp C. (2003) Reactive transport modeling as a technique for understanding coupled biogeochemical processes in surface and subsurface environments. *Netherlands Journal of Geosciences*.
- Regnier P., O'Kane J. P.O., Steefel C. I., and Vanderborght J. P. (2002) Modeling complex multi-component reactive-transport systems: towards a simulation environment based on the concept of a Knowledge Base. *Applied Mathematical Modelling* 26(9),913-927.
- Regnier P., Wollast R., and Steefel C. I. (1997) Long-term fluxes of reactive species in macrotidal estuaries: Estimates from a fully transient, multicomponent reaction-transport model. *Marine Chemistry* 58, 127-145.
- Steefel C. I., and MacQuarrie K. T. B. (1996) Approaches to modeling of reactive transport in porous media. [n *Reactive transport in porous media*. Vol. 34 (ed. P. C. Lichtner, C. I. Steefel, and E. H. Oelkers), pp. 83-130. Mineralogical Society of America.
- Storn R. and Price K. (1995) Differential Evolution - A simple and efficient adaptive scheme for global optimization over continuous spaces. rcs].
- Storn R. and Price K. (1996) Minimizing the real functions of the rCEC'96 contest by Differential Evolution. *IEEE International Conference on Evolutionary Computation*, 842-844.
- van Laarhoven P. J. M. and Aarts E. H. L. (1987) *Simulated Annealing: Theory and Applications*, pp. 186. Kluwer Academic Publishers.
- Wang Y. and Van Cappellen P. (1996) A multicomponent reactive transport model of early diagenesis: Application to redox cycling in coastal marine sediments. *Geochimica et Cosmochimica Acta* 60(16), 2993-3014.
- Yeh G. T. and Tripathi V. S. (1989) A critical evaluation of recent developments in hydrogeochemical transport of reactive multichemical components. *Water Resources Research* 25(1),93-108.

***CURRICULUM VITAE***

Christof Meile, born on August 20, 1970 in Milnsterlingen, Switzerland

- 1990-1996: Swiss Federal Institute of Technology Zurich (ETHZ)  
Department of Environmental Sciences  
Dipl. Nat. Wiss.
- 1996-1997: Swiss Federal Institute of Environmental Sciences (EAWAG)  
Department of Environmental Physics and  
Department of Biogeochemistry  
Research Assistant
- 1998-1999: Georgia Institute of Technology  
School of Earth and Atmospheric Sciences  
M.Sc., Certificate in Geohydrology
- 1999-2003: Utrecht University  
Faculty of Earth Sciences, Department of Geochemistry  
Ph.D.